Imperial College London
Department of Mechanical Engineering

A Stochastic Model for Turbulent Poly-Disperse flows

Ioannis Pesmazoglou

May 2014

Supervised by Salvador Navarro-Martinez and Andreas M Kempf

Submitted in part fulfilment of the requirements for the degree of Doctor of Philosophy in Mechanical Engineering of Imperial College London
and the Diploma of Imperial College London

Abstract

A poly-disperse particle description using a Lagrangian Stochastic (LS) framework coupled to Large Eddy Simulations (LES) of turbulent flows is presented. The aforementioned frameworks are outlined leading to the LES-coupled spray-pdf equation and its equivalent Stochastic Differential Equations. Three particle processes are investigated: particle dispersion, nucleation and aggregation. The aim of this work is to integrate or extend the models of these processes into the LES-LS framework and evaluate the predictive ability of the developed models.

Dispersion in LES is described in conjunction with a stochastic sub-grid model to accurately represent the path of a particle. Such models have a free parameter, the dispersion coefficient, which is not universal. A dynamic model for the evaluation of this coefficient is proposed. The model's predictive ability is investigated in decaying homogeneous isotropic turbulence and a turbulent mixing layer. *Nucleation* is modelled in a probabilistic manner where the frequency of events is determined from local equilibrium conditions. Two methodologies for the sub-grid influence on nucleation rates are implemented. A turbulent Dibutyl-Phthalate laden Nitrogen jet experiment is used for validation. *Aggregation* is an inter-particle process which involves a multitude of different physicochemical mechanisms. Particles in the nano-scale are considered, with a concentration that renders their direct simulation as individual real particles intractable. A stochastic aggregation model is presented and its performance is evaluated against analytic solutions, a Planar Jet, and a turbulent jet configuration. It is concluded that the LES-spray pdf framework can be used to develop models from phenomenological arguments that accurately describe complex turbulent poly-disperse flows.

Copyright Declaration

The copyright of this thesis rests with the author and is made available under a Creative Commons Attribution Non-Commercial No Derivatives licence. Researchers are free to copy, distribute or transmit the thesis on the condition that they attribute it, that they do not use it for commercial purposes and that they do not alter, transform or build upon it. For any reuse or redistribution, researchers must make clear to others the license terms of this work.

Declaration of Originality

I, Ioannis Pesmazoglou, declare that the work presented in the thesis *A Stochastic Model for Turbulent Poly-Disperse flows* is my own and that anyone elses work has been appropriately referenced.

Acknowledgments

The financial support of the EPSRC and Imperial College through a DTA award is gratefully acknowledged. I would like to thank my supervisor Dr. Salvador Navarro-Martinez for his intellectual and psychological support throughout the process of my research. He always found the time to discuss the problems I encountered and always, with a genuine consideration, helped me to overcome any obstacles. I would like to thank Prof. Andreas Kempf for his help in finding the funding to pursue my interest in fluid mechanics at a post graduate level and for his useful support and insight during the project. Alexandros Charogiannis, Benjamin Franchetti, and Fabrizio Cavallo Marincola played a crucial role both with regards to my initial choice of pursuing a PhD and in making the course of my research all the more interesting. I would like to thank the rest of the 'old' group: Stefan Wysocki, Terrence Ma and especially Mike Pettit who devoted a lot of time in helping me when in need. Remaining the sole witness in a 'change-of-guard', which occured in the office, I was lucky to meet the newcomers: Nefeli Dimela, Teddy Szemberg O'Connor, and Shaoxi Yu, who made the final stretch a lot more enjoyable. Thanks also to all of my friends who facilitated a wonderful carrot and stick approach to my weekly routine. Last but not least I would like to thank my parents and Anastasia for their tremendous support and patience; I cannot but dedicate this work to them.

Contents

1. Introduction **27**

1.1. A note on the title 27

1.2. Contextualization of poly-disperse flows: the need for accurate modelling 28

1.3. Thesis Aims 30

1.4. Thesis Outline 31

2. Continuous Phase Fluid Dynamics **33**

2.1. Mathematical description 33

2.2. Turbulence 35

2.3. Numerical modelling of Turbulent Flows 37

2.3.1. Reynolds Average Navier-Stokes (RANS) 38

2.3.2. Direct Numerical Simulation (DNS) 39

2.3.3. Large Eddy Simulation (LES) 39

2.4. Modelling turbulent flows with LES 40

2.4.1. Governing Equations for LES 40

2.4.2. Sub Grid Scale Closure 41

3. Disperse Phase and Stochastic Processes **44**

3.1. Particle Physics Framework 44

3.1.1. The Lagrangian Approach 44

3.1.2. Particle Motion 45

3.1.3. Physical Processes 48

3.2. Stochastic Framework 50

3.2.1. The Stochastic Diffusion Process 50

3.3. Stochastic modelling of Inertial Particles 61

3.3.1. The Spray-PDF Equation 61

3.3.2. Modelling the Jump Term: The PBE 64

3.3.3. Solution Frameworks for the PBE and Spray-pdf . . . 68

4. Modelling the Disperse Phase in Present LES **75**
4.1. Problem Formulation: The Filtered spray-pdf 75
4.1.1. Flow coupling 76
4.1.2. Numerical Implementation 79
4.2. Dispersion 81
4.2.1. A contextualization of the study: the need for sgs modelling in particle dispersion 81
4.2.2. Incorporating the sub grid effects: The Lagrangian Stochastic Model 82
4.2.3. Lagrangian Stochastic Dispersion using the Filtered spray-pdf 86
4.2.4. Proposed dynamic model for the evaluation of the dispersion coefficient 89
4.3. Nucleation 93
4.3.1. Contextualization of nucleation: the need for accurate modelling 94
4.3.2. Nucleation Rate 95
4.3.3. Turbulent coupling 99
4.3.4. Proposed incorporation of nucleation in the spray-pdf equation 101
4.3.5. Modelling the SGS influencing Nucleation rates 107
4.4. Aggregation 112
4.4.1. Contextualization of aggregation: the need for accurate modelling 112
4.4.2. The aggregation kernel 114
4.4.3. Aggregation in Turbulent Flows 123
4.4.4. Proposed incorporation in the spray-pdf equation . . . 133
4.5. Interim Summary 144

5. An Investigation of dispersion in turbulent flows **145**
5.1. Validation of the Dynamic model 145
5.1.1. Configuration and Modelling Parameters 145
5.1.2. Results 149
5.2. Investigating Grid Dependence of C_o in a Shear Mixing Layer: 152
5.2.1. Experimental Configuration and Modelling Parameters 152
5.2.2. Results 155

5.3. Conclusions . . . 167

6. Nucleation in a turbulent jet **170**
6.1. Choice of DBP . . . 170
6.2. Experimental Configuration and Modeling parameters . . . 171
6.3. Results . . . 174
6.3.1. Gas phase . . . 174
6.3.2. Nucleation Rate . . . 175
6.3.3. Particle Concentration . . . 179
6.3.4. Effects of sub grid-scales . . . 181
6.4. Conclusions . . . 186

7. Aggregation in a turbulent jet **188**
7.1. Preliminary model validation . . . 188
7.1.1. Particle depletion due to aggregation . . . 188
7.1.2. Evolution of the Particle Size Distribution . . . 194
7.2. Nanoparticle aggregation in a planar jet . . . 202
7.2.1. Configuration and Modelling Parameters . . . 202
7.2.2. Results . . . 204
7.3. SiO_2 aggregation in a turbulent round jet . . . 210
7.3.1. Experimental Configuration and Modelling Parameters 210
7.3.2. Results . . . 213
7.4. Conclusions . . . 221

8. Summary and Major Conclusions **224**

Appendices **256**

A. PsiPhi Operation **257**
A.0.1. Discretization in Space . . . 257
A.0.2. Discretisatization in Time . . . 261
A.0.3. Boundary Conditions . . . 263

B. Collision Array Calculation **265**

List of Figures

2.1. Energy cascade and length scales 36

3.1. The evolution of the random variable realizations $[x_n, t_n]$ for a continuous process in time and space and a continuous Markov Process 52
3.2. The evolution of the random variable realizations $[x_n, t_n]$ following a Deterministic, Brownian, and Jump process. The blue line represents the sum of the aforementioned and it is mathematically represented by equation (3.19). 58

4.1. 2D weight interpolation between particle position and grid points. 79
4.2. If three cells have a constant nucleation rate of 0.4 particles per cell per second, the whole domain should produce one particle every 0.83 s. However due to the discrete nature of particles, each cell creates 0.4 particles i.e. no physical particles. If fluid enters from the left with a velocity of $U_f =$ 1m/s and a cumulative nucleation term is considered then as transported from the first cell to the last with a time-step of $1s$ a single particle is created in the last cell. 103
4.3. Consider three cells which have a constant nucleation rate of 0.4 particles per cell per second, the time-step is 0.5 s, and the inflow plane velocity is $U_f = 2$ m/s . A transported nucleation rate approach creates a bias towards particle creation in the final cell and a dependence between flow-through time and nucleation residence time. 104
4.4. The β-pdf distribution for different shape parameter values β_1 and β_2. 109

4.5. Aggregation kernels for five processes, where a particle with $d_{p,i} = 20$ nm collides with a particle of size $d_{p,j}$. 121
4.6. Relative (interaction) volume of two colliding parcels i, j. The relative volume is indicated by the dashed line. 135
4.7. Maximum number of real particles represented by one parcel as a function of particle diameter. 136
4.8. The mass exchange and collision events assuming that donor parcels always contain smaller particles than receiver parcels. 140
4.9. Flow chart of multi-collision aggregation model. 143

5.1. Schematic diagram of the case of Ahmed and Elghobashi [3]. A constant shear, S, is applied in the $y-$direction to which a decaying homogeneous isotropic turbulent field is superimposed. 22^2 particles are seeded on each of the $N_S = 22$ planes placed at equidistant positions in the direction of the shear. . 146
5.2. Temporal variation of the normalized Skewness (top) and Total Kinetic Energy (bottom), for the LES and DNS of Ahmed and Elgobashi [3]. 149
5.3. Temporal variation of the displacement variance in directions x and z compared to the DNS of [3] (points) for case A (top) and case B (bottom). 150
5.4. Experimental configuration of [32]. Particles are seeded in the fast stream. 153
5.5. Probability Density (PDF) and Cumulative Density (CDF) functions of the particle diameter in the test section of the flow. 154
5.6. Comparison of the Smagorinsky model and the Germano model for the evaluation of C_s in a medium grid spacing ($\Delta = 2$ mm) simulation. 156
5.7. Instantaneous snapshot of a passive scalar with: (a) $\Delta =$ 4 mm, (b) $\Delta = 2$ mm, (c) $\Delta = 1.5$ mm, (d) $\Delta = 0.8$ mm. A passive scalar to illustrate the mixing process is assigned as 1 in the slow stream (red) and 0 in the fast stream (blue). . 157

5.8. The position where self-similarity is reached for the velocity (red line in normalized sketches) and a linear mixing layer thickness, $\delta_{0.8}(X)$, starts developing, is strongly dependent on the transition length, X_{ss}. A virtual origin, X, is set at the position, X_{ss}, where the dotted line of normalized velocites u^* coincides with the self similar solution (red line). 157
5.9. Mixing ($\delta_{0.8}$, left) and momentum (θ_u, right) thicknesses versus normalized axial position X for different dispersion coefficients C_o=0-3,8 : (a) $\Delta = 0.8$ mm, (b) $\Delta = 1.5$ mm, (c) $\Delta = 2$ mm, (d) $\Delta = 4$ mm. 159
5.10. Normalized velocity u^* versus normalized height y^* for $\Delta =$ 0.8 mm for different dispersion coefficients and LES gas filtered velocity. 160
5.11. Normalized velocity u^* versus normalized height y^* for $\Delta =$ 1.5 mm for different dispersion coefficients and LES gas filtered velocity. 161
5.12. Normalized velocity u^* versus normalized height y^* for $\Delta =$ 2 mm for different dispersion coefficients and LES gas filtered velocity. 162
5.13. Normalized velocity u^* versus normalized height y^* for $\Delta =$ 4 mm for different dispersion coefficients and LES gas filtered velocity. 163
5.14. Mixing and momentum layer thickness absolute errors versus the dispersion coefficient Co, for various grid spacings Δ. Solid straight lines represent equivalent error using the dynamic model for C_{dyn}. 165
5.15. Mixing and momentum layer thickness maximum errors versus the dispersion coefficient Co, for various grid spacings Δ. Solid straight lines represent equivalent error using the dynamic model for C_{dyn}. 165
5.16. Contour plots of ensemble-averaged (top) and instantaneous (bottom) dynamic dispersion coefficient for: (a) $\Delta = 0.8$ mm (b) $\Delta = 1.5$ mm (c) $\Delta = 2$ mm (d) $\Delta = 4$ mm. 166
5.17. Average dynamic coefficient versus height in the mixing layer for the four grid spacings investigated, at $x = 100$ mm. . . . 167

6.1. Experimental configuration of [129]. The heated Nitrogen DBP-laden jet enters through an insulated nozzle in the diffusion chamber. A concentric flow of air at atmospheric conditions is added. Nucleated particles are sampled and counted using a probe leading, through a tube, to the Condensation Particle Counter. 171
6.2. Instantaneous (left) and mean (right) axial velocity contours 173
6.3. Normalized velocity plots 174
6.4. 175
6.5. Instantaneous (left) and mean (right) nucleation rate contour plots. The nucleation rate reached a peak $\sim \mathcal{O}(10^{11})$ [#/m^{3}s]. 176
6.6. Left: LES nucleation rate calculated from time-average instantaneous values, i.e. $\bar{\dot{I}}_{LES} = \left\langle \dot{I}\left(\tilde{\xi}\right)\right\rangle_t$, versus an equivalent 'naive' RANS where the nucleation rate is calculated using the time-averaged scalar values, i.e. $\bar{\dot{I}}_{eqRANS} = \dot{I}(\langle\tilde{\xi}\rangle_t)$. Right: pdf($\tilde{\xi}$) at the two locations marked A and B. 177
6.7. Nucleation diameters 178
6.8. RMS scalar on the centerline. 179
6.9. Instantaneous (left) and mean (right) particle concentrations. The range varies from $Nc = 0 - 3.65$ [# per cell]. 180
6.10. Particle concentration on the centerline in the axial direction. 181
6.11. Particle concentrations without closure are compared to two different sub grid closure models. The radial direction measurements are at positions $z/D_{jet} = 5, 10$, and 20 (moving from the bottom left corner to top right). 182
6.12. Mean nucleation rates without closure are compared to two different sub grid closure models. The radial direction measurements are at positions $z/D_{jet} = 5, 10$, and 20 (moving from the bottom left corner to top right). 183
6.13. Scatter plot of scalar sub-grid variance versus scalar LES value for the two locations 'A' and 'B' of Fig. 6.6 ($z = 10, 40$ mm, respectively). The solid (yellow) lines represent an ensemble averaged variance $\left\langle \widetilde{\xi''^2}|_{\tilde{\xi}}\right\rangle$ for every given value of $\tilde{\xi}$. 183

6.14. Instantaneous nucleation rate at $z/D_{jet} = 10$ calculated from the same LES using the source expansion and β-PDF methods, and with no model. Two details are shown at the locations marked 'A' and 'B'. 185

7.1. Total particle concentration versus dimensionless time for the same initial particle concentration using $n_0^* = 2.5\%$ and 25%. 189
7.2. Total particle concentration versus dimensionless time for the same initial particle concentration using $n_0^* = 25\%$, 2.5%, 0.25% and $n_{int} = 1$. 190
7.3. Error levels for different parcel internal populations n_{int}. . . . 191
7.4. Total particle concentration versus dimensionless time for the same initial particle concentration using $\Delta t^*_{aggr} = 10^{-1}, 10^{-2}, 10^{-4}$, and 10^{-5} and with $n_0^* = 1.0\%$. 192
7.5. Error levels for different temporal discretization. 193
7.6. Evolution of the PSD for an initial exponential distribution for $n_0^* = 25\%$, 2.5%, 0.25% and $n_{int} = 1$. 196
7.7. Relative error in the SMD for three residence times t =0, 10, and 20s for different cases of initial parcel internal population. 197
7.8. Evolution of the PSD with the Golovin kernel for an initial exponential distribution and $n_0^* V_{cell} = 25\%$, 2.5%, 0.25% and $n_{int} = 1$. 199
7.9. Relative error in the SMD for three residence times t =0, 0.5, 2s for different cases of initial parcel internal population. . . . 200
7.10. Configuration of nanoparticle-laden planar jet.. 202
7.11. Continuous phase radial velocity-profiles at four axial locations: $x/D_{jet} = 2, 6, 10$ and 11.5. 205
7.12. Ensemble average particle diameter compared with the results from the DNS of Miller and Garrick [155] at four axial locations: $x/D_{jet} = 2, 6$ and 10. 206
7.13. Pdf of particle sizes at the centerline compared to this at the shear layers at three axial locations. 207
7.14. Ensemble average particle diameter at two axial locations for the range of $D^*_{A,aggr}$ investigated. 208
7.15. Experimental configuration of Zhu *et al.* [277] and simulated domain. 210

7.16. Contour plot of temporal average (top) and instantaneous (bottom) filtered axial-velocity of the continuous phase. . . . 213
7.17. Mean and RMS uniform phase velocity variation in the axial direction. 214
7.18. Mean and RMS uniform phase velocity radial profiles at the four measurement points $x/D_{jet} = 2, 4, 6$ and 8. 214
7.19. Contour plot of temporal average (top) and instantaneous (bottom) particle concentration fields $N_c[\#/\Delta^3]$. 215
7.20. Radial particle concentrations N_c at four axial locations. . . . 216
7.21. Particle size distributions at the simulation inlet for different radial locations. The PSD at R =18mm is used for the background aggregation process. 217
7.22. Comparison of measured and simulated PSDs at four locations. 219
7.23. Variation of aggregation kernel for the range of particle-sizes considered (left) and plot of kernel variation for colliding particles with same diameters (top right). 220
7.24. Cumulative (total) aggregation events that occurred in a residence time of $t = 3.5$ s 221

A.1. Finite Volume Method domain decomposition and indexing. . 258

Nomenclature

Latin Symbols:

−**lowercase**		
a_p	$\frac{\mathrm{m}}{\mathrm{s}^2}$	Conditional rate of change of particle velocity
$b(\cdot)$	-	Breakage daughter distribution function
b_1	-	empirical parcel volume parameter
c	-	generic constant
d_A	m	surface-based aggregate particle diameter
d_{air}	m	air molecule diameter
d_f	m	particle fractal diameter
d_m	m	particle mobility diameter
d_p	m	particle diameter
d_{p0}	m	primary particle diameter
d_p^*	m	nuceation diameter
d_{32}	m	Sauter mean diameter
e_i	-	unit normal vector
$f(\cdot)$	-	generic function
f_c	-	control volume faces
f_D	-	fractal dimension
f_r	-	a factor/ratio of time-steps
g	$\frac{\mathrm{m}}{\mathrm{s}^2}$	gravitational acceleration
i	$\frac{\#}{\mathrm{m}^3\mathrm{s}}$	Lagrangian nucleation rate
k	$\frac{\mathrm{m}}{\mathrm{s}^2}$	kinetic energy

k_B	$\frac{J}{K}$	Boltzmann constant
k_{sgs}	$\frac{\mathrm{m}}{\mathrm{s}^2}$	unresolved kinetic energy of the fluid phase
l	m	length-scale
l_I	m	integral length-scale
l_m	m	mixing length-scale
l_p	m	parcel length-scale
m	kg	mass
$\bar{m}$	kg	mean mass of a monomer
m_k	-	k-th moment
m_p	kg	particle mass
n	-	a number
n_{coll}	-	Lagrangian parcel number of collisions
n_{int}	-	Lagrangian parcel real particle population
n_p	$\frac{\#}{\mathrm{m}^3}$	Lagrangian parcel particle number concentration
n_{pri}	-	number of primary particles in cluster
n_0^*	-	normalized initial parcel internal population
p	Pa	pressure
r	-	flux limiter gradient
$\mathbf{r}$	m	position in space
s_m	m^2	surface area of monomer
s_n	-	simulation number
t	s	time
t_I	s	Integral time-scale
t_k	s	Kolmogorov time-scale
u_i'	$\frac{\mathrm{m}}{\mathrm{s}}$	velocity fluctuation in i-direction
u_k	$\frac{\mathrm{m}}{\mathrm{s}}$	Kolmogorov velocity
u_p	$\frac{\mathrm{m}}{\mathrm{s}}$	Conditional rate of change of particle position

u_{rms}	$\frac{\mathrm{m}}{\mathrm{s}}$	rms velocity
$\bar{u}_T$	$\frac{\mathrm{m}}{\mathrm{s}}$	mean thermal velocity magnitude of continuous phase
$\bar{u}_{Tp}$	$\frac{\mathrm{m}}{\mathrm{s}}$	mean thermal velocity magnitude of disperse phase
$\mathbf{v}_f$	$\frac{\mathrm{m}}{\mathrm{s}}$	Lagrangian fluid velocity vector
$v_{f,i}$	$\frac{\mathrm{m}}{\mathrm{s}}$	Lagrangian fluid velocity component in i-direction
v_m	m^3	volume of monomer
$\mathbf{v}_p$	$\frac{\mathrm{m}}{\mathrm{s}}$	Lagrangian particle velocity vector
$v_{p,i}$	$\frac{\mathrm{m}}{\mathrm{s}}$	Lagrangian particle velocity component in i-direction
v_s	$\frac{\mathrm{m}}{\mathrm{s}}$	particle settling velocity
w_i	-	quadrature weight
x	m	spatial co-ordinate in x-direction
x_i, x_j	m	spatial co-ordinate in i, j-direction
x_{rel}	m	relative distance of interacting parcels
$\mathbf{x}_p$	m	Lagrangian particle position vector
$\mathbf{x}$	m	spatial co-ordinate
$\mathbf{x}$	-	Sec. 3.2: realization of generic random variable
y	m	spatial co-ordinate in y-direction
$\mathbf{y}$	-	Sec. 3.2: realization of generic random variable
z	m	spatial co-ordinate in z-direction

−uppercase

$\mathbf{A}, A_i$	-	generic drift vector and i-component
A	m^2	area
$\mathbf{B}, B_{ij}$	-	generic stochastic diffusion tensor and ij-component
$B(r)$	-	flux limiter for TVD scheme
C_D	-	drag coefficient
C_{dyn}	-	dynamic particle dispersion constant

C_{ij}	$\frac{\#}{\mathrm{m^3 s}}$	collision rate
C_o	-	particle dispersion constant
C_o^*	-	Kolmogorov dispersion constant
C_s	-	Smagorinsky model constant
C_{sgs}	-	expansion model constant
C_ξ	-	scalar variance model constant
CFL	-	Courant-Friedrichs-Lewy constant
D_A^*	-	nucleation Damkholer number
D_{jet}	m	jet diameter
D_n	$\frac{\mathrm{m^2}}{\mathrm{s}}$	mass diffusivity of specie n
D_p	$\frac{\mathrm{m^2}}{\mathrm{s}}$	particle diffusivity
E_0	J	continuous phase initial energy spectrum
E_T	J	continuous phase total kinetic energy
F_B	N	Brownian force
$F_{C_{f_c}}$	-	convective flux through control volume face
F_D	N	drag force
$F_{D_{f_c}}$	-	diffusive flux through control volume face
F_{Ey}	N	electrical force
F_G	N	gravity and buoyancy force
F_I	N	inertial force
F_L	N	shear-induced lift force
F_T	N	thermophoretic force
Fr	-	Froude number
G	$\frac{\mathrm{m^3}}{s}$	particle growth rate
G_i	-	Cunningham slip-flow correction factor
G_Δ	-	filter function
$G_{\hat{\Delta}}$	-	test filter function

$\dot{I}$	$\frac{\#}{\mathrm{m^3 s}}$	nucleation rate
$\mathbf{J}, J_i$	-	Lévy process scaling vector and i-component
Kn	-	Knudsen number
Kn_{air}	-	Knudsen number of air
Kn_p	-	particle equivalent Knudsen number
K_p	$\frac{\mathrm{m}}{\mathrm{s^2}}$	particle kinetic energy
L	m	length-scale
L_{ij}	$\frac{\mathrm{m^2}}{\mathrm{s^2}}$	Leonard stresses
Le	-	Lewis number
M	-	number of independent variables
$\bar{M}$	$\frac{\mathrm{kg}}{\mathrm{kmol}}$	molecular weight
N	-	number of realizations
N_{avg}	$\frac{\#}{\mathrm{kmol}}$	Avogadro number
N_{bg}	$\frac{\#}{\mathrm{m^3}}$	background particle number concentration
N_c	$\frac{\#}{\mathrm{m^3}}$	particle number concentration
N_0	$\frac{\#}{\mathrm{m^3}}$	initial particle number concentration
N_{ps}	-	number of particles per seeding plane
N_s	-	number of seeding planes
N_{tot}	-	total number of particles
P_{sat}	Pa	saturation pressure
P_v	Pa	vapor partial pressure
Pr	-	Prandtl number
Q	$\frac{\mathrm{m^3}}{\mathrm{s}}$	volumetric flow rate
R_{ij}	$\frac{\mathrm{m^2}}{\mathrm{s^2}}$	Reynolds stresses
Re	-	Reynolds number
Re_p	-	particle Reynolds number
Re_t	-	turbulent Reynolds number

Re_{θ_u}	-	Reynolds number based on momentum thickness
Rn	-	random number with uniform distribution
S	-	saturation ratio
$\dot{S}_{mass}$	$\frac{\mathrm{kg}}{\mathrm{s}}$	source/sink of mass term
$\dot{S}_{mom}$	$\frac{\mathrm{kg}}{\mathrm{m^2 s}}$	source/sink of mass term
$\dot{S}_{\mathcal{N}}$	-	PBE source term
$\dot{\mathbf{S}}_{\mathbb{P}}$	-	spray-pdf source term vector
S_{ij}	$\frac{1}{\mathrm{s}}$	strain rate
S_y	$\frac{\mathrm{m}}{\mathrm{s}}$	mean shear velocity in y-direction
Sc	-	Schmidt number
Sc_t	-	turbulent Schmidt number
Sk_u	-	fluid velocity skewness
St	-	Stokes number
T	K	temperature
$\mathbf{U}_f$	$\frac{\mathrm{m}}{\mathrm{s}}$	fluid velocity vector
U_i	$\frac{\mathrm{m}}{\mathrm{s}}$	fluid velocity component in i-direction
V_i	$\frac{\mathrm{m}}{\mathrm{s}}$	Eulerian particle velocity component in i-direction
V_{cell}	m^3	volume of a cell
V_{rel}	m^3	relative volume of interacting parcels
V_{sampl}	m^3	sampling volume
$\mathbf{V}_p$	$\frac{\mathrm{m}}{\mathrm{s}}$	particle velocity vector
$\mathbf{W}, W_i$	-	Wiener term vector and i-component
We	-	Webber number
$\mathbf{X}$	-	generic random variable
$\mathbf{X}_p$	m	particle position random variable
X_v	-	vapor molar concentration

$\mathbf{Y}$	-	generic random variable
Y_n	-	species mass fraction

−miscellaneous

$E[\cdot]$	-	statistical expectation
$\mathbb{F}$	-	fine-grained density function
$\mathcal{K}$	-	generic kernel
$\mathcal{N}$	-	particle number density
$\mathcal{N}_\alpha$	-	conditional particle number density
$\mathcal{O}$	-	order of
$\mathcal{P}$	-	generic probability density function
$\mathcal{P}_{nuc}$	-	nucleation probability
$\mathcal{P}_{aggr}$	-	aggregation probability
$\mathbb{P}$	-	spray probability density function
$\mathcal{U}$	$\frac{\mathrm{m}}{\mathrm{s}}$	velocity scale
$Var[\cdot]$	-	statistical variance
$\mathcal{W}$	-	generic jump term

Greek Symbols:

−lowercase

α	-	dispersion model linearity constant
α_{aggr}	-	aggregation stability constant
β_1, β_2	-	beta-pdf shape factors
β_{aggr}	$\frac{\#}{\mathrm{m^3 s}}$	aggregation kernel

β_b	$\frac{\#}{\mathrm{m^3 s}}$	breakage kernel
β_c	$\frac{\#}{\mathrm{m^3 s}}$	constant aggregation kernel
β_{ij}	$\frac{\#}{\mathrm{m^3 s}}$	aggregation kernel for interacting $i-j$ particles
$\delta(\cdot)$	-	Dirac delta function
δ_{ij}	-	Kronecker delta symbol
$\delta_{0.8}$	m	mixing layer thickness
δN	-	increment of stochastic counting process
ϵ	$\frac{\mathrm{m^2}}{\mathrm{s^3}}$	kinetic energy dissipation rate
$\lvert\epsilon_\phi\rvert$	%	percentage absolute error of generic variable ϕ
η_k	m	Kolmogorov length-scale
θ_u	m	momentum layer thickness
κ	$\frac{1}{\mathrm{m}}$	wave number
λ	-	mean rate of random process
λ_f	m	mean free path of gas molecules
λ_p	m	mean free path of particles
μ_f	$\frac{\mathrm{kg}}{\mathrm{ms}}$	laminar molecular viscosity
μ_{sgs}	$\frac{\mathrm{kg}}{\mathrm{ms}}$	turbulent viscosity
ν	$\frac{\mathrm{m^2}}{\mathrm{s}}$	kinematic viscosity
ξ	-	generic normalized scalar
$\widetilde{\xi"^2}$	-	generic normalized sgs scalar variance
ρ_f	$\frac{\mathrm{kg}}{\mathrm{m^3}}$	fluid density
ρ_p	$\frac{\mathrm{kg}}{\mathrm{m^3}}$	particle density
ρ_l	$\frac{\mathrm{kg}}{\mathrm{m^3}}$	condensing liquid density
σ	$\frac{N}{m}$	surface tension
τ_{ij}	Pa	stress tensor
τ_{aggr}	s	aggregation time-scale

τ_{flow}	s	flow time-scale
τ_i	s	temporal increment
τ_I	s	inertial particle time-scale
τ_{nuc}	s	nucleation time-scale
τ_p	s	particle relaxation time
τ_t	s	turbulence-particle interaction time-scale
υ	m^3	particle volume
ϕ	-	generic flow property
ϕ_i	-	state vector realization
χ_i	-	random variable with normal distribution
ψ_i	-	phase space random variable

−uppercase

$\Gamma(\cdot)$	-	Gamma funciton
Δ	m	LES filter width
ΔA	m^2	control volume face surface area
Δt	s	time-step width
Δt_{aggr}	s	aggregation time-step width
Δx	m	displacement length in x-direction
$\Delta \mathbf{W}$	-	discrete Wiener increment
Υ_p	m^3	particle volume random variable
Φ	-	generic scalar field quantity
$\mathbf{\Phi}$	-	generic state vector
$\mathbf{\Phi}_\Delta$	-	generic state vector within filter volume
$\mathbf{\Psi}$	-	generic phase space
$\mathbf{\Psi}_f$	-	generic fluid phase space

Subscripts, Superscripts, and Operators:

cf	-	co-flow boundary condition
d	-	anisotropic (deviatoric) component
f	-	continuous (fluid) phase
fc	-	control volume surface
i	-	numerical index
ins	-	insulator boundary condition
j	-	numerical index
jet	-	jet boundary condition
k	-	numerical index
n	-	increment number
p	-	disperse (particle) phase
sgs	-	sub grid scale quantity
0	-	initial condition
$'$	-	different value
$*$	-	normalized quantity
$\widetilde{(\cdot)''^2}$	-	sub-grid variance
$@p$	-	evaluated at the particle's location
$\widetilde{\cdot}$	-	LES Favre filtering operation Ch. 2
$\widetilde{\cdot}$	-	LES filtering operation
$\bar{\cdot}$	-	temporal averaging operation
$\widehat{\cdot}$	-	test filtering or test filter derived quantity
$\langle\cdot\rangle_t$	-	ensemble average of temporal samples
$\langle\cdot\rangle_n$	-	ensemble average over n realizations
$\|\|\cdot\|\|$	-	modulus
$[\cdot\|\cdot]$	-	conditionality statement

Frequent Abbreviations:

ADM	Approximate Deconvolution Method
sgs	sub grid scale
SGS	Sub Grid Stress
CFD	Computational Fluids Dynamics
CFL	Courant-Friedrichs-Lewy condition
CDS	Central Differencing Scheme
CDF	Cumulative Density Function
CNT	Classical Nucleation Theory
CPC	Condensation particle Counter
CPU	Central Processing Unit
DNS	Direct Numerical Simulations
DBP	Dibutyl-Phthalate
DQMOM	Direct Quadrature Method of Moments
DSMC	Direct Simulation Monte Carlo method
EMNM	Equivalent Mean Nucleation Method
FVM	Finite Volume Method
IEM	Interaction via Exchange with the Mean
LES	Large Eddy Simulations
LHS	Left Hand Side
LS	Lagrangian Stochastic
MC	Monte Carlo method
MOM	Method of Moments
ODE	Ordinary Differential Equation
PBE	Population Balance Equation
pdf	probability density function

PDF	Probability Density Function methods
PSD	Particle Size Distribution
QMOM	Quadrature Method of Moments
RANS	Reynolds-Averaged Navier Stokes
RHS	Right Hand Side
RMS	Root Mean Square
SDE	Stochastic Differential Equation
SMD	Sauter Mean Diameter
SF	Stochastic Fields method
TVD	Total Variation Diminishing scheme
UDS	Upwind Differencing Scheme

1. Introduction

1.1. A note on the title

The term 'flow' in the title addresses the motion of a continuous fluid, which can be either in a gaseous or a liquid phase. A 'poly-disperse' flow refers to the joint motion of a continuous fluid and a number of particles with a wide range of sizes (poly). In a poly-disperse framework a particle can be understood as a solid, liquid, or gaseous object, whose length scales are much smaller than those of the 'continuous' phase in which it is immersed. Particles understood in such a manner may include: droplets, solid particles, and bubbles. A 'turbulent' flow involves three dimensional swirling motions and randomness emancipated by fluctuations in the velocity field.

The particles in a turbulent poly-disperse flow can interact with each other and with the surrounding fluid. The evolution of such interactions is governed by initial and boundary information regarding the local microscopic and macroscopic conditions, which include but are not limited to: temperature, vapor or particle concentration, and the relative velocity between the disperse and continuous phases. The randomness of turbulence in conjunction with the highly non-linear nature of particle processes render a deterministic solution of the evolution of a poly-disperse flow intractable in practical engineering applications for a number of reasons. Firstly, the chaotic nature of turbulence can magnify the uncertainty resulting from an infinitesimally small inconsistency in the initial information. Secondly, there is a practical limit to the information density that can be stored and used for the description of a particular process. For example, although a macroscopic quantity such as the mean temperature of a field can be 'easily' acquired, the microscopic simulation of all the molecules that comprise the continuous phase is intractable in the majority of engineering applications.

The inability to use a deterministic solution leads to alternative methodologies, one of which is the 'stochastic' framework. A stochastic process

can be defined from an antonym point of view as one that does not evolve deterministically. From an etymological perspective the term 'stochastic' refers to the process of forming a conclusion on the basis of incomplete information and stems from the Greek word stókhos (target) and the process of stokházesthai (to aim at, to conjecture) [168]. A stochastic model aims at predicting the evolution of a system using limited information regarding the initial conditions at a time t and with the outcomes at $t + \Delta t$ formalized in probabilistic terms.

In the context of this work, the evolving system is a turbulent poly-disperse flow. Such flows have applications in atmospheric phenomena, health, and industrial processes. The wide applicability of poly-disperse flows is one of the primary motivations for their computational and experimental investigation.

1.2. Contextualization of poly-disperse flows: the need for accurate modelling

Atmospheric phenomena are highly interlinked with the physics of multi-phase turbulent flows. For example, the intermittent properties of turbulence affect the particle condensation and radiative emissivity of clouds [238]. Moreover, particle pair dispersion, cloud evolution, and surface deposition are properties that can influence a number of engineering and biological applications.

The World Health Organization issued a report stating that in 2012 approximately 3.7 million people died prematurely from illness caused by outdoor air pollution [161]. This mortality is due to exposure to particulates of 10μm or less in diameter that have been linked to cancers, cardiovascular, and respiratory diseases [161]. It is therefore of extreme value to be able to comprehensively control (or predict) the size and population of particulates from industrial and domestic emissions. The mechanisms of particle formation, aggregation, growth, and deposition have received significant attention in medical sciences [86]. For example, in addition to the effects of particulates on health, respiratory induced drugs (e.g. via inhalers) rely on the efficient deposition of the medical particles on the respiratory tract and lungs.

Advances in industrial processes have enabled the synthesis of highly specific nanoparticles (e.g. via spray-drying technologies) for the mass production of commodities such as drugs, detergents, coffee powders, and composite materials. In order to meet consumer demands while maintaining high yields, a level of control of the produced range of particle sizes is required [241]. Furthermore, particle-laden flows are of central importance in combustion processes ranging from the large-scale pulverized coal burners [103] to the small-scale soot formation and agglomeration in Internal Combustion Engines (ICE) [159] and Gas Turbines (GT) [254, 195]. The emission levels and operational efficiency of ICEs and liquid fuel GTs strongly depend on the fundamental processes that control spray combustion and fuel atomization [42].

Lack of abundance in raw materials and fuels, along with the increasing financial cost of designing and manufacturing commodities, has rendered predictive analysis an indispensable part of the design process. With accurate simulations, possible faults and prospects for optimization can be evaluated at a very early stage of design. Design parameters can be isolated and evaluated easily and cost-effectively, compared to experimental methods. Moreover, health risks posed by emissions from either (intentional) combustion processes or (unintentional) fires can be mitigated if the range of particulate-sizes is known beforehand and appropriate precautions are taken (e.g. by means of filters). Consequently, the numerical simulation of multiphase flows has received significant attention in both academia and industry.

The greatest challenge in the numerical description of poly-disperse turbulent flows is the wide range of length- and time-scales governing the motion and processes of the disperse phase. A complete resolution at a microscopic level of all the scales, including both those of the fluid and those of the particles, is intractable. A stochastic framework allows to model any effect caused by the excluded microscopic variables as random/stochastic terms in the equivalent equations of the particle phase motion and processes.

1.3. Thesis Aims

In this work, the particles considered are inertial and the mixtures investigated are dilute. The focus is on particle populations, length-, and time-scales that render a fully resolved (deterministic) solution intractable. A Lagrangian Stochastic (LS) framework is therefore used for the description of the evolution of the particle phase. Individual particle paths are tracked, which allows for a comparatively higher level of resolution and focused computational expense in the regions where particles exist. The continuous phase is modelled using an Eulerian Large Eddy Simulation (LES), which offers a good balance between computational time and level of information provided.

The main aims of this work are:

- To develop, implement, and extend the applicability of the models used to describe the particle phase immersed in a turbulent continuous fluid. This is achieved by combining the information available from a LES of the flow-field with a LS framework for the description of the disperse phase motion and processes.

- To make full use of the advantages of LES as a modelling tool. Namely, the ability of a LES to provide instantaneous values of the field and that the most energetic eddies are directly resolved without a closure model.

- To avoid or minimize the use of additional heuristic (modelling) parameters, which are usually non-universal and may be test-case or grid-resolution specific.

The investigated particle processes are dispersion, nucleation, and aggregation in turbulent flows. Retrieving instantaneous data can be very important due to the non-linearity of the equations describing such processes. Furthermore, avoiding extra modelling parameters when combining the LES and LS frameworks will not restrict further the *a priori* accuracy, and therefore predictive capability, of the developed models. To this end, a Lagrangian code is developed and evaluated linking the stochastic and LES frameworks.

1.4. Thesis Outline

Chapter 2 introduces the mathematical framework for the simulation of the continuous fluid phase. The notion and characteristics of turbulence are outlined along with different methods for the simulation of turbulent flows. Thereafter, the Eulerian LES solver used in the present study is discussed with regards to its mathematical principles and operation.

Chapter 3 addresses the mathematical description of the disperse phase in a Lagrangian framework. The forces experienced by a particle immersed in a flow are outlined along with the various inter-particle processes that the disperse phase may undergo. A separate section is dedicated to the stochastic approach in modelling the evolution of random variables. Section 3.3 links the particle physical processes and the stochastic framework by introducing the spray probability density function (spray-pdf) and Population Balance (PBE) equations.

In Chapter 4 the spray-pdf is revisited in the context of a LES-coupled fluid phase. The unclosed terms arising from the filtering of the spray-pdf are addressed and the numerical schemes used for the coupling of the Eulerian and Lagrangian descriptions are outlined. Thereafter, the three processes investigated in the present study are presented, namely: particle dispersion, particle nucleation, and particle aggregation. Having addressed the physical principles that govern each process, the state of the art and the difficulties posed in the numerical modelling of the disperse phase in an LES-coupled approach are reviewed. For each process, a modelling approach is formulated. The LES-coupled equations implemented and developed in the context of the present study are then summarized in section 4.5.

Chapters 5-7 are devoted to the implementation and validation of the models presented in Chapter 4. In Chapter 5 the dispersion model is firstly validated in the context of an unbound channel with a constant and uniform velocity gradient. Thereafter, the model performance in an unbound turbulent mixing layer is investigated. The conclusions on the model performance and physical characteristics of the dispersion process are presented.

Chapter 6 presents the results of the nucleation model. The test case chosen consists of a heated vapor-laden turbulent round jet. The jet issues into a cold environment and the cooling due to mixing causes the vapor to reach a supersaturated state and consequently to condense. The nucleation

model outlined in Chapter 4 is validated against experimental data for particle concentrations, and an analysis of the relative effects of spatial and temporal averaging on the nucleation rate is carried out.

Chapter 7 investigates the aggregation process in the LES-spray pdf framework. The validity and performance of the aggregation model presented in Chapter 4 is investigated. The model is firstly validated using analytical solutions for the evolution of the Particle Size Distribution (PSD). The effect of the aggregation process in the evolution of the PSD in two flow-coupled test cases are explored. The first case consists of a planar jet, whereas the second of a turbulent round jet. The results of the model employed are compared to those from a DNS and an experiment, respectively.

Chapter 8 summarises the developed models and the major findings from the investigations. Finally, recommendations are made for future work and the potential developments of the methodologies are presented.

2. Continuous Phase Fluid Dynamics

2.1. Mathematical description

A fluid flow can be mathematically described by non-linear partial differential equations derived from the laws of mass, momentum, and energy conservation. The volume of a fluid particle (molecule) is negligible compared to the total volume occupied by a fluid. Flow scales therefore tend to exceed molecular scales, this leads to the formulation of the *continuum hypothesis*. The continuum hypothesis suggests that fluid properties vary continuously in space. The continuity of the fluid properties allows to use differential analysis in the solution of the conservation equations. In the context of this work, it creates an implicit categorization of what can be considered the fluid/continuous phase and the particulate/disperse phase. This Chapter deals with the mathematical description of the continuous phase in an Eulerian framework.

Equations (2.1)-(2.3) describe the evolution of the mass, species mass-fraction, and momentum, respectivelly, of the continuous phase.

Conservation of Mass:

$$\frac{\partial \rho_f}{\partial t} + \frac{\partial}{\partial x_j}(\rho_f U_j) = \dot{S}_{mass}, \tag{2.1}$$

where ρ_f is the density of the fluid, t is time, x_j and U_j are the position and velocity in direction j. The global 'source' or 'sink' term $\dot{S}_{mass}$ may arise for example from: condensation where mass is 'lost' from the gaseous phase, to the liquid-particle phase, or vaporization where mass is 'gained'.

Conservation of Species:

$$\frac{\partial}{\partial t}(\rho_f Y_n) + \frac{\partial}{\partial x_j}(\rho_f Y_n U_j) = \frac{\partial}{\partial x_j}\left(\frac{\mu_f}{Sc_n}\frac{\partial Y_n}{\partial x_j}\right) + \dot{S}_{mass,n}. \tag{2.2}$$

In cases where the continuous phase involves a flow of a number of different species, the mass continuity holds for each of the constituents according to Eqn.(2.2). Here Y_n is the mass fraction of a species n, and $Sc_n = \mu_f/(\rho_f D_n)$ is the Schmidt number, where μ_f is the laminar viscosity of the mixture and D_n the diffusion coefficient of the specie n. Assuming a constant Schmidt number for all species and that Fick's law for binary diffusion holds, a constant diffusion coefficient $D_n = D$ can be used for all species[22, 130].

Conservation of Momentum:

$$\frac{\partial}{\partial t}(\rho_f U_i) + \frac{\partial}{\partial x_j}(\rho_f U_i U_j) = \frac{\partial \tau_{ij}}{\partial x_j} - \frac{\partial p}{\partial x_i} + \rho_f g_i + \dot{S}_{mom,i}. \tag{2.3}$$

The momentum conservation equation links the local change of momentum $(\rho_f U_i)$ in a given time increment dt to the convective transport caused by the fluid motion $\frac{\partial}{\partial x_j}(\rho_f U_i U_j)$, the deformation/shear forces $\partial\tau_{ij}/\partial x_j$, the pressure field gradient $\partial p/\partial x_i$, and the gravitational acceleration g_i. Finally, the term $\dot{S}_{mom,i}$ represents the source/sink of the momentum exchange between phases.

$$\tau_{ij} = 2\mu_f S_{ij} - \frac{2}{3}\mu_f S_{kk}\delta_{ij}. \tag{2.4}$$

The stress τ_{ij} can be split into the hydrostatic $\frac{2}{3}\mu_f S_{kk}\delta_{ij}$ and deviatoric $2\mu_f S_{ij}$ components, where δ_{ij} is the Kronecker delta[1]. The local strain rate S_{ij} is evaluated by:

$$S_{ij} = \frac{1}{2}\left(\frac{\partial U_i}{\partial x_j} + \frac{\partial U_j}{\partial x_i}\right). \tag{2.5}$$

Finally, combining equations (2.3)-(2.5) and omitting source terms the familiar *Navier-Stokes equations* can be formulated:

$$\frac{\partial}{\partial t}(\rho_f U_i) + \frac{\partial}{\partial x_j}(\rho_f U_i U_j) = \frac{\partial}{\partial x_j}\left[\mu_f\left(\frac{\partial U_j}{\partial x_i} + \frac{\partial U_i}{\partial x_j} - \frac{2}{3}\frac{\partial U_k}{\partial x_k}\delta_{ij}\right)\right] - \frac{\partial p}{\partial x_i} + \rho_f g_i. \tag{2.6}$$

[1] $\delta_{ij} = 1$ if $i = j$ and 0 elsewhere

Equation (2.6) describes the Eulerian evolution of a continuous phase (i.e. it describes the fluid motion for length scales that exceed the molecular scales). The balance between microscopic/molecular and macroscopic/inertial forces governs whether a flow is laminar, turbulent, or in transition between the two (laminar to turbulent and vice-versa). In the context of this work, the flow-fields under investigations are turbulent, turbulence is therefore briefly described in the following section.

2.2. Turbulence

Turbulence is not a feature of the fluid but of the fluid flow. It involves three dimensional vortical motions and randomness manifested by fluctuations in the flow's velocity field. One of the main effects of turbulence is enhanced mixing which induces increased mass, momentum, and energy exchange. Reynolds [199, 200] suggested that the onset of turbulence can be quantified as a balance between the inertial and viscous forces of the flow, this quantification is expressed via the dimensionless Reynolds number: Eqn. (2.7). The Reynolds number is the ratio of the destabilizing momentum term $\rho_f U l$ to the stabilizing viscous term μ_f, where l is a characteristic length scale of an eddy (usually a function of the flow's geometry). A Reynolds number exists for every length scale l of the flow (in this case characterized as a function of the wave number $\kappa = 2\pi/l$). A flow will most probably become turbulent if the Reynolds number of the largest/integral length scale is at least of the order of 2000.

$$Re(\kappa) = \frac{\rho_f U(\kappa) l(\kappa)}{\mu_f} \tag{2.7}$$

From a spectral point of view, turbulence has a continuous energy spectrum of length- and time-scales, illustrated in Figure (2.1). The larger scales are determined by the geometry of the encompassing environment and the smallest scales are governed by the molecular viscosity of the flow.

Richardson [202] introduced the concept of *energy cascade*. Energy is extracted from the mean flow by the larger eddies and it is subsequently cascaded to the smaller scales. As the cascade proceeds the turbulence becomes more and more isotropic, this isotropic range of turbulence is referred to as the *equilibrium range*. Finally, the length-scales which are small

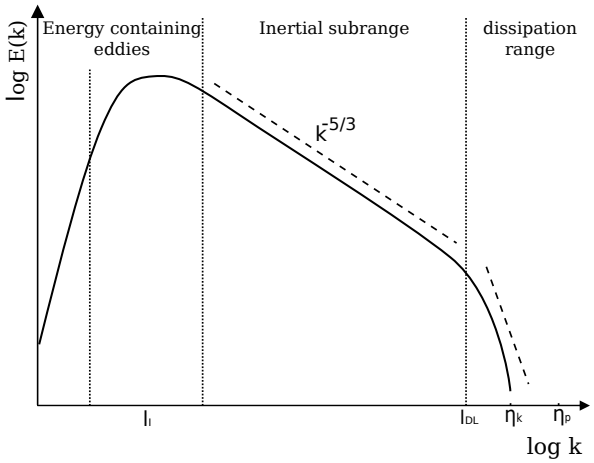


Figure 2.1.: Energy cascade and length scales

'enough' experience molecular/viscous forces that dissipate their kinetic energy transforming it to heat [182, 143, 185].

Turbulence has a continuous energy spectrum of length- and time-scales, yet the persisting mechanisms of energy and momentum transfer differ. Therefore, it is of interest to describe the largest and smallest eddies and categorize them according to those mechanisms. The larger or *integral* time t_I and length l_I scales, are of the order of the geometry of the encompassing (of the flow) environment, for example in a pipe flow the integral length scale will be of the order of the pipe's diameter $l_I \sim \mathcal{O}(d)$ and the timescale $t_I = l_I/U_i$. These scales subtract energy from the mean flow kinetic energy and due to their unstable break-up they transfer the energy to the smaller scales [182].

Conservation of kinetic energy suggests that in the inertial subrange the cascade of energy is constant. Ultimately, energy moves down to the smallest scales and there, dissipation takes part due to viscous forces. Therefore, the rate of turbulent kinetic energy dissipation provides a bridging between the largest and smallest scales and it can be therefore used to quantify the smallest *or Kolmogorov scales* as follows:

$$\epsilon = \frac{Dk}{Dt} \approx \frac{[\mathrm{L}]^2}{[\mathrm{T}]^3} \sim \frac{U_i^3}{l_I}. \tag{2.8}$$

The rate of dissipation ϵ of turbulent kinetic energy k can be dimensionally

equated to the ratio of the square of a length-scale to the cube of a time-scale. The largest eddies (being the most energetic) are representative of the mean flow kinetic energy, and therefore they are used to approximate the dissipation rate as shown in Eqn. (2.8). The Kolmogorov length η_k, velocity u_k , and time t_k scales are defined using the following analogies [112, 113]:

$$\eta_k = (\nu^3/\epsilon)^{1/4}; \quad u_k = (\nu\epsilon)^{1/4}; \quad t_k = (\nu/\epsilon)^{1/2} \ . \tag{2.9}$$

In the above formulation, where $\nu = \mu_f/\rho_f$ is the kinematic viscosity, it is assumed that the viscous effects are negligible for scales larger than the Kolmogorov and become the sole parameter of dissipation at the smallest scales. By estimating ϵ one may therefore evaluate the range and ratio of large to small scales.

A categorization of the energy spectrum, as this shown in Figure 2.1, can be performed according to the dissipation mechanisms. The largest structured motions of the flow are termed *energy containing eddies* [185]. The range of scales where the viscous forces remain irrelevant (i.e. where the kinetic energy is mainly cascaded to the smaller scales) is termed the *inertial subrange* [185]. The *dissipation range* (or viscous subrange) consists of eddies with length-scales small enough such that viscous forces will dissipate their kinetic energy.

2.3. Numerical modelling of Turbulent Flows

To study and quantify the flow structures of turbulent flows numerous experiments [2] have been carried out and many computational and theoretical models [95, 121] employed. The numerical analysis can be used as a complementary tool to the experimental investigation, or directly contribute to fundamental research by considering aspects of the flow and geometries that cannot be easily studied with current experimental techniques. In multiphase flows, numerical modelling can become of central importance in the investigation of correlations between the interacting phases, which cannot be directly measured in an experiment. The following section briefly presents the three most common computational methods for the analysis of turbulent flows, namely: Reynolds Average Navier-Stokes (RANS) Simulations,

Direct Numerical Simulations (DNS), and Large Eddy Simulations (LES).

2.3.1. Reynolds Average Navier-Stokes (RANS)

One of the first models for analysing turbulent flows stems from the solution of the time-averaged Navier-Stokes equations (2.6). This approach follows the principle of *Reynolds averaging*. Each varying property of the flow has a given instantaneous value at a certain position and time, e.g. the velocity at a position x_j and time t is $U_i(x_j, t)$. The mean value of the equivalent instantaneous property is retrieved by applying the RANS operator:

$$\overline{U}_i(x_j) = \lim_{\Delta t \to \infty} \frac{1}{\Delta t} \int_t^{t+\Delta t} U_i(x_j, t) dt. \tag{2.10}$$

The instantaneous value can be therefore split into a mean (indicated by the over-bar) and a fluctuating component, viz:

$$U_i(x_j, t) = \overline{U}_i(x_j) + u_i^{'}(x_j, t). \tag{2.11}$$

The solution is achieved by applying the averaging operation (2.10) to the equations of motion (2.1)-(2.6). The averaging introduces a number of unresolved terms: the *Reynolds stress terms* $\overline{u_i' u_j'}$. These terms cannot be directly solved and appropriate closure models are required. Closures models are frequently based on a phenomenological similarity between the dissipative effect of the turbulent fluctuations to this of the molecular/laminar viscosity (Boussinesq approximation). This similarity gives rise to a *turbulent viscosity*. The turbulent viscosity can be retrieved from turbulent quantities that are directly related to the kolmogorov scales (e.g. the turbulent kinetic energy k and dissipation rate ϵ via the $k - \epsilon$ model [96]), or from algebraic formulations such as the Mixing Length Model [189].

RANS models the full range of turbulent length-scales and does not retain information of instantaneous flow properties, therefore relatively coarser grids can be used which allow for shorter computational times. RANS modelling is therefore extensively used and it is one of the dominant methods employed in industrial CFD codes.

2.3.2. Direct Numerical Simulation (DNS)

As opposed to RANS, DNS involve the direct solution of the Navier-Stokes equations. The direct solution of the equations without the use of closure models make DNS an extremely powerful tool for fundamental studies [157]. However, it has a very high computational cost and it is currently infeasible to investigate large geometries and mixtures at high Reynolds numbers.

DNS resolve all scales down to the smallest Kolmogorov scales. The ratio of large to small scales is of the order of $(l_I/\eta_k)^3 \sim Re^{9/4}$. One must resolve in all three directions, and it has been shown [130, 114] that the number of operations is proportional to Re^3. In the context of particle dispersion and cloud formation in multiphase flows, DNS is rendered inefficient mainly due to its large computational cost. DNS is therefore limited to simple test cases. In addition, the length scales of the particle phase l_p, are in many cases much smaller than the Kolmogorov scales. For example the particle diameters can be of the order of $d_p \sim \mathcal{O}(\text{nm} \rightarrow \mu\text{m})$ whereas $\eta_k \sim \mathcal{O}$ (mm) in engineering applications. A DNS should therefore resolve the disperse phase scales, which would further increase computational demands.

2.3.3. Large Eddy Simulation (LES)

In the context of poly-disperse turbulent flows in complex geometries, Large Eddy Simulations (LES) offer a good compromise between the information retrieved from a RANS and the computational time required for a DNS. Numerical studies [81, 238, 264] have shown that in turbulent multiphase flows the large scales dominate the dispersion process of the particle phase whereas smaller scales tend to be independent of geometry and more isotropic in nature. The scales which dominate the particle dispersion process are directly resolved in LES and no model is required for their closure as in RANS. Arguably, recent work, as for example by Menter and Egorov [152] on Scale Adaptive Simulations (SAS), has shown that RANS modelling may resolve energetic eddies using an improved length-scale equation, as derived by Rotta [210]; however, a Large Eddy Simulation (LES) treatment to obtain the energy spectrum of the unresolved scales is required. Therefore, LES modelling of the continuous phase was selected for the present project.

As in RANS modelling, in LES instantaneous properties are split into an average and a fluctuating component. However, in LES a spatial 'averag-

ing' is used (as opposed to the temporal averaging in RANS), which sets a lower/cut-off limit to the length of the fully resolved eddies. Equivalent to the Reynolds stresses in RANS, LES-filtering results to loss of information giving rise to the *Sub Grid Stresses* (SGS). A model for the SGS components is therefore required to solve the spatially filtered Navier-Stokes equations

2.4. Modelling turbulent flows with LES

2.4.1. Governing Equations for LES

The filtering operation in LES is equivalent to a low pass filter with a cutoff scale Δ. An instantaneous flow field property ϕ is filtered to obtain the instantaneous spatial average $\overline{\phi}$, viz:

$$\overline{\phi(x_i,t)} = \int\int\int G_\Delta(x_i - x_i';\Delta)\phi(x_i',t)dx_1'dx_2'dx_3'. \tag{2.12}$$

Various types of filters (see [143, 185]) can be used for the LES filtering operation such as the Top-Hat, Box, Gaussian or Spectral cut-off, which provide a functional form to the filtering kernel $G_\Delta(x_i - x_i', \Delta)$.

It is common for the solution of the conservation equations to use the density weighted spatial average or *Favre-filtered* $\tilde{\phi}$:

$$\tilde{\phi} = \overline{\rho_f\phi}/\overline{\rho_f} \ . \tag{2.13}$$

As in RANS averaging, a field can be decomposed to its filtered/resolved and unresolved components $\phi = \tilde{\phi} + \phi'$, where ϕ' represents the unresolved fluctuations. The Favre-filtered transport equations can be obtained for mass:

$$\frac{\partial\overline{\rho_f}}{\partial t} + \frac{\partial}{\partial x_i}(\overline{\rho_f}\tilde{U}_i) = \tilde{\dot{S}}_{mass}, \tag{2.14}$$

and momentum:

$$\frac{\partial\overline{\rho_f}\tilde{U}_i}{\partial t} + \frac{\partial\widetilde{\overline{\rho_f}U_iU_j}}{\partial x_j} = \frac{\partial}{\partial x_j}\left[\overline{\mu_f}\left(\frac{\partial\tilde{U}_i}{\partial x_j} + \frac{\partial\tilde{U}_j}{\partial x_i} - \frac{2}{3}\frac{\partial\tilde{U}_k}{\partial x_k}\delta_{ij}\right)\right] - \frac{\partial\overline{p}}{\partial x_i} + \overline{\rho_f}g_i + \overline{\dot{S}}_{mom,i}. \tag{2.15}$$

2.4.2. Sub Grid Scale Closure

The filtered momentum equations (2.15) yield terms such as $\widetilde{\phi U_i} \neq \tilde{\phi}\tilde{U_i}$. These terms require modelling (as they cannot be explicitly evaluated) to provide closure to the equivalent transport equation. The SGS or residual tensor is defined as:

$$\tau_{ij}^{sgs} = \widetilde{U_i U_j} - \tilde{U_i}\tilde{U_j}, \tag{2.16}$$

and it represents a loss of information, which is an outcome of the filtering process. By spliting of the velocity into a filtered and unresolved component, the residual stress tensor τ_{ij}^{sgs} is re-written as:

$$\tau_{ij}^{sgs} = \underbrace{(\widetilde{\tilde{U_i}\tilde{U_j}} - \tilde{U_i}\tilde{U_j})}_{\text{I}} + \underbrace{(\widetilde{\tilde{U_i}u_j'} + \widetilde{u_i'\tilde{U_j}})}_{\text{II}} + \underbrace{(\widetilde{u_i'u_j'})}_{\text{III}}. \tag{2.17}$$

Term I represents the *Leonard Stresses* L_{ij}, which arise from a re-filtering operation of the resolved quantities (since $\tilde{\tilde{\phi}} \neq \tilde{\phi}$). Term II represents the *Cross-Stresses* C_{ij}, which arise from interactions of the subgrid eddies with the resolved flow. Both terms I and II do not appear in RANS, since $\overline{\overline{U}}_i = \overline{U}_i$ and $\overline{\overline{U}_i u_j'} = 0$ in temporal averaging. Finally, term III represents the LES *Reynolds Stresses* R_{ij}, which appear due to interactions of the unresolved scales. The Reynolds stresses are modelled, whereas L_{ij} and C_{ij} are either considered negligible or modelled subject to the filtering kernel employed.

Smagorinsky [224] suggested a closure model that employs a Boussinesq-type approximation for the deviatoric (anisotropic) component R_{ij}^d of R_{ij}:

$$R_{ij} = R_{ij}^d + \frac{1}{3}R_{kk}\delta_{ij} = -2\mu_{sgs}\tilde{S}_{ij} + \frac{1}{3}R_{kk}\delta_{ij}, \tag{2.18}$$

where μ_{sgs} is the SGS or turbulent viscosity, which from the Boussinesq similarity is defined as:

$$\mu_{sgs} = \overline{\rho_f}(C_s\Delta)^2||\tilde{S}_{ij}||, \tag{2.19}$$

where Δ is the filter width and $||\tilde{S}_{ij}||$ is the modulus of the filtered strain tensor, viz:

$$||\tilde{S}_{ij}|| = \sqrt{2\tilde{S}_{ij}\tilde{S}_{ij}}. \tag{2.20}$$

The mixing length scale l_m, as suggested by Prandtl [190], is typically

smaller than the filter width and therefore the model constant C_s (usually $0.065 < C_s < 0.2$) accounts for the difference $l_m < \Delta$.

The effect of the unfiltered length scales is considered via a SGS viscosity or kinematic viscosity $\nu_{sgs} = \mu_{sgs}/\rho_f$. The Navier-Stokes equation for the momentum can be therefore formulated after filtering as:

$$\frac{\partial}{\partial t}(\overline{\rho_f}\tilde{U}_i) + \frac{\partial}{\partial x_j}(\overline{\rho_f}\tilde{U}_i\tilde{U}_j) = \frac{\partial}{\partial x_j}\left[(\overline{\mu_f} + \mu_{sgs})\left(\frac{\partial \tilde{U}_j}{\partial x_i} + \frac{\partial \tilde{U}_i}{\partial x_j} - \frac{2}{3}\frac{\partial \tilde{U}_k}{\partial x_k}\delta_{ij}\right)\right] - \frac{\partial \overline{p}}{\partial x_i} + \overline{\rho_f} g_i + \overline{\dot{S}}_{mom,i} \quad (2.21)$$

Equivalently, the Favre-filtered equation for the transport of a scalar ϕ is:

$$\frac{\partial \overline{\rho_f}\tilde{\phi}}{\partial t} + \frac{\partial \overline{\rho_f}\tilde{u}_i\tilde{\phi}}{\partial x_i} = \frac{\partial}{\partial x_i}\left[\left(\frac{\overline{\mu_f}}{Sc} + \frac{\mu_{f_t}}{Sc_t}\right)\frac{\partial \tilde{\phi}}{\partial x_i}\right] + \overline{\dot{S}}_{\phi}, \quad (2.22)$$

where the turbulent Schmidt number Sc_t is evaluated using the turbulent viscosity.

It must be noted that a number of extensions to the Smagorinsky model can be used [185]. These extensions employ a dynamic evaluation of the constant C_s, the most widely used being the one by Germano [71]. In dynamic closure models C_s is not considered a constant throughout the flow field. An equation for the dynamic evaluation of C_s is derived by comparing the residual stresses with their test-filtered ($\hat{\cdot}$) equivalent, viz:

$$\widehat{\tau_{ij}^{sgs}} = \widehat{\widetilde{U_i}\widetilde{U_j}} - \widehat{\tilde{U}_i}\widehat{\tilde{U}_j} \quad (2.23)$$

The test filter size is greater than Δ by a given factor $f_r > 1$. By implementing the test-filter an unresolved component τ_{ij}^{tf} arises.

$$\tau_{ij}^{tf} = \widehat{\widetilde{U_i}\widetilde{U_j}} - \hat{\tilde{U}}_i\hat{\tilde{U}}_j \quad (2.24)$$

Subtracting (2.23) from (2.24) yields the Germano identity:

$$L_{ij} = \widehat{\tilde{U}_i\tilde{U}_j} - \hat{\tilde{U}}_i\hat{\tilde{U}}_j \quad (2.25)$$

Using an eddy viscosity approach to model the deviatoric components of both τ_{ij}^{sgs} and τ_{ij}^{tf} in the Germano and Lilly [136] implementation, the

constant is assumed to vary as a function of space:

$$Lilly : (C_s\Delta)^2 = -\frac{1}{f_r}\frac{L_{ij}^d M_{ij}}{M_{ij}^2} \qquad Germano : (C_s\Delta)^2 = \frac{1}{f_r}\frac{L_{ij}^d \tilde{S_{ij}}}{M_{ij}\tilde{S_{ij}}} \tag{2.26}$$

where L_{ij}^d is the anistotropic (deviatoric) component of L_{ij}. The parameter M_{ij} is:

$$M_{ij} = \alpha^2 \hat{\overline{\rho_f}} ||\hat{\overline{S}}_{ij}||\hat{\overline{S}}_{ij} - (\overline{\rho_f}||\widehat{\tilde{S}_{ij}||\tilde{S}_{ij}}). \tag{2.27}$$

Finally, other models for the sgs closure exist, for example the WALE model [162] accounts for the effects of both the strain and the rotation rate of the smallest resolved turbulent fluctuations.

In the present work, the Smagorinsky model is used as it offers a simple and computationally stable approach to the modelling of the sgs viscosity. The Germano implementation is used in certain test cases investigated to evaluate the adequacy of the Smagorinsky model. Moreover, the principles of the dynamic evaluation of the Smagorinsky constant by test-filtering are used in the context of modelling the particle motion. The CFD solver employed is 'PsiPhi' [60, 102, 177, 230] and it provides an LES solution of a turbulent velocity field. PsiPhi explicitly transports a number of 'Phi' variables from which a number of 'Psi' variables are derived. Appendix A briefly explains the numerical schemes used in PsiPhi in the context of this work; a thorough analysis of the PsiPhi Eulerian solver can be found in [101, 229]. The following chapter addresses the physical properties and behavior of the particulate phase immersed in a continuous flow field.

3. Disperse Phase and Stochastic Processes

3.1. Particle Physics Framework

3.1.1. The Lagrangian Approach

Apart from the Eulerian representation, a fluid flow can be described using a Lagrangian framework and the concept of *fluid particles*. A fluid particle can be defined as a volume of fluid that is small enough to move with the fluid without significant deformation [216]. In the Lagrangian framework the observer moves with the fluid particle beginning from a set position in space. All the properties are a function of the observation time t given an initial value ϕ_0 at time t_0. Therefore, a Lagrangian property can be written as $\phi(t|\phi_0, t_0)$.

One of the first studies of fluid-particles embedded in a turbulent flow field was this of Richardson [201] in 1926 and under the prism of weather systems. Richardson examined the concept of *relative dispersion*, i.e. the evolution of the relative distance between two marked particles of initial separation Δx_0 at t_0. Richardson suggested that after a certain time the relative dispersion of the particles becomes physically uncorrelated ('governed by planetary action'). The reasoning behind this statement is that larger and larger vortices contribute to the velocity variance and dispersion of the particles since only eddies with comparable size to the separation between the two particles can influence a further separation.

A number of studies (see Sawford [216]) have been carried out, which interlink/correlate the effects of the turbulent flow field to the motion of individual fluid particles. Such studies introduced the correlations between turbulence and the motion of a non-continuous entity. The notion of fluid particles was extended to the use of inertial *tracer particles* for the experimental study of fluid flows (as for example PIV techniques reviewed in

Adrian [2]).

In the present work, the Lagrangian framework is used for non-fluid (inertial) particles. The differentiation can be made by saying that such particles have an average density which is different to that of the fluid, i.e. $\rho_p \neq \rho_f$. Note that from now on the subscript 'p' will denote a non-fluid particle and 'f' will denote the continuous fluid phase. Non-fluid particles can be also represented in an Eulerian framework. Guha [81] and Loth [140] outline the various modelling approaches for the representation of particles (including the Euler-Euler framework where both continuous and disperse phases are modeled using an Eulerian approach). However, an Eulerian treatment introduces a number of turbulent closure issues, and challenges in treating solid boundaries in a physically correct way.

In the context of this project, discontinuities in concentration, and temporal change in the size of individual particles due to condensation/precipitation or aggregation, further complicate the use of an Eulerian framework. In addition, the particle phase is assumed *dilute* and with length scales that are smaller than the Kolmogorov (i.e. $d_p << \eta_k$). This suggests that the volume ratio of the particulate phase to the continuous phase is very small. A Lagrangian description therefore becomes computationally more efficient than an Eulerian since particles are tracked only where they are physically situated.

3.1.2. Particle Motion

There are a number of forces governing the motion of a particle within a flow field which are summarized below:

$$F_{tot} = F_D + F_I + F_G + F_L + F_T + F_{Ey} + F_B \tag{3.1}$$

- ***Drag Force*** F_D: Particles try to 'catch up' with the changing velocities of the surrounding fluid. Different orientations, possible particle rotation, or non-spherical shapes add to the complexity of the analysis of this force.

- ***Inertial Impactation*** F_I: This is essentially the centrifugal force arising when an inertial particle enters an area of high vorticity or a time-averaged curved streamline.

- ***Gravity and Buoyancy*** F_G: A particle experiences a force in the direction of gravity proportional to its weight. In addition, a buoyancy force is experienced in the opposite direction proportional to the displaced fluid weight.

- ***Shear-Induced Lift Force*** F_L: This force is induced by the flow field and acts in the vertical direction of the streamlines. Saffman [213], proposed an equation for the lift forces in the context of particle deposition.

- ***Thermophoretic Force*** F_T: This force emanates from the presence of a temperature gradient. It acts in the opposite direction of a positive temperature gradient and arises by unbalanced molecular impact on the surface of the particles. The energetic (hot side) molecules have a higher impact velocity compared to this of the less energetic molecules of the cold side; this imbalance produces a net force in the direction of the cold side.

- ***Electrical Force*** F_{Ey}: If particles that are charged/ionized, with a total charge q_e, are subjected to an electric field E_e a force $F_{Ey} = q_e E_e / m_p$ is produced, which macroscopically acts as an additional diffusion term.

- ***Brownian Force*** F_B: Is a force arising from the molecular scale and it is similar in nature to the thermophoretic forces. As opposed to F_T, in the Brownian case there is no preferential direction of the resulting force. A particle suspended in a liquid/gas will experience numerous impacts from the molecules of the surrounding fluid. These impacts will produce a net force towards a certain direction. The motion of the particle will appear at the macro-scale as a jump, this results from the fact that the process involves extremely small timescales as the particle is hit by a large amount of molecules at the limit of $dt \to 0$.

It must be noted that additional forces may act on the particle such as shear and surface tension, such forces influence strongly the particle processes and shape. Depending on the particle size and properties (e.g. its shape or if it is charged, heavy, or light) along with the properties of the environment wherein it is suspended (e.g. if the flow is isothermal) the forces

outlined have a relatively greater or smaller influence on the motion of a particle.

The relative effect of each force on the motion of a particle can be quantified by means of dimensionless numbers. For example, the Reynolds number based on the disperse phase can be used to quantify the level of drag experienced by a particle (such as the empirical correlation by Yuen and Chen [269]).

$$Re_p = \frac{\rho_f |\mathbf{U}_f - \mathbf{v}_p| d_p}{\mu_f}, \tag{3.2}$$

where $\mathbf{v}_p$ is the particle velocity and $|\mathbf{U}_f - \mathbf{v}_p|$ is the relative velocity magnitude between the two phases.

The Froude number is defined as the ratio of the inertial to the gravitational force experienced by a particle:

$$Fr^2 = U_f^2/(d_p g), \tag{3.3}$$

where g is the gravitational acceleration and d_p the diameter of the particle. When $Fr >> 1$ gravitational forces may be considered negligible, whereas if $Fr << 1$ the particle motion is dominated by the gravitational force (as for example in cases where the flow velocity is $U_f \approx 0$ and the particle is in free-fall).

The Stokes number St is the ratio of the particle relaxation (response) time τ_p to a characteristic time-scale of the continuous phase $\tau_{flow} = d_p/\mathcal{U}$:

$$St = \tau_p \mathcal{U}/d_p. \tag{3.4}$$

The particle relaxation time τ_p is a measure of the time required for a particle to respond to a change in the relative velocity $|\mathbf{U}_f - \mathbf{v}_p|$ as a result of drag. The term 'stopping distance' is also used for the product $\tau_p \mathcal{U}$, therefore making St a ratio of the stopping distance and the length-scale of the particle d_p. The stopping distance is the length $\tau_p \mathcal{U}$, which a particle immersed in a stationary environment moving with a velocity $|\mathbf{v}_p| = \mathcal{U}$ will travel before it is brought to a complete halt. Similarly if $\mathbf{U}_f = \mathcal{U}$ and $\mathbf{v}_p = 0$, $\tau_p \mathcal{U}$ is the distance a particle will travel before the relative velocity $|\mathbf{U}_f - \mathbf{v}_p| = 0$. Therefore, the Stokes number is a measure of the relative effect of the particle inertial to the drag force that it experiences. Depending on their relaxation time, particles exhibit a *preferential concentration* due

to their inertia. Large particles tend to be expelled from a rotating region. For Stokes numbers of the order of $St \sim 3.0$, particle trajectories 'filter' the continuous flow streamlines. This filtering effect arises because the particles have greater relaxation times and cannot adapt instantaneously to a change in the velocity of the continuous phase; therefore their trajectories tend to deviate from (filter) curved streamlines. Light particles (such as air bubbles in water) tend to concentrate at the centre of a vortical structure. In the case of light particles with high Stokes numbers the buoyancy effects become of pivotal importance in their motion [81] and cannot be neglected.

In the Lagrangian context a simple analysis of the particle motion due to drag can be carried out by making the following assumptions:

- Inertial effects are combined with the drag force.
- Gravitational and Buoyancy effects are insignificant and the Froude number is $Fr >> 1$.
- Thermophoresis and electrical forces can be neglected.
- The particles are large enough to assume Brownian forces negligible.

The trajectory of a particle is therefore represented by (3.5), and the acceleration due to drag forces by (3.6) [148]:

$$\frac{d\mathbf{x_p}}{dt} = \mathbf{v_p}, \tag{3.5}$$

$$\frac{d\mathbf{v_p}}{dt} = \frac{\mathbf{F_D}}{m_p} = \frac{(\mathbf{U}_f - \mathbf{v}_p)}{\tau_I}, \tag{3.6}$$

where $\mathbf{v}_p$ is the particle velocity, $\mathbf{U}_f$ the continuous phase velocity at the location of the particle, and τ_I is a time-scale representative of the inertial effects governed by the assumed type of forcing between the fluid and disperse phases.

3.1.3. Physical Processes

Particles under the influence of a fluid flow interact with each other and with the surrounding turbulence. The most important physical processes of a particle-laden flow are summarized below:

- ***Particle formation due to Nucleation/Precipitation***: New particles can be formed from nucleation, such as soot particles and general crystallization processes. A liquid or vapor interphase, or a very small bubble can become a nucleation site leading to heterogenous nucleation. If particles are not formed at specific nucleation sites the formation process is termed homogeneous nucleation. Nucleation rates are often a function of the environment. A review of the nucleation process and its treatment for this work is given in section 4.3.

- ***Particle collisions leading to Aggregation***: When particles collide with each other they exchange kinetic energy and physical properties. In the case of elastic collisions the particles undergo a redistribution of velocities. On the other hand, inelastic collisions lead to particle aggregation, coagulation, and agglomeration. The three terms refer to the same outcome, i.e. the formation of a new larger particle from two or more smaller ones. The physicochemical mechanism that drives the formation determines which term should be used. A review of the aggregation process and its treatment for this work is given in section 4.4.

- ***Particle Growth/Shrinkage***: A formed particle can grow or decrease in size due to various physicochemical processes [204]. For example liquid droplets may increase in size due to precipitation or decrease due to evaporation, whereas coal particles swell during their devolatilization.

- ***Particle fragmentation/Break-up***: Particles (e.g. fuel droplets) 'break' into two or more *daughter particles*. This process is highly influenced by the continuous flow hydrodynamics. It involves a balance mechanism between the externally applied stresses from the continuous phase, the surface stress of the particle, and the viscous stresses of the fluid inside the particle. Such an analysis leads to the prediction of a maximum stable diameter. For an LES implementation within the context of stochastic Lagrangian droplet atomization, the interested reader may refer to [130]. Various break-up mechanisms and models for the daughter particle size distribution are dealt with thoroughly in the review of Liao and Lucas [131].

The aforementioned processes are governed by size selective mechanisms and are highly correlated with the motions and state of the surrounding fluid. The kernels representing the physicochemical mechanisms of each process are in many cases highly non-linear. The combined effect of the physical processes and the motion of a particle in a turbulent field on the evolution of the particulate phase, create difficult closure issues and complexities in the development of numerical models for the description of such two-phase flows. Depending on the area of interest (i.e. if the physical properties are to be analyzed or the motion of the particle) different models are implemented. Given the currently available computational power, each model attempts to allocate as much of this power as possible to acquire 'reasonably accurate' results for the process it aims to simulate.

3.2. Stochastic Framework

For both completeness and better understanding of the models outlined in the following chapter, the mathematical framework of stochastic methods is hereby presented. To avoid loss of generality, the discussion will be made for a *random variable* termed $\mathbf{X}$. It should not be confused with particle position ($\mathbf{X}_p$), however links are made with particle motion to promote the relation and applicability of stochastic theory to particulate flows. An extensive review of stochastic diffusion processes and their solution is outside the scope of this work, the interested reader may refer to [10, 65, 183, 184] and the excellent review of Minier and Peirano [156] in the context of poly-dispersed two-phase flows.

3.2.1. The Stochastic Diffusion Process

A *stochastic process* is a system that evolves probabilistically in time and governs the outcome or *realization* of a random variable, such as the outcome of a coin toss or the position of a particle. The combined probability of the realizations $[\mathbf{x}_1, t_1; \mathbf{x}_2, t_2; ..\mathbf{x}_n, t_n]$ of the random variable $\mathbf{X}(t)$ can be represented by a joint probability density function (pdf) $\mathcal{P}(\mathbf{x}_1, t_1; \mathbf{x}_2, t_2 ...; .\mathbf{x}_n, t_n)$. The joint-pdf is a measure of the probability of all the events $[\mathbf{x}_i, t_i]$ to occur.

When considering joint probabilities it is of interest to define the conditional probability, i.e. the probability of an event $\mathbf{x}_1$ at time t_1 to occur,

given that an event $\mathbf{x}_0$ has already occurred at a time t_0, i.e. $\mathcal{P}(\mathbf{x}_1, t_1|\mathbf{x}_0, t_0)$. Or for a multi-variable system the conditional probability of a random variable $\mathbf{X}(t)$ to acquire a series of values $[\mathbf{x}_1, t_1; \mathbf{x}_2, t_2...]$, given that a random variable, say $\mathbf{Y}(t)$, has attained the values $[\mathbf{y}_1, \tau_1; \mathbf{y}_2, \tau_2...]$, viz:

$$\mathcal{P}(\mathbf{x}_1, t_1; \mathbf{x}_2, t_2...|\mathbf{y}_1, \tau_1; \mathbf{y}_2, \tau_2...) = \mathcal{P}(\mathbf{x}_1, t_1; \mathbf{x}_2, t_2; ...; \mathbf{y}_1, \tau_1; \mathbf{y}_2, \tau_2; ...)/\mathcal{P}(\mathbf{y}_1, \tau_1; \mathbf{y}_2, \tau_2; ...). \quad (3.7)$$

For a stochastic process we have the following identity [65, 49, 10]:

$$\begin{aligned} \mathcal{P}(\mathbf{x}_3, t_3|\mathbf{x}_1, t_1) &= \int \mathcal{P}(\mathbf{x}_3, t_3; \mathbf{x}_2, t_2|\mathbf{x}_1, t_1) d\mathbf{x}_2 \\ &= \int \mathcal{P}(\mathbf{x}_3, t_3|\mathbf{x}_2, t_2; \mathbf{x}_1, t_1)\mathcal{P}(\mathbf{x}_2, t_2|\mathbf{x}_1, t_1) d\mathbf{x}_2. \quad (3.8) \end{aligned}$$

Note that the integration is over all possible realizations (Universe $\Omega_{\mathbf{x}_2}$) of the integrated variable, and it has been removed for simplicity. The first line of equation (3.8) is intuitive and states that summing over all probable outcomes of an event (right hand side), say $\mathbf{X}(t_2) = [\mathbf{x}_2, t_2]$, is equivalent to eliminating that event (left hand side) from the joint-pdf. Making use of equation (3.7) leads to the identity of (3.8) which is valid for all stochastic processes.

A subclass of stochastic processes is the general *Markov Process* which can be described as "a time dependent stochastic process in which the future is determined by the present, independently of the past" [43]. Therefore, it is a process that can be completely determined from the previous (in time) realization/distribution. In deterministic systems, the realizations depend on the initial conditions throughout the evolution of a given process. On the other hand, stochastic systems have a finite time for which the previous event is correlated to the next, thereafter the events become independent (not in probabilistic theory terms but in physical interlinking, i.e. one cannot acquire a deterministic solution of the state of a system in the next time-step from the state of the system at the previous time-step).

For a Markov process the conditional probability can be rewritten as:

$$\mathcal{P}(\mathbf{x}_1, t_1; ...; \mathbf{x}_n, t_n|\mathbf{y}_1, \tau_1; ...; \mathbf{y}_n, \tau_n) = \mathcal{P}(\mathbf{x}_1, t_1; ...; \mathbf{x}_n, t_n|\mathbf{y}_n, \tau_n), \quad (3.9)$$

given that $\tau_1 \leq \tau_2 \leq ...\tau_n \leq t_1 \leq t_2 \leq ...t_n$.

The identity in (3.8) when combined with the Markov Process assumption results to the *Chapman-Kolmogorov equation*:

$$\mathcal{P}(\mathbf{x}_3, t_3|\mathbf{x}_1, t_1) = \int \mathcal{P}(\mathbf{x}_3, t_3|\mathbf{x}_2, t_2)\mathcal{P}(\mathbf{x}_2, t_2|\mathbf{x}_1, t_1)d\mathbf{x}_2, \tag{3.10}$$

note that the numbering of the time instances is in ascending order. Therefore, and due to the Markovian evolution of the random variable $\mathbf{X}$ with t, only the previous event $[\mathbf{x}_2, t_2]$ is required for the evaluation of the conditional pdf $\mathcal{P}(\mathbf{x}_3, t_3|\mathbf{x}_2, t_2)$. From a particle motion perspective (i.e. if the random variable represents particle position), the Markovian evolution suggests that given only the current position and properties of a particle are required to calculate the probability of its next position.

Finally, a *Continuous Markov Process* is a subclass of the general Markov process. This is the relevant case for a *particle diffusion* process. The continuity does not imply that a particle property follows a continuous path in time, rather it suggests that the realizations of the random variable (for example the position of the particle) are continuous in space. Figure 3.1

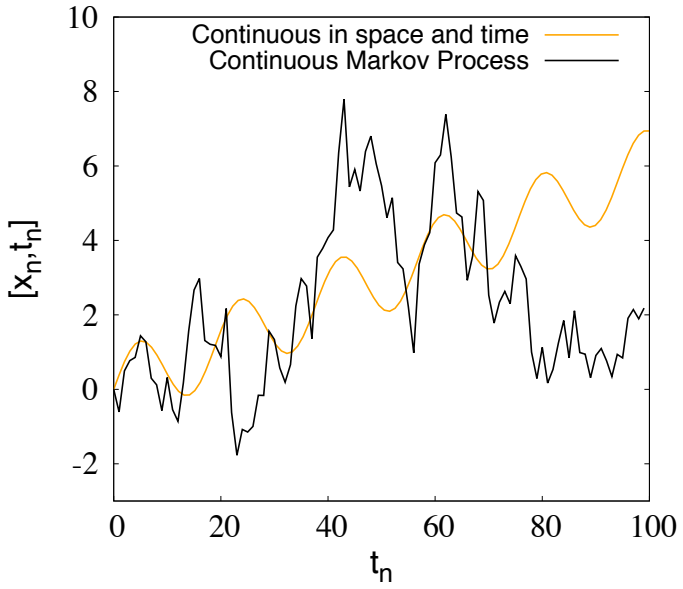


Figure 3.1.: The evolution of the random variable realizations $[x_n, t_n]$ for a continuous process in time and space and a continuous Markov Process

illustrates the difference between a process which is continuous in both time and space and a continuous Markov process. For example, consider the motion of a particle in one dimension with range $\{0 \rightarrow 1\}$ and a random forcing (e.g. due to turbulent motion) acting on it. At any time t_n the particle position can be described using the probability density $\mathcal{P}(\mathbf{x_n}, t_n)$. A *continuous* Markov Process states that the possible values for the random variable at t_n (i.e. for its realization $\mathbf{x_n}$) is continuous in the range $\{0 \rightarrow 1\}$, and *not* that a series of realizations (e.g.$[\mathbf{x}_3, t_3]$, $[\mathbf{x}_2, t_2]$, $[\mathbf{x_1}, t_1]$) vary continuously in time.

Differential Chapman-Kolmogorov equation:
Using the mathematical definition of a continuous Markov process along with equation (3.10), the *Forward Differential Chapman-Kolmogorov* [1] equation for the evolution of a continuous Markov process can be used to provide the link between stochastic theory, the particulate motion, and the physical processes (for a complete description of the derivation refer to [65]).

$$\begin{aligned}\frac{\partial \mathcal{P}}{\partial t}(\mathbf{x}, t|\mathbf{x}_0, t_0) = &\underbrace{-\sum_i \frac{\partial}{\partial x_i}\mathbf{A}(\mathbf{x}, t)\mathcal{P}(\mathbf{x}, t|\mathbf{x}_0, t_0)}_{Drift} \\ &\underbrace{+\frac{1}{2}\sum_{ij}\frac{\partial^2}{\partial x_i \partial x_j}\mathbf{B}^2(\mathbf{x}, t)\mathcal{P}(\mathbf{x}, t|\mathbf{x}_0, t_0)}_{Diffusion} \\ &\underbrace{+\int \left[\mathcal{W}(\mathbf{x}|\mathbf{y}, t)\mathcal{P}(\mathbf{y}, t|\mathbf{x}_0, t_0) - \mathcal{W}(\mathbf{y}|\mathbf{x}, t)\mathcal{P}(\mathbf{x}, t|\mathbf{x}_0, t_0)\right] d\mathbf{y}}_{Jump} \quad (3.11)\end{aligned}$$

Equation (3.11) characterizes the evolution of a continuous Markov process described by its pdf $\mathcal{P}(\mathbf{x}, t)$ and initial distribution for $\mathbf{x}_0$ and t_0. Assuming that the initial conditions are held fixed, $\mathcal{P}$ is considered a function of $(\mathbf{x}, t)$. For simplicity, in what follows the conditionality statements are removed.

The three terms in the RHS of the equation are the *drift, diffusion,* and *jump* respectively. The vector $\mathbf{A}$ is the drift and represents the mean (or

[1] The term *Forward* is used to differentiate from the *Backward* equation which computes the backwards evolution of the pdf i.e. when $t \rightarrow t_0$ and $\mathcal{P}$ is regarded as a function of the initial state $[\mathbf{x}_0, t_0]$ given its final state $[\mathbf{x}, t]$.

deterministic) diffusion coefficient, for example the mean velocity of a particle immersed in a fluid. The tensor $\mathbf{B}$ is the variance of the mean drift (e.g. a forcing caused by either unresolved turbulence or a Brownian force). Finally, $\mathcal{W}$ expresses the discontinuous jump process (e.g. the sudden appearance of a particle due to a nucleation or a fragmentation process).

Master equation:

$$\frac{\partial \mathcal{P}}{\partial t}(\mathbf{x},t) = \int \left[\mathcal{W}(\mathbf{x}|\mathbf{y},t)\mathcal{P}(\mathbf{y},t) - \mathcal{W}(\mathbf{y}|\mathbf{x},t)\mathcal{P}(\mathbf{x},t)\right] d\mathbf{y} \tag{3.12}$$

When both the drift and diffusion terms are zero, the differential Chapman-Kolmogorov equation reduces to the Master equation which describes only jump processes. If for example the random variable is particle position (suggesting that the pdf is equivalent to the particle concentration field), the sudden appearance of a particle due to nucleation or fragmentation and the sudden elimination from aggregation, results in a discontinuous 'jump' in the concentration field. The term $\mathcal{W}(\mathbf{y}|\mathbf{x},t)$ essentially gives the change in probability density per unit time due to a jump of the current state $\mathbf{x}$ to a state $\mathbf{y}$ at a time $t = t_0 + \Delta t$. The accumulation term (LHS of the Master equation) of $\mathcal{P}(\mathbf{x},t)$ loses a particle that jumps from a state $\mathbf{x} \rightarrow \mathbf{y}$, but it might also 'gain' a particle jumping from any other state $\mathbf{y} \rightarrow \mathbf{x}$. This is represented by the negative and positive integrants respectively, of the RHS of equation (3.12). Note that the integration is over all $\mathbf{y}$, which means that we are interested for jumps 'out' or 'into' a certain state $[\mathbf{x},t]$ irrespective of destination or origin $\mathbf{y}$. The pivotal difference to the diffusion process is that jump paths are non-differentiable but also *non-continuous*. For example a particle can either nucleate or not, therefore the set of realizable values for its formation is $\{0,1\}$ (i.e. it can either exist 1 or not 0) and *not* $\{0 \rightarrow 1\}$ (i.e. you cannot have 0.8 or decimal particles created) as was the case for its motion.

Fokker Planck equation:

$$\frac{\partial \mathcal{P}(\mathbf{x},t)}{\partial t} = -\sum_i \frac{\partial}{\partial x_i}\mathbf{A}(\mathbf{x},t)\mathcal{P}(\mathbf{x},t) + \sum_{ij} \frac{1}{2}\frac{\partial^2}{\partial x_i x_j}\mathbf{B}^2(\mathbf{x},t)\mathcal{P}(\mathbf{x},t) \tag{3.13}$$

Assuming that $\mathcal{W}(\mathbf{x}|\mathbf{y},t)$ is zero, (3.11) reduces to the Fokker-Planck equation. Equation (3.13) describes a continuous diffusion process without dis-

continuous jumps. Therefore, the Fokker-Planck equation can be used to describe solely the motion of a particle, excluding the particle creation and depletion processes.

Liouville's equation:

$$\frac{\partial \mathcal{P}(\mathbf{x},t)}{\partial t} = -\sum_i \frac{\partial}{\partial x_i}\mathbf{A}(\mathbf{x},t)\mathcal{P}(\mathbf{x},t) \tag{3.14}$$

Finally, if the diffusion term is zero the Differential Chapman-Kolmogorov equation reduces to a *deterministic process*. As is for example the motion of a single particle in a fully resolved (DNS) flow field, with mass large enough such that Brownian forces are negligible and a diameter of the order of the Kolmogorov scales.

3.2.1.1. Stochastic Differential Equation (SDE): Itô's equivalence

An alternative approach for the description of the diffusive evolution of $\mathcal{P}(\mathbf{x},t)$ is a Stochastic Differential Equation (SDE). This equation describes the trajectory of a single realization (e.g. the motion of one particle in space), instead of the evolution of the probability density for the ensemble of realizations $[\mathbf{x}_n, t_n]$, see Eqn. (3.15). For illustrative purposes, consider as an example the particle's position for the path of the realization $[\mathbf{x}_n, t_n]$. The incremental change $d\mathbf{x}$ is governed by a drift/velocity vector $\mathbf{A}$, and a stochastic diffusion term represented by the diffusion matrix $\mathbf{B}$ and incremental Wiener term $d\mathbf{W}$.

$$d\mathbf{x}(t) = \mathbf{A}[\mathbf{x}(t),t]dt + \mathbf{B}[\mathbf{x}(t),t]d\mathbf{W} \tag{3.15}$$

Although seemingly different to (3.13), a SDE describing a diffusion process can be related to the Fokker-Planck equation via a process of variable exchange (for the complete derivation see Itô's formula in Gardiner [65]). Consider an arbitrary functional form of the vector variable realization $\mathbf{x}(t)$; say $f[\mathbf{x}(t)]$. Using Taylor's expansion, the incremental change $f[\mathbf{x}(t)] \rightarrow f[\mathbf{x}(t) + d\mathbf{x}(t)]$ can be written as:

$$df[\mathbf{x}(t)] = f[\mathbf{x}(t) + d\mathbf{x}(t)] - f[\mathbf{x}(t)] = \\ f'[\mathbf{x}(t)]d\mathbf{x}(t) + \frac{1}{2}f''[\mathbf{x}(t)]d\mathbf{x}(t)^2 + \sim \mathcal{O}(d\mathbf{x}^3), \tag{3.16}$$

substituting (3.15) into (3.16) we get[2]:

$$df[\mathbf{x}(t)] = \{\mathbf{A}[\mathbf{x}(t),t]f'[\mathbf{x}(t)] + \frac{1}{2}\mathbf{B}[\mathbf{x}(t),t]^2 f''[\mathbf{x}(t)]\}dt + \mathbf{B}[\mathbf{x}(t),t]f'[\mathbf{x}(t)]d\mathbf{W}(t). \quad (3.17)$$

Equation (3.16) is also termed *Itô's lemma* and gives the rate of change of a function of a random variable that follows a stochastic process.

Now if we consider that this arbitrary function of $\mathbf{x}(t)$ is conditioned upon the initial distribution of the random variable (i.e. $\mathbf{X}(t_0) = [\mathbf{x}_0, t_0]$) with a pdf $\mathcal{P}(\mathbf{x}, t|\mathbf{x}_0, t_0)$ we can formulate the following equation for the time evolution of the ensemble average:

$$\begin{aligned}\frac{d}{dt}\left\langle f\left[\mathbf{x}(t)\right]\right\rangle_n &= \frac{\partial}{\partial t}\int f[\mathbf{x}(t)]\mathcal{P}(\mathbf{x},t|\mathbf{x}_0,t_0)d\mathbf{x} \\ &= \int\{\mathbf{A}[\mathbf{x}(t),t]\partial_x[f[\mathbf{x}(t)]\mathcal{P}(\mathbf{x},t|\mathbf{x}_0,t_0)] \\ &\quad + \frac{1}{2}\mathbf{B}\left[\mathbf{x}(t),t\right]^2\partial_x^2[f[\mathbf{x}(t)]\mathcal{P}(\mathbf{x},t|\mathbf{x}_0,t_0)]\}d\mathbf{x}, \quad (3.18)\end{aligned}$$

where $< \cdot >_n$ is the average over n realizations of a given random variable, and from the *central limit theorem* it is equivalent to the convolution of the function with the conditional pdf describing the process (or *expectation* $E[f|f_0]$).

From the definition of the functional form of the variable $\mathbf{x}(t)$, i.e. that it is arbitrary, we can choose $f(\mathbf{x}) = 1$. Since the values of the integrants must be equal, the ensemble average of the trajectories $\mathbf{x}$ of equation (3.18) is directly equivalent to the Fokker-Plank equation (3.13). Therefore, the pdf equation can be reconstructed from the ensemble average of the paths of the realizations. In the context of particle dispersion, this means that by averaging all paths originating from $\mathbf{X}_0 = [\mathbf{x}_0, t_0]$ the mean value (or expectation) of the random variable $E[\mathbf{X}|\mathbf{X}_0 = [\mathbf{x}_0, t_0]]$ (i.e. mean particle position) at t can be obtained. Equivalently, for a point source (mean initial position $[x_0, t_0]$) wherefrom particles are constantly seeded, the mean concentration field at any given time-instant can be derived. In general, the ensemble average of stochastic paths of a particle-property will have the

[2]Note that terms of $O(dt^2)$ are ignored and the Wiener term properties $E(dW^2) = dt$ and $E(dW) = 0$ have been used. For completeness the properties of the Wiener term are discussed in section 3.2.1.2

same statistics as the pdf and vice-versa. Therefore, the SDE equation can be used as an alternative methodology to retrieve the differential Chapman-Kolmogorov equation. However, there is an error involved directly related to the amount of particles (realizations) used to describe the pdf (proportional to $1/\sqrt{N}$, with N the number of particle-paths/realizations used to determine the statistical quantity in question).

The phase state evolving as (3.15) can be extended to incorporate Jump processes. Such stochastic differential equations are described by a *Lévy process*, viz:

$$d\mathbf{x}(t) = \mathbf{A}[\mathbf{x}(t), t]dt + \mathbf{B}[\mathbf{x}(t), t]d\mathbf{W} + \mathbf{J}[\mathbf{x}(t), t]\delta N_{dt}^{j,\lambda} \tag{3.19}$$

In a Lévy process a scaling tensor $\mathbf{J}[\mathbf{x}(t), t]$ is added to the SDE of (3.15) that models the influence of a jump process on the change of the random variable path $\mathbf{x}$. The increment $\delta N_{dt}^{j,\lambda}$ is the j^{th} component of a stochastic counting[3] process with time increments dt and mean rate λ. The stochastic counting usually follows a Poisson distribution. The equivalent to (3.19) is (3.11). The Master equation (3.12) using the transition probability from state $\mathbf{x} \rightarrow \mathbf{y}$ (and vice versa) describes a set of trajectories with a SDE formulated only for a Lévy jump process.

Figure 3.2 depicts the evolution of the random variable realizations $[x_n, t_n]$ for three processes, namely: a deterministic (where $\mathbf{B}$ and $\mathbf{J}$ are zero), a pure diffusion process (where $\mathbf{A} = \mathbf{J} = 0$), and a pure jump process (where the drift and diffusion terms are zero). The combined process represented by the blue dot-line in Fig. 3.2 is the equivalent to a single path traced using equation (3.19).

3.2.1.2. Itô's Calculus and the Wiener term

The Wiener term $\mathbf{W}$ has been introduced and a number of its properties were employed in the aforementioned equations (as for example that $\langle d\mathbf{W} \rangle = 0$ and $Var(d\mathbf{W}) \sim \mathcal{O}(dt)$). At this point a further investigation of the Wiener term is required as the foundation of the random walk of a particle and the solution of the stochastic differential equation.

The term $\mathbf{W}$ represents a random variable following a *Wiener process* (see the realization path of figure 3.2 where $\mathbf{B} = 1$) and the need for its

[3]The term 'counting' is used to clarify that the set of realizable values is discontinuous.

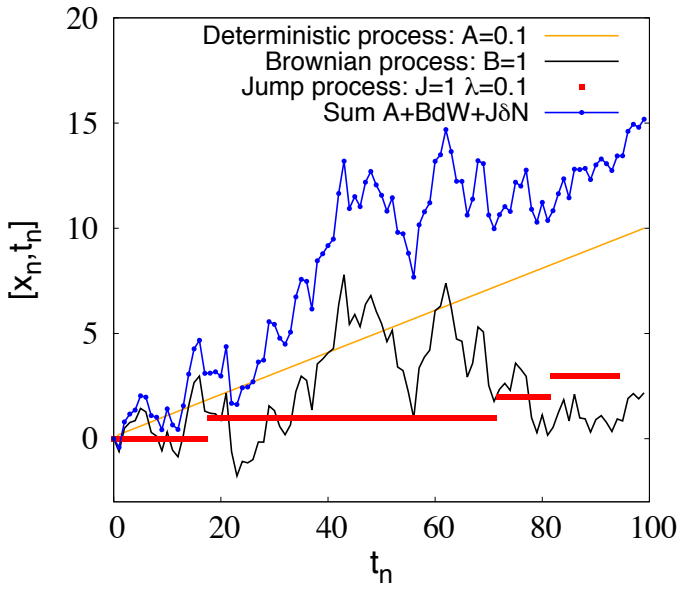


Figure 3.2.: The evolution of the random variable realizations $[x_n, t_n]$ following a Deterministic, Brownian, and Jump process. The blue line represents the sum of the aforementioned and it is mathematically represented by equation (3.19).

integration became apparent for the solution of (3.15). The Wiener process, or *random walk, or drunkard's walk* term depicts a white noise process. This is a discrete-time, countably infinite state space process, as for example the repeated toss of a fair coin with outcomes $\{HEADS, TAILS\}$. Or in terms of the drunkard, taking a step to any direction with equal probability to go to any direction. The Wiener term can be best understood by considering its properties:

$$\mathbf{W}_N = \sum_{n=1}^{N} \Delta \mathbf{W}_n \quad ; \quad \mathbf{W}_t = \int_0^t d\mathbf{W}_t, \tag{3.20}$$

$$E[\mathbf{W}_t|\mathbf{W}_0] = W_0 \quad ; \quad E[d\mathbf{W}_t] = 0, \tag{3.21}$$

$$Var[\mathbf{W}_t|\mathbf{W}_0] = t \quad ; \quad Var[d\mathbf{W}_t] = dt, \tag{3.22}$$

$$d\mathbf{W}_t \quad \sim \quad \mathcal{O}(dt^{\frac{1}{2}}). \tag{3.23}$$

A discrete Wiener term after N realizations each distanced by a time Δt can be described as a summation (over the number of realizations) of

independent $\Delta\mathbf{W}_N$ increments. The continuous equivalent is an integral where $\Delta t \to 0$ and $\Delta\mathbf{W}_N \to d\mathbf{W}_t$ while $N \to \infty$. Since $\mathbf{W}_t$ is a large sum of identically distributed independent random variables, by the *central limit theorem* it has a Gaussian pdf [43]. Such a probability density function (pdf) is fully characterized by its mean/expectation and variance which are shown in equations (3.21) and (3.22), respectively.

In the example of a coin toss, assume that a value of $+1$ or -1 is assigned to the event $HEADS$ or $TAILS$ respectively. If after every coin toss you add or subtract 1 from your initial value W_0 with a 50% chance of doing either of the two, then, after any number of time-steps you expect to have a sum which is equal to your initial value. On the other hand, the possible values that you can get after n steps lie within the range of $n \times (-1)$ and $n \times (1)$, thus the variance is n (or for a continuous process t). A very important outcome of the above is given in (3.23), i.e. that the incremental Wiener term is of the order of the square-root of the time-step. Its usefulness becomes apparent when one tries to integrate the SDE (3.15).

A random walk is continuous but non-differentiable in time; mathematically, using (3.23) we have $d\mathbf{W}_t/dt \sim \mathcal{O}(1/\sqrt{dt})$ and taking the limit $dt \to 0$ the gradient tends to infinity. Therefore, Riemann integration for continuous differentiable functions over a real valued function does not hold. This leads to a different methodology introduced by Kiyoshi Itô, namely Itô's Calculus, which is based on the following formulation for the integral of a stochastic process:

$$\int_{t_0}^{t} f_t dW_t \quad = \quad I_t = \lim_{n\to\infty} \left\langle \sum_{i=1}^{n} \left(f_{\tau_i}[W_{t_i} - W_{t_{i-1}}]\right)^2 \right\rangle, \qquad (3.24)$$

i.e. the stochastic integral is defined as a mean-square-limit of partial sums of n temporal partitions $(t - t_0)/n$ of increments $\tau_i = t_i - t_{i-1}$ as $n \to \infty$. The major difference to an ordinary Riemann integral is that the function f in (3.24) cannot be evaluated at any time (sub-interval) of the partition τ_i and that the widths $[W_{t_i} - W_{t_{i-1}}]$ are random (even thought they are taken at regular time intervals, i.e. $t_i - t_{i-1} = t_j - t_{j-1}$ for all $i, j \in \{1, 2, ..., n\}$).

The Itô integral evaluates the function f at the left end point of the partition τ_i: $f_{\tau_i} \equiv f_{t_{i-1}}$. An alternative methodology for the integration of a stochastic process is the *Stratonovich integral*. In the latter, the function f

is evaluated at the midpoint of the partition τ_i, namely $f_{\tau_i} \equiv (f_{t_i} + f_{t_{i-1}})/2$. One of the advantages of the Stratonovich integral is that the chain rule can be applied in the same way as in ordinary calculus. Itô's integral is usually chosen for applied mathematics whereas the Stratonovich in physics, a comparison of the two methodologies is given in Ch.6 of Kloeden [106]. In the context of this project Itô's integral is used.

To recap, the Differential Chapman-Kolmogorov equation (3.11) was presented under the prism of a Markov processes. Assuming zero jump, the drift and diffusion terms describing a continuous diffusion process were analyzed through the Fokker-Plank equation (3.13). It was shown how such an equation has an Itô equivalent stochastic differential equation (3.15) describing the continuous diffusion of a single realization as a function of time. Similarly the Itô equivalent SDE for the diffusion equation including jump processes (3.19) was presented. Moreover, the concept of the random walk and the Wiener term were presented and connected to stochastic diffusion of the particulate phase. It has to be stressed that only the aspects of SDEs and Stochastic calculus employed within the development of the author's work have been briefly presented. For a much greater insight, the interested reader may refer to [10, 43, 49, 65, 106].

3.3. Stochastic modelling of Inertial Particles

3.3.1. The Spray-PDF Equation

In the context of inertial particle dispersion, Williams [256] introduced a conservation equation for the particle distribution function. The particle distribution function consists of the joint probability of the realization of M variables that represent the state of the particulate phase (e.g. position, velocity, temperature, density, radius and their equivalent rates of change). In theory, all the microscopic variables relevant to the state of a particle within a two-phase flow should be taken into account. For example, in a flow with N particles one would require an N^{th} order distribution function with $3N$ velocity and spatial coordinates and a number of coordinates that would provide the particle size, shape, and their relevant rates of change. Such an exact solution would be intractable; an approximate model is therefore pursued by choosing a state vector $\mathbf{\Phi}$ consisting of a number of selected variables considered sufficient to represent the disperse phase in a given application. Any effects caused by the excluded microscopic variables need to be modeled by the addition of stochastic terms to the deterministic component of the Lagrangian equation for the rate of change of the property in question [206].

For a set of M independent variables the state vector of the jth particle for a given location in space $\mathbf{x}$ and time t is $\mathbf{\Phi}^j = \{\phi_1^j(\mathbf{x},t), ..., \phi_M^j(\mathbf{x},t)\}$. It is possible to characterize the phase space $\mathbf{\Psi}$ of the random variables ψ_i (with realizations $\mathbf{\Phi}^j$ for every j-indexed particle) of an ensemble of N particles using the fine-grained density $\mathbb{F}(\mathbf{\Psi};\mathbf{x},t)$, defined [105] as:

$$\mathbb{F}(\mathbf{\Psi};\mathbf{x},t) = \sum_{j=1}^{N}\prod_{i=1}^{M}\delta[\psi_i - \phi_i^j(\mathbf{x},t)], \tag{3.25}$$

where δ is the Dirac delta function, ψ_i the ith random variable of the phase space, and ϕ_i^j is its realization by the jth particle. To clarify, a realization of the phase space means that a particle acquires a specific set of values for its state vector.

Now one may formulate an expression for the fine-grained probability density function $\mathbb{P}(\mathbf{\Psi};\mathbf{x},t)$ as the expectation of the fine-grained density function. Assuming that the particles are independently distributed and

due to the law of large numbers the expectation can be written as a sum over an infinite number of realizations (i.e. particles):

$$\mathbb{P}(\mathbf{\Psi};\mathbf{x},t) = \lim_{N\to\infty}\frac{1}{N}\sum_{j=1}^{N}\prod_{i=1}^{M}\delta[\psi_i - \phi_i^j(\mathbf{x},t)]. \tag{3.26}$$

To comply with the characteristics of a probability density, the fine grained pdf must be integrated to unity: a result that is approached as the number of realizations increases. The assumption of independently distributed particles has been used in the derivation of Bini [22] for simplicity; however, Subramaniam [233] has shown that it is not a necessary condition to define the pdf of the population of the particles. Finally, by differentiating (3.26) with respect to time following the motion of the phase space the evolution of the spray pdf can be obtained:

$$\frac{\partial}{\partial t}\mathbb{P}(\mathbf{\Psi};\mathbf{x},t) = -\sum_{i=1}^{M}\frac{\partial}{\partial\psi_i}\left[E[\dot{\psi}_i|_{\mathbf{\Psi}=\mathbf{\Phi}}]\mathbb{P}(\mathbf{\Psi};\mathbf{x},t)\right] \tag{3.27}$$

where $E[\dot{\psi}_i|_{\mathbf{\Psi}=\mathbf{\Phi}}]$ is the expectation of the rate of change of the random variable ψ_i of the phase space $\mathbf{\Psi}$ conditioned upon the local state vector $\mathbf{\Phi}$. As mentioned, from the central limit theorem the expectation can be expressed as an ensemble average over independent realizations of the particle state vector.

At this point, the similarity of the spray-pdf to equation (3.14) is clear. One of the major differences is that the spray-pdf is an Eulerian pdf, whereas the Liouville equation is Lagrangian. The spray-pdf follows a Markov assumption leading to [183]:

$$\int \mathbb{P}_L(\mathbf{\Psi};\mathbf{x},t|\mathbf{\Psi}_0;\mathbf{x_0},t_0)d\mathbf{x}_0 = \mathbb{P}(\mathbf{\Psi};\mathbf{x},t), \tag{3.28}$$

where $P_L(\mathbf{\Psi};\mathbf{x},t|\mathbf{\Psi}_0;\mathbf{x_0},t_0)$ is the Lagrangian spray-pdf conditioned to the initial distribution for $[\mathbf{\Psi}_0;\mathbf{x_0},t_0]$. Consequently, both the Lagrangian and Eulerian spray-pdf are solutions to the Differential Chapman-Kolmogorov equation. In fact, the spray-pdf equation, where Brownian motion is assumed negligible, is equivalent to the Liouville equation. If the random variable phase space can be influenced by discontinuous processes, equation (3.27) can be readily extended to include jumps in the form of sinks/source

terms, viz:

$$\frac{\partial}{\partial t}\mathbb{P}(\mathbf{\Psi};\mathbf{x},t) = -\sum_{i=1}^{M}\frac{\partial}{\partial \psi_i}\left[E[\dot{\psi}_i|_{\mathbf{\Psi}=\mathbf{\Phi}}]\mathbb{P}(\mathbf{\Psi};\mathbf{x},t)\right] + \dot{\mathbf{S}}_{\mathbb{P}}, \tag{3.29}$$

where the spray-pdf source term $\dot{\mathbf{S}}_{\mathbb{P}}$ is a vector corresponding to the chosen state vector.

For example, if the phase state includes particle number density of a given particle size $n(\upsilon)$, the source $\dot{\mathbf{S}}_{\mathbb{P}[n(\upsilon)]}$ would be equivalent to the formation (or depletion) of particles with size υ due to nucleation, aggregation, or fragmentation. In the case where the only variable is particle velocity, the source $\dot{\mathbf{S}}_{\mathbb{P}[\mathbf{v}_p]}$ is zero, even if jump processes do exist. If the state vector includes only velocity, the jump due to a formation of a particle is represented by an addition of a realization j (i.e. an extra physical particle) of the state vector.

By equivalence, the spray-pdf can be reformulated as a trajectory problem with a set of SDEs. In its current form of equation (3.29), the spray-pdf can be written as a set of paths of the phase space:

$$d\psi_i^j = A_i(\mathbf{\Psi})dt + J_i(\mathbf{\Psi})\delta N_{dt}^{j,\lambda}. \tag{3.30}$$

Any continuous random forcing can be added both to the spray-pdf and the trajectory problem with a Brownian diffusion term quantified by an equivalent diffusion tensor B_{ik}:

$$d\psi_i^j = A_i(\mathbf{\Psi})dt + B_{ik}(\mathbf{\Psi})dW_{t,k} + J_i(\mathbf{\Psi})\delta N_{dt}^{j,\lambda}. \tag{3.31}$$

The appearance of such a term will be revisited when investigating the effect of LES filtering onto the spray-pdf equation in section 4.1.

The analysis thus far has not addressed the equivalence of the Jump term to the particle processes discussed in 3.1.3. Equation (3.11) introduces the jump process in the context of a pdf diffusion problem of a given state vector $\mathbf{X}$, whereas (3.29) as a source term to the spray-pdf. Moreover, the equivalent Lagrangian equations of the evolution of the realization of $\mathbf{X}$ were presented in (3.19). By equivalence to the Differential Chapman-Kolmogorov equation, Eqn. (3.31) represents the trajectory approach to the solution of the spray-pdf.

3.3.2. Modelling the Jump Term: The PBE

Particle processes affect both the concentration field of the particles (e.g. when new particle are formed from nucleation/fragmentation) and their relative sizes (e.g. due to growth, fragmentation, or aggregation). A Particle Size Distribution (PSD) can be used to illustrate the range of sizes of the disperse phase. Strictly speaking, the PSD is a function of particle size (e.g. diameter or volume) at a given time and position in space $[\mathbf{x}_n, t_n]$. The evolution of the PSD within a flow field can be described by accurately selecting the random variables of the state vector of the spray-pdf (e.g. by including size, position, and time in $\mathbf{\Psi}$) or using a Population Balance Equation (PBE). The description of the discontinuous processes is better documented in the literature of the PBE compared to that of the spray-pdf (which has been used mainly for dispersion studies and combustion). The equivalence of the spray-pdf with the PBE will become apparent, but for the purpose of this work the PBE modelling of discontinuous jumps was investigated and the respective solution methods are hereby briefly presented; for a thorough review the reader may refer to [131, 132, 204].

The Population Balance Equation is based on a distribution function of a given number of independent properties and their rate of change (similarly to the spray-pdf); see (3.32). These properties form the state vector of the distribution and may include a number of parameters relative to the particle description such as their volume, position, velocity, temperature etc, and respective rates of change.

$$\mathcal{N}(x_1, ..., x_A, \dot{x}_1, ..., \dot{x}_A) \equiv \mathcal{N}(\mathbf{x}, \dot{\mathbf{x}}) \tag{3.32}$$

It is different from the spray-pdf in that the number density $\mathcal{N}$ has dimensions $[\#/units\text{-of each property}]$. When integrated over all the phase space variables, the distribution provides the total number of particles (as opposed to a probability of 1 in the case of a pdf). Therefore, $\mathcal{N} = \mathcal{N}(\upsilon)$ gives the number of particles per unit volume in the field with size υ. It is common to consider intervals of volumes since υ is a continuous variable. In this case, the number of particles per unit volume with size in the range of $\upsilon + d\upsilon$ is $\mathcal{N}(\upsilon)d\upsilon$.

At this point a note must be made on the phrasing used for the various probability distributions. Generally, the choice of a state vector is subject

to the application in question. But it also governs the terminology used to refer to the equivalent pdf in the literature. For example, the PSD is a pdf with a single random variable being the particle size. The Chapman-Kolmogorov equation is a pdf that represents the diffusion of any random variable(s) of the chosen state without loss of generality (obviously given that the evolution is Markovian in nature). The PBE equation and the spray-pdf equations are in essence differential Chapman-Kolmogorov equations. The various names of the approaches are depictive of the context of their implementation rather than their mathematical origin.

In what follows, the particle number density distribution $\mathcal{N}$, will be a function of the particle volume v, position $\mathbf{x}$, and time t. The equivalent PBE for particles immersed in a fluid flow can be formulated [204] as:

$$\frac{\partial \mathcal{N}(v;\mathbf{x},t)}{\partial t} + \nabla(\mathbf{U}_f \cdot \mathcal{N}(v;\mathbf{x},t)) + \frac{\partial}{\partial v}(G(v,Y_p)\cdot \mathcal{N}(v;\mathbf{x},t)) = D_p \cdot \nabla^2 \mathcal{N}(v;\mathbf{x},t) + \dot{S}_{\mathcal{N}}(Y_p,\mathcal{N}). \quad (3.33)$$

The first term of the LHS represents the *accumulation* of the distribution, the second term the spatial *convective diffusion* arising from the uniform phase motion, and the fourth term the *diffusive* contribution to the accumulation of $\mathcal{N}$. The particle diffusivity D_p can be considered constant for all particles [242] and it is an outcome of Brownian diffusion. The *growth* process is governed by the function $G(v, Y_p)$, which depends on the local condensing species mass fraction Y_p and the volume of the particle. The mass fraction Y_p (where the subscript p depicts the species that takes part in the equivalent particle process) evolves in time and space according to (2.2). Finally, $\dot{S}_{\mathcal{N}}$ is a source term that incorporates a number of physico-chemical processes, viz:

$$\begin{aligned}\dot{S}_{\mathcal{N}}(Y_p,\mathcal{N}) = {} & \dot{I}(Y_p,T)\cdot\delta(v-v_0) \\ & + \frac{1}{2}\int_0^v \beta_{agg}(v-v',v')\cdot\mathcal{N}(v-v';\mathbf{x},t)\cdot\mathcal{N}(v';\mathbf{x},t)dv' \\ & - \mathcal{N}(v;\mathbf{x},t)\int_0^\infty \beta_{agg}(v,v')\cdot\mathcal{N}(v';\mathbf{x},t)dv' \\ & + \int_v^\infty \beta_b(v')b(\frac{v}{v'})\mathcal{N}(v';\mathbf{x},t)dv' - \beta_b(v)\mathcal{N}(v,t). \quad (3.34)\end{aligned}$$

The first term of (3.34) is the particle *nucleation* (reviewed in chapter 4). This process is mathematically described by the highly non-linear nucleation rate $\dot{I}(Y_p, T)$, which depends on the local species concentration and temperature. The delta function $\delta(\upsilon - \upsilon_0)$ states that the process will add a particle to the PBE only for a certain nucleation volume υ_0, which is governed by local thermodynamic conditions.

A particle of size υ is formed by the *aggregation* of two particles with volumes υ' and $\upsilon - \upsilon'$. The rate of formation is assumed to be proportional to the number of collisions and a scaling coefficient; namely, the aggregation kernel β_{agg}. This kernel incorporates the physicochemical characteristics of the process and it is also known as the aggregation frequency. It depends on various parameters such as the flow conditions (laminar/turbulent), the relative motion of particles, and their size compared to the mean free path of the molecules of the carrier phase (see chapter 4). The two integrals of (3.34) involving aggregation express the formation of a particle of size υ from two smaller ones, and the depletion of a particle of size υ which itself takes part in an aggregation event to form a larger one.

Finally, *breakage*[4] is also quantified by an integration process as is the case of aggregation. The number of particles with size υ produced in a fragmentation event of a particle with volume υ', is the product of the rate of breakage β_b with the number density $\mathcal{N}(\upsilon'; \mathbf{x}_p, t)$ and the daughter size distribution $b(\upsilon/\upsilon')$. Summing over all particle sizes (larger than υ) gives the total creation of particles with size υ due to fragmentation. The daughter size distribution quantifies the probability of the particle υ' to form a particle υ, given that it breaks. Equivalent to the case of aggregation, the particles of size υ breaking to different sizes have to be subtracted from the total production. As expected, in such a case the daughter distribution is not required since we are interested in the outward flux of the population of size υ regardless of the outcoming size.

At this point the similarity of (3.33) to the differential Chapman-Kolmogorov equation (3.11) is clear. The drift, diffusion, and jump terms of the latter appear as the flow velocity and particle growth, the particle Brownian diffusivity, and the source term in the PBE, respectively. The drift and diffusion

[4]Breakage is not considered in this work but included here for completeness. The interested reader may refer to the review of [131] for the breakage kernel and modelling methods, and to [97, 130] for an LES spray-pdf implementation.

terms are therefore directly analogous to the equivalent of the PBE; the source term with greater investigation is also analogous to the transitional probabilities of (3.11). For example in the case of nucleation we have:

$$\mathcal{W}_{nuc}(v|v_0,t) = \left\{ \begin{matrix} \dot{I}/N_{tot}, & \text{if } v = v_0 \\ 0, & \text{otherwise} \end{matrix} \right\} = \frac{\dot{I}}{N_{tot}} \delta(v - v_0), \tag{3.35}$$

and a process involving only nucleation is described by:

$$\frac{\partial \mathcal{N}(v;\mathbf{x}_p,t)}{\partial t} = \int \mathcal{W}_{nuc}(v|v_0,t)\mathcal{N}(v_0;\mathbf{x}_p,t)dv_0 = \dot{I}\delta(v - v_0), \tag{3.36}$$

note that in (3.35) N_{tot} represents the total number of particles per unit volume in the distribution (zeroth moment of the PBE).

Similarly, the spray-pdf equation (3.29) is analogous[5] to the PBE. However, in the case of the former, the Brownian diffusion is considered negligible for the particle size-range usually considered in spray injection and atomization studies. Even so, as mentioned, a random force acting on a random variable of the spray-pdf can be modeled with the addition of a diffusion tensor $\mathbf{B}$ for the equivalent state vector variable (by equivalence to a stochastic diffusion process).

Another major difference of the PBE and spray-pdf is that the latter provides great versatility in its trajectory formulation. The choice of the state vector of the spray-pdf can exclude, for example, the number density if each trajectory represents a physical particle. A jump process due to nucleation in the spray-pdf, where number density is excluded from the state vector, is simply represented by an addition of a particle (i.e. the phase space realization) from the ensemble of tracked paths. Somewhat differently but on the same lines, an addition of a particle due to fragmentation would add a new path for the phase space, but at the same time a jump will appear in the volume variable of the fragmented particle's state vector.

In the case of the PBE, a trajectory, of say number density, does not necessarily represent the motion of a single real particle in space. In fact, it represents the evolution of a single realization (*notional* 'particle' moving in space) of the number density. Such notional particles may represent from

[5]The term *analogous* is used to clarify that the PBE is not a pdf; the formal definition of a pdf states that when integrated over the phase space it should normalize to 1.

zero to the total number of real particles. It is therefore common to use the term *stochastic parcel* when referring to notional particles in order to differentiate them from real particles. As an example consider that in the case of nucleation a real particle with volume v_0 is created at some location $\mathbf{x}_0$. This event will increase the number of real particles represented by the stochastic parcel that characterizes the path of the realization of the distribution $\mathcal{N}(v_0)$. Nonetheless, a stochastic parcel is tracked prior to the location $\mathbf{x}_0$ and it therefore represents zero physical particles until the nucleation event occurs. This may lead to increased computational expense as stochastic parcels that do not represent physical particles are traced. However, it must be noted that the spray-pdf can incorporate the number density in its phase space formulation; in that case it becomes directly *analogous* to the PBE.

Finally, although the mathematical representation of the PBE appears straight forward, the non-linearities involved create a number of difficulties in the solution of (3.33) even for the simplest cases. Moreover, a number of restrictions and fundamental closure issues occur depending on the flow field conditions and modelling approach. The modelling of the PBE and its solution becomes of great interest and complexity especially when considering a turbulent flow field. In turbulent flows every variable of the PBE's phase space (even the PSD itself) becomes a random variable with fluctuations that require closure. Even so, because of its similar mathematical formulation to the spray-pdf, the PBE solution methodologies can be applied in the spray-pdf framework.

3.3.3. Solution Frameworks for the PBE and Spray-pdf

For consistency with the available literature, the solution framework of the aforementioned distributions will be presented for the PBE. As noted, this framework can be readily applied for the spray-pdf if considerations are made regarding the normalization properties and phase vector choice. In fact, the Williams spray-pdf is considered one of the first works in Population Balance modelling of inertial particles [205].

The problem of solving the PBE is twofold. Firstly, one needs to deal with the inherently non-linear terms of the equation. Secondly, the unclosed terms arising from coupling with a given flow field require further

modelling. A number of methodologies for the solution of the PBE exist of which the predominant are: the *Analytical*, the *Method of Moments* (MoM) and *Approximate Moment Method*, the *Discretization Methods* , the *PDF closure* and *Monte-Carlo methods*, and combinations thereof. The choice of method depends on the framework in question (e.g. if inertial-particles are considered, or if the continuous flow field is turbulent). In the context of this work we are interested in frameworks that enable the retreival of the PSD in a turbulent environment and that allow for solutions where non-linear particle processes influence the evolution of the PSD.

Firstrly, *Analytical methods* treat the particle formation, growth, and aggregation processes along with their size, position and time as independent random variables. Non-linear terms such as growth and aggregation are assumed constant or to vary linearly. For example, the recent work of Peglow *et al.* [172] uses an analytical solution to calculate moisture distributions at the outlet of a continuous fluidized bed dryer. However, in their generality, they may lead to erroneous results and can only be implemented after many simplifying assumption [204, 232].

The Method of Moments (MOM) is one of the most popular solution techniques. Partly due to its functionality –it transforms the multi-dimensional PBE to a set of Ordinary Differential Equations (ODE)– and partly because it is one of the first solution frameworks developed [70, 78, 88]. The k^{th} moment of the particle number density distribution is defined as:

$$m_k = \int_0^\infty \upsilon^k \mathcal{N}(\upsilon) d\upsilon. \tag{3.37}$$

The zeroth moment is simply the total number of particles in a given volume, whereas the second moment gives the total volume of particles within a given volume i.e. the volume fraction[6]. In simplified cases where the various kernels are assumed either constant or to have a certain functional form that is size-independent, the formulated ODEs solve for the k^{th} moment making use of the $k^{th} - 1$ moment. On the other hand, the equation is unclosed if the kernels are size-dependent and non-linear. Another shortcoming of such methods is that the distribution is not directly retrieved unless an assumption is made for its shape. However, if the distribution is somehow approximated then both unclosed terms can be dealt with, and

[6]Given that $\mathcal{N} = \mathcal{N}(\upsilon)$ only.

the distribution can be reconstructed from a set of moments.

On this basis, the *Approximate Methods of Moments* are used to approximate the unknown continuous distribution $\mathcal{N}(v)$. The aim is to replace the continuous integrals of the moment-PBE with a sum of weights representative of the distribution. The parameters of this approximation are then acquired from a closed set of moments. There are various alternatives for this approximation including orthogonal polynomial [88] and quadrature based methods.

The Quadrature Method of Moments (*QMOM*), proposed by McGraw [151], employs Gaussian Quadrature weights[7] to approximate the particle size distribution. The integrals which describe particle processes are reformulated as sums of the products of the quadrature weights, and equivalent kernels $\mathcal{K}$ and volumes (to the power of the respective moment equation), viz:

$$\int v^k \mathcal{N}_v \mathcal{K}(v) dv \approx \sum_i w_i v_i^k \mathcal{K}(v) \tag{3.38}$$

The parametrization is not known. Therefore, the quadrature parameters must represent consistently a finite number of moments. To obtain the quadrature parameters an inversion matrix is required that uses the solution of the moment-based PBE for a single time step. Thereafter, the quadrature parameters are used for the integration of the moments. This inversion process may create errors as the matrix can be ill-conditioned[204].

To mitigate the issues of inversion in QMOMs Marchisio and Fox [144] suggested the Direct Quadrature Method of Moments (DQMOM). The DQMOM directly formulates the ODE for the quadrature parameters (as opposed to the moments) basing it on a distribution as the one shown in (3.39). For a complete description the interested reader may refer to Fox [59], Appendix B.

$$\mathcal{N}(v) \approx \sum_i^n w_i \delta(v - v_i) \tag{3.39}$$

One of the most important short-comings of the moment-based methods is that, in essence, it is an inverse problem hindered from a number of mathematical considerations. An assumption for the initial distribution is required to solve the moment equations. Furthermore, the evolution of $\mathcal{N}$ is

[7] $\int_{-1}^{+1} w(x) f(x) \approx \sum_{i=1}^{n} w_i f_i$

only resolved by a number of tracked moments, thus without any assumptions for its shape the complete $\mathcal{N}$ cannot be acquired. Some methodologies for the closure of the Moment equation do not require the shape of the distribution. In such methods, the moment equation is formulated using the discrete version of the PBE, as for example the Method of Moments with Interpolative closure reviewed in [62]. A complete description of moment based methodologies exceeds the purpose of this work, a very good overview can be found in the works of Su *et al.* [232] and Yu and Lin [266] in the context of nanoparticle laden flows.

The *Discretization methods* (also termed *Sectional Methods*) directly compute the entire distribution instead of reconstructing $\mathcal{N}$ from its moments. Also, they can be used in conjunction with a moment based distribution. The discretization of the population balance has the large advantage of avoiding the need to solve the unclosed terms of the moment based ODEs. As the name suggests, this method discretizes the PBE phase domain in a certain number of states (bins). The discretization can be carried out either using approximated local functions over neighboring nodes (essentially variations of the finite-element method)[70], or by a step function where between a given interval $v + dv$ the value is assumed constant and equal to v_i [205]. The latter method is often termed *Method of Classes* or *Discretized Population Balances* and its origin can be traced to the work of Bleck [25]. As expected, the computational cost of the simulation is subject to the number of grid points required to discretize the PBE. For example, in cases where a wide range of sizes is investigated a coarse approximation may lead to miss-calculations of the low order moments resulting to mass discontinuities. On the other hand, such methods avoid the need for reconstructing the PBE from its moments, and retain the advantage of transforming the PBE into a set of ODEs.

At this point it must be noted that the majority of the aforementioned methods focus mainly on the solution of homogeneous systems. The coupling with transient flow environments further complicates the problem. The situation becomes even worse when considering turbulent flows where fluctuations of the uniform phase variables affecting particle processes must be coupled to the chosen particle-evolution description. The non-linearity of the kernels representing particle processes suggests that mean flow quantities cannot be used for the evaluation of a certain kernel; consequently,

additional closure models have to be used.

PDF[8] *methods* were introduced to accommodate the non-linearities in the flow-coupled closure terms (such as these caused by the turbulent micro-mixing) and also as a method to directly solve the PBE and spray-pdf. PDF methods can be split into two categories based on their operation, namely: the presumed and transported approach.

The former transports a number of moments, for example the mean and variance of a scalar concentration affecting the particle formation rate, and assuming a certain shape (e.g. a β-pdf for scalar variation or a log-normal for the PSD) the full distribution at that location in space and time is retrieved. Similarly, the solution of the moment PBE can be classified as a presumed PDF method. Presumed methods have been used in particle formation and growth studies using the $\beta - pdf$ [14, 16] or in the context of soot formation with the Conditional Moment Closure (CMC) method [115]. The CMC is different to the aforementioned presumed method in that it uses a passive scalar as an independent dimension. The local conditional means (conditioned upon the passive scalar) of the remaining scalars are then used to evaluate the equivalent source term kernels.

On the other hand, transported PDF methods solve for the evolution of the PBE or a joint-pdf (as for example the spray-pdf or the pdf of the continuous phase variables affecting the particle processes) therefore making no *a-priori* assumption for their shape. A discretized PBE where the phase space includes the local continuous phase temperature and species concentration distributions can be classified as a transported PDF method. In such cases the PBE is formulated similarly to the spray-pdf equations, i.e. as an ensemble of fine-grained densities giving the joint probability of the chosen phase vector [142]. For example, Rigopoulos [203] developed a PDF-PBE method where the formulated probability density function describes the joint probability of the particle number density $\mathcal{N}(v)$ and the species mass fraction Y_p of the uniform phase. In the context of transported PDF methods an alternative approach has been suggested by Valino [240] and Sabel'nikov and Soulard [212] and applied in particle formation studies in

[8]The upper case letters are used to differentiate from the aforementioned pdf equations. The PDF methods include both the approaches used to provide closure to terms that require knowledge of the fluid phase properties at the location of the particle (or parcel) such as temperature or certain species concentration and the approaches for the solution of the aforementioned distribution equations (PBE and spray-pdf).

conjunction with MOM by [66], namely the *Stochastic Fields* (SF) method. In the SF formulation, the *Eulerian* pdf is decomposed to a number of 'fields' which represent values of each required scalar of the phase space at every node of the Eulerian domain. The evolution of this field is governed by a stochastic partial differential equation. The ensemble of the fields at every node provides the Eulerian pdf (as opposed to ensemble averaging the trajectories of the Lagrangian pdf).

Concluding, analytical methods cannot be applied in multi-variate situations with non-linear kernels and there are no general solutions that include coupling with a turbulent flow field. Moment based methods, with the exception of few simplified particle systems, lead to unclosed terms. The need to assume a shape for the PSD and the possible ill-conditioning of the initial moments of the PBE can lead to inaccurate solutions. If discretization methods are used the number of equations to be solved for each size class increases proportionally to the range of sizes. In applications where wide size-ranges exist, such as processes involving particle formation, growth and aggregation, the computational demands render the solution in-tractable. Therefore, it is hard to say that a single method can have all-inclusive benefits. Finally, for the aforementioned methodologies the solution of the equivalent distribution (moment, discretized, PDF) can follow either an Eulerian (nodal domain decomposition) or a Lagrangian (trajectory/Monte-Carlo) approach. The major advantage of the Eulerian description is that accuracy is not subject to the number of traced paths, as it is in the trajectory formulation. On the other hand, a significant shortcoming of the Eulerian approach is that in many practical applications the particles are only present in a limited section of the domain (such as the case of sprays). If physical particles (as opposed to stochastic parcels) are tracked the computational expense is focused in solving only for locations where particles exist. In addition, the convection terms are directly incorporated to the particulate motion.

The versatility of the spray-pdf state vector choice further promotes the afformentioned advantage. As opposed to PBE solutions where sizes with zero populations have to be traced, the spray-pdf allows for a 'more physical' representation of the disperse phase. In the following chapter, the spray-pdf is revisited in the context of LES-coupled turbulent flows. Turbulence

induces a level of randomness to the continuous-phase-coupled parameters that govern the motion and size-evolution of particles. A joint Eulerian Lagrangian solution is sought where all the particle phase space realizations (trajectories) are tracked, and the influence of the uniform phase on particulate processes at the trajectory position is interpolated from the local Eulerian quantity. The effects of the unresolved fluctuations are considered and incorporated accordingly to the particle phase vector variable influenced. The underlying incentive is to make full use of the LES ability to produce instantaneous realizations of the flow field.

4. Modelling the Disperse Phase in Present LES

In the previous chapter, the various forces that govern the particle motion in a fluid flow were outlined. Moreover, the physical processes that occur due to particle interactions and phase transitions were discussed. With regards to the particulate phase, the framework of stochastic diffusion processes was presented leading to the differential Chapman-Kolmogorov equation (3.11) and its equivalent path solution (3.19).

The spray-pdf formulation for inertial particles (3.29) was outlined noting its equivalence to the Chapman-Kolmogorov equation. Finally, the Population Balance framework was presented under the prism of modelling the jump processes. The PBE is extensively used for studies of the PSD evolution in turbulent flows and hence offers a wide range of solution methods. Its similarity to the spray-pdf equation allows the adaptation of the modelling methods to solve the former with the added advantage of the spray-pdf's versatility in choosing a state vector and incorporating jump processes.

At this point, the spray-pdf is revisited in the context of an LES-coupled fluid phase. Thereafter, the modelling of particle dispersion, nucleation, and aggregation in this work is presented.

4.1. Problem Formulation: The Filtered spray-pdf

In the context of LES, equation (3.26) is filtered spatially with a filtering kernel G_Δ of width Δ as shown in equation (4.1).

$$\tilde{\mathbb{P}}(\mathbf{\Psi};\mathbf{x},t) = \int \mathbb{P}(\mathbf{\Psi};\mathbf{x}',t)\cdot G_\Delta(\mathbf{x}-\mathbf{x}';\Delta)d\mathbf{x}' \tag{4.1}$$

The filtering kernel has to be positive-definite in order to maintain non-negative probabilities, which means that a spectral cut-off filter cannot be

used. In this way the pdf can be evaluated at the LES grid points and depends only on the local conditional filtered variables. Note that in the literature this equation is sometimes termed the filtered density function or filtered spray-pdf; for consistency, the term *spray-pdf* will be used here.

Due to the integral formulation of the distribution's transport, the filtering leads to the the familiar spray-pdf transport [22]:

$$\frac{\partial}{\partial t}\tilde{\mathbb{P}}(\mathbf{\Psi};\mathbf{x},t) = -\sum_{i=1}^{M}\frac{\partial}{\partial \psi_i}\left[E[\dot{\psi}_i|_{\mathbf{\Psi}=\mathbf{\Phi}_\Delta}]\tilde{\mathbb{P}}(\mathbf{\Psi};\mathbf{x},t)\right] + \dot{\mathbf{S}}_{\tilde{\mathbb{P}}}, \tag{4.2}$$

In general, the rate of change of the jth variable of the phase space $\dot{\psi}_j$ is conditioned upon the phase space being equal to the state vector $\mathbf{\Phi}_\Delta$ (i.e. its realization) at any point within the filter volume $E[\dot{\psi}_j|_{\mathbf{\Psi}=\mathbf{\Phi}_\Delta}]$.

4.1.1. Flow coupling

In a flow-coupled framework, this conditional acceleration also depends on the local state vector defining the continuous phase environment $\mathbf{\Phi}_f = [\mathbf{v}_{f@p}, \rho_{f@p}, Y_{n@p}]$ at a particle's location[1]. Therefore, the phase space rates of change of (4.2) are also conditioned on the local flow state vector, viz:

$$E[\dot{\psi}_i|_{\mathbf{\Psi}=\mathbf{\Phi};\mathbf{\Psi}_f=\mathbf{\Phi}_f}], \tag{4.3}$$

where the notation indicating the dependence of the phase states on filter volume ($\mathbf{\Phi}_\Delta$ and $\mathbf{\Phi}_{\Delta,f}$) is dropped for simplicity.

In a DNS the entire spectrum of the motions at the location of a particle is known, and the solution would proceed as dictated by equation (4.2). On the other hand, with LES the realizations are only known for the filtered scales and therefore the fluid state at the location of the particle can be decomposed to a –known– filtered and –unknown– sub grid contribution: $\mathbf{\Phi}_f = \tilde{\mathbf{\Phi}}_f + \mathbf{\Phi}'_f$ (as in the LES decomposition implemented in section 2.4). As noted, the length scales of the particles can be smaller than the Kolmogorov scales, and consequently much smaller than the equivalent grid spacing Δ. Therefore, intuitively, one may imagine that the unresolved flow scales may influence the particle phase evolution.

[1]Note that this state vector can be included in the particle phase space. The realization would be equivalent to the uniform phase values at the position of the particle. Here, for clarity, a different vector is used to denote the continuous phase.

The motion of the particle and any physicochemical processes it undergoes could be (in theory) resolved sufficiently to be described by a deterministic process. For example, Brownian forcing involves numerous collisions of the molecules of the gaseous phase onto the particle. To an external observer this looks like an incremental 'jump' of the position of the particle. If every molecule is resolved sufficiently in time and space, every collision event could be described with an equivalent equation for the momentum exchange between the colliding molecule and the particle. Therefore, the motion of the particle would be simulated in a deterministic manner; obviously such a simulation is far from realizable in engineering applications. The fact that such temporal resolution cannot be achieved led to the Markovian assumption and stochastic Brownian diffusion of particle paths. A Markov process can be seen as a good approximation of a coarse temporal/spatial resolution of a physical process.

Extending the aforementioned concept, a link can be made with the LES coupling with the particle phase processes. From a phenomenological point of view, it can be argued that the effect of the SGS to the path of a particle's property is equivalent to the effect that Brownian forcing has on the position of a particle. For example, the unresolved contributions of the flow involve length- and time-scales that affect the rate of change of the velocity of a particle but cannot be analyzed as a continuous process by the observer due to the coarse temporal and spatial resolution. What is seen/modelled as a stochastic diffusion process, if resolved sufficiently, becomes a continuous motion of the particle path captured by a number of small (previously unresolved) eddies. Similarly, a nucleation event involves continuous collisions of the condensing phase molecules, which adhere and dissociate until a stable nucleus is formed. What the 'LES/macroscopic-observer' can see is merely the creation of a particle emancipated by the sudden addition of a trajectory (or jump in number density). However, it must be stressed that the evolution of the particle property influenced by the SGS must exhibit small correlations in both time and space such that the Markovian assumption is justified.

The important realization at this point, is that the nature of the two problems, namely Brownian motion (or stochastic diffusion processes in their generality) and SGS contributions have similarities that allow one to use a phenomenological analogy between the two concepts to provide closure

for the state vector path equation of a particle. The evolution of the state vector of a given particle in LES can be therefore described by:

- A deterministic contribution directly related to the local resolved LES flow state.
- A stochastic continuous and non-differentiable in time variation caused by the unresolved flow-scales.
- A stochastic discontinuous jump process to simulate the physicochemical processes that cause an abrupt change in the particle phase space either with the addition of a realization (particle formation) or by a discrete size fluctuation (fragmentation/aggregation).

Consequently, the trajectory formulation of the jth-particle path is described by:

$$d\psi_i^j = A_i(\mathbf{\Psi}, \tilde{\mathbf{\Psi}}_f)dt + B_{ik}(\mathbf{\Psi}, \tilde{\mathbf{\Psi}}_f)dW_{t,k} + J_i(\mathbf{\Psi}, \tilde{\mathbf{\Psi}}_f)\delta N_{dt}^{j,\lambda}, \tag{4.4}$$

and the ensemble average over all paths gives equation (4.3) for the equivalent rate of change of ψ_i at a given position and time. If (4.2) is conditioned upon the initial distribution for $[\mathbf{\Psi}_0, t_0]$ the equivalent Chapman-Kolmogorov equation arises (where the positional dependance is added to the state vector as the realization $\mathbf{x}_p$ of the random variable $\mathbf{X}_p$ for particle position):

$$\begin{aligned}\frac{\partial}{\partial t}\tilde{\mathbb{P}}(\mathbf{\Psi}, t|\mathbf{\Psi}_0, t_0) = &-\sum_i^M \frac{\partial}{\partial \psi_i}\left[A_i(\mathbf{\Psi}, \tilde{\mathbf{\Psi}}_f, t)]\tilde{\mathbb{P}}(\mathbf{\Psi}, t|\mathbf{\Psi}_0, t_0)\right] \\ &+\sum_{i,j} \frac{\partial^2}{\partial \psi_i \partial \psi_j}\left[\frac{1}{2}B_{ij}(\mathbf{\Psi}, \tilde{\mathbf{\Psi}}_f, t)]\tilde{\mathbb{P}}(\mathbf{\Psi}, t|\mathbf{\Psi}_0, t_0)\right] \\ +\int \left[\mathcal{W}(\mathbf{\Psi}, t|\mathbf{y}, t)\tilde{\mathbb{P}}(\mathbf{\Psi}, t|\mathbf{\Psi}_0, t_0) - \mathcal{W}(\mathbf{y}|\mathbf{\Psi}, t)\tilde{\mathbb{P}}(\mathbf{\Psi}, t|\mathbf{\Psi}_0, t_0)\right] d\mathbf{y}.\end{aligned} \tag{4.5}$$

Note that the drift vector A_i and diffusion tensor B_{ij} are functions of the local phase state of both the particles and flow. The jump term gives the net flux into $\mathbf{\Psi}$ from all possible states $\mathbf{y}$.

In the present study the trajectory equation (4.4) is solved, as opposed to the Eulerian solution of Eqn. (4.2). In this way computational resources

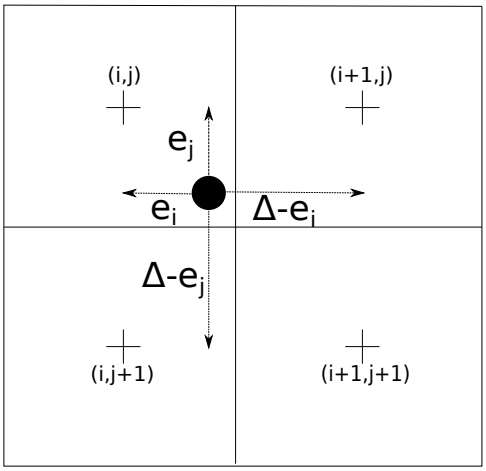


Figure 4.1.: 2D weight interpolation between particle position and grid points.

are allocated only for the solution of trajectories at locations where particles are physically situated.

4.1.2. Numerical Implementation

The filtered Eulerian continuous phase properties are retrieved at the particle location using a weighted bi-linear interpolation of six neighboring cells, shown in Figure 4.1 for two dimensions. The sub grid contributions are modelled depending on the particle phase space variable in question, and the equivalent models are discussed in the following sections. For the cases investigated, the particle phase is dilute with volume fractions of the order $\sim \mathcal{O}(10^{-7})$ and the particle sizes considered in the nano- and micro-scales, therefore a one-way coupling[2] is implemented [37].

A first-order explicit integration scheme is used for the deterministic paths, i.e. for the variable paths that exclude continuous diffusion and jump processes. The continuous stochastic diffusion processes are modelled with the means of a Wiener term increment taken as $\Delta W_i = \chi_i \sqrt{\Delta t}$, where χ_i is a random variable sampled from a normal distribution of mean 0 and standard deviation 1. The Wiener term is scaled by an equivalent diffusion tensor to capture the physicality of the diffusing variable. An Euler-Maruyama

[2]For a thorough description of the qualitative criteria regarding phase coupling the interested reader may refer to chapter 2.7 in Crowe *et al.* [37].

scheme is used for the temporal integration of the SDE which is consistent with the Itô integration [65]:

$$\psi_i^{t_{n+1}} = \psi_i^{t_n} + A_i{}^{t_n}\Delta t + B_{ik}{}^{t_n}\Delta W_i^n + \mathcal{O}(\Delta t^{1/2}), \tag{4.6}$$

where $\Delta t = t_{n+1} - t_n$ and $\Delta W_i^n = W_i^{n+1} - W_i^n$. The time-step width is limited by the CFL condition (A.19) extended to the particle phase velocity, viz:

$$\Delta t \leq CFL\left(\frac{\Delta}{\max(|\mathbf{U}_f|, |\mathbf{v}_p|)}\right). \tag{4.7}$$

Finally, the jump term follows a phenomenological representation depending on the application in question. In such processes, the limit for the time-step width is heuristic. A criterion commonly used for the time-step width is that only a single jump event may occur during a residence time of Δt. Consequently, limits to the width of Δt used for the integration of a jump process depend on the particle process in question; therefore, the equivalent limits are discussed separately for each process investigated.

The following sections present the modelling approaches of the present work for particle dispersion, nucleation and aggregation. Each section reviews the need for modelling as well as the state of the art with regards to existing methodologies.

4.2. Dispersion

4.2.1. A contextualization of the study: the need for sgs modelling in particle dispersion

A number of experimental studies [122, 123, 124, 125] have investigated the characteristics of particle laden flows, concluding that the dispersion process and resulting particle concentration field are highly dependent on particle size. Moreover, computational modelling has been receiving increasing attention, because it allows for an in-depth investigation of the coupling between the continuous and dispersed phases.

A number of studies using LES have been carried out in the context of particle dispersion [239, 251, 264], where it is assumed that the sub grid-scale effects are negligible for Stokes numbers much greater than one ($St >> 1$). Miller and Bellan [154] carried out an *a priori* analysis and concluded that for $St \sim 1$ neglecting the sub grid-scale velocity fluctuations may lead to significant errors. Kuerten and Vreman [117] used an *a priori* DNS and a LES to simulate and compare turbophoresis in a particle laden flow. Fede and Simonin [51] also used a DNS and an *a posteriori* filtered-DNS (equivalent to a LES) in their study of unresolved fluid turbulence effects on the disperse phase and concluded that although the most energetic eddies contribute the most in the particle dispersion process, within a range of Stokes numbers ($0.5 < S_t < 5$) the sub grid turbulence acts as a random force which should be accurately taken into account. Shotorban and Mashayek [222] concluded that including the unresolved velocities is critical when large filter sizes are employed and/or particles have a relatively fast relaxation time. More recently, Berrouk *et al.* [21], Bini and Jones [24], Pozorksi and Apte [187], and Pozorski *et al.* [188] confirmed that a model to compensate for the sub grid continuous phase velocity fluctuations is required to reproduce the dispersion statistics of the particulate phase in an LES.

Therefore, the resolved LES field cannot (on its own) accurately predict particle dispersion and particle velocity statistics. Consequently, a model to compensate for the effects of the unresolved scales is required. This study focuses on a Lagrangian stochastic model implementation for the incorporation of sgs velocity effects on the particulate phase.

Alternative methodologies exist, such as the Approximate Deconvolution Method [231] (ADM) proposed by Kuerten [116] and Shotoban and

Mashayek [221]. ADM is a deterministic alternative to stochastic methods; the fluid velocity seen by the particle is de-convoluted in a series of steps using a filtering operator which approximates the inverse of the LES filtering function. Kuerten [116] noted that the deconvolution operator must be constructed from the same filtering operator as the one used for the LES and Shotorban [221] reported a dependence of the model performance to the number of de-convolution steps performed. It has been shown [221] that ADM improves results for particle dispersion in a turbulent shear layer comparatively to no use of a model. However, ADM cannot reconstruct scales smaller than the LES filter width[3] and consequently has been limited to fairly low Reynolds numbers and highly resolved LES i.e. $\Delta \approx 2{-}4\ \Delta_{DNS}$ [76, 221]. For a comparison between ADM and Lagrangian Stochastic models in the context of particle dispersion and their relative performance for various Stokes and Reynolds numbers the interested reader is referred to Gobert [76] and Gobert and Manhart [77].

4.2.2. Incorporating the sub grid effects: The Lagrangian Stochastic Model

A promising effort to incorporate the sub grid-scale contribution to the particle motion has been attempted with the use of Lagrangian Stochastic (LS) models. LS models were initially developed for non-inertial fluid particle tracers in RANS but the implementation was readily extended to inertial particles. The methodology stems from a basic assumption that the evolution of the Lagrangian fluid velocity is equivalent to a continuous Markov Process [65].

It is not easy to mathematically justify that the particle velocity follows a Markovian evolution, however it can be justified using a phenomenological argument. In high Reynolds number flows the Lagrangian acceleration correlation is small over time increments much larger than the Kolmogorov time-scale. Therefore for a time-increment, much larger than the Kolmogorov and much smaller than the inertial time-scale, the changes of the velocity between two successive increments are nearly independent and

[3] In other words, the ADM reconstructs scales that are larger than the LES mesh size (and smaller than the minimum scale that is fully resolved by the LES i.e. $\Delta < l_{ADM} < n\Delta$, where l_{ADM} are the scales retrieved from deconvolution and n the number of cells required to fully resolve an eddy)

depend only on local conditions (as opposed to the change of position which is strongly correlated to the integral scales of the turbulent motion, suggesting that the particle position does not evolve in a Markovian manner). The term 'nearly' is used because if the acceleration was completely uncorrelated the variance of the velocity could increase unboundedly with time. To correlate the particle acceleration to the particle velocity the incremental change in particle velocity is made to depend on the previous time-increment's velocity.

LS models have been extended to model the evolution of the dispersed phase concentration probability density function in a turbulent flow both in RANS and LES studies. The LS models offer a great advantage to an Eulerian solution of the evolution of the particulate phase in that non-linear advection terms are implicitly included without approximation when following the particle motion [258]. Haworth [85] and Pope [185] offer an extensive review of pdf methods in turbulent flows including particle dispersion in a Lagrangian framework [184].

Some fundamental work on LS models was conducted by Thomson [237], who introduced criteria for the selection of stochastic models to represent 'marked fluid particle' (i.e. non-inertial particle) trajectories in turbulent flows. Thomson argued that at a high Reynolds number, molecular diffusion effects can be considered negligible, and fluid particles can be assumed to travel with the local velocity of the fluid. Any change in the concentration field is due to the redistribution of fluid particles [258]. Therefore a correct description of the particle trajectories would allow the reconstruction of the concentration statistics, as for example the ensemble mean concentration field. Thomson introduced the *well mixed condition*[4] as the sole criterion required for the physical consistency of the model.

Using the Markov assumption for the evolution of the particle tracer velocity, a generalized Langevin stochastic differential equation can be formulated [65]:

$$d\mathbf{v}_f = \mathbf{A}_f dt + \mathbf{B}_f \cdot d\mathbf{W} \tag{4.8}$$

[4]The well mixed condition as introduced by Thomson [237], is a thermodynamic constraint that suggests that particles that are initially well mixed in position and velocity space must remain that way under turbulent flow conditions. It is effectively the reason for which Thomson argued that fluid particles can be assumed to travel with the local velocity of the fluid and molecular diffusion effects can be considered negligible.

where $\mathbf{v}_f$ is the fluid particle Lagrangian velocity, $\mathbf{A}_f$ is the deterministic contribution to the acceleration, $\mathbf{B}_f$ is a two dimensional diffusion tensor and $d\mathbf{W}$ is the incremental Wiener vector [65]. The second term of equation (4.8) is the stochastic contribution to the fluid particle acceleration.

From the well mixed condition a suitable equation is derived for the deterministic component to the fluid particle acceleration $\mathbf{A}_f$ (also called the damping function, or drift term). The Markovian evolution of the particle velocity serves as the modelling assumption for the stochastic diffusion tensor $\mathbf{B}_f$.

For locally isotropic turbulence and time increments dt within the inertial range of turbulence and larger than the Kolmogorov time-scale, Kolmogorov's similarity theory [113] suggests that the statistics of $d\mathbf{v}_f$ take a universal form:

$$< dv_{f,i} dv_{f,j} >= \delta_{ij} C_o^* \epsilon dt. \tag{4.9}$$

The Lagrangian velocity *structure function* of a fluid particle, equation (4.9), depends only on the time increment and the mean rate of dissipation of turbulent kinetic energy ϵ, where δ_{ij} is the Kronecker delta. The constant of proportionality is the universal Kolmogorov constant C_o^*. The structure function is equivalent to the variance of the velocity and therefore its square root can be used as the standard deviation of the diffusion process of equation (4.8) i.e.

$$dv_{f,i} = A_{f,i} dt + \sqrt{C_o^* \epsilon} dW_i. \tag{4.10}$$

At this point it is important to note two aspects of the LS model briefly described. Firstly, the model describes *non-inertial* particles in a RANS framework. The model compensates for the *temporal* fluctuations of the continuous phase velocity using a stochastic Lagrangian forcing quantified by the diffusion coefficient in equation (4.10). In the context of LES the stochastic contribution is required to simulate the unresolved turbulent scales, i.e. to compensate for the fluid phase *spatial* velocity fluctuations. Therefore, Kolmogorov's theory cannot be readily applied to derive the diffusion tensor $\mathbf{B}_f$ from first principles. On the other hand, models are heuristic and their constant of proportionality –equivalent to C_o^*– is *not* universal, but is rather a modelling parameter scattered in the interval of $2 - 8$ depending on the test case [184, 133]. The true particle trajectory is assumed to be

approximated by a model trajectory. The LS models described stem from the concept of a fluid particle, i.e. a notional parcel of fluid with a constant concentration. Physical particles are different as they may influence, or be influenced by the flow, due to their inertia or mass exchange, etc.

In a number of studies the LS model is employed to acquire the fluid velocity at the particle location i.e. the velocity 'seen' by the inertial particle $\mathbf{v}_{f@p}$. Shotorban and Mashayek [222] added a stochastic diffusion term to compensate for the unresolved fluctuations of the uniform phase velocity seen by the particles and carried out an *a priori* (filtered DNS) and *a posteriori* (LES simulation) investigation on the effects on the motion of the particles in isotropic decaying turbulence. Pozorski and co-workers [187, 188] implemented an equivalent model for stochastic dispersion in an analysis of preferential particle concentration in turbulent structures and in an LES of a heated channel flow. They reported that sub-filter particle velocity variations influence the results. Fede *et al.* [52] model the incremental change of the *unresolved* fluid velocity seen by the particle using a Langevin equation derived from the Navier-Stokes equation. The fluctuating component is superimposed to the resolved fluid phase velocity seen by the particle to determine its acceleration.

One of the main problems arising from such LS-LES models is the evaluation of the eddy interaction time-scale seen by the particle and the dispersion coefficient C_o^* required to evaluate the turbulent diffusion coefficient of equation (4.10). These parameters exhibit a dependence on the Stokes number and the grid spacing and an effort has been made to fit empirical curves for the eddy interaction time-scale such as in the work of Jin *et al.* [93]. However, to the author's knowledge, there has not been a comprehensive evaluation of the dispersion coefficient C_o^*.

The LS models mentioned thus far are different to the one employed in this study, the main difference being the fact that in the method of Bini and Jones [23, 24, 22], the stochastic contribution is directly accounted for in a SDE for the particle acceleration following a heuristic procedure. On the other hand, the aforementioned LS models use the Langevin equation to simulate the Lagrangian fluid phase velocity *viewed* by the particle starting from the Lagrangian description of the Navier-Stokes equations. Bini [22] proposes an equation for the particle equation of motion which stems from the Lagrangian solution (Itô equivalent) of the spray-pdf equation of

Williams [256] (outlined in 3.3.1). Bini's model has shown good agreement in particle acceleration statistics [23] and dispersion characteristics in a turbulent shear layer[24].

The present work extends the applicability of this model by proposing a methodology for the dynamic evaluation of the dispersion constant C_o.

4.2.3. Lagrangian Stochastic Dispersion using the Filtered spray-pdf

For plain dispersion processes, the obvious choice for a state vector with ith variable realizations ψ_i^j is one with six state variables, the three-dimensional particle velocity $\mathbf{v}_p$ and position $\mathbf{x}_p$. Replacing the equivalent phase state to equation (4.2), the following LES spray-pdf equation may be formulated for the random variables $\mathbf{V}_p$ and $\mathbf{X}_p$ [22]:

$$\frac{\partial\tilde{\mathbb{P}}(\mathbf{V}_p;\mathbf{X}_p,t)}{\partial t}+\frac{\partial}{\partial\mathbf{X}_p}(u_p\tilde{\mathbb{P}}(\mathbf{V}_p;\mathbf{X}_p,t))+\frac{\partial}{\partial\mathbf{V}_p}(a_p\tilde{\mathbb{P}}(\mathbf{V}_p;\mathbf{X}_p,t))=0 \quad (4.11)$$

The first term of equation (4.11) represents the rate of change of the probability density in physical space. The second and third terms incorporate the advection process due to the conditional rate of change 'u_p' and 'a_p' of particle position and velocity, respectively. As opposed to 'u_p' which is only a function of the ensemble of particles and their velocity , the conditional filtered particle acceleration is not readily available and depends on the full spectrum of turbulent motion, see the individual path equations (3.5) and (3.6); a model is therefore required.

Itô's equivalent SDE for inertial particles is solved instead of the spray-pdf equation (4.11) following the solution proposed by Jones *et al.* [23, 24, 99]. Inertial effects are combined with the drag force, and it is assumed that the gravitational and buoyancy effects for Froude number of the particle are insignificant for $Fr >> 1$, and that thermo- and electro-phoresis can be neglected (see section 3.1.2). With these assumptions, the particles' equation of motion can be described by the Lagrangian equations (3.5) and (3.6):

$$\left(d\mathbf{x}_p=\mathbf{v}_p dt \quad ; \quad \frac{d\mathbf{v}_p}{dt}=\frac{\mathbf{U}_f-\mathbf{v}_p}{\tau_I}\right), \text{ respectively.}$$

The RHS of equation (3.6) is equivalent to a single realization of the

acceleration a_p (i.e. the acceleration of one particle) in the spray-pdf equation (4.11). One may notice that it is a function of the full spectrum of the gaseous velocity, which can be decomposed into a filtered and sub-filter component ($\mathbf{U}_f = \tilde{\mathbf{U}}_f + \mathbf{U}_{sgs}$). By equivalence to a stochastic diffusion process [65], the influence of the unresolved SGS velocity fluctuations, $\mathbf{U}_{sgs}$, on the particle acceleration is modelled by adding a stochastic forcing to the resolved/deterministic component of (3.6).

Miller and Bellan[154] and Okong'o and Bellan[166] proposed that for a scalar, this contribution can be related to the realization of a normally distributed random variable with a standard deviation proportional to the standard deviation of the sub grid fluctuation of the scalar. In the context of this study the component of interest is the particle velocity which is a vector variable and therefore a different approach is needed to comply with a vector's transformation properties [24].

Jones and Bini [23, 24] model the unresolved contribution by a Wiener term scaled by a 'turbulent' diffusion coefficient; see equation (4.12). By dimensional analysis this coefficient is expected to be proportional to the time- and length-scales of the unresolved stresses quantified by the sub grid kinetic energy, k_{sgs}, and the time-scale of turbulent interactions between the two phases, τ_t. This results in:

$$d\mathbf{v}_p = \frac{(\tilde{\mathbf{U}}_f - \mathbf{v_p})}{\tau_p} dt + \sqrt{C_o \frac{k_{sgs}}{\tau_t}} d\mathbf{W}, \tag{4.12}$$

where, C_o is the dispersion constant. Following Bini[23], the unresolved kinetic energy of the gas phase is calculated as: $k_{sgs} = 2\Delta^2 C_s^{4/3} \tilde{S}_{ij} \tilde{S}_{ij}$ where $\tilde{S}_{ij}$ is the filtered strain tensor. The particle relaxation time τ_p indicates the time it will take for a particle to adjust to a change in the carrier phase velocity $\tilde{\mathbf{U}}_f$ (or to come to rest in a stationary flow), and it is described by:

$$\tau_p^{-1} = \frac{3}{4} \frac{\rho_f C_D}{\rho_p d_p} |\tilde{\mathbf{U}}_f - \mathbf{v_p}|, \tag{4.13}$$

where ρ_p and ρ_f are the particle and continuous phase densities, d_p is the particle diameter, and C_D is the drag coefficient.

The drag coefficient, C_D, is evaluated using an empirical relation to the particle Reynolds number $Re_p = \rho_f d_p |\tilde{\mathbf{U}}_f - \mathbf{v_p}|/\mu$ (where μ is the viscosity of

the continuous phase), defined by the drag law of Yuen-Chen[269] assuming spherical particles.

$$C_D = \begin{cases} \frac{24}{Re_p}(1 + \frac{Re_p^{2/3}}{6}) & 0 < Re_p < 1000 \\ 0.424 & Re_p > 1000 \end{cases} . \tag{4.14}$$

Note that particles in the nano-scale tend to follow the flow closely, however when they have a comparable size to the mean free path of the fluid molecules they may not view the fluid as a continuum. The incorporation of the Cunningham slip correction G_i (see for example the formulation of Knudsen and Weber [107]) could alter the modelled drag coefficient (by a factor $C_D \cdot 1/G_i$) and therefore particle path depending on their diameter and relative magnitudes of turbulent and molecular diffusivity.

The turbulent time scale proposed[23] τ_t depends on the constant α, which determines the degree of non linearity introduced in the model:

$$\tau_t = \tau_p \left(\frac{\tau_p k_{sgs}^{1/2}}{\Delta} \right)^{2\alpha - 1} . \tag{4.15}$$

Following a detailed evaluation of the parameter α, Bini and Jones [24] concluded that a value of 0.8 is required to produce suitable levels of kurtosis in turbulent flow acceleration pdfs. The limits of $\alpha = 0$ and $\alpha = 1$ correspond to normal and log-normal pdfs of acceleration, respectively [23]. Finally, a proportionality constant is required for the stochastic diffusion term, in this case C_o, which scales the stochastic contribution to the velocity of the Lagrangian particles.

Finally, the ensemble average of all particle paths should give the Eulerian equivalent of the positions and velocities of the particles, $U_d = \langle \mathbf{v_p} \rangle_n$, where the brackets $\langle \cdot \rangle$ indicate averaging over an ensemble of n particle paths. Similarly the remaining moments and distribution of the particle position/velocity/acceleration at a given location can be constructed form the individual realizations (paths).

4.2.4. Proposed dynamic model for the evaluation of the dispersion coefficient

The expression (4.12) is heuristic and uses the Markovian assumption to model the sub grid contribution with a Brownian diffusion term. The scaling of the Lagrangian forcing to the sub grid kinetic energy is controlled by C_o. However, this dispersion coefficient cannot be related to the Kolmogorov constant arising from the velocity structure function [237]. Moreover, C_o cannot be evaluated analytically from a spectral analysis as performed by Lilly [136] for the Smagorinsky constant.

Results of Jones *et al.* [99] have shown that the choice of C_o influences the dispersion process and in this work it is shown that the coefficient exhibits significant grid and particle relaxation time dependence.

As in the turbulent stress model implementation of Piomelli [181], a test-filtering process is suggested by convolution of a LES generic variable $\tilde{\phi}$ with a test filtering kernel $G_{\hat{\Delta}}$, viz:

$$\hat{\tilde{\phi}}(\mathbf{x}) = \int \tilde{\phi}(\mathbf{x}') \cdot G_{\hat{\Delta}}(\mathbf{x}, \mathbf{x}') d\mathbf{x}'. \tag{4.16}$$

Where $\hat{\cdot}$ signifies a test-filtered quantity and the test-filter width is taken in this work as $\hat{\Delta} = 2\Delta$. At this point, one must make a clarification in terms of what is test-filtered in the context of the proposed model. The drift and diffusion terms of the SDE, equation (4.12), are functions of local interpolated LES Eulerian quantities ($\tilde{\mathbf{U}}_f$, k_{sgs}) and Lagrangian particle properties. The test filter is applied to all the Eulerian quantities used for the calculation of the drift and diffusion terms prior to their interpolation to the local particle position.

For simplicity $\hat{\cdot}$ will imply both test-filtered and test-filtered derived quantities, i.e. $\widehat{d\mathbf{v_p}}$ is the change in Lagrangian particle velocity due to its interaction with the test-filtered Eulerian field within an increment $\widehat{dt}$ (where $\hat{\cdot}$ is included to specify that the integration is over the time-step limited by the CFL condition applied to the test-filtered Eulerian velocity field).

Similarly the test-filtered drift $\hat{\mathbf{A}}$ and diffusion $\hat{B}$ terms are functions of the interpolated test-filtered Eulerian values ($\widehat{\tilde{\mathbf{U}}}_f$, $\widehat{k_{sgs}}$), the test-filter derived relaxation and turbulent interaction time-scales ($\widehat{\tau}_p$, $\widehat{\tau}_t$), and the Lagrangian filter-independent quantities i.e. the particle velocity $\mathbf{v_p}$ and

mass m_p. Therefore, one may formulate an equation for the test-filtered derived acceleration:

$$\begin{aligned} \widehat{d\mathbf{v}_p} &= \frac{(\widehat{\tilde{\mathbf{U}}}_f - \mathbf{v_p})}{\widehat{\tau}_p}\widehat{dt} + \sqrt{C_o \frac{\widehat{k_{sgs}}}{\widehat{\tau}_t}} d\mathbf{W} \\ &= \hat{\mathbf{A}}\widehat{dt} + \sqrt{C_o}\hat{B}d\mathbf{W}. \end{aligned} \tag{4.17}$$

It must be stressed that, unless stated otherwise, the parameters in (4.17) are not explicitly test-filtered, but are derived from the Eulerian test-filtered quantities. Also note that for simplicity, the dispersion coefficient has been taken out of the diffusion term $\hat{B}$. The diffusion and drift terms could then be replaced without any loss of generality to a phenomenological, SDE based, model.

Having established the filtering process, one must formulate an assumption on which the comparison (between LES filtered and test-filtered quantities) is based. The evident difficulty in direct comparison of acceleration arises from the Wiener process. Since it is stochastic in nature with a zero mean, the ensemble average acceleration of all particles within a given cell should not be a function of the diffusion coefficient (given the number of samples/particles is sufficiently high).

In the present work it is assumed that the ensemble-averaged change in kinetic energy of particles, $< dK_p >$, with same initial conditions within a cell should be the same for the two filtering levels (Eulerian LES and the *a posteriori* test-filtered equivalent). Physically, this means that the total energy transfer from the Eulerian to the Lagrangian phase within a given time increment should be grid independent and only a function of the flow characteristics. Equation (4.18) gives the kinetic energy of a single particle, which at a time t_0 is the same for the two filtering levels:

$$K_p = \frac{1}{2} m_p \mathbf{v}_p^2 = \frac{1}{2} m_p (v_{p_1}^2 + v_{p_2}^2 + v_{p_3}^2). \tag{4.18}$$

To calculate the variation of particle kinetic energy dK_p from t_0 to $t_0 + dt$ it should be noted that the kinetic energy is a function of the random variable $\mathbf{v}_p$, which is continuous but not differentiable in time. Therefore conventional calculus cannot be employed, and the variation of kinetic energy is retrieved using Itô's Lemma (3.16) for a time-dependent function of

a stochastic process:

$$dK_p = \left[A_i \cdot \frac{dK_p}{dv_{p_i}} + \frac{1}{2} C_o B^2 \frac{d^2 K_p}{dv_{p_i}^2} \right] dt + \sqrt{C_o} B \frac{dK_p}{dv_{p_i}} \cdot dW_i. \tag{4.19}$$

Taking the ensemble average of equation (4.19) and assuming a large number of particles, such that $< d\mathbf{W} >_n \rightarrow 0$ the following equations can be written for the variation of particle phase kinetic energy derived from the LES (4.20) and test-filtered (4.21) velocities:

$$\langle dK_p \rangle = \left\langle \left[m_p A_i \cdot v_{p_i} + \frac{3}{2} m_p C_o B^2 \right] dt \right\rangle, \tag{4.20}$$

$$\left\langle \widehat{dK_p} \right\rangle = \left\langle \left[m_p \widehat{A}_i \cdot v_{p_i} + \frac{3}{2} m_p C_o \widehat{B}^2 \right] \widehat{dt} \right\rangle. \tag{4.21}$$

Note that all the terms in the RHS of (4.19) are evaluated at t_0; therefore the Lagrangian particle velocity and mass is the same for the two filtering levels. Moreover note that because the diffusion tensor is isotropic, the summation over all directions reduces to the second terms of the RHS of equations (4.20) and (4.21). Equating (4.20) and (4.21) for a common time increment one may formulate the following expression for the dynamically derived dispersion coefficient C_{dyn}:

$$C_{dyn} = \left| \frac{\left\langle m_p \left[v_{p_1} \left(f_r A_1 - \hat{A}_1 \right) + v_{p_2} \left(f_r A_2 - \hat{A}_2 \right) + v_{p_3} \left(f_r A_3 - \hat{A}_3 \right) \right] \right\rangle}{\left\langle \frac{3}{2} m_p \left(\hat{B}^2 - f_r B^2 \right) \right\rangle} \right| \tag{4.22}$$

Where the factor f_r relates the time increments of the two differential equations to compare the transfer of kinetic energy from the Eulerian phase to the particulate phase in the same time-step. For simplicity this time-step is chosen, to be that from the LES, for which values are readily available. The time increment is a function of global maximum velocity (which is constant since at t_0 the particle velocities are the same for the two filtering levels) and grid-spacing as given by the CFL condition (4.7), therefore the factor $f_r = \widehat{dt}/dt$ is $\hat{\Delta}/\Delta = 2$. The absolute value in equation (4.22) is taken to enforce a positive constant, since its square root is required for the evaluation of the SDE equation (4.12). Similar to the Germano model for the evaluation of the Smagorinsky constant, the dispersion coefficient is test-filtered to ensure smoothness.

Although the methodology for the evaluation of C_{dyn} is similar to that of the dynamic Germano model, C_{dyn} does not have to acquire a value of 0 in a laminar flow (unless $\tilde{U}_f \approx v_p$); instead C_{dyn} has to attain a *finite* value. It can be shown that in the limit $\hat{\tilde{U}} \to \tilde{U}$ in laminar flows, C_{dyn} is proportional to $\alpha(\tilde{U}_f - v_p)^{2(1-\alpha)}$. Yet, the stochastic contribution at the filtering level in the limit of a laminar flow $\sqrt{C_{dyn} k_{sgs}/\tau_t} \to 0$ will vanish as $k_{sgs} \to 0$. The model is investigated in the context of turbulent shear flows in Chapter 5.

4.3. Nucleation

One way to separate between a molecular cluster and a particle of the aerosol (i.e. a 'larger' molecular cluster) is by its motion in the uniform phase. A molecule, or extremely small group of molecules, will undergo discontinuous changes in position as characterized by Brownian motion. On the other hand, particles that are heavy enough so as to smooth the trajectories caused by the continuous molecular collisions on their surface [197]. Therefore, one may differentiate between the uniform and disperse phases, on the basis that the latter is comprised of particles.

Uniform phase processes may reach a supersaturated state which suddenly collapses due to a phase transition of the supersaturated vapor to an aerosol. This process is termed *nucleation* and it involves the use of either a nucleus composed of vapor molecules of the same material, or an exogenous (to the vapor) surface such as an ionic cluster, an impurity on the surrounding enclosure (e.g. bubbles formed at the surface of a glass of sparkling water), or a small particle of a different material (e.g. dust particles).

Homogeneous nucleation describes the process whereby one or more gases condense without the aid of an exogenous surface to form particles. Homomolecular nucleation occurs when a single gas species nucleates, binary and ternary nucleation when two or three gases nucleate to form a single particle of joint composition, such as sulfuric acid with ammonia and water [91]. For homogeneous nucleation to occur, the vapor must first reach a supersaturated state. Thereafter, a small 'embryo' must form that will allow additional vapor molecules to attach and cause the embryo to grow. Nucleation embryos are continuously formed and disintegrated by random processes; depending on the local thermodynamic conditions, a stable nucleus might form and grow to become a particle [197].

Heterogeneous nucleation on the other hand uses nuclei of a dissimilar material on which the supersaturated vapor condensates and grows into a particle. Effectively, instead of the use of an embryo of the same material, an impurity is used on which the vapor condenses to form a stable nucleus. Such condensation nuclei, e.g. dust particles, render the high supersaturations unnecessary for nucleation to occur. On the contrary, spontaneous condensation is not significant until very high supersaturations.

4.3.1. Contextualization of nucleation: the need for accurate modelling

Nucleation is the driving process in a number of industrial and atmospheric applications, such as soot formation in combustion processes and fugitive emissions from industrial sources [173], nano-particle synthesis [191, 235], and crystal precipitation in liquid phase reactors, among others. All these processes highly depend on nucleation rates [243]. A correct description of nucleation and growth processes may lead to a successful retrieval of the Particle Size Distribution (PSD). The ability to influence or control the PSD is a very useful tool for generating filter test particles [109] or for preventing health-related effects of newly formed particles [135].

From the aforementioned theoretical overview, the nucleation process is described; however, the critical parameters affecting the rates and formed particles are not addressed. Namely, how the level of saturation (quantified by the saturation pressure ratio $S = P_v/P_{sat}$) relates to the nucleation rates, $\dot{I}$? What is the critical diameter, d_p^*, at which particles will grow and not collapse?

Any first order phase transition requires the surmounting of an energy barrier. A fluctuation in temperature, pressure, or concentration modifies the activation energy and therefore locally modifies the rate of phase transition. This process makes nucleation rates extremely sensitive to changes in local thermodynamic properties [120]. This non-linearity is the primary challenge and incentive for the examination of nucleation events.

Traditional nucleation experiments aimed at retrieving the critical saturations needed to produce a certain nucleation rate. Further developments in experimental techniques allowed for an investigation of a large range of produced concentrations. For homomolecular nucleation the following two methods and their variations have been widely used: firstly, diffusion chambers in which the saturated vapor diffuses in a colder inert gas causing the vapor to condense; secondly, expansion chambers, used to create nucleation pulses by rapid expansion of the supersaturated vapor. In contrast to the continuous operation of a diffusion chamber, in an expansion chambers the vapor is cooled rapidly by a piston expansion or with the use of a shock tube. A slight re-compression of the piston and the reflection of the pressure wave from the end wall, in the case of the shock tube, are used to quench further

nucleation and thus allow one to calculate the resulting concentrations. The motivation is to measure nucleation rates at given initial saturation ratios at a constant temperature. For a thorough review, the reader is referred to Laaksonen *et al.* [120], who categorized the various experimental techniques available for nucleation studies and explained in detail their operation and experimental findings.

Direct measurement of nucleation rates is difficult in non-stationary environments. Although there are a number of ways to retrieve the PSD and concentration densities (e.g. with the use of a Condensation Particle Counter), the rate of particle formation at an exact location cannot be measured directly. This occurs because at any position of the domain, the measured instantaneous concentration includes particles that nucleated upstream and were subsequently transported to that location.

A deeper understanding of the nucleation process therefore requires a close examination of experimental data along with rigorous computational modelling. Early investigations of turbulent-coupled nucleation were almost exclusively theoretical or experimental. A description of species concentration, temperature, and velocity fluctuations was limited; nucleation rates were therefore rendered unreliable [276]. With the recent advance in computational power various approaches have been introduced for the coupling of the particulate phase evolution with a turbulent flow.

In this work work a new implementation of the nucleation theory in the context of a Large Eddy Simulation is outlined. The direct use of instantaneous data from LES can be very important due to the non-linearity of the nucleation rate. To investigate the significance of the sub-grid scale contributions on homogeneous nucleation rates two models are implemented to account for the sgs.

4.3.2. Nucleation Rate

There are three approaches to nucleation (of which a thorough review can be found in Oxtoby [170]):

- Firstly, the phenomenological approach were a required free energy of formation is established with the use of macroscopic fluid quantities such as the surface tension σ and the condensed particle's liquid density ρ_l.

- Secondly, kinetic approaches, which evaluate the forward and backward rate constants without direct reference to formation free energies of clusters. Instead, nucleation rates are approximated from the interaction potential between particles which depend again on quantities such as the surface tension and liquid vapor density.
- The third is the microscopic method, such approaches avoid certain issues of the phenomenological theories by applying first principle models developed for cluster structures and the free energy of cluster formation. The aim is to define a physically consistent cluster definition based on a stable cluster radius.

Uncertainties in kinetic approaches force the theories to fit parameters to experimental data for surface tension, condensed vapor density, or even nucleation rate itself, therefore limiting its theoretical results [170]. The major short-back in microscopic theories is that the volumes and times involved restrict the theory to supersaturations much larger than experimental methods can produce and thus the focus is on isolated cluster properties [170]. The latter two methods do not explicitly calculate the nucleation rate, instead, the formation process is simulated using a PBE for size-classes of small clusters and monomers [75]. Therefore, although the treatment can be considered 'exact' there is a major disadvantage in computational economy. The interested reader may refer to [120, 170] for a thorough review of both theoretical and experimental progress on nucleation.

4.3.2.1. Classical Nucleation Theory

In this work a phenomenological approach is used to model nucleation, namely: the Classical Nucleation Theory (CNT) [19, 61, 270]. This choice is based upon the physical characteristics of the framework in which it is examined, where a significant number of particles is produced in a large domain and the production is coupled to the flow properties. The nucleation rate $\dot{I}[\#/\mathrm{m}^3\mathrm{s}]$ is given by the CNT as:

$$\dot{I} = \frac{P_v X_v}{k_B T}\sqrt{\frac{2\sigma}{\pi \bar{m}}}\exp\left[\frac{-16\pi\sigma^3\bar{m}^2}{3(k_B T)^3\rho_l^2(lnS)^2}\right]. \tag{4.23}$$

The partial pressure and concentration of the nucleating vapor are P_v and X_v, respectively; $S = P_v/P_{sat}$ is the saturation ratio, with the saturation

pressure P_{sat}; the surface tension σ and condensed density ρ_l are retrieved from experimentally fitted functions depending on the nucleating species; T is the temperature in Kelvin; k_B is the Boltzmann constant; and $\bar{m}$ is the mass of a monomer, given by $\bar{m} = \bar{M}/N_{avg}$, where $\bar{M}$ is the molecular weight of the condensing species and N_{avg} is Avogadro's number.

Equation (4.23) stems from a thermodynamic equilibrium model, viz:

$$\dot{I} = I_o \exp(-\Delta G_{hom}/k_B T), \tag{4.24}$$

where: I_o is a non-exponential scaling function; and ΔG_{hom} is the thermodynamic barrier to homogeneous nucleation and represents the increase of free energy of a system due to the formation of a nucleus of critical size d_p^*, which is given by:

$$d_p^* = \frac{4\sigma v_m}{k_B T \ln S}, \tag{4.25}$$

where v_m is the surface volume of a monomer. Higher saturation ratios and temperatures allow smaller droplets to be stable. Equation (4.23) thus gives the rate of creation of particles of size d_p^* at a given thermodynamic state. A full derivation can be found in [91, 197, 217].

The wide use of the CNT in the analysis of nucleation may be attributed to the availability of data for many substances with regards to their macroscopic thermodynamic properties (σ, ρ_l, S) and the availability of critical supersaturation values [120]. However, the popularity of the CNT has also lead to numerous heuristic expressions for these properties in the literature, of which a selection (including these used in the present work) are presented in Table 4.1. A small fluctuation in any of these macroscopic parameters may lead to a difference of several orders of magnitude in the nucleation rates. For example, a small variation in the surface tension $\sigma + \Delta\sigma$ will result in a nucleation rate of the order $\mathcal{O}(\exp[(\sigma + \Delta\sigma)^3])$.

Additionally there have been a great number of modifications to the CNT, and therefore to the expression for $\dot{I}$. Lothe and Pound [141] considered transitional and rotational degrees of freedom contributing to the free energy ΔG, increasing nucleation rates by 17 orders of magnitude! Reiss [196] argued that using the experimental values for surface tension variation incorporates these degrees of freedom, since the partial derivative of the Gibbs free energy with respect to surface area is the surface tension. In an

Table 4.1.: DBP condensation properties

$\bar{M} = 278.35\text{kg/kmol}$	ref.[4]*
$\rho_l = 1063 - 0.826(T - 273)\text{kg/m}^3$	ref.[129, 167, 66]*
$\rho_l = 1049 - 0.67(T - T_o)\text{kg/m}^3$	ref.[243, 20]
$P_{sat} = \exp\left(16.27 - \frac{5099}{T-109.51}\right)\text{mmHg}$	ref.[167]
$P_{sat} = \exp\left(16.27 - \frac{5099}{T-109.65}\right)\text{mmHg}$	ref.[84]
$P_{sat} = 10^{7.065-1666/T-547700/T^2}\text{mmHg}$	ref.[66, 20]*
$P_{sat} = 10^{-4501/T+12.88}\text{Pa}$	ref.[243, 186]
$\sigma = (35.3 - 0.0863(T - 273)) \times 10^{-3}\text{N/m}$	ref.[129, 167]
$\sigma = (33.93 - 0.0894(T - 293.15)) \times 10^{-3}\text{N/m}$	ref.[243, 20]
$\sigma = 0.059663 \times (1 - \frac{T}{T_{crit}})^{1.2457}\text{N/m}$	ref.[4]
$\sigma = 1.04(35.3 - 0.2(T - 273)) \times 10^{-3}\text{N/m}$	ref.[66]
$\sigma = 1.0(35.3 - 0.13(T - 273)) \times 10^{-3}\text{N/m}$	*

*Unless stated otherwise, these are the expressions used in this work

attempt to formulate a self-consistent theory, Girshick *et al.* [74] proposed a correction factor to the nucleation rate such that $\dot{I}_{sc} = \dot{I} \times \exp(\theta)/S$, where $\theta = \sigma s_m / k_B T$ is a dimensionless surface energy and s_m is the surface area of a monomer, such that for a monomer $\Delta G = 0$.

Several authors [39, 119] modified the nucleation rate by altering the energy barrier to include the differences between the surface free energy of a cluster and of a liquid droplet. They included the self-consistent theory-driven parameter $1/S$ in the nucleation term but added a contribution of additional degrees of freedom and a curvature dependence of the surface energy on local thermodynamic properties. Hale [83] assumed a linear variation of the surface tension with respect to temperature, and suggested that critical supersaturation can be calculated with the use of a universal constant that measures the excess entropy of a molecule's surface. Granasy [80] suggested a parametrization where both enthalpy and density profiles of the droplets are shifted by a constant amount which is independent of droplet size. In this way he obtained a curvature correction without having to re-establish relationships for the macroscopic thermodynamic parameters. A thorough review of the literature describing the various corrections to the CNT can be found in the work of Laaksonen [120].

From the above discussion it can be concluded that there are a number of problems posed by the CNT. CNT has shown good agreement with experimental results, however usually subject to modifications. It can be argued that the parameter with the least certainty is the surface tension (rather than the critical saturation temperature or pressure). A correct treatment and calculation of σ may mitigate the effects of additional degrees of freedom on the activation energy required for nucleation, along with material-based inconsistencies.

4.3.3. Turbulent coupling

A number of nucleation studies [66, 128, 243, 259] have shown that the calculation of nucleation rates from mean values leads to erroneous results, due to the high non-linearity of Eqn. (4.23). The test case studied in this work has been simulated using a number of methods which stem from population balance modelling, and these are outlined below.

The diameter-based PBE for growth, nucleation, and excluding Brownian diffusion is:

$$\frac{\partial \mathcal{N}(d_p;\mathbf{x},t)}{\partial t}+\frac{\partial}{\partial \mathbf{x}}(\mathbf{U}_f\cdot\mathcal{N}(d_p;\mathbf{x},t))+\frac{\partial}{\partial d_p}(G\cdot\mathcal{N}(d_p;\mathbf{x},t))=\dot{I}\cdot\delta(d_p-d_p^*), \tag{4.26}$$

where $\mathcal{N}$ is the particle number density for a given particle diameter d_p, at a position $\mathbf{x}$ and time t.

Garmony and Mastorakos [66] implemented a two-dimensional RANS simulation using a stochastic fields method for the solution of the PBE. The nucleation rate was considered as a source term, adding newly formed particles of size d_p^* to the equivalent class of the number density equation. To avoid the fine discretization of size classes required for an accurate solution of the discretized PBE, a moment-based approach [192] was used in which a log-normal distribution was presumed for the unresolved moments. A Itô equivalent Stochastic Partial Differential Equation was solved for the evolution of five scalars (temperature, concentration and the first three moments of the PBE) from which the ensemble average gave values for the PSD at all of the positions of the Eulerian domain.

Veroli and Rigopoulos [243] followed the method proposed by Rigopoulos

[203] for the solution of a PBE-PDF equation. Closure of the turbulent PBE is accomplished by transporting a one-point joint-PDF of temperature T and concentration X_v and a set of discretized number densities. The unclosed terms are modelled using a turbulent diffusivity and the Interaction via Exchange with the Mean (IEM) [40] for the micromixing terms. A two-dimensional RANS-PDF simulation was carried out using the Lagrangian particle tracking method [244] for the solution of the PDF transport equation. Stochastic parcels were injected into the domain with an average of 20 parcels per cell carrying values for the scalars and each discrete size class.

Zhou and Chan [276] proposed an Equivalent Mean Nucleation Method (EMNM) coupled with an LES. The EMNM splits the nucleation equation (4.23) into its exponential and pre-exponential terms. The pre-exponential term, as well as the surface tension, density, and saturation ratio, varies much slower with temperature than the exponentiated function. These values are therefore taken to be constant within the narrow temperature range over which nucleation takes place. By integrating the product of the strongly-dependent exponential term with a temperature PDF, the temporal fluctuations are taken into account. The EMNM assumes that due to the sensitivity and rapid nature of nucleation the distribution of the nucleation rate over the temperature is equivalent to a top-hat function with a 'characteristic width' $\delta T|_{0.5\dot{I}_{max}}$. The width $\delta T|_{0.5\dot{I}_{max}}$ extends from $T|_{\dot{I}_{max}} - T|_{0.5\dot{I}_{max}}$ to $T|_{\dot{I}_{max}} + T|_{0.5\dot{I}_{max}}$, where $T|_{\dot{I}_{max}}$ is the temperature corresponding to the maximum nucleation rate and $T|_{0.5\dot{I}_{max}}$ is the temperature at half of this maximum. The integral over the temperature PDF of the strongly-dependent exponential term is therefore reformulated as the product of the width $\delta T|_{0.5\dot{I}_{max}}$ with the exponential term and temperature PDF (both evaluated at $T|_{\dot{I}_{max}}$). From the mean flow and temperature PDF, a mean nucleation rate was obtained for every point in the domain [276]. The mean particle concentration was assumed to be independent of fluctuations in the source term, and on that basis the time-averaged nucleation rate was used for all time-steps.

4.3.4. Proposed incorporation of nucleation in the spray-pdf equation

In the present work, nucleation and particle transport are investigated in the context of LES. The implementation of the homogeneous rate equation is different from the aforementioned implementation and has not been studied before. Following the particle transport approach the nucleation is modelled using the filtered spray-pdf equation:

$$\frac{\partial \tilde{\mathbb{P}}}{\partial t} + \frac{\partial}{\partial \mathbf{X}_p}(u_p \tilde{\mathbb{P}}) + \frac{\partial}{\partial \mathbf{V}_p}(a_p \tilde{\mathbb{P}}) + \frac{\partial}{\partial N_c}(\dot{N}_c \tilde{\mathbb{P}}) = 0, \tag{4.27}$$

where the number concentration N_c has been added to the particle state vector of equation (4.11). Therefore, the state vector includes seven variables: the three dimensional velocity $\mathbf{V}_p$ and position $\mathbf{X}_p$, and the number concentration N_c. Lower-case letters are used to describe the Lagrangian realizations n_p, $\mathbf{x}_p$ and $\mathbf{v}_p$ of the (upper-case) equivalent random variables.

It is important to note that N_c is *not* the number density of the PBE, but a number concentration indicating the total number of particles per unit volume as a function of space and time; the number density $\mathcal{N}$ is additionally a function of particle size d_p. Mathematically the relation between the number density and number concentration is:

$$N_c(\mathbf{x}, t) = \int \mathcal{N}(d_p; \mathbf{x}, t) d(d_p). \tag{4.28}$$

If only nucleation is considered (i.e. neglecting fragmentation and aggregation), every formed particle of size d_p^* is represented by a single numerical parcel which has a constant number concentration, n_p, throughout its motion. Therefore for the equivalent path and Eulerian formulations we have:

$$\frac{dn_p}{dt} = \mathrm{i} \tag{4.29}$$

$$\dot{N}_c = \dot{I} - \mathbf{U}_f \frac{\partial N_c}{\partial \mathbf{x}}, \tag{4.30}$$

where the rate 'i' is used to differentiate from the Eulerian nucleation rate $\dot{I}$. Note that the convective effects in (4.30) are included implicitly in the particle path equations (3.5) and (4.12), as the rate in (4.29) is Lagrangian and represents a total derivative.

If physical particles are used the spray-PDF is only a function of $\mathbf{X}_p$, $\mathbf{V}_p$ and time t. The addition of a particle by nucleation simply adds a path (realization) to the trajectories of position (3.5) and acceleration (4.12). If notional particles (i.e. stochastic parcels) are used, in which the real particle number concentration can vary from and include zero, equation (4.29) must be solved as well.

If physical particles are used, the Eulerian variable $N_c(\mathbf{x}, t)$ representing particle concentration in a given position and time is reconstructed from the instantaneous *sum* of the individual paths conditioned upon their location $\mathbf{x}$. Once temporally averaged, $\langle N_c(\mathbf{x}, t)\rangle_t$ gives the mean particle concentration at a given location of the Eulerian domain. In contrast, if the number density is included in the particle state vector, the *ensemble average* of the number density paths of the stochastic parcels would give $\mathcal{N}(d_p; \mathbf{x}, t)$, and the conditional *ensemble average* rate of change of the individual paths would be required to evaluate $\dot{\mathcal{N}}(d_p; \mathbf{x}, t)$, whose evolution is described by (4.26).

Using equation (4.27), the PSD can be readily retrieved at any location in the domain by constructing a histogram of the number of particles at that location as a function of their size. This is equivalent to including the particle size in the spray-PDF formulation and calculating the joint probability of particle concentration and diameter by eliminating the remaining state vector variables, where N_{tot} is the total particle number concentration in the domain:

$$\mathcal{N}(d_p, t) = N_{tot} \int_{\mathbf{X}_p} \int_{\mathbf{V}_p} \mathbb{P}(\mathbf{V}_p; \mathbf{X}_p; d_p; N_c, t) d\mathbf{X}_p d\mathbf{V}_p \tag{4.31}$$

The proposed method takes advantage of the ability of LES to provide instantaneous values of the uniform phase velocities, temperatures and concentrations, thus enabling the calculation of an *instantaneous nucleation rate*. Therefore, a model to compensate for temporal fluctuations is not required. Before describing the method used in the present work, the drawbacks of other approaches are presented to illustrate the need for an alternative methodology.

The first consideration relates to the framework in which the nucleation rate should be calculated: namely, should the rate be transported: Eqn. (4.29), or calculated on a purely Eulerian-node basis: Eqn. (4.30)? To

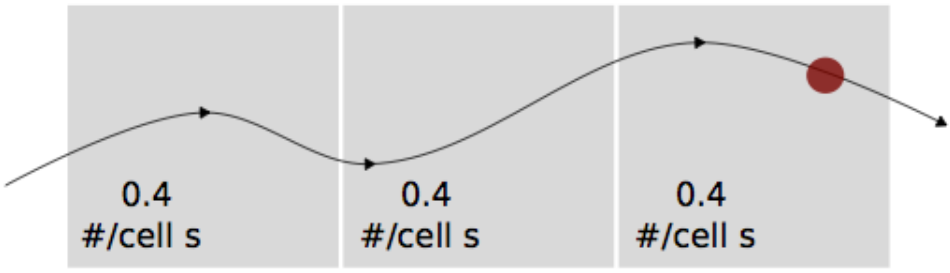


Figure 4.2.: If three cells have a constant nucleation rate of 0.4 particles per cell per second, the whole domain should produce one particle every 0.83 s. However due to the discrete nature of particles, each cell creates 0.4 particles i.e. no physical particles. If fluid enters from the left with a velocity of $U_f = 1\text{m/s}$ and a cumulative nucleation term is considered then as transported from the first cell to the last with a time-step of $1s$ a single particle is created in the last cell.

illustrate this, consider a 3-cell grid of a 3×1 m domain with a constant velocity inflow plane and thermodynamic conditions giving a constant rate $\dot{I} = 0.4\#\text{s}^{-1}/\text{cell}$, as in Fig. 4.2.

If the time-step is $\Delta t = 1$ s, the grid-spacing is $\Delta = 1$ m, and the velocity is $U_f = 1$ m/s, then assuming $CFL = 1$ for the whole domain a single particle should be created after every time-step. Nucleation is a jump process, a particle can either be created or not. On a cell basis, after a single time-step, 0.4 particles are created; therefore no physical particles are added to any of the cells. Arguably one may avoid this by creating an accumulation parameter for every cell and adding one particle to every cell after 3 s. However, using an accumulation parameter implicitly assumes time-averaging of the instantaneous nucleation rate in cases where $\dot{I}$ is not constant in a cell.

By considering an 'accumulant', i.e. a transported source term 'i', the above problem can be surpassed. The nucleation rate is transported such that after the first time-step 0.4 notional particles are created in the first cell; in the next time-step, after moving to the next cell, 0.8 notional particles are created; and in the final time-step a physical particle is added into the last cell. Such a transported approach creates two additional issues. Firstly, a bias is created towards particle creation in the final cell, even though in

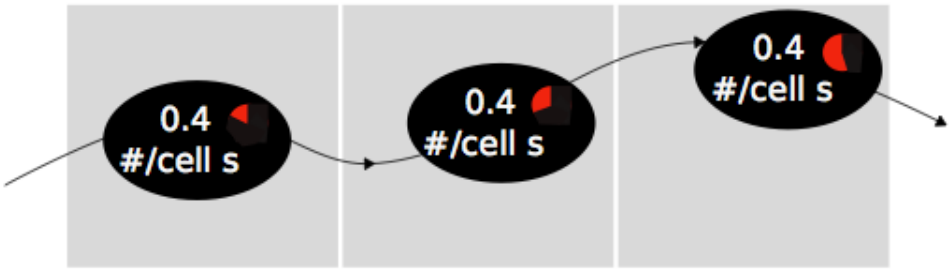


Figure 4.3.: Consider three cells which have a constant nucleation rate of 0.4 particles per cell per second, the time-step is 0.5 s, and the inflow plane velocity is $U_f = 2$ m/s . A transported nucleation rate approach creates a bias towards particle creation in the final cell and a dependence between flow-through time and nucleation residence time.

theory the nucleation rates are constant throughout the domain (suggesting that the same number of particles are created everywhere).

Secondly, a transported approach creates a dependence of particle creation on the relation between flow-through time and nucleation residence time. To illustrate this, consider the same example as above (where the local concentrations and temperatures give a constant nucleation rate for every cell of 0.4 particles per second), but with a reduced time-step of 0.5 s and a velocity of $U_f = 2$ m/s (Fig. 4.3). By transporting a notional particle which accumulates 'substance' in every cell (red semi-circle in Fig. 4.3), by the end of the domain 0.6 notional particles are created; therefore no physical particles are added. If the control volume moves with $U_f = 2$ m/s and constant thermodynamic conditions, the residence time of nucleation τ_{nuc} (i.e. one particle per cell in 2.5 s) must be less than or equal to the flow-through time $\tau_{flow} = 3\Delta/U_f$ for a particle to be created. For the present case this tracking would result in no particles being created even after $t > \tau_{nuc}$, even though the local thermodynamic conditions should create a particle in the domain approximately every 0.83 s.

CNT stems from a thermodynamic equilibrium theory where the saturation and concentration levels are known for a closed system. The challenge is how to treat such an equilibrium theory in non-stationary turbulent flows.

In Fig. 4.2, it is noticeable that the derivation of the nucleation rate from an equilibrium theory involves a lack of information, since it is a predicted

mean. From the overall nucleation of the domain we expect a particle to be created within 0.83 s, but there is no knowledge in terms of *when* it will occur, and (in the case of the transported example in Fig. 4.3) *where*. The nucleation rate, gives a sufficient condition for a number of particles to be formed within a volume in a given time, but it does not provide a conditionality for this creation.

In this work it is assumed that the nucleation rate can be treated as the transient *probability* of a stable embryo being formed, and not just a steady-state condition for its creation. This assumption agrees well with the suggestion of McDonald [150], that nucleation is intrinsically a probabilistic process. The inverse of the nucleation rate can be considered as the average time required for a particle to nucleate. By calculating the instantaneous nucleation rate for each time-step at each node of the Eulerian domain, one may calculate the residence time required for a single particle to be created in the vicinity of the node, viz:

$$\tau_{nuc} = \frac{1}{\dot{I} \times V_{cell}}, \tag{4.32}$$

where V_{cell} is the volume of the cell. The time τ_{nuc} represents an event with unit probability $\mathcal{P}_{nuc}(\tau_{nuc}) = 1.0$, i.e. a single particle will be created in time $t = \tau_{nuc}$. The probability of a particle being created in the interval $0 \leq t \leq \tau_{nuc}$ is assumed to increase linearly with t :

$$\mathcal{P}_{nuc}\,(t) = \frac{t}{\tau_{nuc}}. \tag{4.33}$$

$\mathcal{P}_{nuc}$ is a Cumulative Distribution Function (CDF), and provides the probability of an event to occur at *any* time within the interval $0 \rightarrow t$. The linear increase of the CDF suggests a uniform PDF of value $d\mathcal{P}_{nuc}/dt = 1/\tau_{nuc}$ in the range $0 \leq t \leq \tau_{nuc}$. It must be stressed that nucleation is an activated process and not a probability *per se* and that the CNT gives the steady-state transition rate (in this case DBP vapour→liquid). In stochastic theory, the Mean First-Passage Time (MFPT) is defined as the average time elapsed until a certain system leaves a prescribed domain for the first time [206]. The MFPT as a function of current and initial state has a characteristic sigmoidal shape [253]. The inverse of the steady state MFPT is directly related to the transition rate $\dot{I}$ and this is the scale we term τ_{nuc}. For sim-

plicity, we assume a linear increase in the probability (i.e. uniform pdf) of the activation barrier crossing in the range of $0 < t < \tau_{nuc}$. However, the sigmoidal shape suggested by the MFPT-theory in the work of Wedekind and co-workers could be better approximated, for example, using a Poisson distribution.

Using the definition of equation (4.33) the nucleation jump term is modelled as a particle injection into the domain, and the particle is thereafter transported as described by Eqs. (3.5) and (4.12). The injection process can be summarized as follows:

- The probability of a particle being created in a cell in one time-step of the simulation is calculated using equation (4.33).
- If $\mathcal{P}_{nuc} > 1$ the simulation time-step is reduced.
- A gambling process is performed using a random number Rn, sampled from a uniform distribution in the range $0 \leq Rn \leq 1$ to decide whether to inject a particle:

$$\text{Inject} = \begin{cases} 1, & Rn \leq \frac{\Delta t}{\tau_{nuc}} \\ 0, & \text{otherwise} \end{cases} . \tag{4.34}$$

- If (4.34) is true a particle with size equal to the nucleation diameter d_p^* at that location is injected.
- The particle injection position is random (within the cell boundaries), with a uniform probability distribution.
- The velocity and temperature of the newly-formed particle are linearly interpolated from the cell-centred (Eulerian) values of the surrounding cells.

The above method allows for the calculation and direct use of instantaneous nucleation rates, instead of mean quantities, without the addition of any modelling parameters. In addition, by recalculating the residence time in every time-step, positional biases of the type mentioned in the examples of Figs. 4.2 and 4.3 are removed. Most importantly, this method takes advantage of the intrinsically probabilistic nature of the nucleation process. The method can be readily applied in the Lagrangian framework using an

SDE described by a Levy jump process (3.19) where the drift and diffusion terms are zero, viz:

$$\frac{dn_p}{dt} = \mathrm{i} = \mathbf{J}[\mathbf{x}(t), t]\delta N_{dt}^{j,\tau_{nuc}} \tag{4.35}$$

where $\mathbf{J}$ is a scaling tensor representative of the local nucleation rate i. The increment $\delta N_{dt}^{j,\tau_{nuc}}$ is the j^{th} component of a stochastic counting[5] process with time increments dt and a mean rate τ_{nuc}, which usually follows a Poisson distribution. The advantage of a Lagrangian description is that the exact location of nucleation is retrieved, since the species, temperature, and pressure are transported (or interpolated) at the exact location of the notional parcel. The number of parcels used to simulate the unformed-particles directly influences the accuracy of the retrieved rates. The major drawback of using a Lagrangian nucleation rate is that the paths of unformed particles have to be traced and this increases the computational expense.

In this study, the nucleation rate is modelled in an Eulerian framework and the parcels represent physical particles which are subsequently transported in a Lagrangian framework using equations (4.12) and (3.5).

4.3.5. Modelling the SGS influencing Nucleation rates

The time-averaging of nucleation may lead to both implementation errors and a problematic description of equation (4.23) when applied to non-stationary flow conditions. LES filtering introduces unresolved sub-grid fluctuations of the transported quantities. These fluctuations may influence the nucleation rates, depending on the level of concentration and temperature information resolved by the LES (and consequently the level of lost information regarding fluctuations) within a cell.

Recently, Fager *et al.* [50], investigated the relative effects of sub-grid scales on the nucleation rate by *a posteriori* filtering of DNS of a turbulent jet. They concluded that the filtered nucleation rate is under-predicted in inner-regions of the jet and over-predicted in the outer regions. Similarly, Murfield and Garrick [160] found that the overall sub-grid effect is to increase the values of nucleation when these were high, and to decrease them when they were low.

Assuming that T and X are linear, a single scalar $\tilde{\xi}$ can be defined from

[5]The term 'counting' is used to clarify that the set of realizable values is discontinuous.

the normalized temperature or vapor concentration, viz:

$$\tilde{\xi} = \frac{\tilde{T} - T_{min}}{T_{max} - T_{min}} = \frac{\tilde{X} - X_{min}}{X_{max} - X_{min}}. \tag{4.36}$$

The tilde corresponds to the LES-filtered value of the defined scalar $\tilde{\xi}$, temperature field $\tilde{T}$, and concentration $\tilde{X}$. The nucleation rate can therefore be written as $\dot{I}(T, X) \approx \dot{I}(\xi)$, while its filtered equivalent is $\widetilde{\dot{I}(\xi)}$. However:

$$\widetilde{\dot{I}(\xi)} \neq \dot{I}(\tilde{\xi}). \tag{4.37}$$

The inequality of equation (4.37) implies that a model is needed. The models employed in the present work are a presumed β-PDF and a source expansion approach outlined below:

4.3.5.1. β-PDF

The scalar PDF $f_\xi(\psi; \mathbf{x}, t)$ represents the distribution of the realizations ψ of the scalar ξ at a given position $\mathbf{x}$ and time t [58]. Note that in the context of LES the scalar PDF is also termed the filter density function; the term PDF will be used here for consistency. For a complete review of the derivation and applications of the scalar PDF the interested reader may refer to [85, 156, 183].

One may retrieve the filtered-average source term at a given location from its convolution with f_ξ:

$$\widetilde{\dot{I}(\xi)} = \int_0^1 \dot{I}(\psi) f_\xi(\psi; \mathbf{x}, t) d\psi \tag{4.38}$$

There are two approaches for the use of the scalar PDF. The first is the 'transported PDF' approach, in which there is no assumption made regarding the shape of the distribution. The transported PDF method is therefore capable of capturing inhomogeneities, but suffers from an increased computational expense. The second method has a significant advantage in computational time by making an *a priori* assumption for the shape of the PDF, of which the most popular is the β-PDF. The presumed PDF method has been used in a number of precipitation studies [16, 145]. The β-PDF for the sub-grid distribution of a passive scalar has shown good agreement with experimental data and *a priori* studies in a range of applications including

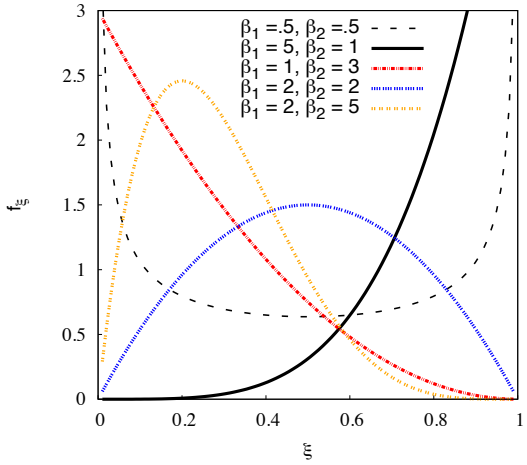


Figure 4.4.: The β-pdf distribution for different shape parameter values β_1 and β_2.

confined jets [53] and turbulent mixing [73], among others [17, 54, 250].

It must be noted that apart from the β-pdf, other functions are also suitable for the description of the sgs scalar distribution. In fact it has been pointed out that the pdf describing the variations of a scalar in space (LES-sgs) can be different to this describing the temporal variations of a scalar in RANS [57]. For example, Floyd *et al.* [57] suggest a top-hat function to describe the sub-grid variation of a passive scalar.

In this work the β-pdf is used and compared to an alternative method for the evaluation of the filtered source term. The β-pdf reads:

$$f_\xi(\psi;\mathbf{x},t) = \frac{\Gamma(\beta_1+\beta_2)}{\Gamma(\beta_1)\Gamma(\beta_2)}[\psi^{\beta_1-1}(1-\psi)^{\beta_2-1}], \tag{4.39}$$

where Γ is the gamma function, which is defined as an integral over $\chi \in \mathbb{R}[0:\infty]$:

$$\Gamma(\beta) = \int_0^\infty \chi^{\beta-1}e^{-\chi}d\chi \tag{4.40}$$

Figure 4.4 shows the β-pdf for different shape parameters. The shape parameters β_1 and β_2 are evaluated using the first two moments of the

distribution, i.e. the mean $\tilde{\xi}$ and variance $\widetilde{\xi''^2}$:

$$\beta_1 = \tilde{\xi}\left[\frac{\tilde{\xi}(1-\tilde{\xi})}{\widetilde{\xi''^2}} - 1\right], \tag{4.41}$$

$$\beta_2 = (1-\tilde{\xi})\left[\frac{\tilde{\xi}(1-\tilde{\xi})}{\widetilde{\xi''^2}} - 1\right]. \tag{4.42}$$

The mean $\tilde{\xi}$ is derived from the evolution of the temperature (or concentration field) making use of equation (4.38). The sub-grid variance $\widetilde{\xi''^2}$ is calculated using the proposed method of Pierce and Moin [179], as used in [28, 118]:

$$\widetilde{\xi''^2} = C_\xi \Delta^2 |\nabla\tilde{\xi}|^2, \tag{4.43}$$

with a model constant of $C_\xi = 0.1$ as proposed by Branley and Jones [28]. Wall *et al.* [249] have shown that because of the dependence of f_ξ on the shape parameters the model used for the variance $\widetilde{\xi''^2}$ may influence directly the rates that are convoluted with the β-pdf. An investigation of the temporal variation of the sgs scalar variance is carried out to evaluate the sensitivity of the constant C_ξ on the filtered nucleation rate.

The β-pdf and the derived filtered source terms are tabulated for all combinations of means $\tilde{\xi}$ and variances $\widetilde{\xi''^2}$ to minimize computational time.

4.3.5.2. Source Expansion

An alternative method for the evaluation of the filtered source term has been proposed by Vogiatzaki and Navarro-Martinez [246], and is implemented here in the context of nucleation. This approach stems from a Taylor series expansion of the nucleation rate about the filtered scalar $\tilde{\xi}$:

$$\dot{I}(\xi) = \dot{I}(\tilde{\xi}) + \frac{\partial \dot{I}(\xi)}{\partial \xi}\bigg|_{\tilde{\xi}} \frac{\partial \xi}{\partial x_i}\delta x_i + \frac{1}{2}\frac{\partial^2 \dot{I}(\xi)}{\partial \xi^2}\bigg|_{\tilde{\xi}} \frac{\partial \xi}{\partial x_i}\frac{\partial \xi}{\partial x_j}\delta x_i \delta x_j + ... \tag{4.44}$$

where use of $\delta\xi = \delta x_i \partial\xi/\partial x_i$ has been made to relate the variation of the scalar space to spatial space.

Equation (4.44) is subsequently filtered. Assuming that spatial gradients and the vector $\delta\mathbf{x}$ are uncorrelated (i.e. $\widetilde{\delta\mathbf{x}^m g} \approx \widetilde{\delta\mathbf{x}^m}\tilde{g}$), one may define the moments of $\delta\mathbf{x}$ as $M_m = \int |\delta\mathbf{x}|^m G_\Delta dV$. The odd moments of the filtered spatial variation are zero, and for a Gaussian filter the even moment is

$M_2 = \Delta^2/12$ [215]. Ignoring the higher-order terms, the resulting filtered expansion reads:

$$\widetilde{\dot{I}(\xi)} \approx \widetilde{\dot{I}(\tilde{\xi})} + \frac{\Delta^2}{24}\frac{\partial^2 \dot{I}(\xi)}{\partial \xi^2}\bigg|_{\tilde{\xi}} \widetilde{\frac{\partial \xi}{\partial x_i}\frac{\partial \xi}{\partial x_j}} + \mathcal{O}(\Delta^4). \tag{4.45}$$

The unfiltered terms can be evaluated directly from the filtered scalar value. The first term of the RHS requires additional modelling since $\widetilde{\dot{I}(\tilde{\xi})} \neq \dot{I}(\tilde{\xi})$. To do so a quadrature method is employed using the trapezoidal rule for the weights, ω_{ij}, and the values of the source term from eight neighboring cells evaluated at the equivalent filtered scalar values, viz:

$$\widetilde{\dot{I}(\tilde{\xi})} = \omega_{ij}\dot{I}_{ij}(\tilde{\xi}) \tag{4.46}$$

The last term of the RHS of (4.45) involves filtering. It is therefore split into its filtered and SGS parts. The sub-grid contribution $\dot{I}_{sgs}$ (by analogy with the scalar variance) is modelled using equation (4.47) with a constant of proportionality $C_{sgs} = 0.1$ by equivalence to Eqn. (4.43).

$$\dot{I}_{sgs} = \widetilde{\frac{\partial \xi}{\partial x_i}\frac{\partial \xi}{\partial x_j}} - \frac{\partial \tilde{\xi}}{\partial x_i}\frac{\partial \tilde{\xi}}{\partial x_j} \approx C_{sgs}\frac{\partial \tilde{\xi}}{\partial x_i}\frac{\partial \tilde{\xi}}{\partial x_j} \tag{4.47}$$

Combining equations (4.45), (4.46), and (4.47) results in the following expression for the evaluation of the filtered source term:

$$\widetilde{\dot{I}(\xi)} \approx \omega_{ij}\dot{I}_{ij}(\tilde{\xi}) + \frac{\Delta^2}{24}\frac{\partial^2 \dot{I}(\xi)}{\partial \xi^2}\bigg|_{\tilde{\xi}} (1 + C_{sgs})\frac{\partial \tilde{\xi}}{\partial x_i}\frac{\partial \tilde{\xi}}{\partial x_j} \tag{4.48}$$

The second derivative of the nucleation rate was derived analytically and tabulated with 10000 bins of the scalar ξ to minimize computational time.

4.4. Aggregation

The intersection of particle paths may lead to a collision event and an inelastic collision event to aggregation. The terms aggregation, coagulation, and agglomeration refer to the formation of a new larger particle from two or more smaller ones. The physicochemical mechanism that drives the formation determines which term should be used. Aggregation tends to be used for nano- and micro-scale solid particles. Coagulation is used interchangeably with aggregation, however, coagulation usually refers to particle collisions that undergo immediate coalescence. Agglomeration on the other hand refers to non-coalescing collision processes [63].

A particle of volume v is formed by the *aggregation* of two particles with volumes v' and $v - v'$. However, its resulting diameter is subject to the level of coalescence (also termed 'sintering' for solids), i.e. the extent to which the colliding-pair volumes merge. Depending on the phase of the particle (solid, liquid, or gaseous), the local thermodynamic conditions (e.g. temperature which affects particle surface tension), and the collision process (angle of attack, relative velocity etc.) the particle will attach to the 'receiver'[6] particle differently, forming fractal aggregate structures (such as soot) or spherical aggregates. In the present study, particles in the nano-scale are considered and instantaneous coalescence of the colliding pair is assumed.

4.4.1. Contextualization of aggregation: the need for accurate modelling

Binary droplet and particle collisions are an area of interest with applications ranging from meteorological to industrial processes. Meteorological phenomena such as cloud formation and raindrop formation drove research on experimental studies of aqueous coalescence in atmospheric air [1, 12]. Maximova and Dahl [149] offer an extensive review of the environmental implications of aggregation phenomena in the context of wastewater and gas emission treatment. They conclude that a deeper understanding of the complicated mechanisms of aggregation is vital for the development of environmental technologies.

Spray atomization and injection processes are directly influenced by the

[6] The term 'receiver' is used for simplicity to establish a frame of reference between the colliding particle pair

level of (fuel) droplet coalescence. Therefore, research on hydrocarbon aggregation has also received attention [92]. Moreover, it provided an incentive for the investigation of the effect of coagulation on the particle velocity statistics. For example, Gavaises *et al.* [69] concluded that coagulation greatly influences the PSD and consequently controls the particle relaxation times and velocities during injection. The modelling of soot aggregates from combustion precursors [279] has also become an area of great importance following reports [29, 55, 158, 165] on the effects of the size of aggregates on health.

With the development of processes to handle nanoparticle formation and use (e.g. in pharmaceutic inhalers), there has been a significant interest in aggregation taking place in the nano-scales. Spray drying[7] technology is an area of direct application of industrial-scale nanoparticle aggregation. Among other applications, spray-drying is used for the manufacturing of detergents, instant water-dissolvable powders (dairy, coffee, chocolate, etc.), and pharmaceuticals [163]. During the drying processes aggregates form. The level of aggregation governs the size of the formed particles and consequently their (commercial) properties. Consumers want a product, as for example instant coffee, that will dissolve rapidly without forming lumps, while manufacturers require a product that is easily handled and results in low wastage. Therefore, the PSD of instant coffee powder must provide a range of sizes for which particles are small enough to dissolve rapidly in water but big enough to reduce the levels of deposition on the walls of the spray-dryer. Such requirements can be met by controlling the aggregation process and therefore the aggregate size [180, 198, 241].

The complexity and the scale of the spray drying process makes it very difficult to use a predictive analysis for the formed aggregates. Nijdam *et al.* [163] outline the difficulties posed in simulating the spray drying processes. They conclude that a Lagrangian approach offers a greater ease of implementation and range of applicability compared to an Eulerian framework. Efforts using both experiments (as for example the work of Piatkowski and Zbicinski [178]) and numerical modelling (see [163, 241] among others) are made to enable the accurate prediction of the resulting PSD from spray-

[7]Spray drying is an industrial process whereby a solute is rapidly heated to form a dry powder. For example, powder milk can be produced using a spray drying process where the moisture of the milk evaporates rapidly leaving a powder compound which upon re-moisturizing (e.g. by adding water) liquefy.

drying processes.

Aggregation can be both wanted and unwanted depending on the area of application. For example, aggregation is promoted in spray drying technologies and in mining applications to reduce wastage and make separation easier (e.g. enhance settling rates in gravity based separations [56]). On the other hand, aggregation may reduce product quality by widening the PSD. In order to control the PSD, there has been an increasing effort to combine numerical modelling and experiments to investigate the aggregation process. At this point it must be noted that aggregation has been studied extensively both regarding its chemical or physical collision mechanism and with respect to the resulting structure and properties of the aggregate.

The objective of this work is to develop a model for the aggregation process in the LES-spray pdf framework outlined in sec. 4.1. The focus is on scales and particle concentrations where a one-to-one collision approach is intractable due to large number of particles $> \mathcal{O}(10^8)$, and macroscopic statistical models are hence sought. The aim is twofold: firstly, to model macroscopic kernels in a Lagrangian framework; secondly, to implement a numerical algorithm that maximizes the representation of the physics involved in the aggregation process, yet at the same time retains the advantages of the Lagrangian framework and the versatility of the spray-pdf regarding the choice of a state vector.

4.4.2. The aggregation kernel

The aggregation process involves collisions of particles to form new ones with larger volumes. Consequently, as in the case of nucleation, both microscopic and phenomenological approaches can be sought.

In microscopic approaches each collision event is considered separately (such as the hard sphere collision model in [234, 262, 263]). For example, Qian and Law [194] measured binary droplet collisions and classified their observations in five distinct regimes of the coalescence process: I) Coalescence with minor deformation II) Bouncing III) Coalescence with substantial deformation IV) Coalescence followed by separation for near head-on collisions V) Coallescence followed by separation for off centre collisions. Orme [169] reviewed the experimental findings on droplet collision and coalescence processes. He categorized the results with respect to the Webber

number[8] We and an impact parameter b, which is defined as the distance from the centre of one of the colliding droplets to the relative velocity vector v_{rel} positioned at the centre of the other droplet. They concluded that for water experiments there was an observable consistency in the critical numbers causing transitions from one regime to another. However, such critical values are not universal since the collision outcome is a function of droplet surface tension and viscosity, and gas density, viscosity and pressure [169]. More recently, Kollár and coworkers [110, 111] investigated droplet coalescence along with evaporation and cooling in an icing wind tunnel to compare microscopic models based on We and b to experimental results. They reported good agreement between the categorization based on We and b and the experiment.

Microscopic approaches are extremely useful because they reveal the physics involved in the aggregation processes. Liao and Lucas [132] categorize the numerous models for fluid particle coalescence processes and their relation to findings from binary (microscopic) collision experiments. However, in particle-laden flows in engineering applications, the number of particles N_{tot} render microscopic approaches intractable.

Phenomenological approaches treat the collision process in a macroscopic framework. It is usually assumed that a collision event will result in the immediate coalescence of the two particles. Consider that C_{ij} is the number of collisions per unit time per unit volume between two size classes i and j, which form a class k with $v_k = v_i + v_j$. The joint probability of a collision to occur and an aggregate to form is quantified by the aggregation kernel (also termed aggregation frequency) β_{ij} and the respective concentrations $N_{c,i}$ and $N_{c,j}$ such that:

$$C_{ij} = \beta_{ij} N_{c,i} N_{c,j}. \tag{4.49}$$

The summation over all possible pairs i, j leading to a size class v_k gives rise to the Smoluchowski equation [226] (or discrete PBE) solely for aggregation processes:

$$\frac{dN_{c,k}}{dt} = \frac{1}{2} \sum_{i+j=k} \beta_{ij} N_{c,i} N_{c,j} - N_{c,k} \sum_{i=1}^{\infty} \beta_{ik} N_{c,i}. \tag{4.50}$$

The kernel β_{ij} incorporates the physicochemical characteristics of the

[8] Defined as: $We = \rho v_{rel}^2 d_{ps}/\sigma$, where d_{ps} is the diameter of the smaller droplet and σ is the surface tension

process. Macroscopic parameters of both the continuous and disperse phases may influence β_{ij} depending on the physical mechanism which drives the aggregation process.

4.4.2.1. Brownian Collision Kernel

Particles in the nano-scale tend to aggregate due to path intersections occurring because of their Brownian motion. The length-scale of such particles is a lot smaller than the smallest structured fluid motion ($d_p << \eta_k$). The size of the particles can be smaller than the mean free path of the molecules of the continuous phase λ_f (i.e. $d_p << \lambda_f$). In such cases the Brownian kernel stems from the kinetic theory of gasses. On the other hand, if the mean free path is smaller than the particle size, the kernel is defined using a continuous diffusion approach.

The Knudsen number Kn is used to differentiate between the continuum and free-molecular regimes of aggregation:

$$Kn = \frac{\lambda_f}{d_p}, \tag{4.51}$$

where λ_f is the mean free path a molecule of the continuous phase will travel before it collides with another molecule of the same phase. The mean free path is evaluated from macroscopic quantities of the continuous phase:

$$\lambda_f = 2\frac{\nu_f}{\bar{u}_T}, \tag{4.52}$$

where $\bar{u}_T$ is the mean thermal velocity magnitude of a molecule of the uniform phase:

$$\bar{u}_T = \sqrt{\frac{8k_BT}{\pi\bar{m}}}. \tag{4.53}$$

If $Kn << 1$ the particle is said to be in the *continuum regime*. The particle 'views' the uniform phase as a continuum and not as an ensemble of molecules. Consequently its resistance to motion will be an outcome of the fluid phase continuum properties (ν_f, U_f, etc.). The aggregation kernel is therefore constructed from the equivalent diffusion coefficients D_p (of which the derivation can be found in [63]):

$$\beta_{ij} = 2\pi(d_{p,i} + d_{p,j})(D_{p,i} + D_{p,j}), \tag{4.54}$$

the coefficient D_p is evaluated from:

$$D_{p,i} = \frac{k_B T}{3\pi d_{p,i} \mu_f} G_i, \tag{4.55}$$

where G_i is the Cunningham slip-flow correction (see for example Knudsen and Weber [107] for the evaluation of G_i). When $G_i = 1$ Eqn. (4.55) is termed the Stokes-Einstein relation. In the Stokes-Einstein relation it is assumed that particles are large enough to see the flow as a continuum and that the relative velocity $U_f - v_p$ at a particle's surface is always zero because molecules of the fluid are continuously in contact (hitting) the particle surface. The factor $G_i > 1$ is required when particles diameters are of the order of λ_f. Such particles may 'slip' between molecules of the fluid and therefore their diffusivity increases (and equivalently the drag force is also reduced).

If $Kn >> 1$ the particle is said to be in the *free-molecular regime*. For the free-molecular regime, the particle path intersections are attributed to the random motion of the particles, which resembles that of a molecule of the continuous phase. The continuous phase influences the motion of the particles by the fact that molecules of the continuous phase collide 'discretely' and exchange momentum with the particles. The kernel therefore reads:

$$\beta_{ij} = \frac{\pi}{4}(d_{p,i} + d_{p,j})^2 (\bar{u}_{Tp,i}^2 + \bar{u}_{Tp,j}^2)^{\frac{1}{2}}, \tag{4.56}$$

where $\bar{u}_{Tp,i}$ is the mean thermal velocity magnitude of a particle of mass $\rho_p \upsilon_i$ and it is evaluated using equation (4.53).

Finally, if the Knudsen number is $Kn \approx 1$ then the particle is said to be in the *transition regime*. The aggregation kernel for the transition regime can be calculated using the interpolation formula of Fuchs [64]:

$$\beta_{ij} = \frac{2\pi(d_{p,i} + d_{p,j})(D_{p,i} + D_{p,j})}{\frac{d_{p,i}+d_{p,j}}{d_{p,i}+d_{p,j}+2\sqrt{\delta_i^2+\delta_j^2}} + \frac{8(D_{p,i}+D_{p,j})}{(d_{p,i}+d_{p,j})(\bar{u}_{Tp,i}^2+\bar{u}_{Tp,j}^2)^{\frac{1}{2}}}}, \tag{4.57}$$

where δ_i and $\lambda_{p,i}$ are given by:

$$\delta_i = \frac{(d_{p,i} + \lambda_{p,i})^3 - (d_{p,i}^2 + \lambda_{p,i}^2)^{3/2}}{3 d_{p,i} \lambda_{p,i}} - d_{p,i} \;\; ; \;\; \lambda_{p,i} = \frac{8 D_{p,i}}{\pi \bar{u}_{Tp,i}}. \tag{4.58}$$

Equation (4.57) reduces to Eqn. (4.54) for small Kn and to Eqn. (4.56) for large Kn.

The aforementioned Brownian aggregation kernels are subject to change due to the influence of external forces. Inter-particle forces may exist resulting from dipoles produced in the fluctuations of the electron clouds (Van der Waals forces) or if the particles are charged. Such forces may either increase (if attractive) or decrease (if repulsive) the collision frequency. Consequently, a correction factor $c_{\beta_{ij}}$, established by Fuchs [64], is used to modify the collision rate. Moreover, when large particles (yet still within the range of the Brownian aggregation mechanism) move in a fluid, a wake is created downstream of their path. This wake may enhance diffusion of other particles to its surface [91]. Pruppacher and Klett [193] suggested a modification (termed *diffusion enhancement*) to the continuum regime Brownian aggregation kernel; this modification is a function of the larger particle's Schmidt and Reynolds numbers.

In the present study no interaction forces are assumed; the interested reader may refer to Friedlander [63] and Jacobson [91] for a thorough review of the various modifications and a complete derivation of the Brownian kernels stemming from Brownian diffusion theory. The particle sizes considered in this work are small $d_p \leq 1\mu$m and therefore Brownian collision processes dominate. In what follows, alternative collision mechanisms and their equivalent kernels are briefly discussed for both completeness and to show that the method pursued in this study can easily incorporate the use of an alternative kernel.

4.4.2.2. Gravitational Settling Collision Kernel

Particles with size-ranges that are influenced by gravitational forces may collide primarily due to their settling velocities v_s. Different gravitational forces are exerted on particles of different size and therefore particles experience different settling velocities. Consider a population of particles under free-fall suspended in a fluid. Larger particles will have a larger v_s compared to smaller ones. Their paths will therefore intersect as an outcome of different settling velocities. In such cases the collision kernel becomes a

function of the relative settling velocity of two colliding classes i and j, viz:

$$\beta_{ij} = \frac{\pi}{4}(d_{p,i} + d_{p,j})^2 \left| v_{s,i} - v_{s,j} \right| . \tag{4.59}$$

Equation (4.59) is usually modified by a collision efficiency pre-multiplier [91] because not all path intersections lead to aggregation events. The validity of the expression (4.59) is subject to the particle size discrepancy. When particles are of similar size, their relative settling velocity is very small and aggregation (if present) will possibly be an outcome of a different collision mechanism.

4.4.2.3. Laminar and Turbulent Shear Collision Kernel

The laminar shear is similar to the gravitational settling mechanism, but it also applies to particle-pairs of similar size. Their relative velocity is this time induced by a mean shear gradient of the flow-field wherein the particles are suspended. The equivalent kernel is:

$$\beta_{ij} = \frac{(d_{p,i} + d_{p,j})^3}{8} \left(\frac{4}{3} \frac{dU_f}{dy} \right), \tag{4.60}$$

where dU_f/dy is the mean shear of the continuous phase. The collision essentially occurs due to an 'overtaking' of the slow particle by the fast particle, which is positioned at an adjacent streamline with higher mean velocity.

A similar mechanism to laminar shear arises in turbulent flows and it mainly influences particles of similar size. Saffman and Turner [214] suggested an aggregation kernel for particle concentrations that are high enough such that the distance between colliding particles is smaller than the Kolmogorov length-scales. Assuming that the particles are uniformly distributed, for a unit volume the concentration must be $(N_{c,i} + N_{c,j})^{-1/3} << \eta_k$. In this case, the kernel is [214]:

$$\beta_{ij} = \frac{(d_{p,i} + d_{p,j})^3}{8} \left(\frac{8\pi\epsilon}{15\nu_f} \right)^{\frac{1}{2}} \tag{4.61}$$

At lower concentrations the particles are too far apart to be influenced by the small-scale motion.

4.4.2.4. Turbulent Inertial Collision Kernel

If there is a large difference between the particle sizes, their relative motion is induced by differences in their respective relaxation times $\tau_{p,i}$ and $\tau_{p,j}$. In such cases the aggregation kernel reads [214]:

$$\beta_{ij} = \frac{(d_{p,i} + d_{p,j})^2}{4} |v_{s,i} - v_{s,j}| \left(\frac{\pi \epsilon^{3/4}}{g \nu_f^{1/4}} \right)^{\frac{1}{2}} . \tag{4.62}$$

In equation (4.62) the intrinsic assumption that the particles are densely populated such that the Kolmogorov scales influence their relative motion is made.

There exist a number of modification and different collision frequencies for the turbulent inertial mechanism. These exceed the purpose of this work as the size-range of interest is in the order of the nano-scales which are influenced by Brownian mechanisms. For an extensive review of the various kernels and their derivations, the interested reader may refer to [6, 7, 63, 147].

4.4.2.5. Relative magnitudes of the aforementioned kernels

It must be noted that the turbulent kernels discussed are phenomenological because they address collisions of particles smaller than the Kolmogorov-scales and for large concentrations. At low concentrations and for larger than the Kolmogorov-scale particles (i.e. when $Kn >> 1$ and $d_p > \eta_k$), a microscopic (one-to-one collision modelling) approach is more accurate.

Figure 4.5 depicts the magnitude of the different aggregation kernels for a colliding pair $i - j$ [63]. The smaller particle i has a radius of 10 nm and the various kernels along with their sum (noted as 'Total') are plotted against a range of sizes of the second particle j. It is clear that the Brownian aggregation kernel is the dominant collision mechanism in the nano-scales. The sum of all kernels nearly coincides with the Brownian kernel. The turbulent driven kernels are negligible within this range. Moreover, the collision rate due to gravitational settling is 7 orders of magnitude lower than this of the Brownian mechanism and it is clear that the relative settling velocity depends on the size-discrepancy of the colliding pair. Particles of similar size therefore do not collide due to gravitational effects nor due to

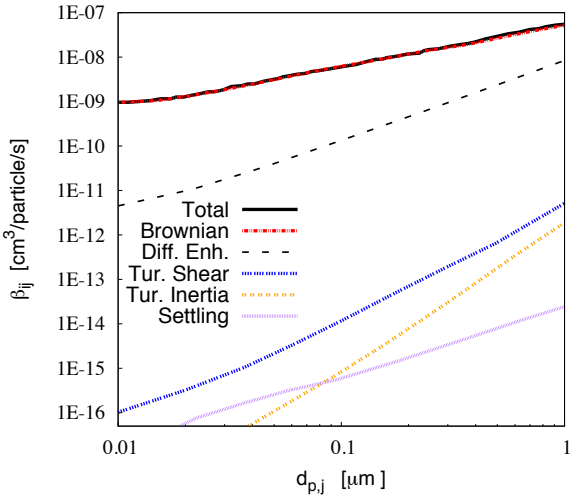


Figure 4.5.: Aggregation kernels for five processes, where a particle with $d_{p,i} = 20$ nm collides with a particle of size $d_{p,j}$.

differences in their relaxation time.

4.4.2.6. Limitations of aggregation kernels

In addition to the Van der Waals and Coulomb forces, there are a number of limitations regarding the accuracy of the aforementioned kernels. The assumption made for their derivation is that the particles are rigid spheres that undergo immediate coalescence during a collision event. If particles are relatively large, they will affect the fluid motion in their vicinity. This fluid motion may reduce the collision efficiency (i.e. collisions leading to aggregation) due to an increased resistance to attachment as particles approach each other and enter the region of affected fluid motion. In such circumstances, the kernels represent a maximum aggregation rate. Friedlander [63] outlines various modifications in which a collision efficiency is multiplied to the equivalent aggregation kernel.

Moreover, some kernels may have limited range of applicability. For example, Boer *et al.* [26] measured the collision frequency of monodispersed spherical particles (d_p >1µm) in a stirred tank. Different shear rates were applied and they concluded that for shear rates up to 50s^{-1} theoretical rates predicted, within a margin of $10-30\%$ error, the experimental collision rates. At higher shear, the difference between theoretical and experimental results

increased.

An additional limitation to the aggregation kernels outlined is a result of the assumption of immediate coalescence. Aggregates can retrieve an irregular or fractal shape. Moreover, aggregates may not be rigid structures and may experience internal restructuring (sintering) [46, 261]. Agglomerates of irregular shape are usually described using a *primary particle* framework. Such agglomerates are comprised of a number of primary particles. These primary particles are assumed to be rigid spheres and to have a monodisperse distribution with diameter d_{p0} (arguably their distribution can be poly-disperse and change during sintering affecting the aggregate structure and shape [45]). The way in which primary particles attach to each other forms the structure of the agglomerate. The type of the structure of the agglomerate is quantified using the *fractal dimension* f_D. When $f_D \to 3$ the agglomerate resembles a rigid sphere whereas when $f_D \to 1$ it has a chain-like structure. The fractal dimension should be understood in a statistical sense: f_D is an average quantity calculated from the density autocorrelation function applied to an ensemble of agglomerates. If agglomerates are treated in a fractal sense, the rates of aggregation may increase as an outcome of their increased surface area [11]. Making use of the fractal dimension, the fractal diameter is defined as:

$$d_f = d_{p0} \ (n_{pri})^{1/f_D} \tag{4.63}$$

where n_{pri} is the number of primary particles which form the agglomerate.

The resistance to motion experienced by a non-spherical particle differs to this by an equivalent sphere. The *mobility radius* (or diameter) is defined to represent the motion of the agglomerate by an equivalent sphere of diameter d_m experiencing the same drag force as the fractal agglomerate. For example, Rogak and Flagan [208] proposed the following expression for the evaluation of the mobility diameter:

$$d_m = \max\left[\frac{d_f}{2\left[\ln(d_f/d_{p0})+1\right]}\ ,\ d_f\left(\frac{f_D-1}{2}\right)^{0.7}\ ,\ d_A\right], \tag{4.64}$$

where d_A is the diameter of a sphere which has the same surface area as

that of the agglomerate:

$$d_A = d_{p0}\sqrt{\max\left[n_{pri}^{\frac{2}{3}}, \min\left(1+\frac{2}{3}(n_{pri}-1), \frac{1}{3}f_D(n_{pri})^{\frac{2}{f_D}}\right)\right]}. \qquad (4.65)$$

The research on agglomerate structures and particle interactions is vast and exceeds the purpose of this project; the interested reader may refer to the works of Pratsinis and coworkers [44, 45] and the recent review of Eggersdorfer and Pratsinis [47] on agglomerate and aggregate structures. Fractal aggregation is therefore not directly considered, yet modifications to the kernels could be readily implemented in which the particle diameters are replaced by d_f, however modifications would be also required to the particle trajectories (e.g. by using d_m for the calculation of the drag force).

4.4.3. Aggregation in Turbulent Flows

4.4.3.1. Effects of turbulence

There is not an all-encompassing effect of turbulence on aggregation, rather the effect depends on the relative length-scales of the turbulent motion and aggregate size. Equations (4.61) and (4.62) were developed to simulate a macroscopic collision process due to small-scale turbulent motion for particles smaller than the Kolmogorov length scales.

If the particles are of comparable size to the flow length-scales the turbulence directly influences the collision process. Derksen [38] implemented a DNS of homogeneous isotropic turbulence where particles larger than the Kolmogorov length scales were injected. He reported that turbulence has a double role: firstly, it promotes collisions leading to more aggregation events; secondly, the fluid deformation may lead to breakage of the formed aggregates. Derksen noted that higher levels of turbulence lead to the formation of smaller aggregates. Similar results were reported recently by Anne-Archard *et al.* [9] in their experimental investigation of silica nanoparticle aggregation under turbulent-shear flow conditions.

From Figure 4.5 it is noticeable that for nanoparticles the collision process is dominated by the Brownian mechanism. In such cases, it can be argued that turbulence influences the process indirectly. Essentially, aggregation depends on the levels of particle concentration which is directly influenced by turbulent-driven dispersion. Therefore, the local concentration may vary

significantly on an instantaneous basis (compared to the equivalent local mean values) leading to discrepancies of local aggregation statistics. Moreover, since for nano-particles the eddy diffusion rate of particles exceeds their Brownian diffusion rate, turbulent eddies will transport the particles in ensembles wherein aggregation will still be dominated by Brownian motion [94]. Consequently, turbulence can influence the PSD of aggregates in a multi-phase environment even when $d_p << \eta_k$.

An additional parameter that has been reported to influence the aggregation process is the turbulent time-scale. For example, Nijdam *et al.* [164] suggested that in jets, the highest discrepancies in the produced PSD are viewed in the shear layer and at positions downstream of the potential core. Similarly, Siera-Pallares *et al.* [223] performed a numerical simulation using QMOM (see section 3.3.3) to model particle nucleation growth and aggregation and the relative effect of mixing for the precipitator configuration of Cocero *et al.* [35]. They concluded that mixing time-scales have a decisive role in the resulting PSD. At regions with large mixing time-scales the residence time for aggregation is also longer, therefore allowing for more collisions to partake which lead to bigger cluster sizes. Arguably, this does not necessarily mean that the collisions are more than in the potential core in terms of absolute numbers. However, due to the longer residence time, a particle may undergo multiple sequential collisions, which lead to a bigger cluster size than equivalent particles in the jet core.

In the context of particle-laden turbulent jets there have been a number of attempts to simulate and measure the effects of flow-coupling on the aggregation process. Miller and Garrick [155] performed a DNS of nanoparticle coagulation in a planar jet. They used a sectional (discretization) method for the solution of the PBE. They found that the largest particles are at the shear layer surrounding the jet potential core. At locations downstream of $x/D_{jet} \approx 8$ the entrained particle-free fluid suppresses further aggregation by diluting the mixture. The standard deviation of the geometric mean diameter was found to increase in regions of intense mixing with values up to 8% larger than time-averaged values. Garrick *et al.* [68] in a DNS of a mixing layer with Brownian aggregation, showed that large structured motion reduced the level of particle growth due to the diluting effect of 'engulfed' particle-free fluid in such vortical structures.

Yu *et al.* [267], performed an LES of a jet flow with nanoparticle coag-

ulation. Their aim was to investigate the effects of coherent structures on the coagulation process. The moment PBE was solved with a Brownian coagulation kernel and an initial log-normal distribution. They concluded that coherent structures influence the particle number concentration and the PSD, while stressing the importance of retrieving instantaneous data to investigate flow structure and particle evolution correlations. The effect of coherent structures was also investigated in an impinging jet [268] using a QMOM, where they concluded that coherent structures dilute the particle-laden fluid resulting in a decrease of aggregation events due to the lower average particle concentration levels.

Yan *et al.* [263] performed a DNS of a particle-laden turbulent jet with $Re = 3000$. They used Lagrangian tracking of the particulate phase and a deterministic hard sphere model to simulate inter-particle collisions. The particle Stokes number ranged from 0.01 to 100 and batches of 462 particles were injected every six time-steps. They report that the level of collisions correlates well with the local particle concentration. Moreover, they observed that the mean particle concentration levels in the jet tend to be lower than the equivalent instantaneous levels, thus they stress the importance of considering the influence of turbulence on particle dispersion. Recently, Bordas *et al.* [27] measured particle velocity statistics and size distributions in a turbulent wind tunnel. Their experimental results were compared to a simulation of the discretized PBE evolution using a Finite-Element method for the discretization and stressed the need for accurate modelling of the flow-coupled particle phase processes.

Finally, Rigopoulos [204] reviewed the effect of the numerical coupling of the PBE with a turbulent flow. He stressed that in a RANS framework the averaging of the flow-coupled aggregation integrals of (3.33) reveals a number of unknown correlations of the type $\langle \mathcal{N}'(v - v')\mathcal{N}'(v')\rangle_t$, where here $\langle\cdot\rangle_t$ represents temporal averaging. Friedlander [63] notes that such correlations have not been studied extensively. Rigopoulos [203] has also demonstrated that the aforementioned correlations may become significant when considering the relation between the mixing time-scale to the aggregation residence time. Koch and Pope [108] observed a negative correlation between particle volume fraction and turbulent shear rate, suggesting an increase in the primary particle collisions (they assumed an initially mono-disperse distribution) in regions of the flow characterized by large shear. Schwarzer

et al. [219] investigated nanoparticle precipitation and aggregation using both experimental and numerical methods. They used Lagrangian particle tracking to simulate the paths of a scalar representative of the condensing phase and found good quantitive agreement to the experimental results. They therefore stressed the importance of considering spatial and temporal fluctuations when modelling the aforementioned processes. Similar correlations occur due to the spatial filtering in the context of LES. Garrick [67] used an Eulerian moment-based method for nanoparticle aggregation coupled to a DNS of three dimensional temporal mixing layers with a $Re = 200$. Using an *a posteriori* top-hat filter he obtained the equivalent LES values for the transported moments of the PBE. These values were subsequently used to calculate an LES-aggregation rate $C_{ij,LES}$. The sgs aggregation rate $C_{ij,sgs}$ was calculated from the equivalent DNS C_{ij} and LES rates as: $C_{ij,sgs} = C_{ij} - C_{ij,LES}$. He concluded that this SGS aggregation rate can be from $0 - 100\%$ of the DNS equivalent. He noted that the main effect of the SGS particle-particle interactions was to decrease the aggregation rates. However, it must be noted that the *a posteriori* filtering was directly applied to the moments of the PBE. This arguably reduces, apart from the fluctuations of the particle concentration, the poly-dispersity of the particles in the vicinity of the filter width. In the present study the SGS effects on particle concentration statistics are incorporated into the Lagrangian particle dispersion model, therefore such errors are indirectly taken into account.

4.4.3.2. Modelling the coupled kernel

The solutions of the flow-coupled aggregation stem from those of the uncoupled kernel, namely: analytic, MOM and their variations (QMOM, DQMOM, etc), discretization methods, MC methods, and combinations thereof (see section 3.3.3). These can be solved either in an Eulerian or in a Lagrangian framework.

Analytic methods solve the aggregation integrals or the equivalent closed set of moment integrals. Such solutions are confined to a limited number of kernels (e.g. β_{ij} =constant, $\beta_{ij} = v_i + v_j$, or $\beta_{ij} = v_i \times v_j$) for which the simple integrals can be directly evaluated (see [220]) or used to close the moment-PBE for specific initial PSDs (e.g. log-normal or mono-disperse). However, if the particles have a wide range of initial sizes, the aggregation

kernel cannot be considered size-independent and analytic methods fail to produce accurate results.

Eulerian frameworks used for the population balance solve a set of ODEs which result from a reconstruction of the PBE using a MOM (or QMOM), DQMOM, or a discrete number of size classes. For example, Balakin *et al.* [15] solved the PBE using a MOM for nucleation, growth, aggregation and breakage of hydrate particles in a turbulent flow. They used measured parameters from Wang *et al.* [252] for turbulent dissipation ϵ and ν_f along with the zeroth to third moment of the PBE to calibrate their moment-based method. Along with MOM, QMOM (e.g. [146]) are restricted in that when the initial particle distribution is poly-disperse, such models do not accurately accommodate the effects of different sizes on the aggregation process and the resulting PSD. To address this issue, Marchisio and Fox [144] proposed a DQMOM for the solution of the flow-coupled PBE, which directly tracks the variables appearing in the quadrature aproximation instead of the moments of the PSD. Yu and Lin [266] recently reviewed the solution of nanoparticle-laden flows via the moment methods. In their generality, the derived moment equations may involve unresolved correlations which require additional modelling to be closed [204], or inaccuracies due to an ill-conditioning of the inversion matrix which provides the quadrature weights for the formulated moment-PBE [280].

Discretization (sectional) methods are widely used for the solution of the flow coupled PBE in an Eulerian framework (e.g. [265, 155]). To ensure accuracy of the solution the equivalent number of bins used for the discretization must be sufficient such that the PSD is represented accurately. Therefore, a large number of bins might be required in problems where the PSD has a large range or when the distribution widens significantly due to the particle processes [204]. Azizi and Al Taweel [13] identified errors resulting from the discretization of the PBE. They proposed an approach where the PSD is recalculated if its range requires expansion or contraction and it is then equivalently discretized using a spline interpolation. A corrective action is therefore taken aiming to avoid the error propagation which would occur if the PSD of a previous time-step is used as a boundary condition for the next time-step. The aforementioned methods are also termed *deterministic* in that the integrals of Eqn. (3.33) are solved directly.

Stochastic/MC methods on the other hand simulate the aggregation pro-

cess within a probabilistic framework. The common stochastic model for the coagulation equation is a Markov Jump process whereby two clusters merge into a single cluster with a given rate C_{ij} [248]. For a complete review of the mathematical framework regarding the solution of the analytic and stochastic models of the aggregation-based PBE the interested reader may refer to the works of Aldous [5] and Wagner [248].

Stochastic and deterministic solutions of the PBE may be combined. For example, Zou *et al.* [278] combined a QMOM with a MC method. A set of moments is used as coarse-grained variables, from which one may extrapolate a fine-level state, namely the PSD. Fine-level states are evolved in time through what they term an 'inner' MC simulation. The coarse grained variables are then restricted to the evolved fine-level state. From this, they estimate the coarse-grained variable temporal derivatives, which are then incorporated to an 'outer' integration scheme. The reason for this dual loop is that the evolution of the moments is significantly slower compared to the coagulation/sintering events, and therefore one may choose a time-step which is significantly longer. The moment equation is therefore computed using the 'outer' integration scheme and the derivatives of the moments are obtained from short bursts of computational experiments using the 'inner' MC for the fine-level state. Rosner *et al.* [209] offer an extensive review of mixed moment and MC methods, in which the PBE evolution is solved deterministically apart from the aggregation kernel which is treated in a MC framework.

Lagrangian solutions of the PBE are usually combined with MC methods. Direct Simulation Monte Carlo (DSMC) methods involve the solution of the PBE using stochastic particles which represent a single physical particle [48]. In many practical applications and in the context of this work, the number of particles suspended in the flow-field exceeds the computational capacity for a DSMC. MC methods therefore simulate a subset of the evolution of real particles using stochastic parcels. These parcels may represent a set of moments of the PBE, a set of discrete classes of the PBE, or a number of real particles representing a sampled size from the particle population. A significant advantage of Lagrangian MC methods is that any number of properties representing the state vector of a particle is easily implemented. The main disadvantages of MC are: higher CPU time compared to Eulerian Deterministic models, and a statistical error which creates a lower limit for

the number of samples (parcels) used.

MC methods in this context can be broadly categorized into two approaches, namely: constant number and constant-volume. The former keep a constant number of simulated particles, whereas the latter retain a constant volume of real particles (usually combined with differentially weighted parcels).

In costant-number MC when the real particle population is reduced due to an aggregation event the 'vacant positions' of the stochastic parcel array are refilled with the properties of the remaining real particles. The incentive is to reduce the statistical noise which would occur as a result of a decrease in simulation parcels after aggregation. For example, Liffman [134] developed a MC in which the simulation progressed until a given portion of the population of the particles was depleted and then he filled the empty spaces of the parcel array with copies of the surviving particles. Smith and Matsoukas [225] and Lin *et al.* [138] extended the method of Liffman by introducing a continuous refilling of the array. The vacant spot of the particle array is refiled with the properties of a randomly selected particle that has survived. Therefore, the average mass of the simulated particles is also a random variable which depends on the mass of the (fictitious) new particle, which is randomly selected to fill the vacant position of the depleted particle. The aggregation kernel is separated into a dimensional and a non-dimensional part, where the latter is only a function of particle sizes. To ensure that the coagulation rate is captured accurately, even though fictitious particles are created, they alter the waiting time between successive coagulation events (for a complete description refer to [225]). The simulation therefore does not progress in time with a given time-step; instead, the time-step is updated subject to the coagulation event, i.e. the number of depleted real particles. Such MC methods are termed *event-driven*. *Time-driven* MC methods on the other hand set a given time-step Δt_{aggr} during which a mean number of coalescence events between parcels i and j equal to $C_{ij} * V_{rel} * \Delta t_{aggr}$ will occur.

Time-driven MC methods are usually combined with constant-volume differentially weighted parcels. The weight of a parcel is representative of the number of real particles n_{int} that it accommodates. Constant-number MC simulations use the same number of real particles per parcel, hence the tails of the PSD may not be sufficiently represented. Patterson *et al.*

[171] suggested that parcels must be distributed homogeneously over the PSD, i.e. even though regions might have low populations they must be represented by a sufficient number of parcels to statistically capture the poly-dispersity. Differential weighting of parcels may therefore mitigate errors that arise from a low resolution of the tails of the PSD. Moreover, the implementation becomes more intuitive as the depleted population of real particles is matched with a reduction in the weight of a parcel.

A number of methods exist to simulate the aggregation event. For example, Koch and Pope [108] use stochastic parcels of a given internal particle number n_{int} to simulate aggregation in homogeneous isotropic turbulence. They assume that n_{int} is large enough such that the parcel has an equivalent volume larger than the Kolmogorov length-scale 'cube' therefore allowing one to use a given dissipation rate ϵ and viscosity μ_f per parcel. The particle depletion within a parcel is modelled using the turbulent shear kernel along with a Interaction by Exchange with the Mean mixing model (IEM) (as suggested by Villermaux and Devillon [245]) to model the depletion of particles due to exchange with other parcels. Inter-parcel aggregation is therefore not directly considered.

Sommerfeld [228] and Ho and Sommerfeld [87] use a Lagrangian tracking framework to calculate the collision probability of a parcel in a turbulent flow-field by generating a fictitious-particle with a set of properties sampled from the local real-particle phase properties. The size and trajectory of the fictitious-particle are used to calculate both the collision probability and the coagulation efficiency. By generating a random number they decide if the collision will occur or not. When the parcel 'collides' with the fictitious-particle, they assume that all real particles collide with the same number of fictitious-particles.

Nijdam *et al.* [163] use the model of Ruger *et al.* [211] to calculate the collision frequency between two parcels with a given relative velocity v_{rel}, maximum real particle number $max(n_i, n_j)$, and relative volume of interaction V_{rel}. All but V_{rel} are readily available; to calculate the relative volume which confines the two parcels they use $V_{rel} = b_1 x_{rel}^3$, where x_{rel} is the relative distance between the position of the parcels and b_1 is a parameter. The value of b_1 effectively defines the size of the parcel 'cloud' in which n_{int} real particles are located. The parameter b_1 is empirical and it is arbitrarily chosen assuming a relation between the interacting volume and that of a

sphere with a diameter equal to the inter-parcel distance (for example Guo *et al.* [82] use $b_1 = 5$ to perform a base calculation and then alter the constant in a trial and error process). The aggregation event is modelled using a comparison of the calculated collision probability to a critical value as defined by Guo *et al.* [82]. If the calculated probability is greater than this critical value the two parcels merge.

Zhao and Zheng [273] couple the differentially weighted MC method of Zhao *et al.* [271, 272, 274] with a turbulent flow field. They assume that $V_{rel} = V_{cell}$ and define a 'full coagulation rule' whereby all the real particles of a parcel i collide instantaneously with the most probable partner j given that i contains less particles than j. The aggregation event is modelled using an accept/reject probabilistic coagulation rule in which a random number is generated and compared to a probability $\mathcal{P}_{aggr,i}$. The probability $\mathcal{P}_{aggr,i}$ is modelled as a Poisson distribution with a mean rate which is equivalent to the sum of all collision rates between i and all parcels j of a cell of V_{cell}, namely $C'_i = \sum_j C'_{ij}$ (where the prime is used to denote that the rate is modified according to the full coagulation rule; for details see [271]). All of the collisions are then included in a single aggregation event with the most probable partner j of parcel i. The partner is selected either using a cumulative probabilities method [134] or with an acceptance-rejection method [138]. The event proceeds by the redistribution of the particle weights and properties (for example a weighted momentum exchange is used to update the velocity of the particles).

4.4.3.3. The Interaction Volume and Aggregation Time-step.

At this point it is important to make a note regarding the choice of the interaction or relative volume V_{rel}. In the context of this work, the Brownian aggregation mechanism is used wherein the kernels are Eulerian in nature and require particle concentrations for their evaluation. It is therefore important to choose an interaction volume that is phenomenologically accurate. The straight forward choice would be to take advantage of the (already) discretized Eulerian domain and consider the aggregation events per cell (as for example in [273]). However, in such a method collisions of adjacent particles that are in neighboring cells are not considered even though the particles might be physically closer compared to others in their

equivalent cells. The advantage of using a relative volume of interaction is that a higher information content is used from the Lagrangian simulation of the parcel paths in the calculation of β_{ij}. The collision probability of two parcels that are next to each other therefore increases, compared to this calculated if the volume of interaction is considered to be that of the computational cell in which the parcels are located. The disadvantage lies in that the calculation is very sensitive to the choice of this relative volume. In Guo *et al.* [82] b_1 is a heuristic free-parameter. A particle cloud (parcel) model [18, 139, 33] represented by a single mean position has the intrinsic disadvantage that the volume of the parcel depends on the internal dispersion of real particles represented by the parcel. The level of internal dispersion may increase due to turbulence or decrease due to aggregation events. Litchford and Jeng [139] suggest that each parcel position represents a normal pdf with a mean value μ and a standard deviation σ which provides the probability of finding the set of real particles at the location surrounding μ. It is therefore assumed that σ is representative of the parcel (cloud) radius. The standard deviation is expressed in terms of a two-particle velocity correlation function. The parcel radius is 3σ which is the equivalent of a 99.2% confidence interval to find all the real particles within a volume $36\pi\sigma^3$ centered at μ. Alternative methods also exist. For example, in Johannessen *et al.* [94] a parcel represents a certain particle concentration $[\#/m^3]$ which is known at the boundaries of the simulation. The effect of the flow field in diluting the parcel concentration (i.e. increase its equivalent volume if real particles are considered and not concentration) is modelled using a dilution factor.

An additional parameter that should not (however it may) influence the aggregation process is the time-step used for the temporal integration of Eqn. (4.50). To the author's knowledge there has not been a definitive method for the selection of an appropriate time-step. In selecting a time-step the aim is twofold: first, to de-couple the aggregation process from the dispersion process; second, to accurately capture the aggregation events (since aggregation does not occur instantaneously for all particles and therefore their relative collision rates change if aggregation is viewed sequentially). The first problem can be easily addressed using the CFL condition if the volume of interaction is considered to be that of a cell V_{cell}. However, it is more complicated to treat this de-coupling directly if the interaction volume

is a function of particle position (as in the method of Ruger *et al.* [211]), since the relative distance between parcels changes within a time-step and therefore the volume which is proportional to x_{rel}^3 may change significantly.

The second problem is addressed in a more heuristic manner. In theory aggregation events should be treated sequentially, since the kernels $\beta_{ij} = \beta_{ij}(\upsilon_i, \upsilon_j)$ change after every event. In practice a limit is usually set by defining a time-step which is less than the residence time of a number of aggregation events. For example Zhao and Zheng [273] calculate this residence time τ_{aggr} from the maximum total coagulation rate of a parcel in a cell, i.e. $\tau_{aggr} = 1/\max_i(V_{cell}C_i')$. If $\Delta t > \tau_{aggr}$ then the aggregation is divided into sub-steps Δt_{aggr} for which they recalculate the rates and perform the aggregation events without solving the flow-field.

4.4.4. Proposed incorporation in the spray-pdf equation

In the present work, aggregation is investigated in a Lagrangian framework for particle populations that render the numerical representation of all particles on a one-to-one (particle to parcel) basis intractable. Each numerical parcel represents a set of real particles with the same average trajectories. The path (3.5) and velocity (4.12) SDEs are solved for a given parcel and they represent the trajectories of the average position and velocity of the ensemble of real particles.

Aggregation is incorporated into the spray-pdf by the addition of particle number concentration to the state vector of the particles, similarly to the nucleation process; see Eqn. (4.27), but also the addition of the particle volume random variable Υ_p with realizations υ_p (or diameter or mass assuming a constant density). Therefore the equivalent spray-pdf evolution for $\tilde{\mathbb{P}}(\mathbf{V}_p; \mathbf{X}_p; N_c; \Upsilon_p, t)$ reads:

$$\frac{\partial \tilde{\mathbb{P}}}{\partial t} + \frac{\partial}{\partial \mathbf{X}_p}(u_p \tilde{\mathbb{P}}) + \frac{\partial}{\partial \mathbf{V}_p}(a_p \tilde{\mathbb{P}}) + \frac{\partial}{\partial N_c}(\dot{N}_c \tilde{\mathbb{P}}) + \frac{\partial}{\partial \Upsilon_p}(\dot{\Upsilon}_p \tilde{\mathbb{P}}) = 0. \qquad (4.66)$$

For nucleation a probabilistic Eulerian approach is used to simulate the creation of parcels which subsequently have a constant internal (real) particle number. However, in aggregation the number of real particles and the average size represented by a parcel does not remain constant; instead both change due to inter-particle interactions. Therefore a Lagrangian trajectory

for each property has to be formulated and solved.

This part of the work will restrict to the nano-scale, for which the Brownian aggregation mechanisms dominate. The respective kernels Eqts. (4.54), (4.56), and (4.57) depend on particle concentration and they are Eulerian in nature. The first consideration therefore relates to how the equivalent densities will be retrieved. In an approach similar to this of Johannessen *et al.* [94], the trajectory would directly represent the particle concentration of a stochastic parcel, as in Eqn. (4.29). Alternatively, the real particle number of a parcel can be traced and the equivalent concentrations for the evaluation of the Brownian kernels can be retrieved by defining a volume of interaction V_{rel}. This volume can either be equal to that of an Eulerian cell (as in [273]) or equal to an interaction volume which assumes a certain parcel cloud radius (as in [82]). The former method where the concentrations are transported allows for an easy calculation of the inter-parcel aggregation rates. However, its implementation is less intuitive when treating both the boundary conditions and the dilution due to turbulence (since in polydisperse flows each parcel will exhibit a different dilution rate depending on the size d_p that it represents).

In the context of this work, the latter approach is used (where the real particle population per parcel is tracked) in order to maintain a physically more intuitive representation of the particulate phase and to allow for a direct extension of the spray-pdf methodology outlined thus far. The following stochastic trajectory is therefore formulated:

$$dn_{int} = -\dot{n}_{coll}dt = J_{aggr}[\mathbf{x}(t), t]\delta N_{dt}^{j,\tau_{aggr}}, \tag{4.67}$$

where n_{int} is the number of real particles in a given parcel, $\dot{n}_{coll}$ is the rate of collisions of real particles of the parcel. The number of collisions n_{coll} that cause a change dn_{int} in a given time dt is modelled along the lines of a Levy jump process where J_{aggr} is the component of the scaling tensor $\mathbf{J}$ representative of the local aggregation rate, and the increment $\delta N_{dt}^{j,\tau_{aggr}}$ is the j^{th} component of a stochastic counting process with time increments dt and a mean rate τ_{aggr}.

The parcel concentration is therefore defined as:

$$n_p(t) = \frac{n_{int}(t)}{V_{rel}}, \tag{4.68}$$

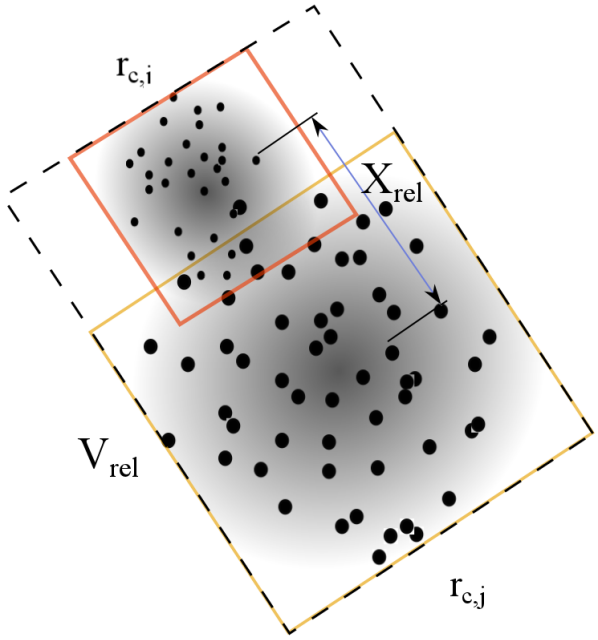


Figure 4.6.: Relative (interaction) volume of two colliding parcels i, j. The relative volume is indicated by the dashed line.

and the Eulerian particle number concentration for a certain sample volume V_{samp} centered at a position $\mathbf{x}$ is:

$$N_c(\mathbf{x}, t) = \sum_{i=1}^{\forall i \in V_{samp}} \frac{n_{int,i}}{V_{samp}}, \tag{4.69}$$

i.e. the Eulerian concentration is the sum of the real particles of every parcel belonging in the sample volume. For simplicity this sampling volume is chosen to be that of a cell, i.e. $V_{samp} = V_{cell}$.

The evaluation of the volume of interaction V_{rel} for the aggregation processes can be modelled using two different methodologies. In the first $V_{rel} = V_{cell}$ whereas in the second a specific parcel cloud cube of equal sides r_c is defined and the interaction volume between two parcels i, j is assumed to be equal to:

$$V_{rel,ij} = \frac{1}{2}(r_{c,i} + 2x_{rel} + r_{c,j})\max(r_{c,i}, r_{c,j})^2, \tag{4.70}$$

i.e. the volume of interaction is equal to the length of the two aligned parcels multiplied by a height and width equal to that of the largest parcel,

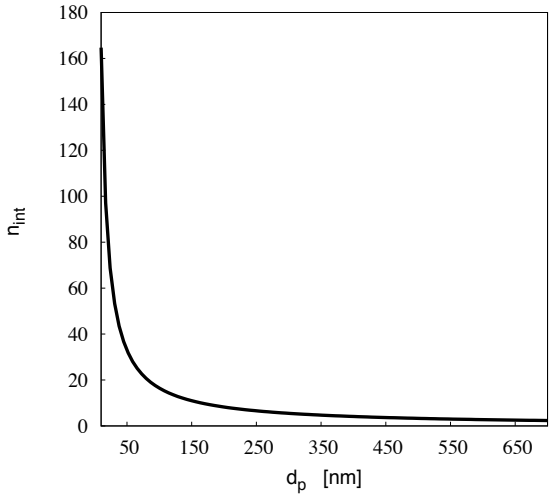


Figure 4.7.: Maximum number of real particles represented by one parcel as a function of particle diameter.

as shown in the 2D Figure 4.6. The sides of the parcel cube are equal and modelled as:

$$r_c = n_{int}^{\frac{1}{3}} \mathrm{Kn}_{air} d_p. \tag{4.71}$$

Equation (4.71) assumes that the population n_{int} is small enough, such that the corresponding parcel is smaller than the the Batchelor scale[9]. Assuming that the Knudsen number based on particle mean free path and diameter is equal to this of the carrier-fluid phase i.e. $\mathrm{Kn}_p = \lambda_p/d_p = \mathrm{Kn}_f = \lambda_f/d_f$ the mean distance between each particle is $\mathrm{Kn}_f d_p$.

The aforementioned assumption sets a maximum limit to the number of internal particles, namely:

$$n_{int} \leq \left(\frac{l_B}{\mathrm{Kn}_f d_p} \right)^3. \tag{4.72}$$

Figure 4.7 shows a plot of the maximum number of particles per parcel versus diameter for a Kolmogorov scale of 0.28 mm, unity Sc, and a $\mathrm{Kn}_{f=air} = 170$. Depending on the computational demands of the simula-

[9]The Batchelor scale ($l_B = \eta_k/Sc^{0.5}$) is the smallest length-scale fluctuation in scalar concentration. In other words, it describes the size of a the smallest scalar-parcel that will diffuse at the same rate as a Kolmogorov eddy dissipates.

tion upper and lower limits can be set (for example that the minimum is $n_{int} = 10$ and that the maximum is $n_{int} = 100$).

The limit for n_{int} offers a number of advantages from a phenomenological perspective:

- Particles are not influenced by vortical motions and their concentration can be considered analogous to this of the molecules of the gas phase (gravitational effects can be considered negligible). This analogy can be used as a measure for the parcel concentration and therefore the definition of V_{rel}; see Eqn. (4.70).

- The relative distance between the particles is not influenced by the flow-field. Therefore, it is more applicable to assume that they will be transported as an ensemble and that their relative internal dispersion will not increase due to fluid structures.

- Nanoparticle size distributions usually have a log-normal shape wherein large diameters have very low populations. The limit (4.72) of real particles per parcel decreases as the particle diameter increases. This way more parcels are used to describe less populated regions of a polydisperse PSD. For this reason the limit of Eqn. (4.72) can be kept even when $V_{rel} = V_{cell}$.

An additional parameter analysis was carried out to measure the sensitivity of the choice of n_{int}, which is presented in section 7.1.

In this work a multi-collision model is developed whereby the particles of a parcel may collide with a number of different parcels. The major issue that would arise with such an approach is that if every collision event created an additional parcel then the number of parcels in the simulation may increase to an intractable number. Therefore, it is assumed that the aggregated particles from a colliding parcel-pair are added to one of the two colliding parcels. The parcel that accommodates the aggregated particles is termed 'receiver' whereas the other parcel is termed 'donor'. For this purpose three further assumptions are made:

- The receiver parcel always has a greater mean particle diameter compared to that of the donor parcel.

- More than one donor particle may collide with a single particle of the receiver parcel but not vice-versa.
- Internal parcel collisions are allowed, i.e. particles of the same parcel can collide with each other to form aggregates.

The first assumption adds a 'directionality' to the aggregation event (small $\rightarrow$ large). The second assumption suggests that if a large population of small particles (represented by a donor parcel indexed i) interacts with a few large particles (represented by a receiver parcel indexed j), the large particles may experience more than one collision event; i.e. in the example given collisions are not limited to a number equal to $n_{int,j}$. However, when the parcels representing a larger mean diameter have a population greater than this of the other parcel, the total number of collision events is limited to the internal population of the donor parcel, i.e. for the same notation of i, j parcels:

$$\sum_{j}^{\forall j \in V_{cell}} n_{coll,ij} = \min \left(\sum_{j}^{\forall j \in V_{cell}} n_{coll,ij} \ , \ n_{int,i} \right). \tag{4.73}$$

The suggested directional approach also prevents collisions from being double counted since although $\beta_{ij} = \beta_{ji}$, the number $n_{coll,ij}$ is not equal to $n_{coll,ji}$. The third assumption of internal collisions is a logical extension of the multi-collision approach hereby presented.

The computational advantage of this method compared to this of Zhao and Zheng is that a second loop to find the most probable partner is not required; for example, array operations can be employed by formulating the tensor $n_{coll,ij}$. The particles are allowed to collide with any set of particles within V_{cell} instead of colliding with a single most probable partner. The *a priori* disadvantage of this method is that the size of the newly-formed aggregates is described by the ensemble average size (average over total internal particles) of the receiver parcel. Therefore, if insufficient events are simulated a poly-dispersed PSD may be smoothened. However, the condition of Eqn. (4.72) partly mitigates such errors as parcels with larger particles have lower populations.

The collision tensor $n_{coll,ij}$ gives the number of collision events that occur from parcel i to parcel j. A probabilistic approach is used for the simulation

of such events, whereby the probability of $n_{coll,ij}$ collisions to take place between two parcels i and j, within a volume V_{rel} and in a time t is given by:

$$\mathcal{P}_{aggr}(n_{coll,ij}, t) = \frac{1}{n_{coll,ij}} \frac{t}{\tau_{aggr}}, \tag{4.74}$$

where τ_{aggr} is the aggregation residence time:

$$\tau_{aggr}^{-1} = \frac{\beta_{ij} n_{int,i} n_{int,j}}{V_{rel}}. \tag{4.75}$$

As in the case for nucleation a linear increase of probability with t is assumed and the measure $\mathcal{P}_{aggr}(n_{coll,ij}, t)$ is the CDF representing the probability of $n_{coll,ij}$ events to occur at any time in the range $[0 : t]$. The division by $n_{coll,ij}$ is made to normalize the probability to a maximum of $\mathcal{P}_{aggr}(n_{coll,ij}, t) = 1$ for any number of collision events. Note that V_{rel} may be equal to V_{cell} for any i, j pair, or evaluated separately for each i, j pair using equation (4.70).

By sampling a random number Rn from a uniform distribution of range $0 \rightarrow 1$, the equivalent ij element of the collision tensor for a time-step Δt is constructed as follows:

$$n_{coll,ij} = \begin{cases} \text{floor}\left(\frac{\Delta t}{\tau_{aggr}} + Rn\right), & \text{if } \upsilon_i < \upsilon_j \\ 0, & \text{otherwise} \end{cases}, \tag{4.76}$$

where the function 'floor' produces the integer part of a real number.

Equation (4.76) states that the total number of collisions in the direction $i \rightarrow j$ during an elapsed time Δt and given that $\upsilon_i < \upsilon_j$ is equal to the integer (or definite) number of collisions plus the floor of the sum of the remainder and Rn. If for example $P_{aggr}(1, \Delta t) = \Delta t / \tau_{aggr} = 0.8$ then there is an 80% probability that $Rn \geq 0.2$ (since it is sampled from a uniform distribution with range $0 \rightarrow 1$) and therefore that a collision will take place. Note that $n_{coll,ji} = 0$ if $\upsilon_i > \upsilon_j$. To optimize the number of operations required and also to include the cases where $\upsilon_i = \upsilon_j$ without double-counting, the collision array $n_{coll,ij}$ (4.76) for all pairs $i - j$ and internal collisions $i - i$ is constructed using a particle sorting algorithm outlined in Appendix B.

To ensure that the aggregation events are sufficiently resolved in time the

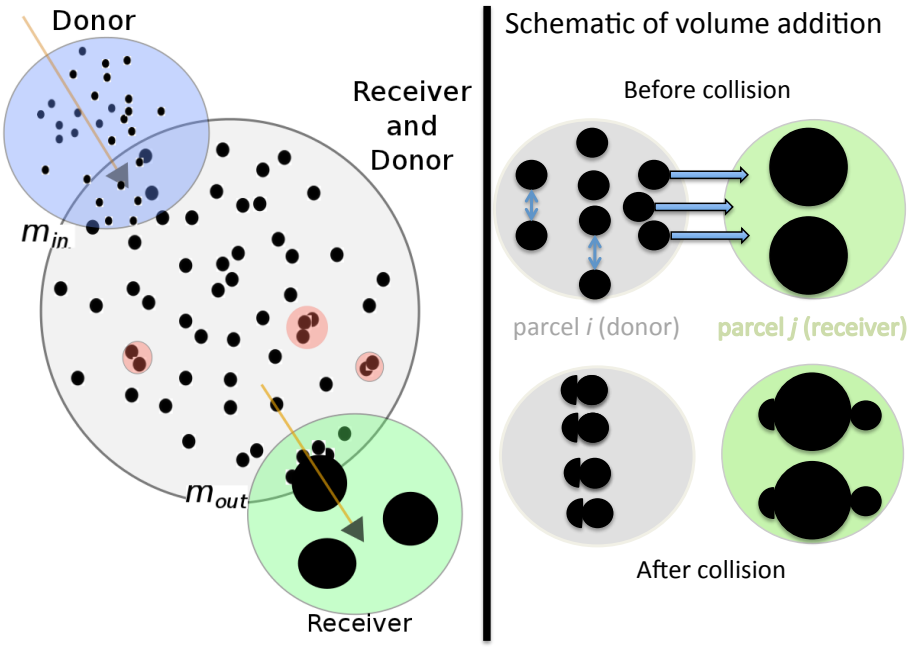


Figure 4.8.: The mass exchange and collision events assuming that donor parcels always contain smaller particles than receiver parcels.

following limit is used, as in the work of Zhao and Zheng [273], viz:

$$\Delta t_{aggr} \leq \min_{\forall\, i \,\in\, \text{Domain}} \left[\left(\sum_{j}^{\forall\, j \,\in\, V_{cell}} \frac{\beta_{ij} n_{int,i} n_{int,j}}{V_{rel,ij}} \right)^{-1} \right], \tag{4.77}$$

i.e. the simulation time-step is limited to this of the maximum total aggregation rate of all parcels in the domain. An additional parameter analysis was carried out to measure the sensitivity of the choice of Δt_{aggr}, which is presented in section 7.1.

Figure 4.8 summarizes the collision events graphically. Some of the small-size particles of the blue parcel collide with, and therefore are added to, the total mass of the grey parcel. The internal number of particles of the grey parcel remains unchanged and therefore their average mass increases. However, the size of the particles of the blue parcel remains the same, since the outward mass-flux is balanced by a decrease in the internal number of particles. The grey parcel undergoes a number of internal collisions (indicated by the red regions), which do not change its total mass but, since the in-

ternal number of particles reduces, the average mass per particle increases, i.e. their average size assuming a constant density. The collisions with the larger particles of the green parcel cause a net outward flux of mass from the grey parcel towards the green parcel. Although the total mass of the grey parcel reduces, the average mass of the internal particles is unchanged as the population of the parcel also decreases. Finally, the receiver green parcel will increase its total and average mass as n_{int} is constant.

For every parcel i the effect of the collision events are incorporated to the equivalent trajectories of each partner j. Note that a constant particle density ρ_p is assumed for all the following calculations. The change in velocity due to aggregation is updated using a conservation of linear momentum between the two colliding parcels (with $i \neq j$), viz:

$$[d\mathbf{v}_{p,j}]_{aggr,ij} = \frac{(\mathbf{v}_{p,i} - \mathbf{v}_{p,j})}{1 + \frac{\upsilon_j}{\upsilon_i}\frac{n_{int,j}}{n_{coll,ij}}}. \tag{4.78}$$

The equivalent velocity trajectory becomes a function of a variable ($n_{coll,ij}$) sampled from a stochastic jump process and equation (4.12) is therefore extended to:

$$d\mathbf{v}_{p,j} = \frac{(\tilde{\mathbf{U}}_f - \mathbf{v}_{p,j})}{\tau_p}dt + \sqrt{C_o\frac{k_{sgs}}{\tau_t}}d\mathbf{W} + \sum_{\forall i \in V_{cell}} [d\mathbf{v}_{p,j}]_{aggr,ij}. \tag{4.79}$$

The change in particle mean volume of a parcel j is updated using a weighted sum of the colliding particle volumes (see schematic in Fig. 4.8). It is therefore assumed that each particle of the receiver parcel will increase in average size according to:

$$[d\upsilon_j]_{aggr,ij} = \frac{n_{coll,ij}}{n_{int,j}}\upsilon_i \tag{4.80}$$

Therefore the equivalent trajectory for the average parcel volume of the receiver j due to collisions with all donor parcels i is:

$$d\upsilon_j = \sum_{\forall i \in V_{cell}} [d\upsilon_j]_{aggr,ij}. \tag{4.81}$$

Finally, having updated the aforementioned properties, the new internal

particle number of each parcel is updated according to:

$$dn_{int,i} = - \sum_{\forall j \in V_{cell}} n_{coll,ij}. \tag{4.82}$$

Figure 4.9 is a flow-chart which briefly outlines the aforementioned methodology. Assuming that within an LES time-step the particles do not change cells, the aggregation process can be readily re-iterated for a shorter time-step following the steps outlined previously. A separate sensitivity test for the aggregation time-step was carried out in stationary (no flow) conditions. In its generality the multi-collisional approach for stochastic parcels outlined can be used with different aggregation mechanisms and kernel modifications to include a fractal shape; see Chapter 7.

In some cases, such as in an experimental configuration where the environment is contaminated or the co-flow stream is not filtered, it is possible that a background (noise) particle concentration may be present. Such 'noise' can influence the aggregation events and usually there is little knowledge regarding the PSD of the background particles. The one-directional multi-collision approach allows for the calculation of 'background aggregation' events for every parcel. In essence, each parcel can be a receiver of background particles. The background particle concentration N_{bg} is transported in an Eulerian framework as a passive scalar (assuming negligible depletion) and interpolated at the location of a parcel $N_{bg@p}$. The condition (4.76) can be therefore readily evaluated to give the number of collisions from the background phase 'i', with the interpolated concentration $n_{int,i} = N_{bg@p}$, to the parcel 'j'. Assuming for simplicity a mono-disperse PSD, background collisions are implemented in the context of nanoparticle aggregation in a turbulent jet outlined in section 7.3.

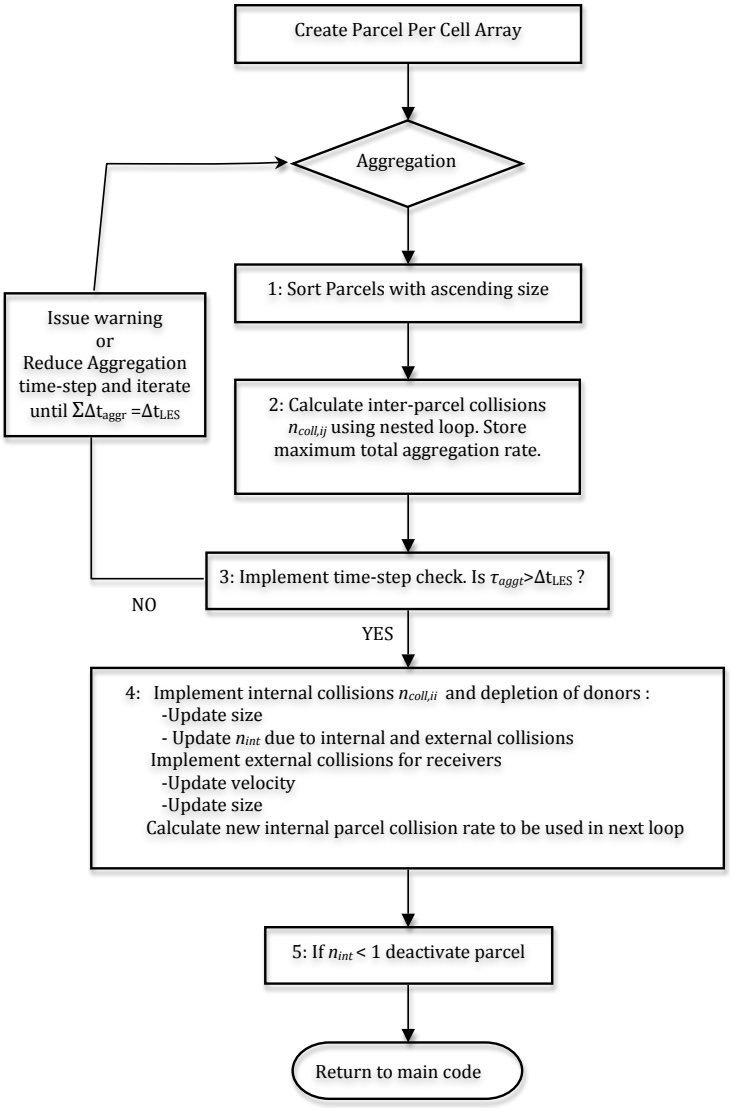


Figure 4.9.: Flow chart of multi-collision aggregation model.

4.5. Interim Summary

This chapter outlined the models implemented and developed in the context of this project. Table 4.2 summarizes the trajectories of the particle phase properties that are treated in a Lagrangian framework.

Table 4.2.: Summary of Equations

$\frac{\partial}{\partial t}\tilde{\mathbb{P}} + \frac{\partial}{\partial \mathbf{X}_p}(u_p\tilde{\mathbb{P}}) + \frac{\partial}{\partial \mathbf{V}_p}(a_p\tilde{\mathbb{P}}) + \frac{\partial}{\partial N_c}(\dot{N}_c\tilde{\mathbb{P}}) + \frac{\partial}{\partial \Upsilon_p}(\dot{\Upsilon}_p\tilde{\mathbb{P}}) = 0$	LES Spray-pdf
$d\mathbf{x_p} = \mathbf{v}_p dt$	Path
$d\mathbf{v}_p = \frac{(\tilde{\mathbf{U}}_f - \mathbf{v_p})}{\tau_p}dt + \sqrt{C_{dyn}\frac{k_{sgs}}{\tau_t}}d\mathbf{W}$	Velocity change with C_{dyn}
$\mathcal{P}_{nuc}(t) = \frac{t}{\tau_{nuc}} \quad ; \quad \tau_{nuc} = \frac{1}{\dot{I}\times V_{cell}}$	Nucleation Probability
$\mathcal{P}_{aggr}(n_{coll,ij}, t) = \frac{1}{n_{coll,ij}}\frac{\beta_{ij}n_{int,i}n_{int,j}}{V_{rel}}t$	Aggregation Probability
$d\mathbf{v}_{p,j} = \frac{(\tilde{\mathbf{U}}_f - \mathbf{v}_{p,j})}{\tau_p}dt + \sqrt{C_o\frac{k_{sgs}}{\tau_t}}d\mathbf{W} + \sum_{\forall i\in V_{cell}}[d\mathbf{v}_{p,j}]_{aggr,ij}$	Velocity change with Aggregation
$dn_{int,i} = -\sum_j^{\forall j\in V_{cell}} n_{coll,ij}$	Parcel population
$d\upsilon_j = \sum_{\forall i\in V_{cell}}[d\upsilon_j]_{aggr,ij}$	Average Size

The trajectories for energy conservation equations using a two-way coupling with the continuous phase can be easily included and has been implemented previously by Franchetti *et al.* [60] and Jones *et al.* [99].

In the following chapters the developed models are tested and compared to experimental and numerical works of other researchers. Each chapter deals with one of the models developed, namely: the dispersion model, the nucleation model, and the aggregation jump process.

5. An Investigation of dispersion in turbulent flows

5.1. Validation of the Dynamic model

For the purpose of validating the model outlined in section 4.2.4 the simple DNS test case of Ahmed and Elghobashi [3] was chosen. It consists of an unbound channel with a constant and uniform velocity gradient in one spatial direction. Decaying homogeneous isotropic turbulence is superimposed to the constant shear. The uniform phase is subsequently seeded with particles to measure their dispersion statistics. The work shown here has been presented in Pesmazoglou *et al.* [174].

5.1.1. Configuration and Modelling Parameters

Figure 5.1 depicts the configuration of the test case. The domain is periodic in x and z, and a shear-periodic boundary condition is used in the direction of the imposed mean velocity gradient (y). Details for the implementation of the shear-periodic condition can be found in Gerz *et al.* [72].

The dimensionless velocity gradient $S = (d\bar{U}_{f_1}/dy)(L/\Delta\bar{U}_{f_1})$ is equal to 1 for a unity length scale L [m] and velocity difference $\Delta\bar{U}_{f_1}$ [m/s], where the over-bars signify temporal means. The axial velocity at a given location is derived by the mean shear and superimposed turbulence, viz:

$$U_{f_1}(x, y, z) = u'_{f_1}(x, y, z) + Sy \tag{5.1}$$

where $u'_{f_1}(x, y, z)$ is the axial turbulent velocity field.

The turbulent velocity field is isotropic, periodic in all spatial directions and divergence free. The initial velocity fields, u'_{f_i} for $i = x, y, z$ are gener-

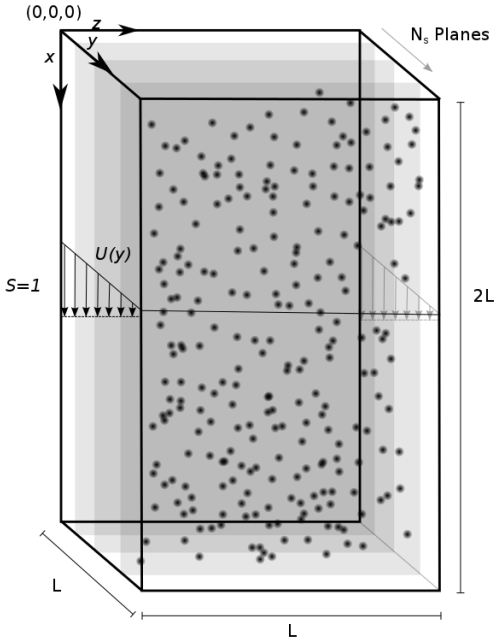


Figure 5.1.: Schematic diagram of the case of Ahmed and Elghobashi [3]. A constant shear, S, is applied in the $y-$direction to which a decaying homogeneous isotropic turbulent field is superimposed. 22^2 particles are seeded on each of the $N_S = 22$ planes placed at equidistant positions in the direction of the shear.

ated from a prescribed energy spectrum:

$$E_0(\kappa) = 16(2/\pi)^{1/2}(3/2)u_{0,rms}\frac{\kappa^4}{\kappa_p^5}exp(-2(\kappa/\kappa_p)^2) \tag{5.2}$$

where $E_0(\kappa)$ is the initial kinetic energy of a wave number κ. The initial root mean square velocity is $u_{0,rms} = 0.03530$ and $\kappa_p = 5.0$ is the wave number around which the maximum energy of the spectrum is concentrated. At the begining of the simulation, the total kinetic energy is $E_{T0} = \int E_0(\kappa)d\kappa = 0.0018696$. The initial Integral and Kolmogorov length scales are $l_0 = 0.072980$ and $\eta_{k_0} = 0.006761$ respectively. For the choice of a kinematic viscosity $\nu = 0.000105$, the initial turbulent Reynolds number based on the integral length scale is $Re_{t_0} = 24.5$. All quantities are dimensionless; normalized with the mean velocity difference $\Delta\bar{U}_{f_1}$ and length scale L.

Ahmed and Elghobashi used a grid of $160 \times 80 \times 80$ cells in the x, y, and z directions, respectively. In the context of this study, the initial turbulent fields where generated from the prescribed energy spectrum for the same grid as in the DNS. Subsequently, the velocity fields were *a-posteriori* filtered into an LES with $80\times40\times40$ cells for the same domain dimensions $2L\times L\times L$. This is equivalent to a ratio of $\Delta/\eta_{k_0} = 1.85$ suggesting that more than 90% of the energy spectrum is resolved, as proposed by Celik *et al.*[31]. The unknown sub grid-scale stresses of the momentum equation in the LES are closed using the Smagorinsky eddy-viscosity model [224] with the model constant of $C_s = 0.173$ suggested by Lilly [137]. The time-step width is set according to the extended CFL condition to include the particle phase: equation (4.7), with a constant of 0.3.

Ahmed and Elghobashi [3] register statistics from $t = 0$ where the turbulence corresponds to the initial random isotropic velocity field. The skewness Sk_u based on the gaseous velocity derivatives is 0 at $t = 0$ (since the flow is divergence free) and is defined as:

$$Sk_u(t) = \sum_{i=1}^{3} \frac{-\frac{1}{3}\left\langle(\partial u_i/\partial x_i)^3\right\rangle}{[\frac{1}{3}\left\langle(\partial u_i/\partial x_i)^2\right\rangle]^{3/2}}, \tag{5.3}$$

here $\langle\cdot\rangle$ implies ensemble averaging over all the cells of the domain.

Ahmed and Elgobashi[3] use the first peak in Sk_u as the particle injection

criterion. They suggest that this peak signifies that a fully developed turbulence is established [3]. For consistency, the same condition is used in this study. At this time particles are initialized on $N_s = 22$ planes positioned at equidistant locations in the y-direction. On each (x, z) plane, $N_{ps} = 22^2$ particles are seeded randomly with initial velocities equal to those of the uniform phase. A total of $N_p = 22^3$ particles are tracked using equation (3.6) for the DNS of [3] from which equation (4.12) is derived and used in the LES of this work.

Two different particle sizes are considered. The first case consists of particles with $d_p = 40$ μm and the second with $d_p = 125$ μm. The ratio of disperse to continuous phase density is the same for both cases and equal to $\rho_p/\rho_f = 19000$. Ahmed and Elghobashi [3] assume a constant particle relaxation time –i.e. un-corellated to the particle relative velocity as is the case of equation (4.13)– of $\tau_p = 0.1$ and $\tau_p = 1.0$ for the first and second case respectively. For consistency, their definition for the particle relaxation time is also used here.

The particle positions are tracked in time and their mean-square displacement, $\left\langle x_{p_i}^2(t)\right\rangle$, is calculated using:

$$\left\langle x_{p_i}^2(t)\right\rangle = \frac{1}{N_{tot}} \sum_{j=1}^{Ns} \sum_{k=1}^{N_{ps}} \{[x_{p_i}(t) - x_{p_i}(t_0)]_k - [\langle x_{p_i}(t)\rangle]_j\}^2 \tag{5.4}$$

where $\langle\cdot\rangle$ imply ensemble averaging over all particles, and with

$$[\langle x_{p_i}(t)\rangle]_j = \frac{1}{N_{ps}} \sum_{k=1}^{N_{ps}} [x_{p_i}(t) - x_{p_i}(t_0)]_k \,. \tag{5.5}$$

Particles released in different planes have different initial velocities due to the imposed mean shear. To remove this bias from the dispersion variance, the corresponding mean displacement $[\langle x_{p_i}(t)\rangle]_j$ of particles released from a given plane j is subtracted as shown in (5.4). The displacement variance therefore takes into account only the effects of turbulence [3].

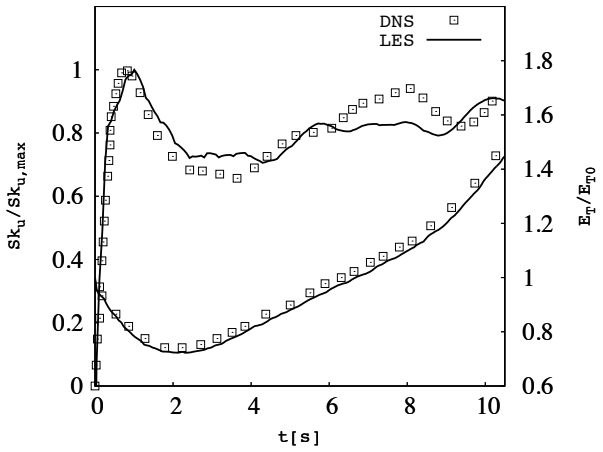


Figure 5.2.: Temporal variation of the normalized Skewness (top) and Total Kinetic Energy (bottom), for the LES and DNS of Ahmed and Elgobashi [3].

5.1.2. Results

Figure 5.2 presents the variation of the total kinetic energy $E_T(t)$ (bottom), and skewness $Sk_u(t)$ (top), of the Eulerian phase as a function of time. Good agreement was found with the DNS values of the total kinetic energy. The initial dip in E_T can be attributed to a faster dissipation rate compared to the forcing on large scales induced by the mean shear. As the flow evolves the Integral and Kolmogorov length scales increase in size and the cascade of energy from the forced wave numbers proceeds[3]. The rate of dissipation of the –now increased– $\eta_k(t)$ is lower than the energy input from the mean shear effecting in the gradual increase of the E_T. The slight underestimation of the LES-E_T can be attributed to the cut-off of the filtering process resulting to a –nearly constant– loss of the order of 5% which is in accordance with the assumption that the grid spacing chosen resolves over 90% of the energy spectrum.

The Skewness of the velocity derivatives, Sk_u, follows a similar trend to the DNS results with peaks and throughs dampened. The dampening can also be attributed to the filtering process as velocity gradients are smoothened over the domain due to the reduced resolution compared to this of the DNS. A first peak is observed at approximately 1 s after the

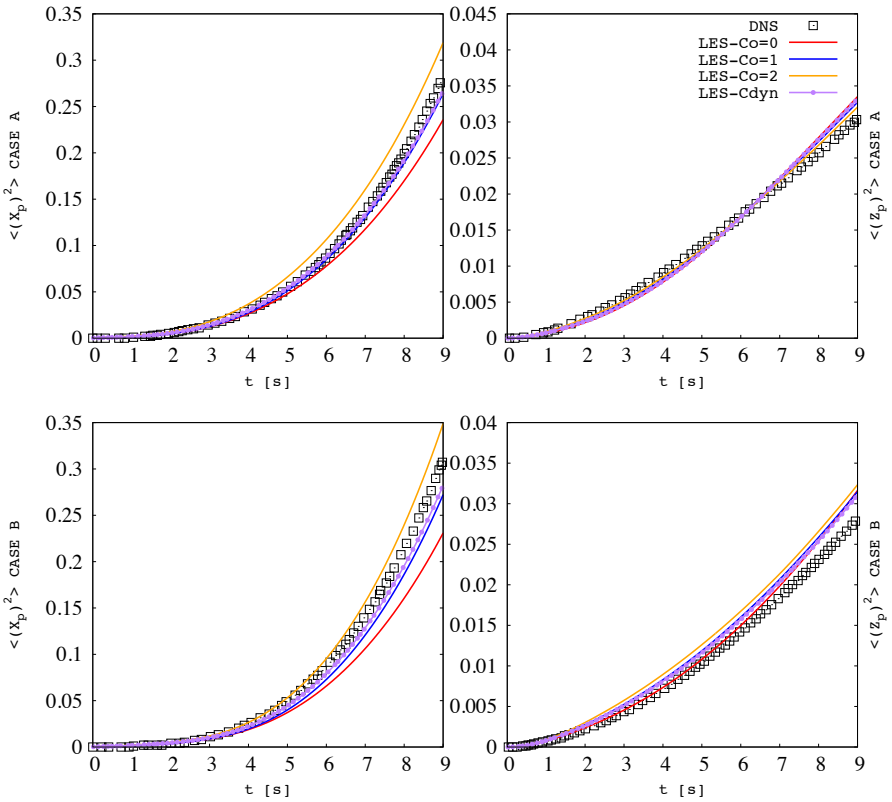


Figure 5.3.: Temporal variation of the displacement variance in directions x and z compared to the DNS of [3] (points) for case A (top) and case B (bottom).

simulation is initialized. At this time instance the particles are injected in the domain with the Eulerian phase velocities.

Figure 5.3 presents the displacement variance for the two particle sizes, hereafter referred to as case A for the $d_p = 40$ μm and case B for the $d_p = 125$ μm particles. Statistics where available for directions x and z, and four particle transport methodologies where used for each case, namely: no dispersion model $C_o = 0$, static coefficient with values $C_o = 1, 2$, and the dynamic model for C_{dyn}.

For both cases, the span-wise displacement variance, $\langle z_p^2 \rangle$, is an order of magnitude lower than this of the axial direction. Results for case A nearly collapse on the same line for all dispersion implementations. Similarly for case B there are small visible differences in the various models, the common

trend being to produce good results for case A and slightly over-estimate the dispersion levels in case B.

On the other hand, the effect of modeling the sub grid-scale contribution becomes visible for the dispersion variance in the axial direction. Ignoring the SGS contribution to the particle transport ($C_o = 0$) results to a significant underestimation of the mean dispersion variance. The value of a constant dispersion coefficient has no analytical solution, as discussed in section 4.2, but it is suggested [22, 98] that it lies in the range of $0.5 - 2$. For this particular grid spacing, it seems that the $C_o = 1$ would be the most appropriate choice. The dispersion levels are overestimated for both the light (case A) and heavier (case B) particles with $C_o = 2$.

As a first order validation, the proposed dynamic model performs very well. The dispersion levels produced are closest to the DNS equivalent for both cases. Moreover, when the dynamic model is employed, $\langle x_p^2(t) \rangle$ lies between the two static choices of $C_o = 1$ and 2. Such boundedness in conjunction with the produced levels of dispersion suggests that the phenomenological assumption of the model is sound.

Moreover, the two cases shown in Fig. 5.3 are different with regards to particle diameter and consequently relaxation time. Therefore, a number of conclusions can be drawn regarding the dynamic model in the context of a poly-disperse flow. Although for light particles, the $C_0 = 1$ and C_{dyn} are very similar, for heavier particles the results exhibit a noticeable divergence. In the Lagrangian Stochastic model of Bini and Jones[24] the diffusion term is a function of the particle relaxation time, which depends on the particle diameter, and the assumption of linear scaling of C_o for all diameters is made intrinsically. On the other hand, the dynamic coefficient is calculated from a local mass weighted ratio, (4.22), making its evaluation size-dependant.

From what has been presented thus far, one may conclude that using a model to incorporate SGS is required for the correct prediction of particle motion. It was shown that the dynamic model accurately predicts the dispersion variance of the disperse phase. Moreover, the size-weighting of the dynamic coefficient results to smaller variations in the dispersion statistics between particles of different size compared to a static model.

5.2. Investigating Grid Dependence of C_o in a Shear Mixing Layer:

In this section the static model's grid dependence and performance in steady state statistics (temporally averaged dispersion levels) compared to the proposed dynamic model is investigated. A shear mixing layer allows for such an investigation. Particles are initialized in a region of 0 mean shear with the velocities of the uniform phase. Thereafter, particles encounter regions of shear formed by the mixing of two streams with different mean velocities. The mixing layer grows monotonically in the axial direction and consequently the resolution of the mixing layer also increases linearly. This enables the investigation of model performance in scenarios of not fully-resolved shear with regards to temporally-averaged dispersion levels, consequently allowing for an in-depth investigation of the models' ability to enhance numerical accuracy –restricted by sub grid-scale shear– of the disperse phase. Part of the results shown here have been presented in Pesmazoglou *et al.* [174].

5.2.1. Experimental Configuration and Modelling Parameters

The case considered here was studied experimentally by Tageldin and Cetegen [32], and numerically by Jones *et al.* [98]. It consists of a shear mixing layer produced by two parallel air flows within a $200 \times 150 \times 150$ mm domain in the x, y, and z directions respectively as depicted in Figure 5.4. The two flows have a bulk velocity of $U_{slow} = 2$ and $U_{fast} = 7.1$ ms^{-1}. The two streams are separated prior to the test section with a splitter plate. Honeycomb straighteners and mesh screens are used to create a uniform velocity profile for each stream. Wires of 1.5 mm diameter are used to trip the boundary layers produced on either side of the splitter plate in order to achieve self-similarity in a shorter distance. A Reynolds number, based on air properties and momentum thickness of $Re_\theta = 225$ was measured at the splitter plate.

The fast stream is homogeneously seeded with water droplets with diameters ranging from 2 to 50 μm with a count mean diameter of approximately 15 μm as shown in Figure 5.5. The Stokes number for the mean particle

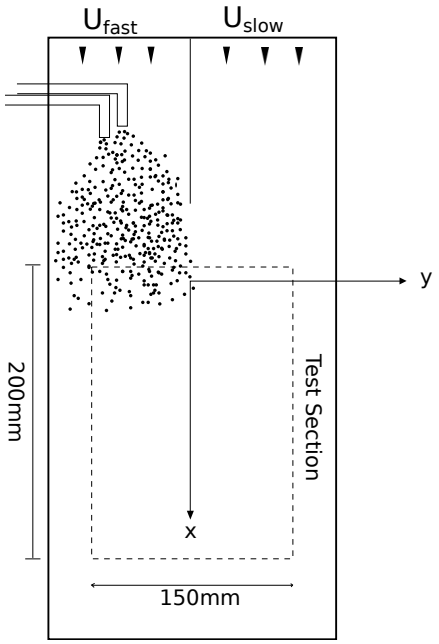


Figure 5.4.: Experimental configuration of [32]. Particles are seeded in the fast stream.

diameter varies from 0.08 near the exit of the domain to 1.2 in the near field of the mixing layer [98, 32]. The resulting spray can be considered dilute, with a volumetric void fraction of the order of $5.5 \cdot 10^{-6}$; therefore, droplet interactions are considered negligible. In addition, the streams are at ambient temperature and evaporation rates are assumed to be very small. A concentration of $4 \cdot 10^6$ droplets is conserved by injecting in the fast stream, upstream of the mixing layer, the number of droplets that have left the domain. Dropplets are assumed rigid spheres with a point mass.

Fully developed turbulence is considered with an intensity of 2% and $4-5\%$, in the fast and slow streams respectively, based on the mean velocity of the droplet seeded stream. The Kolmogorov length- and time-scales were estimated from the experiment [32] to be $\eta_k = 0.15$ mm and $\tau_k = 0.2$ ms respectively in the shear layer. Pseudo-turbulence with the experimental values of rms velocities and length-scales is created as outlined in Appendix A. Four different grid cases are considered, the fine are $\Delta = 0.8$ and 1.5 mm and the coarse are $\Delta = 2$ and 4 mm. The computational time varied from 180 to 5000 CPU hours for the finest case.

For the investigation of the effects of the dispersion constant C_o, two

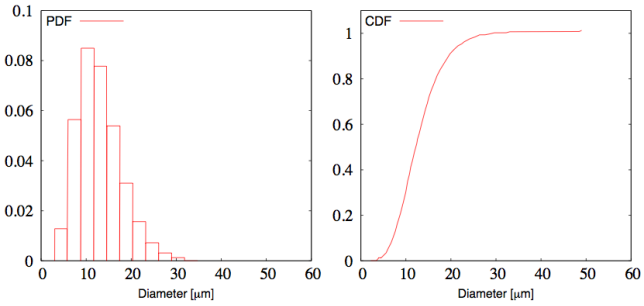


Figure 5.5.: Probability Density (PDF) and Cumulative Density (CDF) functions of the particle diameter in the test section of the flow.

well-documented downstream spreading measures where considered: the mixing layer thickness, $\delta_{0.8}$, and the momentum layer thickness, θ_u. Firstly a dimensionless velocity u^* is defined:

$$u^* = \frac{U_d - U_{slow}}{U_{fast} - U_{slow}}. \tag{5.6}$$

From which the thicknesses $\delta_{0.8}$ and θ_u are defined as:

$$\delta_{0.8}(x) = y|_{u^*=0.1} - y|_{u^*=0.9}, \tag{5.7}$$

$$\theta_u(x) = \int_{-\infty}^{\infty} u^*(1-u^*)dy. \tag{5.8}$$

For the definition of u^* the Eulerian particle velocity field, $U_d(x, y)$, constructed from the Lagrangian particle velocities $\mathbf{v_p}$, is used. For a given cell, the average velocity of all particles passing through it in a given time interval ΔT_n is calculated. The time ΔT_n is a generic temporal interval equal to $2000 \times \Delta t$, where Δt is the simulation time-step width. The final Eulerian particle velocity U_d is calculated by averaging the values from each temporal interval.

The mixing layer thickness $\delta_{0.8}$ at a given axial location x, is defined as the position on the y-axis where the particle normalized velocity equals to 0.1, minus the position where it is 0.9 (for the co-ordinate system shown in Figure 5.4). Therefore, the mixing layer thickness is a positional measure on a velocity basis.

The momentum layer thickness (5.8) definition of Tageldin and Cetegen

[32] is retained to allow for direct comparison with the experimental results. Evaluating θ_u involves the integration over the entire range of cells that contain particles, i.e. the entire particle domain. This integration method is used to avoid negative values of momentum thickness at positions where there are no particles (i.e. $U_d = 0$) since the normalizing velocity, U_{slow}, used in the experiment is constant and positive.

For the normalized velocity plots of both the gaseous and fluid phases the dimensionless height $y^* = (y - y_{0.5})/\theta_u$ is used. It must be noted here that for the normalization of y^* the same baseline momentum thickness is used for all the different C_o cases at a given grid spacing, to allow for a direct comparison.

5.2.2. Results

The discussion of the results begins by analyzing the effects of the static dispersion coefficient C_o on the momentum and mixing layer thickness for the fine (0.8 and 1.5 mm) and coarse (2 and 4 mm) grid cases. To investigate the sufficiency of the Smagorinsky model, a simulation using the dynamic Germano implementation of Piomelli and Liu [181] was carried out for a medium grid spacing with $\Delta = 2$ mm, showing that the Smagorinsky model produces adequate results for the continuous phase (Figure 5.6). In addition to a reduced computational cost, the Smagorinsky model allows a direct evaluation of the sub grid kinetic energy. Moreover, the influence of a dynamic C_s on the particle dispersion coefficient is removed, facilitating the investigation of the grid spacing dependence of the stochastic dispersion coefficient C_o. Therefore, the Smagorinsky model was used for the remaining simulations.

Figure 5.7 shows instantaneous snapshots of a passive scalar to represent the mixing process in the test section for different grid spacings. The passive scalar is equivalent to a mixture fraction, and is transported using the LES code with boundary conditions of 1 for the slow stream and 0 for the fast stream. One may note the ability of the LES to capture instantaneous fields, but also the pivotal effect of the grid spacing on the flow. The 4 mm and 0.8 mm filter widths are arguably the equivalent of a poorly-resolved and a well-resolved LES, respectively; in the coarsest $\Delta/\eta_k \approx 26.6$ and in the finest mesh $\Delta/\eta_k \approx 5.3$.

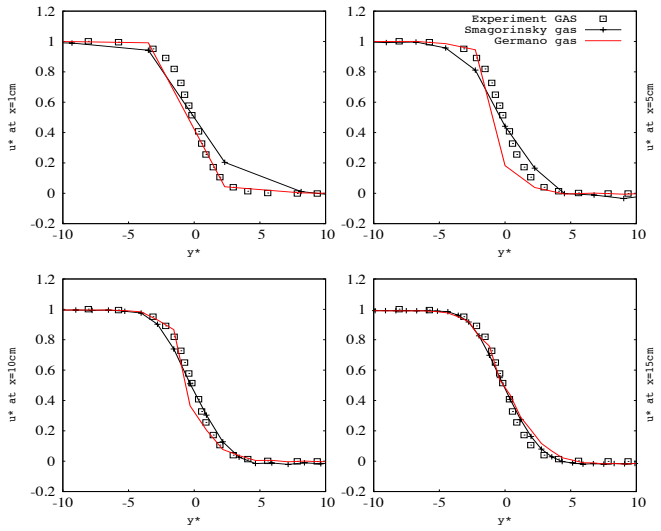


Figure 5.6.: Comparison of the Smagorinsky model and the Germano model for the evaluation of C_s in a medium grid spacing ($\Delta = 2$ mm) simulation.

Celik *et al.* [31] suggest that simulations with $\Delta/\eta_k \leq 7.25$ will resolve more than 80% of the energy spectrum in an equivalent homogenous isotropic turbulence and can therefore be considered *good* LES [185, 31]. Although this result must be taken with caution as we are considering a shear flow, it suggests that both fine meshes are well resolved and the coarsest meshes are not.

In Figure 5.8, the position where self-similarity in velocity is reached is defined as the transition length, X_{ss}. This depends on the grid spacing for numerical simulations, and the flow configuration and splitter plate properties in the experiment. The ability to predict the exact distance X_{ss} requires a highly resolved simulation of the splitter plate and experimental configuration, which is outside the scope of this work. Therefore, experimental data are compared to the self-similar results. A normalized dimensional value $X = x - X_{ss}$ is employed, where X_{ss} is used to compensate for the splitter-plate-to-test-section distance and the position where self similarity is reached, and x is the absolute distance from the inflow of the simulation. The values of $X_{ss} = 50$mm for the fine and $X_{ss} = 0$ for the coarse cases were chosen from investigation of the normalized velocity plots and

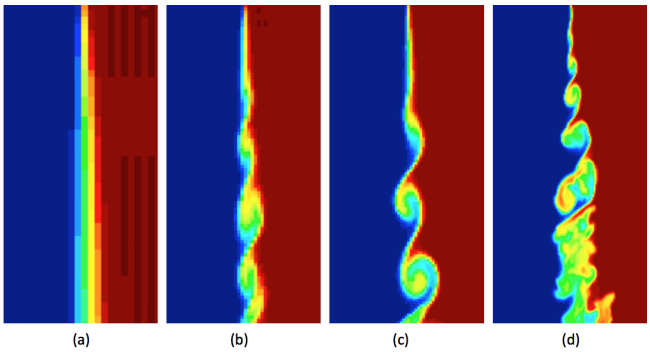


Figure 5.7.: Instantaneous snapshot of a passive scalar with: (a) $\Delta = 4$ mm, (b) $\Delta = 2$ mm, (c) $\Delta = 1.5$ mm, (d) $\Delta = 0.8$ mm. A passive scalar to illustrate the mixing process is assigned as 1 in the slow stream (red) and 0 in the fast stream (blue).

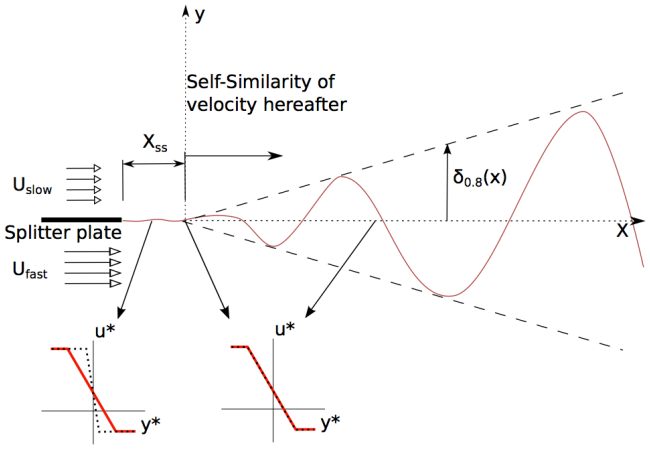


Figure 5.8.: The position where self-similarity is reached for the velocity (red line in normalized sketches) and a linear mixing layer thickness, $\delta_{0.8}(X)$, starts developing, is strongly dependent on the transition length, X_{ss}. A virtual origin, X, is set at the position, X_{ss}, where the dotted line of normalized velocites u^* coincides with the self similar solution (red line).

momentum and mixing layer thicknesses. The zero positional shift for the coarse cases can be due to an unrealistic or artificial early development of the flow. When the integral length-scale over the mesh spacing is close to unity ($\mathcal{L}/\Delta \simeq 1$), i.e. in a poorly-resolved LES, numerical errors may cause early development of the flow.

5.2.2.1. Dispersion with a static coefficient C_o

Figure 5.9 shows plots of the momentum and mixing layer thicknesses increasing with normalized axial position. For the two fine cases (Figures 5.9(a-b)), the mixing layer is better predicted when the stochastic dispersion is included (i.e. $C_o > 0$) whereas the $C_o = 0$ cases under-predict the two thicknesses (apart from the position furthest upstream). The stochastic contribution is higher on the 1.5mm grid than on the 0.8mm grid.

The momentum thickness exhibits a significant correlation with C_o seen mainly in the pre-developed region of the flow (where self-similarity of the gas-phase velocity has not been reached, i.e. $x < X_{ss}$). Once the flow reaches a self-similar solution the effect of C_o decays as exhibited by the converging lines for $C_o = 0 - 8$ in Figure 5.9a_2.

On the coarser grids ($\Delta = 2$ and 4 mm) it is found that the effect of C_o has a decisive role on the dispersion. It can be seen that a stochastic dispersion contribution must be employed to give results near the experimental levels. Such results are expected since a wider range of scales are unresolved, which contribute to the sub grid-transport. Therefore, the lack of a model will cause an underestimation of the particle dispersion. In the very coarse (4 mm) mesh of Figure 5.9d, it is noticeable that the mixing and momentum thicknesses are nearly constant throughout the domain for the $C_o = 0$ configuration.

For $\Delta = 4$ mm the model overestimates the mixing layer, but provides fairly accurate levels for the momentum thickness. Such a result can be understood by considering the definitions of the two thicknesses. The mixing layer thickness is defined on a positional basis by calculating the cell where the averaged particle velocity fulfills the conditions of (5.7), and therefore the error is directly proportional to the grid spacing. On the other hand, the momentum thickness is based on the velocity.

In the pre-developed region, the effect of C_o is to increase/enhance mo-

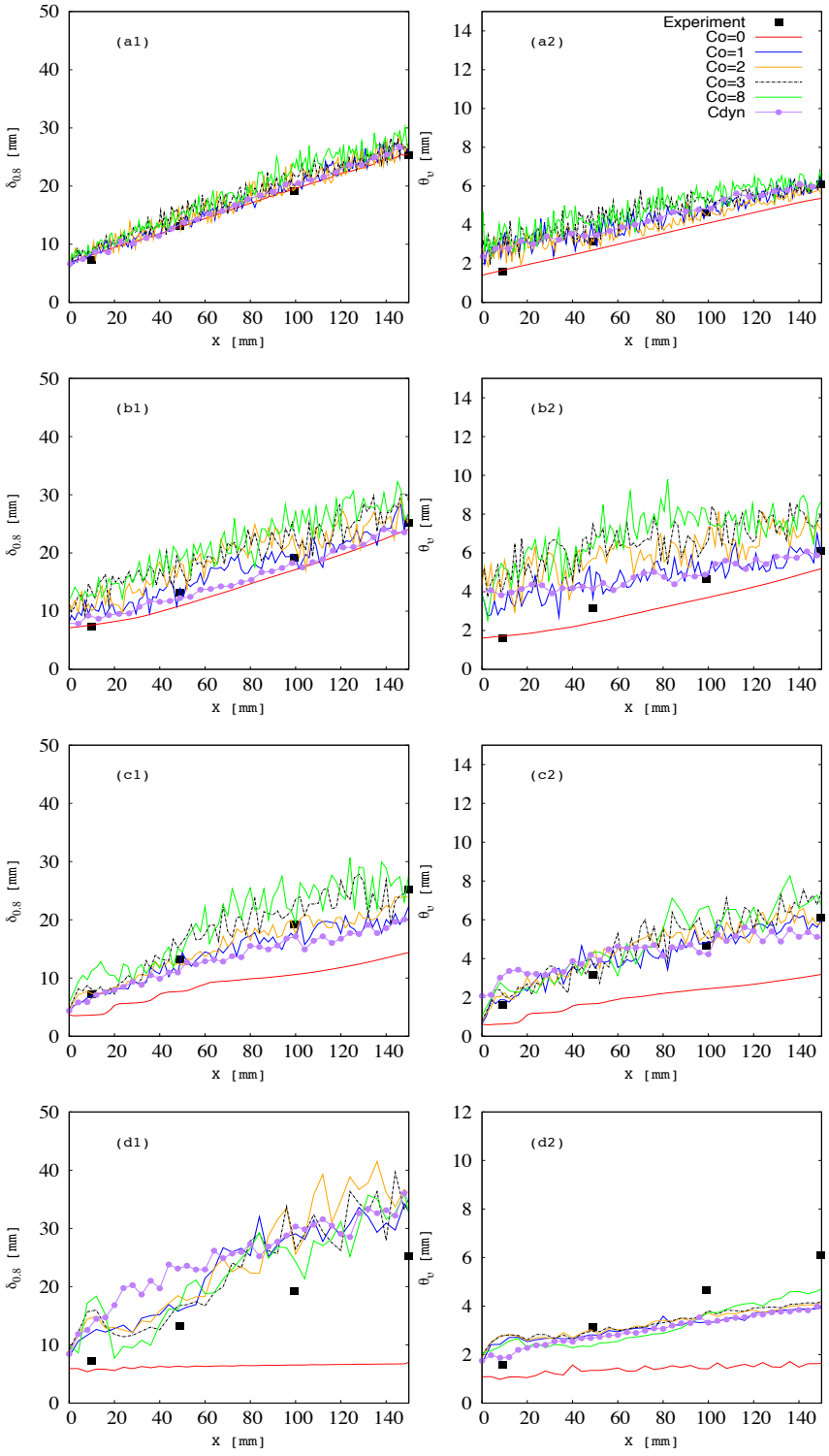


Figure 5.9.: Mixing ($\delta_{0.8}$, left) and momentum (θ_u, right) thicknesses versus normalized axial position X for different dispersion coefficients C_o=0-3,8 : (a) $\Delta = 0.8$ mm, (b) $\Delta = 1.5$ mm, (c) $\Delta = 2$ mm, (d) $\Delta = 4$ mm.

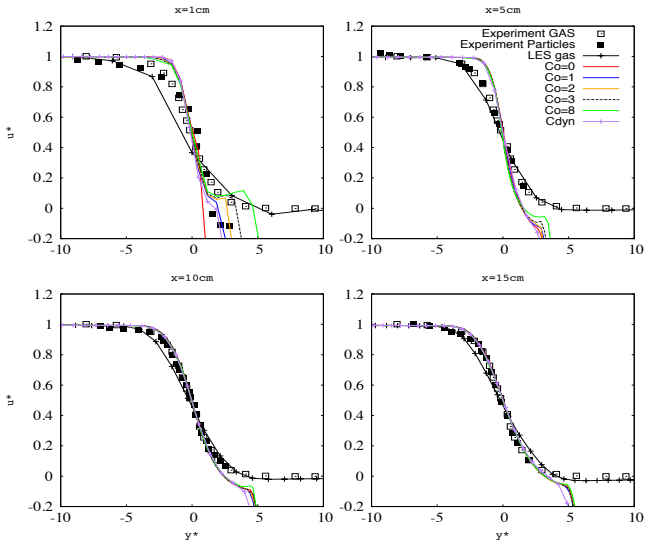


Figure 5.10.: Normalized velocity u^* versus normalized height y^* for $\Delta = 0.8$ mm for different dispersion coefficients and LES gas filtered velocity.

mentum. Particles move from the stream interface to the top (slow) stream with a higher vertical velocity than in lower or zero C_o cases. The sharp velocity gradient of the flow upstream translates into high turbulent diffusion of the particles, increasing C_o enhances this effect on particle motion, as the stochastic contribution increases with the static coefficient. The velocity gradient seen by a particle is steeper, inducing a higher stochastic contribution. Depending on the magnitude of the vertical particle velocity (governed by C_o) and the relaxation time τ_p, the particles will re-adjust downstream to the velocity of the flow. Downstream, the overall stochastic contribution decreases (as the gas velocity gradient smoothens) and the dispersion levels of the various static C_o cases converge.

Figures 5.10 and 5.11 illustrate the "numerical advancement" of the particle velocity distribution. The upstream over-prediction of θ_u apparent in Fig. 5.9 may be understood by comparing the normalized velocity plots for the two fine grids (Figs. 5.10-5.11). The LES gas velocity of the $\Delta = 0.8$ mm case converges to the self-similar solution of the experimental data faster than that of the $\Delta = 1.5$ mm grid. In addition, it is noticeable that the effects of the model constant differ depending on the position of the flow.

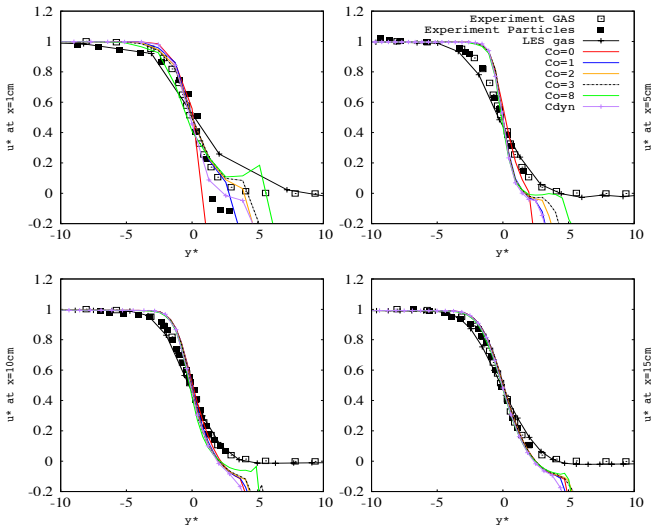


Figure 5.11.: Normalized velocity u^* versus normalized height y^* for $\Delta =$ 1.5 mm for different dispersion coefficients and LES gas filtered velocity.

Upstream, it is clear that for higher values of C_o, particles have moved further into the slow stream. In the $\Delta = 0.8$ mm cases the deeper penetration of the particles is only clear up to $x = 50$ mm, whereas for the 1.5 mm cases it is clearly visible even at $x = 150$ mm.

Finally, note the negative values of the normalized velocities in the results of the experiment and simulations, signifying that the particle velocity U_d is less than U_{slow} in the slow stream. Depending on the particle relaxation time and vertical velocity component, the particle axial velocity gradually adjusts to the free stream velocity downstream. The tails of the normalized velocity plots tend to $u^* = -U_{slow}/(U_{fast} - U_{slow})$, i.e. where there are no particles and $U_d = 0$.

Similar patterns are observed in the development of the two thicknesses in the coarse grids. In the cases of Fig. 5.9(c-d) the numerical overshoot is much higher. Arguably, this is an outcome of the inability of the coarse grid to capture flow phenomena. From Figs. 5.12 and 5.13 it can be seen that the mixing layer is captured by a few cells only. Therefore the velocity gradients between each cell are much steeper, (with respect to cell spacing not physical space), causing high sub grid shear levels and thus increasing the momentum

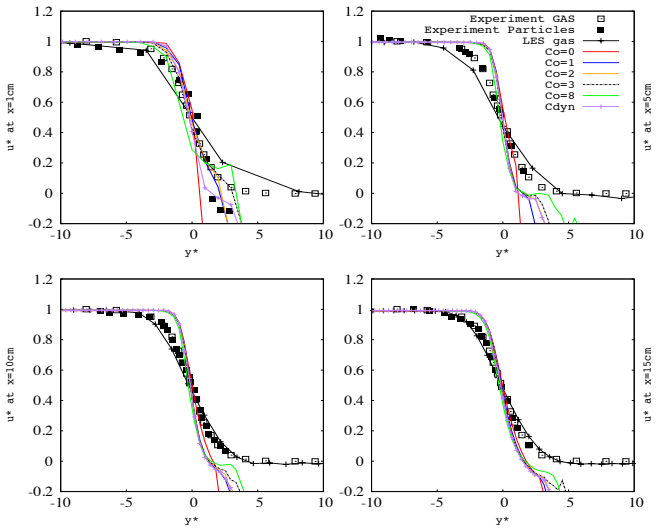


Figure 5.12.: Normalized velocity u^* versus normalized height y^* for $\Delta =$ 2 mm for different dispersion coefficients and LES gas filtered velocity.

thickness, while at the same time also increasing the positional error of the mixing layer thickness.

From the normalized velocities in Figs. 5.12 and 5.13, the effect of the dispersion coefficient is clear in the tails of the profiles. The penetration level increases proportionally to C_o. Lack of a stochastic dispersion model influences the coarse cases in that particles do not move into the slow stream; the $C_o = 0$ lines lead the other cases until they intersect them. This intersection is caused by the steeper particle velocity gradient, which translates into narrower mixing and momentum layer thicknesses.

From the analysis thus far we can argue that a model to incorporate the sub grid-scale effects must be employed to produce the observed dispersion levels. Both the mixing and momentum layer thicknesses require $C_o > 1$ for all grid spacings. Secondly, it can be argued that the choice of C_o is *not* universal and that the optimal dispersion coefficient depends on the grid spacing.

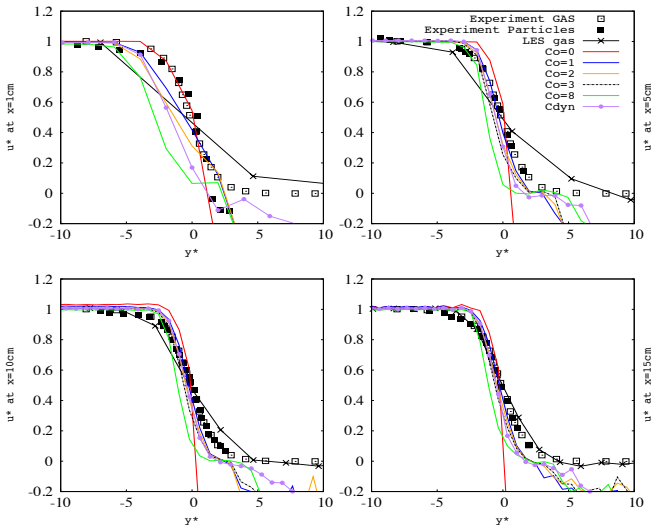


Figure 5.13.: Normalized velocity u^* versus normalized height y^* for $\Delta =$ 4 mm for different dispersion coefficients and LES gas filtered velocity.

5.2.2.2. Dispersion with a dynamic coefficient C_o

In the finest case of $\Delta = 0.8$ mm, shown in Fig. 5.9a, the dynamic model produces accurate dispersion levels for the mixing and momentum thicknesses. Arguably, the mixing layer thickness is similar to the simulation without a model for the sub grid-scale, but the $C_o = 0$ case underestimates the momentum thickness. By comparing the two thicknesses shown in Figs. $5.9a_1$ and $5.9a_2$, one may conclude that even though the particles reach the correct dispersion levels, the velocity distribution is underestimated in the $C_o = 0$ case. It is clear that the use of the dynamic model provides better results than with $C_o = 0$.

Moreover, the simulations using a dynamic model for the evaluation of the dispersion coefficient have a smaller fluctuation suggestsing a faster convergence to the correct dispersion levels compared to the static model implementations. One may therefore conclude that a dynamic dispersion field can enhance stability by varying the stochastic contribution depending on local flow characteristics, as opposed to a global static C_o. Most importantly, it seems that the dynamic model can predict the dispersion

coefficient at various locations in the flow. Some over-predictions are still observed at upstream positions, but this may be attributed to the fact that the gas phase has not yet reached a self-similar solution at these locations.

For $\Delta = 1.5$ mm, depicted in Fig. 5.9b, the dynamic model produces comparatively better results than any choice of static coefficient. The difference between no model and the dynamic model in terms of the two thickness measures is greater compared to that of the finer mesh.

For $\Delta = 2$ mm the dynamic model gives good agreement, though, closer agreement was found overall in the static model with $C_o = 2$. Figure 5.9d shows the mixing and momentum thicknesses for $\Delta = 4$ mm. Once again, the two mixing layer measures are highly under-estimated when a model is not employed, showing minimal to no dispersion. Therefore, from an on/off point of view, the dynamic model is required to provide a level of dispersion, although the mixing layer measures are over-predicted. The non-zero static dispersion coefficient cases exhibit a similar degree of over-prediction.

As may be expected, the correct levels of dispersion are not predicted by any of the models at the coarsest resolution, as the continuous phase velocity field is under-resolved. The dynamic evaluation in such grid spacings cannot offer accurate predictions since the test filter width is 8 mm, which is bigger than the momentum thickness ($\theta_u = 0 \rightarrow 5$ mm) and hence outside of the inertial range. Nonetheless, the dynamic model provides dispersion levels similar, and less 'noisy', to the ones produced by the various static dispersion coefficient simulations.

Figures 5.14 shows the average absolute errors in the mixing and momentum layer thicknesses. The average error was calculated as the mean deviation between simulation results and linearly-interpolated experimental data. The on/off effect of the dispersion coefficient is obvious, as in all cases the mean error decreased when the model was implemented. After this initial drop there are slight fluctuations which suggest a non-monotonic behavior with a minimum error at $C_o \approx 1$. Absolute errors with C_{dyn} (solid straight lines) are lower than the the majority of choices of a static coefficient and are close to the minimum error produced by the investigatory choice of C_o.

Figure 5.15 shows that the inclusion of a dispersion model affects the maximum error differently depending on the grid spacing. The maximum error of the two thicknesses represents the maximum deviation from the expected

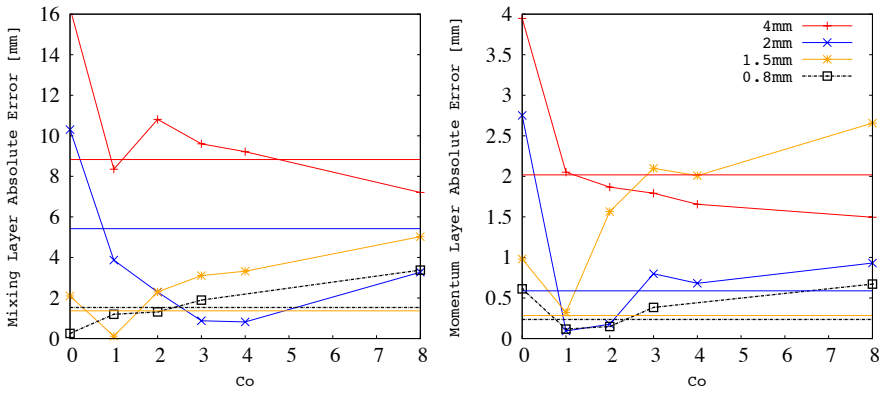


Figure 5.14.: Mixing and momentum layer thickness absolute errors versus the dispersion coefficient Co, for various grid spacings Δ. Solid straight lines represent equivalent error using the dynamic model for C_{dyn}.

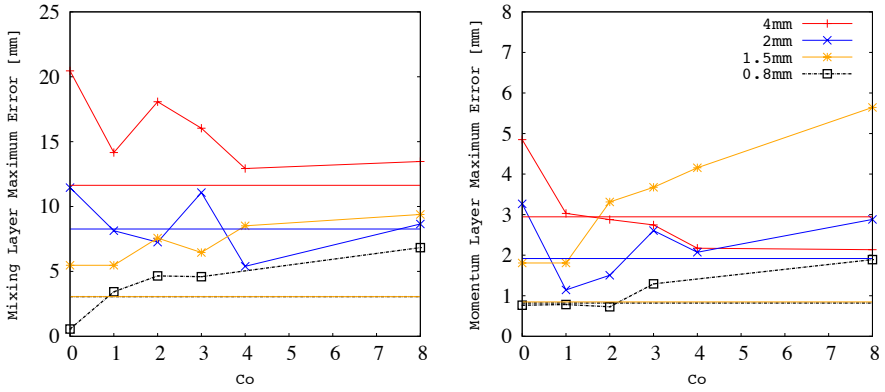


Figure 5.15.: Mixing and momentum layer thickness maximum errors versus the dispersion coefficient Co, for various grid spacings Δ. Solid straight lines represent equivalent error using the dynamic model for C_{dyn}.

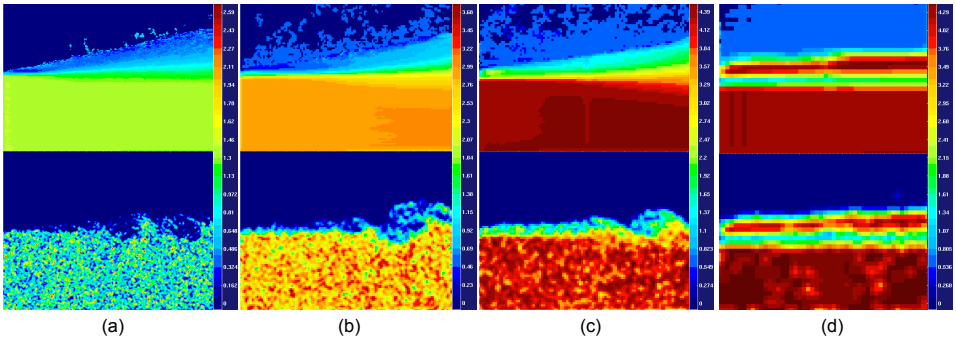


Figure 5.16.: Contour plots of ensemble-averaged (top) and instantaneous (bottom) dynamic dispersion coefficient for: (a) $\Delta = 0.8$ mm (b) $\Delta = 1.5$ mm (c) $\Delta = 2$ mm (d) $\Delta = 4$ mm.

experimental dispersion statistics. The dynamic model has lower mixing layer thickness maximum errors compared to all non-zero static dispersion coefficient choices for the finest cases and coarsest case. Secondly, the level of maximum deviation from the experimental data is similar for the 0.8 and 1.5mm grid spacings, for both the momentum and mixing layer thicknesses. For $\Delta = 2$mm, the dynamic model produces lower maximum errors than the $C_o = 0$ simulation, but it does not give the best results. Arguably, however, the error levels are similar to those produced by the static coefficients on the same grid spacing. As opposed to the static coefficient, the dynamic method enhances or reduces the dispersion coefficient according to the local flow conditions. Consequently, using the proposed methodology one may obtain a more stable solution for the particle dispersion statistics.

From what follows, the dynamic coefficient can be represented by an Eulerian field. The instantaneous ensemble averages of C_{dyn} are calculated for each Eulerian node at every time-step. Therefore, a time averaged $\langle C_{dyn} \rangle_t$ can be readily calculated.

Figure 5.16 depicts the instantaneous (particle ensemble-averaged) and time-averaged dynamic coefficient distribution for the different grid spacings investigated. Figure 5.16(a) depicts the average and instantaneous C_{dyn} field of the finest grid spacing. The Eulerian fields show that the coefficient is far from constant. The instantaneous plots indicate a correlation with the flow structures. The level of resolution is directly related to the values of the C_{dyn} field.

Figure 5.17 shows the variation of the dynamic dispersion coefficient in

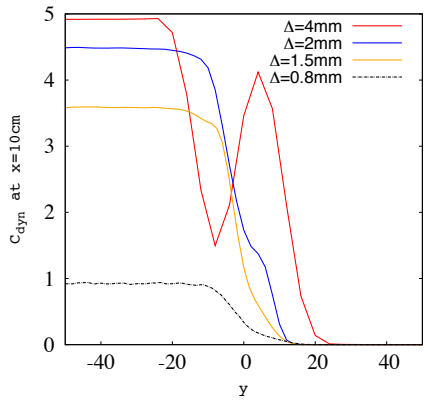


Figure 5.17.: Average dynamic coefficient versus height in the mixing layer for the four grid spacings investigated, at $x = 100$ mm.

the y-direction at $x = 100$ mm. The dispersion coefficient acquires its highest value in the fast stream where the turbulent rms velocity is higher comparatively to the the slow stream. A twofold increase in the grid spacing from 2 to 4 mm results in only a 10% increase in C_{dyn} in the fast stream, as opposed to the (more than) threefold increase from the 0.8 to 1.5 mm grid spacing.

Within the mixing layer there is a sharp drop in the dispersion coefficient. It is the whole stochastic diffusion term that increases and not the coefficient in particular. What the model suggests is that the increase in $\sqrt{k_{sgs}/\tau_t}$, due to the sharp velocity gradient, is in fact over-predicted, thus requiring a smaller dispersion coefficient to realistically represent the energy transfer from the gaseous phase to the particulate phase. Given the same flow conditions, a constant C_o would over-predict the local energy transfer, thus 'shooting' the particle with a higher velocity towards the slow stream. The particle would then reach the next cell and, depending on the local conditions, its velocity will re-adjust.

5.3. Conclusions

The Lagrangian Stochastic model of Bini and Jones[24, 22] has previously shown very good predictions for particle velocity and acceleration statistics. However, the dispersion constant was found to be very grid dependent.

In this work, using similar assumptions to scale similarity models, a model has been derived that dynamically evaluates the dispersion coefficient. The method uses a test-filtering process for the Eulerian variables of the continuous phase to derive a test-filtered equivalent particle acceleration SDE. Assuming that the ensemble average rate of change of kinetic energy of the disperse phase must be constant for a given time increment, an equation for the dispersion coefficient was derived.

For the purpose of validating the model a test case was chosen consisting of an unbound channel, with a constant and uniform velocity gradient in one spatial direction and decaying homogeneous isotropic turbulence. The uniform phase was seeded with particles to measure their dispersion statistics. It was concluded that using a model to incorporate SGS is required for the correct prediction of particle motion. It was shown that the dynamic model accurately predicts the dispersion variance of the particle phase. In addition, the size-weighting of the dynamic coefficient results to smaller variations in the dispersion statistics between particles of different size compared to a static model.

The model performance was further investigated with respect to grid dependence and temporally-averaged dispersion statistics. For this purpose a series of LES of a droplet-laden mixing layer were carried out with different grids and static dispersion coefficients. The mixing layer and momentum layer thicknesses are under-predicted without a model, and from an on/off perspective the use of a stochastic dispersion model is required for an accurate prediction of the experimental results.

Using the dynamic model, the predicted levels of mixing and momentum layer thicknesses are significantly better than any single choice of static dispersion coefficients when the LES is well resolved. The ability of the dynamic model to predict correct levels of dispersion is impeded at very coarse grid spacings, where the test-filter width lies outside the inertial range. Even so, the dispersion statistics were similar to those produced by the static coefficient models.

Although it was used here in the model proposed by Bini and Jones, the dynamic model could, in theory, be extended to different choices of drift and diffusion coefficients, such as in non-inertial LS models. The assumption of a constant average rate of change of particle kinetic energy could arguably be the same, however excluding the mass weighting of the dynamic coefficient

as the particles are non-inertial.

Finally, the dynamic model offers advantages to the static equivalent. Firstly, one does not require to choose a static coefficient. Secondly, it provides better results than the static coefficient when the only parameter varied is the particle size. Thirdly, due to its coupling with the flow, it has shown that it produces smoother results than static coefficients.

6. Nucleation in a turbulent jet

6.1. Choice of DBP

In the present work, a supersaturated Dibutyl-Phthalate (DBP)-laden Nitrogen (N_2) turbulent jet is investigated; the chapter is based on the results presented in Pesmazoglou *et al.* [175, 176]. DBP is a stable compound with low toxicity, and it can be considered representative of a heavy organic fugitive emission. DBP has been favored in nucleation studies because it can reach high supersaturations with low concentrations. A number of experimental studies using DBP as the condensable material coupled to a flow have been carried out. Liquid droplet concentrations have been measured in laminar diffusion chambers by [8, 30]. Wilck *et al.* [255] evaluated nucleation rate theories against experimentally derived nucleation rates for DBP. Okuyama *et al.* [167] and Hameri *et al.* [84], compared their measured concentrations to those predicted by nucleation theory. Moreover, Mikheev *et al.* [153] used a laminar flow tube reactor to compare their results with theoretical nucleation rates and to obtain critical cluster sizes and the excess of internal energy of the critical cluster.

In addition, the turbulent jet is a configuration with many practical applications in industry, ranging from small-scale injectors to industrial chimneys. Furthermore there is a significant amount of literature for its particular flow characteristics, as well as self-similar solutions for the velocities and passive scalar distributions [34, 89, 227].

For the investigation of a turbulent-flow-coupled nucleation rate, the test case of Lesniewski and Friedlander [127, 128, 129] is examined. In their study, a turbulent diffusion chamber was used to measure concentrations and retrieve the PSD produced by a supersaturated DBP vapor in a heated Nitrogen jet mixing with atmospheric air. This particular case has been examined in a number of computational studies [66, 243, 276], allowing for further comparison of data and implementation methods.

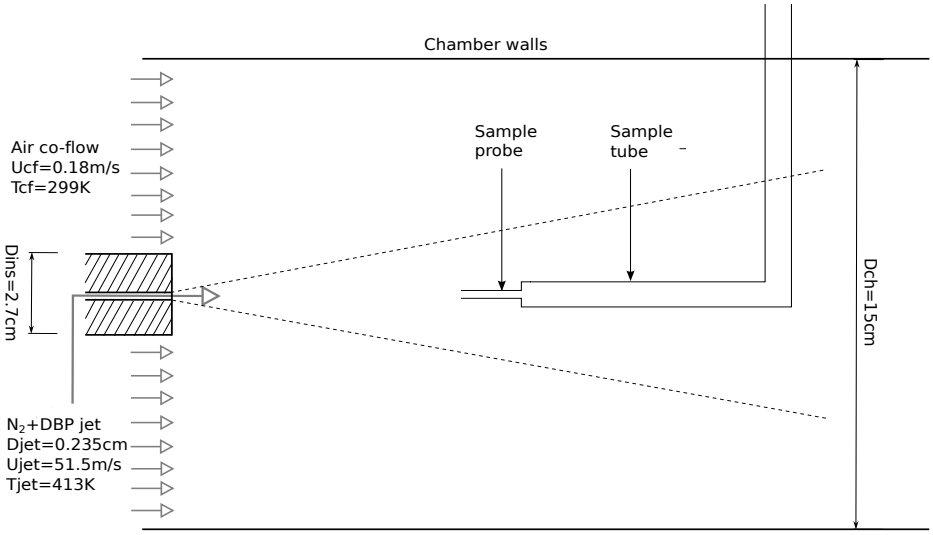


Figure 6.1.: Experimental configuration of [129]. The heated Nitrogen DBP-laden jet enters through an insulated nozzle in the diffusion chamber. A concentric flow of air at atmospheric conditions is added. Nucleated particles are sampled and counted using a probe leading, through a tube, to the Condensation Particle Counter.

6.2. Experimental Configuration and Modeling parameters

Lesniewski and Friedlander [127, 128, 129] used a turbulent diffusion chamber to conduct a series of experiments and measure particle concentrations and size distributions for a DBP-laden Nitrogen jet diffusing in atmospheric air. The Nitrogen stream was heated and passed through a bubbler where it was saturated with DBP at a saturation temperature assumed to be equal to the temperature of the bubbler. The DBP-laden gas was then passed through a filter to remove particles from the carrier phase and sent with high velocity into a chamber via an insulated nozzle with an inner diameter D_{jet} and outer diameter D_{ins}. An air co-flow entered concentrically into the chamber. An outline of the diffusion chamber is shown in Fig. 6.1.

The jet was turbulent, with velocities varying from 30 to 80 m/s. Only one case was examined here where a jet bulk velocity of $U_{jet} = 51.5$ m/s was chosen with a co-flow velocity of $U_{cf} = 0.18$ m/s. The pressure was held constant at approximately atmospheric conditions. The jet inlet tempera-

ture was measured experimentally using a thermocouple under the nozzle exit and was held at 413 K, while the co-flow air temperature was 299 K.

For a nozzle volumetric flow-rate of $Q_{jet} = 1.6 \cdot 10^{-4} \mathrm{m}^3/\mathrm{s}$ the jet engulfed the domain at $z/D_{jet} \approx 90$, where z is the axial distance. The nozzle diameter in the experiment was varied. In the context of this work a nozzle diameter of $D_{jet} = 2.35$ mm and an insulator diameter $D_{ins} = 27$ mm were chosen; see Fig. 6.1. No recirculation was observed near the nozzle outlet in [129]. The experimental chamber had a diameter of 150 mm and 460 mm length. The simulated domain had dimensions $50 \times 50 \times 100$ mm, with a second simulation performed in a domain of $50 \times 50 \times 200$ mm to compare the particle concentration axial trend with the experimental data.

Measurements of the particle concentrations were taken using a sampling probe positioned in various axial locations. According to Lesniewski and Friedlander [129], the probe did not affect the upstream flow conditions. Once a sample was extracted, it was passed via a stainless steel tube to a Condensation Particle Counter (CPC). The residence time in the tube was 0.3 s; the sample was diluted to prevent further growth of the particles and heated to quench further nucleation. Measurements were taken after the CPC had a steady output for 30 s. The initial DBP mole fraction was measured using a flame ionization detector and was varied from $1 - 5 \times 10^{-4}$ in different experimental runs. In this study an initial mole fraction of 3.8×10^{-4} was used. Both the detector and counter data had a $\pm 10\%$ random error [129].

6.2.0.3. Nucleation modelling assumptions:

For the purpose of the simulation a Lewis number $Le = 1$ was assumed. It must be noted that for DBP-laden Nitrogen $Le \approx 5$ [160] and therefore fluid is cooled faster than it is diluted, creating a difference in nucleation rates in laminar regions. At high Reynolds numbers, molecular effects of temperature on fluid properties can be considered negligible when compared to turbulent-driven diffusion, although high Lewis number effects on nucleation may exist. The assumption of unity Lewis number in the present configuration allows for a direct comparison with the methodologies used in similar computational studies [66, 129, 243, 276].

The condensed vapor was only a small fraction of the total concentration

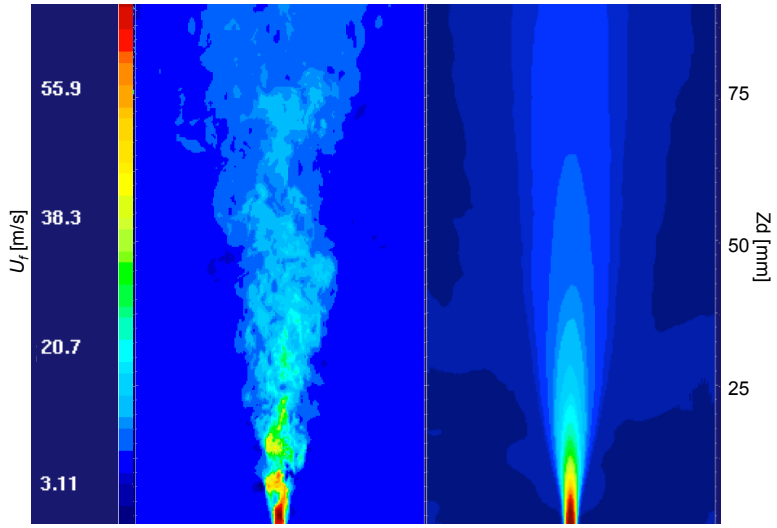
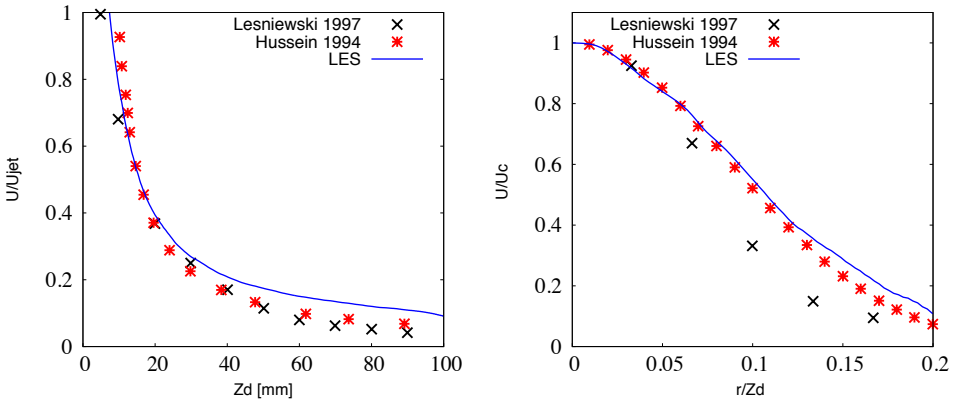


Figure 6.2.: Instantaneous (left) and mean (right) axial velocity contours

[129], therefore DBP depletion due to nucleation was considered negligible. Note that particle formation rates may significantly alter when the nucleation process competes with condensation of the vapor phase. No growth was considered in this model and all nucleated particles were assumed spherical with a diameter equivalent to the critical nucleation diameter d_p^*.

The Brownian diffusivity of nucleated particles is estimated to be $\mathcal{D}_p \sim \mathcal{O}(10^{-6})$ based on the jet temperature and $d_p = 2$ nm, (with a Cunningham slip correction of 100). This diffusivity can be considered negligible compared to the eddy diffusivity, $\mathcal{D}_{eddy} \sim \mathcal{O}(10^{-2})$, and the sub-grid diffusivity represented by Eqn. (4.12).

The turbulent rms velocity was chosen to be 10% of the jet bulk velocity with an integral length-scale of half the jet diameter. A grid-spacing of $\Delta = 0.25$ mm is found to sufficiently resolve the jet evolution, which corresponds to roughly 10 points across the jet diameter. Pseudo-turbulence, with a prescribed rms velocity of 10% the jet bulk velocity and an integral length-scales of half the jet diameter is created (as outlined in Appendix A). The computational time is approximately 15000 CPU hours per simulation.



(a) Centerline velocity normalized by the jet velocity along the domain.

(b) Radial velocity normalized by the centerline velocity and axial location.

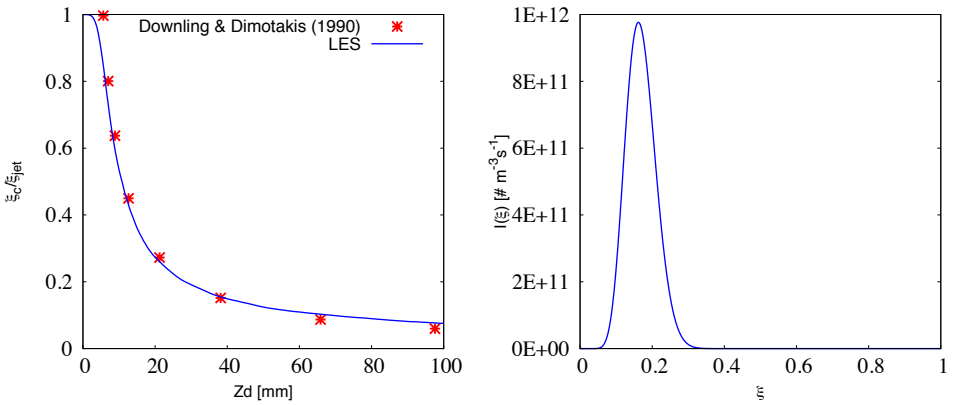
Figure 6.3.: Normalized velocity plots

6.3. Results

6.3.1. Gas phase

Figure 6.2 shows the instantaneous and mean axial velocity contours of the LES. The jet enters the chamber via an insulated nozzle and mixes with the co-flow of air. After an initial undisturbed region a shear-mixing layer develops and co-flowing air is entrained into the developing jet.

The LES solution of the velocity distribution was compared to the experimental data [127] and the self-similar jet solution of Hussein [89]. Figure 6.3a depicts the centerline velocity normalized by the jet velocity along the domain. A good agreement is found with the experimental data near the jet outlet; the slower decay observed further downstream was also present when refining the simulation and with the use of the dynamic Germano model [71]. A more gradual radial decay (compared to the experimental findings of [127]) was also observed in the LES of Zhou and Chan [276] and the RANS of Veroli and Rigopoulos [243]. It can be seen that the LES results are closer to the self-similar solution than to the experimental data. The radial profile collapses on to a single self-similar solution beyond $z/D_{jet} = 30$, as shown in Fig. 6.3b. Hussein [89] observed a similar position at which self-similarity is reached.



(a) Centerline scalar distribution normalized by the initial jet concentration.

(b) Nucleation rate as a function of the scalar ξ.

Figure 6.4.

6.3.2. Nucleation Rate

As in previous work [66, 243, 276], the CNT was found to significantly underestimate the observed nucleation rates by six orders of magnitude. A modification to the surface tension similar to the work of Garmony and Mastorakos [66] was implemented to compensate for this discrepancy (see Table 4.1).

In the experiment, temperature and concentration axial decay was not measured. The self-similar solution for a turbulent jet of [41] is therefore used for comparison with the LES results (see Fig. 6.4a). Figure 6.4b shows the variation of the nucleation rate with the scalar ξ for DBP at the reference temperatures of the experiment. The nucleation rate is significant only for a narrow (30%) range of the values of ξ.

Figure 6.5 shows a snapshot of instantaneous (left) and mean (right) nucleation rates from the LES. From the mean profiles of Fig. 6.5 it is noticable that the highest nucleation rates are observed near the centerline between $z = [30 - 50]$ mm. On the other hand, the positions where high nucleation rates occur instantaneously are highly irregular. It should be noted that the mean values shown in Fig. 6.5 are the time-averaged instantaneous nucleation rates from the LES. These mean values are *not* calculated from time-averaged scalar concentrations, i.e. the mean nucleation rate from the

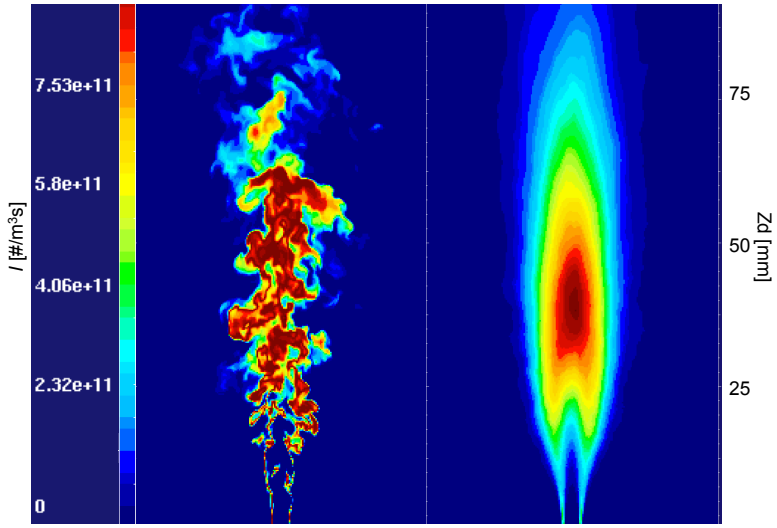


Figure 6.5.: Instantaneous (left) and mean (right) nucleation rate contour plots. The nucleation rate reached a peak $\sim \mathcal{O}(10^{11})$ [#/m^{3}s].

LES simulation is $\bar{\dot{I}}_{LES} = \left\langle \dot{I}\left(\tilde{\xi}\right)\right\rangle_t$, where $\langle\cdot\rangle_t$ denotes averaging over a number of temporal samples. In contrast, for RANS simulations and the LES performed by Zhou and Chan [276], the mean nucleation rate was calculated from the converged mean scalar distribution (i.e. $\bar{\dot{I}}_{RANS} = \dot{I}(\bar{\xi})$ and $\bar{\dot{I}}_{EMNM} = \dot{I}\left(\langle\tilde{\xi}\rangle_t\right)$, respectively, where the same notation is used and $\bar{\xi}$ represents the converged RANS scalar distribution).

An equivalent RANS nucleation rate has been calculated using the values of the LES time-averaged scalar concentration on the centerline (shown in Fig. 6.4a) and is compared to the LES time-averaged nucleation rate. It must be noted that the term *equivalent* is used because RANS simulations should include treatment of the temporal fluctuations. This is therefore a 'naive' RANS of a type that would not be implemented in practice.

Figure 6.6 (left) depicts that the non-linearity of the nucleation term produces different mean rates when those rates are calculated from a temporal mean scalar, as opposed to temporal averaging of the rates calculated from the instantaneous LES-filtered scalar. Although the total levels of nucleation are approximately equal, calculation of $\dot{I}$ from the mean scalar overestimates the peaks and underestimates values throughout the centerline. The use of instantaneous values of the scalar broadens the distribution of the mean rate and slightly shifts the position of the peak downstream. The

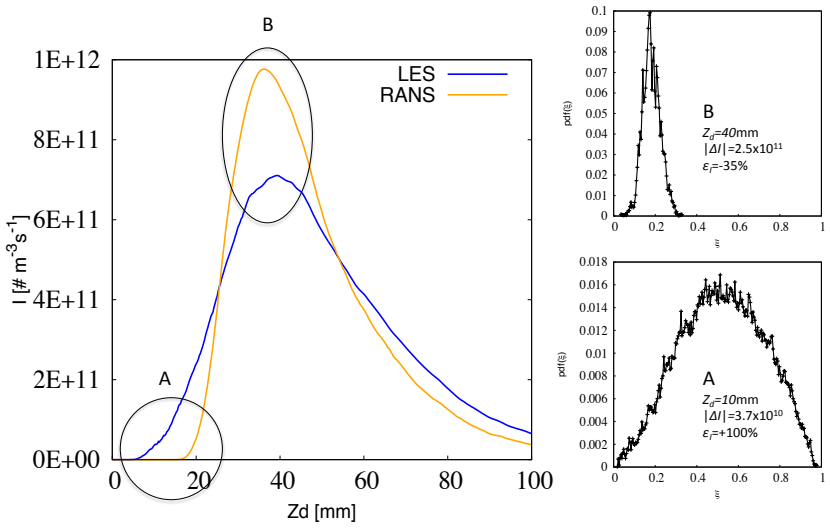
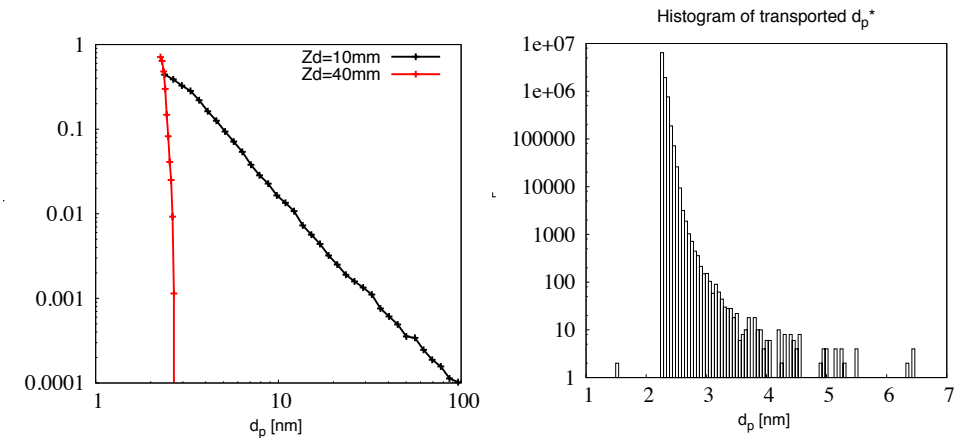


Figure 6.6.: Left: LES nucleation rate calculated from time-average instantaneous values, i.e. $\bar{\dot{I}}_{LES} = \left\langle \dot{I}\left(\tilde{\xi}\right)\right\rangle_t$, versus an equivalent 'naive' RANS where the nucleation rate is calculated using the time-averaged scalar values, i.e. $\bar{\dot{I}}_{eqRANS} = \dot{I}(\langle\tilde{\xi}\rangle_t)$. Right: pdf($\tilde{\xi}$) at the two locations marked A and B.

RANS equivalent case suggests that no particles will form before $z = 18$ mm, which contradicts the experimental findings [129]. At the two locations marked 'A' and 'B' ($z = 10, 40$ mm, respectively) the equivalent probability density functions of the LES scalar $\tilde{\xi}$ are shown along with the absolute and relative difference of the two nucleation rates ($\Delta\dot{I} = \bar{\dot{I}}_{LES} - \bar{\dot{I}}_{eqRANS}$ and $\epsilon_{\dot{I}} = \Delta\dot{I}/\bar{\dot{I}}_{LES}$, respectively). The flapping of the jet near the location 'A' produces a wide temperature pdf and a significant difference in the nucleation rates calculated from the LES and the 'naive' RANS. At location 'B', the pdf is narrower and therefore the relative difference between the two rates is smaller, yet significant: $\mathcal{O}(35\%)$. If the formation process is viewed as a probabilistic extension of the governing equilibrium theory, namely that in the transient conditions of a turbulent jet the CNT provides the probability of a stable nucleus forming and not a deterministic condition, one must take into consideration the possible fluctuations of the scalar and not only its temporal average.

Figure 6.7a depicts the fluctuations of the critical nucleation diameter d_p^*, as predicted by the CNT Eqn. (4.25), at the two axial locations 'A' and



(a) PDF of d_p^* predicted by the CNT at two axial locations.

(b) Histogram of formed particles tracked in the simulation.

Figure 6.7.: Nucleation diameters

'B'. The range of stable diameters given by the CNT for the instantaneous scalar value at $z = 10$ mm spans over two orders of magnitude. A sharp delta-type function is observed at $z = 40$ mm as expected from the narrow scalar pdf of the equivalent location shown in Fig. 6.6.

Figure 6.7b is a histogram of all the *formed* particles tracked in the simulation at a given instant in time. The majority of the particles nucleated with a diameter of $d_p \approx 2.3$ nm, which corresponds approximately with the peak diameters of Fig. 6.7a.

Figure 6.8 shows the scalar fluctuations on the centerline from the LES. In the near-nozzle region the scalar deviates from its mean by up to 0.2, which corresponds to a fluctuation of 23 K. This suggests that although the mean vapor concentration may result in insignificant or zero nucleation, instantaneous rates may reach values of the order of $\mathcal{O}(10^{11})$ [# /m^{3}s].

Instantaneous data include a higher level of information than mean values, so that LES provides a significant advantage over RANS for this configuration. Moreover, when nucleation is viewed in conjunction with particle injection the differences between using mean and instantaneous values have been highlighted in the examples of figures 4.2 and 4.3.

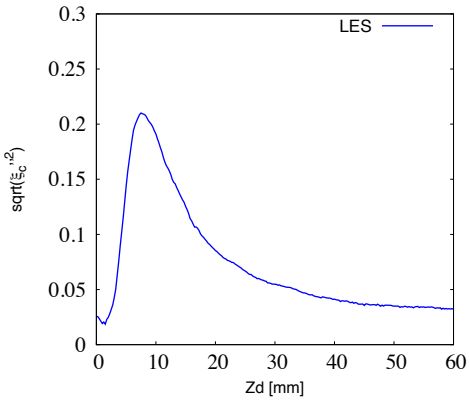


Figure 6.8.: RMS scalar on the centerline.

6.3.3. Particle Concentration

Figure 6.9 shows a snapshot of instantaneous and mean particle number concentrations N_c [# per cell]. These fields are constructed from an ensemble summation over the Lagrangian particles. In a given cell the particle number concentration is calculated at every time-step. When compared to the nucleation contours in Fig. 6.5, one may notice that the position of peak concentration is downstream of the position of the peak formation rate. This is an outcome of the flow-field, i.e. 'cumulative nature' of this experimental set up where particles accumulate as the jet decelerates. At a given axial location, particles are counted using the CPC; however, the exact origin of each nucleation event cannot be determined experimentally. Measurements of particle concentration therefore have a cumulative bias, as particles nucleated elsewhere in the domain are transported by the flow to the position of the counter.

If particles always nucleated with the same initial diameter and constant growth rate one would be able to determine their nucleation location from their current size and the required time to reach that size; in a turbulent flow however, there are fluctuations in the nucleation diameter as well as in the position at which a particle is formed. The cumulative effect in the CPC measurement becomes one of the primary reasons for which nucleation rates cannot be directly measured in an open system. In contrast, expansion

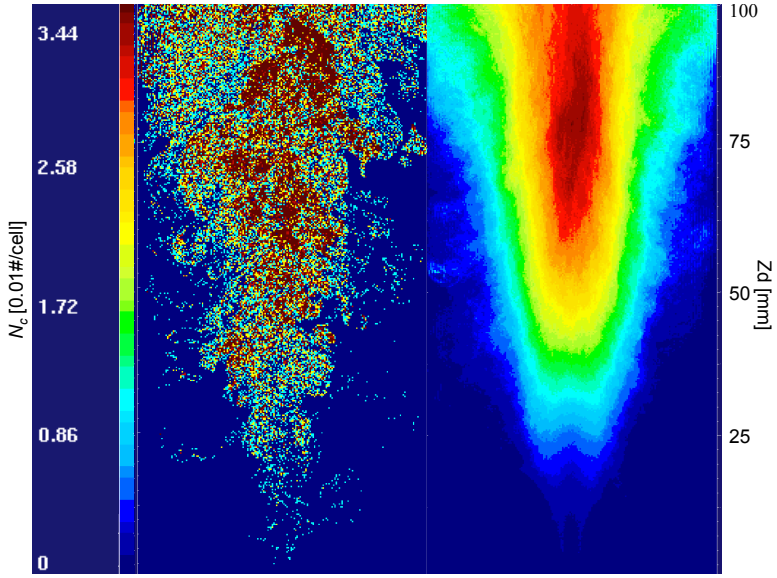
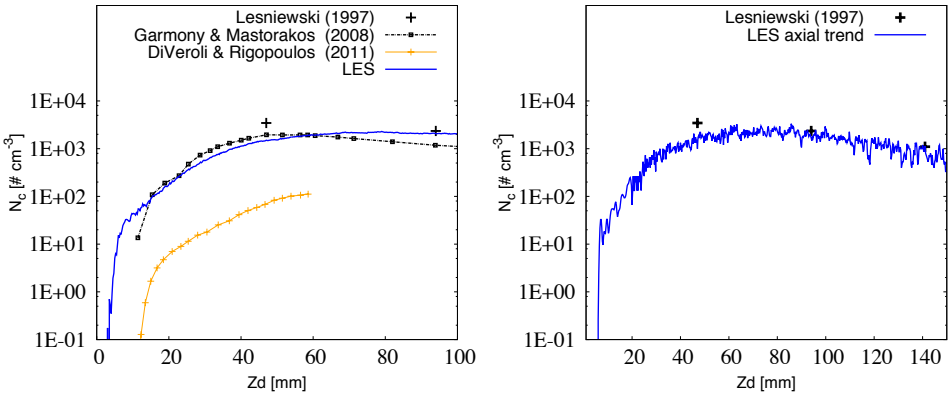


Figure 6.9.: Instantaneous (left) and mean (right) particle concentrations. The range varies from $Nc = 0 - 3.65$ [# per cell].

chambers[1], which are used to measure nucleation rates in a confined volume, allow for a certain residence time (equivalent to the expansion stroke of the piston) before nucleation is quenched (by a slight re-compression of the piston). Nucleation rates can be therefore measured by counting the number of particles produced within the volume of the chamber, in the allowed residence time, under the enforced macroscopic thermodynamic state. In turbulent nucleating jets (and in open systems in their generality) it becomes extremely difficult to trace the exact origin of a nucleation event, and hence the formation rate at a given location cannot be determined.

The LES results with no SGS contributions are compared to the experimental results in figures 6.10a and 6.10b. Good agreement is found with the experimental results and with the computations of Garmony and Mastorakos [66]. DiVeroli and Rigopoulos [243] underestimated the concentration levels by at least one order of magnitude. It should be noted that

[1]In an expansion chamber a saturated mixture of gaseous components is adiabatically expanded by the motion of a piston. The temperature drop, caused by the expansion, creates a supersaturated state for one of the mixture components which will consequently nucleate. To de-couple the nucleation process from growth a slight re-compression of the piston quenches further nucleation and growth; a technique termed 'pulse nucleation' [218]. The interested reader may refer to p. 129 in Wagner [247] for the experimental measurement techniques using expansion chambers.



(a) Compared to the experimental data and numerical solutions.

(b) Longer domain for axial trend investigation.

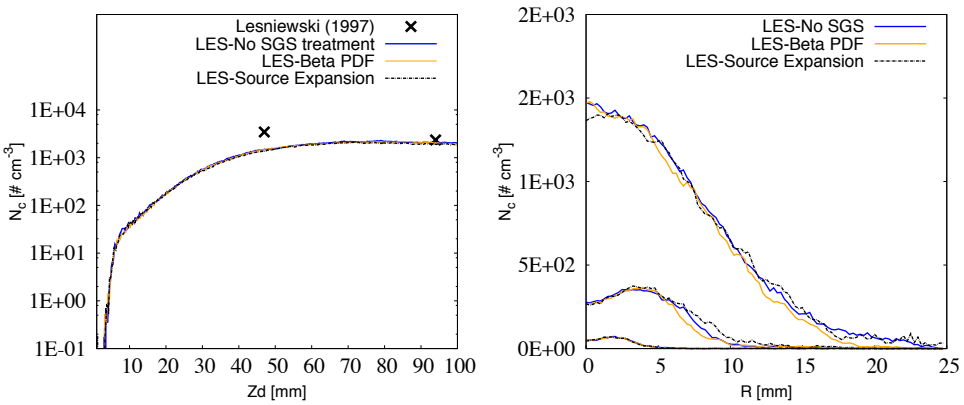
Figure 6.10.: Particle concentration on the centerline in the axial direction.

the LES underestimates the first particle concentration measured experimentally. However, the axial trend in particle concentration levels is well-captured by the LES further downstream, as shown in Fig. 6.10b. A good agreement was found with the work of Garmony and Mastorakos [66]. The discrepancy between the LES and the experiment may be caused by extra nucleation in the sampling tube: the residence time in the sampling tube leading to the CPC is around 0.3 s, which may lead to additional nucleation at upstream locations where the DBP vapor concentration is still high.

6.3.4. Effects of sub grid-scales

The β-PDF and source expansion methods described in section 4.3.5 were implemented to examine the effects of the sub grid-scales on nucleation rates and particle concentrations. From Fig. 6.11a it can be seen that there is no significant difference in the particle concentration distributions from the three cases (no model, β-PDF, and source expansion) in the axial direction along the centerline. However, the cumulative effect in the particle dispersion process may mask a possible discrepancy between models. Therefore a closer examination is required both of nucleation rates and of particle concentrations.

Figure 6.11b shows the radial distribution of particle concentration at three positions in the domain ($z/D_{jet} = 5, 10$, and 20). Further downstream



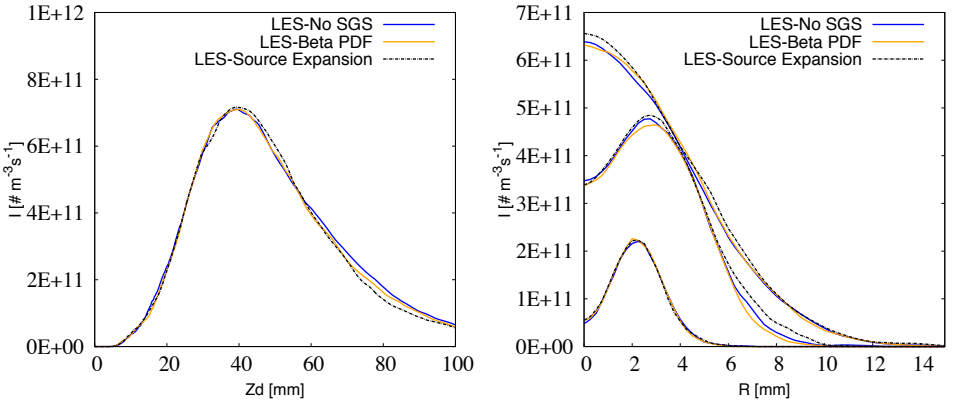
(a) Axial direction. (b) Radial direction.

Figure 6.11.: Particle concentrations without closure are compared to two different sub grid closure models. The radial direction measurements are at positions $z/D_{jet} = 5, 10$, and 20 (moving from the bottom left corner to top right).

the particle concentrations are higher, but there seems to be no systematic difference in nucleation rates between the three approaches for the treatment of the SGS fluctuations.

Following a similar analysis to the particle concentrations, Figures 6.12a and 6.12b depict the axial and radial LES mean nucleation rates. From these figures one may deduce that the differences between the models are small. The inclusion of an SGS closure model results in a slightly higher mean nucleation rate near the peak around $z = 40$ mm and lower values downstream (figure 6.12a). Similarly, small differences are observed in Fig. 6.12b which shows the mean nucleation rates in the radial direction at positions $z/D_{jet} = 5, 10$, and 20.

Figure 6.13 is a scatter plot of the sub grid scalar variance $\widetilde{\xi''^2}$ versus the equivalent LES value $\tilde{\xi}$. Data pairs are collected for the two locations of Fig. 6.6, where $z = 10$ and 40 mm, respectively. As expected from Fig. 6.6 the range of values that the scalar $\tilde{\xi}$ acquires in the LES is considerably smaller at location 'B' compared to those at 'A'. For every value of the scalar $\tilde{\xi}$ the equivalent ensemble averaged variance $\left\langle \widetilde{\xi''^2} | \tilde{\xi} \right\rangle$ is calculated and represented by the solid lines of Fig. 6.13. The modeled variance is $\widetilde{\xi''^2} << 0.1$ in both locations. Therefore (and by comparison to $\dot{I}(\xi)$ in Fig. 6.4b) a negligible



(a) Axial direction. (b) Radial direction.

Figure 6.12.: Mean nucleation rates without closure are compared to two different sub grid closure models. The radial direction measurements are at positions $z/D_{jet} = 5, 10$, and 20 (moving from the bottom left corner to top right).

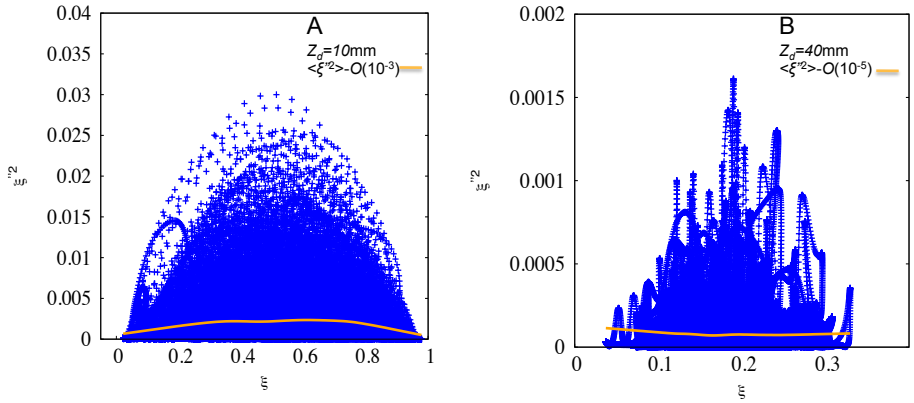


Figure 6.13.: Scatter plot of scalar sub-grid variance versus scalar LES value for the two locations 'A' and 'B' of Fig. 6.6 ($z = 10, 40$ mm, respectively). The solid (yellow) lines represent an ensemble averaged variance $\left\langle \widetilde{\xi''^2} | \tilde{\xi} \right\rangle$ for every given value of $\tilde{\xi}$.

variation is observed in the mean nucleation rate because of the modeled sub grid scale fluctuations.

From the above results one may draw the following conclusions regarding the SGS contribution to nucleation rates. The mean nucleation rate seems to be unaffected by the fluctuations of the scalar within a cell, however, it is strongly affected by temporal fluctuations: the use of time-averaged scalar values for the calculation of the mean nucleation rate leads to results that are significantly different to the time-averaged instantaneous nucleation rates, as depicted in Fig. 6.6. Considering the nucleation rate as a source term equivalent to a reaction source term, one may suggest that within a cell of volume Δ^3, the sub grid mixing is much faster than the nucleation residence time (i.e. similar to the case of a well-stirred reactor). This can be quantified using an equivalent to the Damkholer number, D_A^*, defined here as the ratio between an SGS time-scale (conservatively calculated as the integral length scale l_I and the RMS velocity) and the nucleation residence time:

$$D_A^* = \frac{l_I/u_{f,rms}}{\tau_{nuc}}. \tag{6.1}$$

Considering a fluctuation of the order of 10% of U_{jet} and the conservative case of the maximum nucleation rate (i.e. the minimum residence time) the time τ_{nuc} required for a single particle to form in a cell is of the order of $O\ (10^{-1})$ s, whereas the SGS mixing time-scale is of the order of $O(10^{-4})$ s. Therefore $D_A^* << 1$, suggesting that the LES cell volume is homogeneous and well-stirred with regards to the temperature and species concentration. This helps to explain why such small differences are observed when a model is included for the SGS contributions.

The analogy to a well-stirred reactor suggests that the temporally-averaged filtered values are unaffected by the unresolved fluctuations of species concentration and temperature. However, this does not mean that the instantaneous nucleation rates for the three approaches at a given time would coincide.

Figure 6.14 shows the instantaneous nucleation rate for three cases, namely: no-SGS, β-PDF and Source Expansion model. The nucleation rates are evaluated from the same instantaneous scalar field, at a cross-section of the domain ($z/D_{jet} = 10$) specified by the dashed line on the contour plot of the same figure. One may notice that the sharp peaks and the sharp changes in

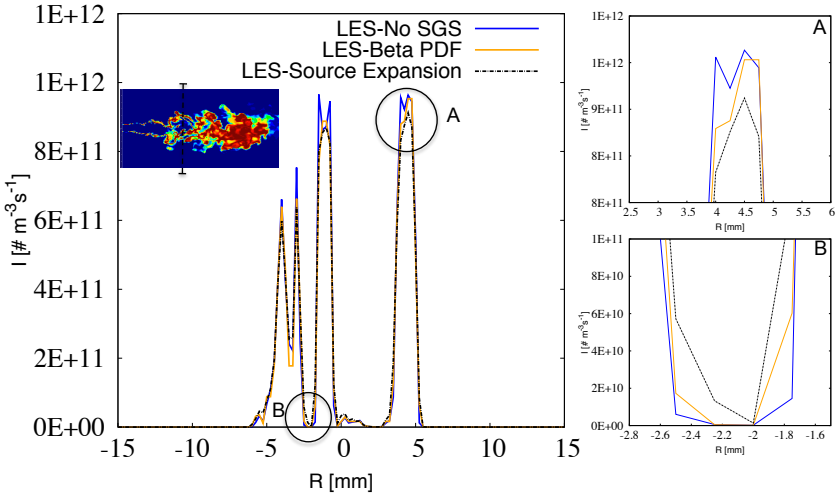


Figure 6.14.: Instantaneous nucleation rate at $z/D_{jet} = 10$ calculated from the same LES using the source expansion and β-PDF methods, and with no model. Two details are shown at the locations marked 'A' and 'B'.

the gradient produced by the calculation without a model are smoothened (up to 20% see detail 'A' and 'B' in Fig. 6.14) when accounting for the SGS fluctuations.

The two models react similarly, but not identically. The β-PDF method follows the no-model case closer than the source expansion method. The source expansion method seems to be smoother; this can be attributed to the nature of the model, namely that it performs a Gaussian filtering.

Arguably, for $Le \neq 1$ as in the works of Garrick and co-workers [50, 160], the instantaneous filtered nucleation rate would depend on fluctuations of both temperature and DBP concentration, which should be treated separately. Therefore, for example equation (4.38), would require to be convoluted with a joint species concentration and temperature pdf.

Two main points can be drawn from the investigation of the sgs nucleation rate: firstly, for the particular test case and LES the conditions can be considered to be similar to those of a well-stirred reactor, hence, mean filtered values remain unaffected by the filtered-out scales. Secondly, the models do affect the instantaneous results by reducing the peaks and smoothing the sharp gradients.

6.4. Conclusions

Being the underlying physical process for many applications, nucleation has received significant attention in both industry and academia. The highly non-linear nature of the expression for the nucleation rate renders its numerical simulation extremely difficult, but recent increases of computational power have allowed a more in-depth investigation of the phenomenon.

This study has focused on an LES implementation of the nucleation rate provided by the CNT for a turbulent DBP-laden nitrogen jet diffusing in atmospheric air. The main incentives of this work have been to take advantage of the instantaneous rates delivered by the LES and to subsequently evaluate their significance in comparison to the time-averaged values from more traditional approaches. Moreover, the impact of incorporating the effects of unresolved scales due to the spatial filtering have been evaluated using different SGS approaches. Having established the numerical treatment and physical characteristics of the test case in question, the results have been presented and discussed.

The proposed parameter-free method for the treatment of the nucleation rate as a probabilistic event has been found to predict particle concentrations accurately in comparison to experimental values and previous computations. The differences between the LES and RANS-equivalent mean nucleation rates have been highlighted, and the advantages of using the former have been discussed. The proposed probabilistic method allows the advantages of LES to be extended to nucleation-governed parameters, namely particle concentrations.

It has been shown that for the particular LES performed here, the effects of the unresolved scales are insignificant for time-averaged mean values. The β-PDF and source expansion methods predicted very similar particle concentrations and nucleation rates in the radial and axial directions. Considering the particle nucleation rate as a source term equivalent to a chemical reaction source term, an order-of-magnitude analysis of the timescales involved has shown that the case could be considered to be well-stirred within the volume of a cell; this may explain the minimal effect of the sub grid-scales on the mean LES values. However, by closer examination of the instantaneous values it has been shown that the models do affect the results. Both sub grid-scale models reduce peaks and smooth gradients when

compared to the instantaneous nucleation rate calculated without a model. The source expansion method appears to have a more pronounced effect compared to the β-PDF.

Most importantly, no significant difference could be seen for the particle concentrations. This becomes important when comparing to alternative approaches for the simulation of nucleation rates, where it has been shown that the exclusion of fluctuations (temporal in RANS and spatial in the EMNM) leads to significant differences in the calculation of particle nucleation rate and concentration.

7. Aggregation in a turbulent jet

7.1. Preliminary model validation

For the preliminary validation and development of the aggregation model outlined in Chapter 4, the analytic solutions of the PBE for two aggregation kernels are used. The aim is to investigate the performance of the multi-collision model with respect to particle concentration depletion, particle total mass conservation, and the PSD evolution. In addition, the influence on the aforementioned statistics of the aggregation time-step Δt_{aggr} and internal particles per parcel n_{int} selected is investigated. The particle depletion process is investigated using a constant aggregation kernel $\beta_{ij} = \beta_c$ and the PSD evolution using both a constant and a sum kernel $\beta_{ij} = \beta_c(v_i + v_j)$ (also termed the *Golovin* kernel [79]). The simulation time varied from a few CPU minutes to 40 CPU hours in the finest cases.

7.1.1. Particle depletion due to aggregation

For the uncoupled PBE with a constant aggregation kernel an equation for the total particle concentration N_c can be retrieved by summing over all the classes of the discrete PBE of Eqn. (4.50), by:

$$\begin{aligned}
\frac{dN_c}{dt} &= \sum_{k=1}^{\infty} \frac{1}{2} \sum_{i+j=k} \beta_c N_i N_j - \sum_{k=1}^{\infty} N_k \sum_{i=1}^{\infty} \beta_c N_i \\
&= \frac{\beta_c}{2} \sum_{k=1}^{\infty} \sum_{i+j=k} N_i N_j - \beta_c N_c^2 \\
&= -\frac{\beta_c}{2} N_c^2. \qquad (7.1)
\end{aligned}$$

and integrating yields:

$$N_c(t) = \frac{N_0}{1 + t^*}, \qquad (7.2)$$

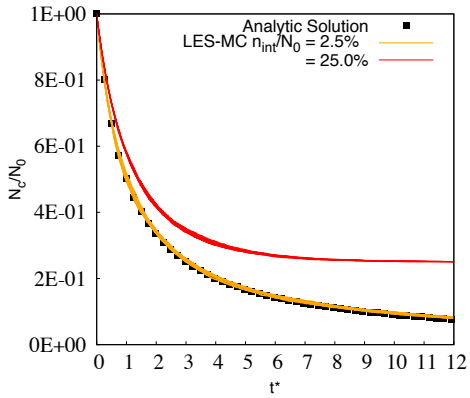


Figure 7.1.: Total particle concentration versus dimensionless time for the same initial particle concentration using $n_0^* = 2.5\%$ and 25%.

where N_0 is the initial particle concentration at $t = 0$ and $t^* = t/\tau'_{aggr}$ is a dimensionless time with $\tau'_{aggr} = 2/(\beta_c N_0)$; note that the prime is used to differentiate from the aggregation residence time of Eqn. (4.75); for the complete derivation refer to Friedlander [63].

Making use of Eqn. (7.1) it is possible to investigate the proposed MC aggregation model with respect to total particle depletion and mass conservation. For every parameter investigated a minimum of $s_{n,tot} \geq 10$ MC runs were carried out to investigate their convergence and performance, where s_n is the MC run number/index. The equivalent errors are calculated for a generic variable ϕ as:

$$\langle |\epsilon_\phi| \rangle_{s_n} = \frac{1}{s_{n,tot}} \sum_{s_n=1}^{s_{n,tot}} \frac{\phi^{analytic} - \phi^{MC,s_n}}{\phi^{analytic}}, \tag{7.3}$$

and are ensemble averaged over the total number of simulation runs $s_{n,tot}$.

For simplicity the dimensionless ratio of initial internal parcel population n_{int} to total particle population $N_0 V_{cell}$ at $t = 0$ can be defined as:

$$n_0^* = \frac{n_{int}|_{t=0}}{N_0 V_{cell}}. \tag{7.4}$$

Figure 7.1 compares the analytic solution of the particle depletion for two cases. In the first case the initial concentration N_0 is represented by parcels with an internal population equivalent to $n_0^* = 2.5$ %, whereas in the second

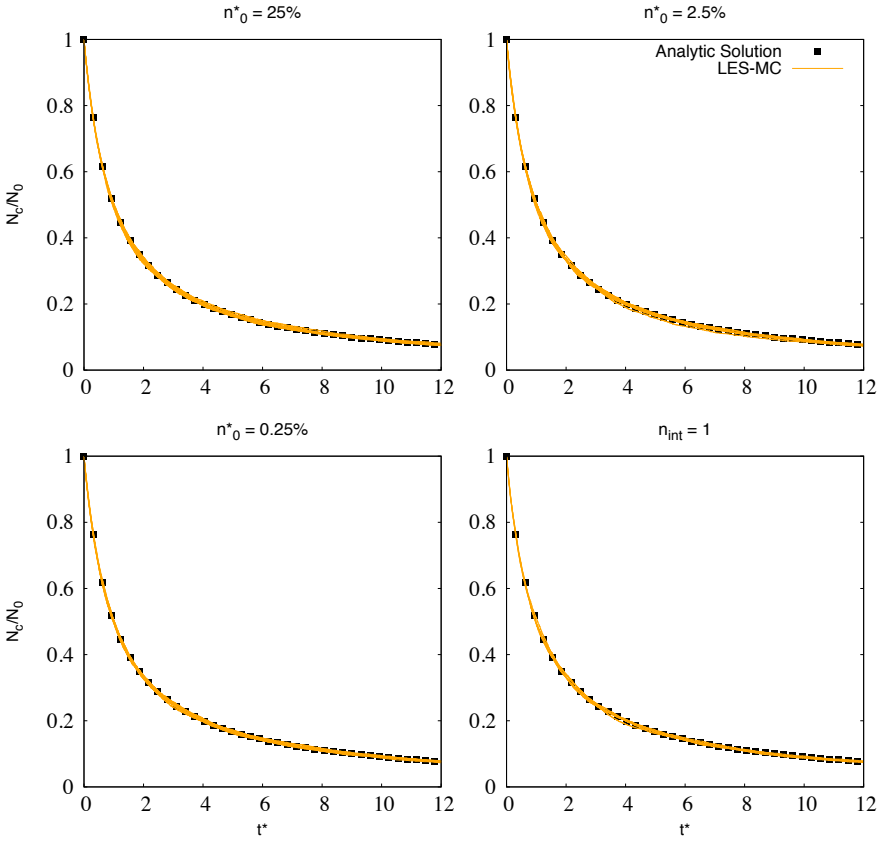
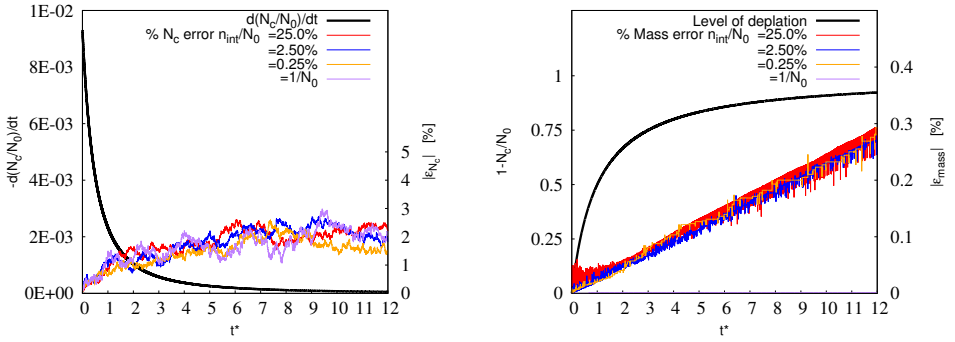


Figure 7.2.: Total particle concentration versus dimensionless time for the same initial particle concentration using $n_0^* = 25\%$, 2.5%, 0.25% and $n_{int} = 1$.

case $n_0^* = 25$ % (e.g. for a total of 1000 particles the first case has parcels with $n_{int} = 25$ and the second has parcels with $n_{int} = 250$). From Fig. 7.1 it is clear that neglecting internal collisions may lead to significant errors in the particle depletion statistics; $\langle|\epsilon_{N_c}|\rangle \sim \mathcal{O}(200\%)$ and $\mathcal{O}(8\%)$ for the $n_0^* = 25$ % and 2.5%, respectively, where $\langle|\epsilon_{N_c}|\rangle$ is calculated using Eqn. (7.3) with $\phi = N_c$.

Figure 7.2 shows the variation of particle concentration including internal collisions for four different initial n_{int}, namely: $n_0^* = 25\%$, 2.5%, 0.25% and $n_{int} = 1$. Good agreement is found with the analytic solution for all four cases. Comparing Figs. 7.1 and 7.2 it becomes clear that internal collisions need to be included, when parcels representing many physical particles are used, in order to capture accurately the depletion statistics. Therefore one



(a) Rate of particle depletion (left). Absolute concentration error (right).

(b) Level of particle depletion (left). Absolute mass error (right).

Figure 7.3.: Error levels for different parcel internal populations n_{int}.

may conclude that the initial parcel internal population does not affect the depletion characteristics when a *constant* aggregation kernel is used[1].

Figures 7.3a and 7.3b show the error in total particle concentration and in total particle mass, respectively. Once the rate of depletion $d(N_c/N_0)/dt$ is very low the steady-state concentration error $\langle|\epsilon_{N_c}|\rangle$ is $0-2\%$ for all initial n_{int} investigated. The mass error $\langle|\epsilon_{mass}|\rangle$ for all cases where $n_{int} > 1$ exhibits a similar monotonic increase with time. However, the absolute error values do not exceed 0.3% and are therefore negligible (especially for open systems with a low aggregation residence time). In the case where $n_{int} = 1$ the error is $\langle|\epsilon_{mass}|\rangle = 0$. Therefore, it can be argued that the mass error stems from the rounding-off errors which appear due to the weighted update of the parcel volumes; see equation (4.80). Rounding-off error accumulation also explains the observed monotonic increase of the percentage mass absolute error.

In the simulations presented thus far a 'medium' temporal discretization has been employed, where the dimensionless time-step $\Delta t^*_{aggr} = \Delta t_{aggr}/\tau'_{aggr}$ is of the order of 10^{-3}. Figure 7.4 presents the variation of particle concentration with time for four different time-steps in the range $10^{-1} - 10^{-5}$ and with $n^*_0 = 1.0\%$. As expected the largest discrepancies between the analytic

[1]Note that a constant kernel suggests that a single parcel could represent the total population of particles. Since at this point the PSD evolution is not considered, it is therefore expected that the mean volume and number concentration characteristics that a single parcel depicts are sufficient to represent the particle depletion process for a constant kernel.

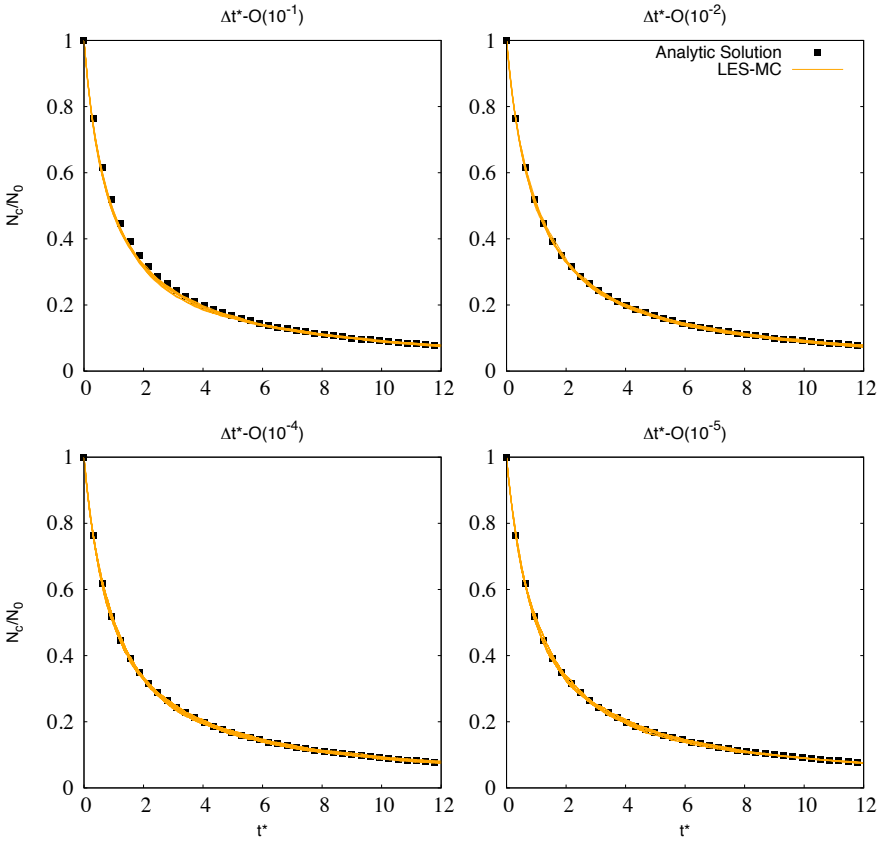


Figure 7.4.: Total particle concentration versus dimensionless time for the same initial particle concentration using $\Delta t^*_{aggr} = 10^{-1}, 10^{-2}, 10^{-4}$, and 10^{-5} and with $n^*_0 = 1.0\%$.

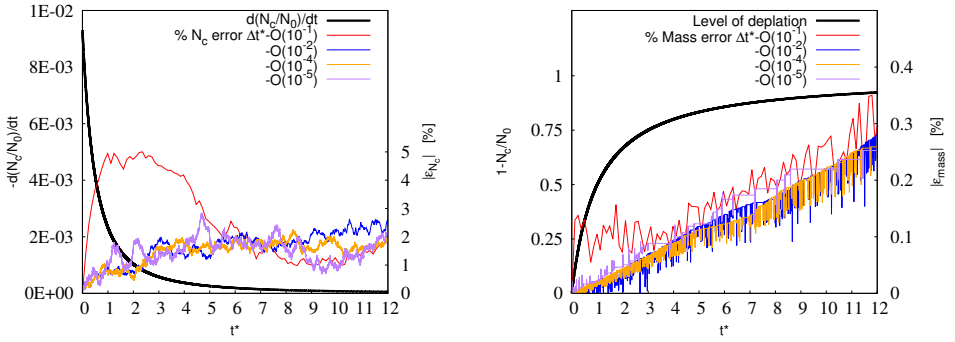
and MC concentrations are for the coarsest temporal discretization, where $\Delta t^*_{aggr} \geq 10^{-1}$.

It is observed that for $\Delta t^*_{aggr} \leq 10^{-2}$ the particle concentration evolving in time is accurately represented by the MC model. Therefore the following stability condition can be used to de-couple the aggregation process:

$$\Delta t < \alpha_{aggr} \tau'_{aggr}, \tag{7.5}$$

where α_{aggr} is a constant with a value of order $\mathcal{O}(10^{-2})$.

Figure 7.5a shows the error in total particle concentration for different aggregation time-steps and with $n^*_0 = 1.0\%$. The error in concentration seems to be fairly unaffected by the temporal discretization for $\Delta t^*_{aggr} \leq$



(a) Rate of particle depletion (left). Absolute concentration error (right).

(b) Level of particle depletion (left). Absolute mass error (right).

Figure 7.5.: Error levels for different temporal discretization.

10^{-2} and it is at the same levels with this of Fig. 7.3a. Therefore, one may suggest that an error of the order of 0-2% in concentration for a particle depletion level of 80% is due to the MC methodology. It is important to note that, as opposed to n_{int}, a coarse temporal discretization (i.e. the equivalent of $\Delta t^*_{aggr} \approx 10^{-1}$) has a pronounced effect on the evolution of the particle concentration. The aggregation rate is overestimated leading to an underestimation of the particle concentration N_c. Aggregation rates are proportional to the square of the particle population present in the reference volume at the beginning of a time-step. When the rate of depletion $|d(N_c/N_0)/dt|$ is high, the collision events reduce the particle population and therefore intermediate time-steps should be used to avoid over-predicted aggregation rates. In theory the temporal discretization should only allow for a single aggregation event to occur in every time-step. Arguably, a more conservative limit for the time-step should be used when the kernels are also a function of the particle volume v.

Figure 7.5b shows the error in total particle mass for different aggregation time-steps and with $n^*_0 = 1.0\%$. For $\Delta t^*_{aggr} \leq 10^{-2}$ the error is at the same levels and shows a similar monotonic increase as the results of Fig. 7.3b. In general, it can be said that the mass errors are at negligible levels for both temporal and parcel internal particle number discretization.

7.1.2. Evolution of the Particle Size Distribution

The model thus far has exhibited good agreement with mean population values and with small dependence on the choice of initial n_{int} and Δt^*_{aggr}. However, it is important to investigate the effect of the aforementioned parameters with respect to the evolution of a full PSD. To this end, analytic solutions for the temporal evolution of the PSD of an aggregating population of particles are used. The initial PSD is exponential and reads:

$$\mathcal{N}(v)|_{t=0} = \frac{N_0}{v_0}\exp(v/v_0), \tag{7.6}$$

where v_0 is the initial count mean particle volume.

In MC simulations the level of statistical error is proportional to the number of samples and therefore the error scales with $1/\sqrt{s_n/n_{int}}$. To enable a comparison between different n_{int}, the initial particle population is constant and equal to: $N_0 V_{cell} = 1000$. For every n_{int}-case investigated, the simulation is repeated 450 times until the total number of initialized *real* particles is equal to $4.5 \cdot 10^5$, i.e. $s_{n,tot} = 4.5 \cdot 10^5/(N_0 V_{cell})$ (note that the number of total parcels/samples initialized decreases with n_{int}, i.e. a total of $0.018 \cdot 10^5$, $0.18 \cdot 10^5$, $1.8 \cdot 10^5$ and $4.5 \cdot 10^5$ parcels are initialized for the $n_0^* =$ 25%, 2.5%, 0.25% and $n_{int} = 1$ cases, respectively). The resulting PSDs from a given n_{int} case are constructed from the cumulative (total) number of parcels present at the prescribed time-instances after every simulation s_n. This cumulative sampling can be considered representative of the PSD of s_n cells used to discretize a domain with a given initial particle concentration N_0 and particle size distribution $\mathcal{N}(v, 0)$.

To quantify the level of error the resulting cumulative Sauter Mean Diameter (SMD) is calculated after every simulation s_n. The SMD (or d_{32}) is defined as:

$$d_{32} = \frac{\sum_{k=1}^{\infty} \mathcal{N}(v_k) v_k}{\sum_{k=1}^{\infty} \mathcal{N}(v_k) v_k^{2/3}}, \tag{7.7}$$

and it represents a higher-order moment ratio with the dimensions of particle diameter.

7.1.2.1. Constant kernel $\beta_{ij} = \beta_c$

Scott [220] derived analytically the equation for the evolution of Eqn. (7.6) as a function of time for a constant aggregation kernel β_c, viz:

$$\mathcal{N}(v,t) = \frac{4N_0}{v_0(\beta_c N_0 t + 2)^2} \exp\left[\frac{-2v}{v_0(\beta_c N_0 t + 2)}\right]. \tag{7.8}$$

For simplicity an initial concentration N_0, initial particle mean volume v_0, and aggregation kernel β_c equal to 1 are used.

As in the work of Rigopoulos and Jones [205], the PSD is evolved in time for 10 and 20 seconds ($t^* = 5$, 10). These residence times are equivalent to a depletion level of 82% and 90%, respectively, of the initial concentration N_0. The time discretization is fixed to $\Delta t^*_{aggr} = 10^{-4}$ and the initial parcel concentration n_{int} is varied.

Figure 7.6 presents the PSD at $t = 0, 10$ and 20s for four choices of initial parcel internal population, namely: $n^*_0 = 25\%$, 2.5%, 0.25% and $n_{int} = 1$ (i.e. the number of initial parcels is 4, 40, 400, and 1000, respectively, for every simulation run s_n). From an order of magnitude perspective the model performs very well for all the choices of initial n_{int}. For $n^*_0 \leq 0.25\%$ the initial PSD at $t = 10$ and 20 s agree very well with the analytic equivalent. For larger internal parcel populations ($n^*_0 = 2.5\%$ and 25%) the discrepancies become evident.

The source of this discrepancy is twofold. Firstly, there is an intrinsic error in the solution of the aggregation integral, but most importantly for the discretization of the PSD at $t = 0$. As noted, this error relates to the total number of samples (i.e. parcels) used to discretize the size distribution of the initialized real particle population. In the case of Fig. 7.6, where each parcel represents 25% of the concentration N_0, the 'linear' sets of points at $t = 0$ represent exactly the aforementioned error. Every volume in the range of $v/v_0 = 6 \rightarrow 10$ is, for example, represented by a single parcel. When the initial PSD is not captured perfectly the errors will propagate to the subsequent distributions as the aggregation of particles proceeds.

The second source of error is due to the methodology employed for the aggregation process. It can be seen that both types of errors are eliminated as $n_{int} \rightarrow 1$, therefore it is arguably difficult to evaluate the relative effect of the methodology error while excluding the discretization error. For the

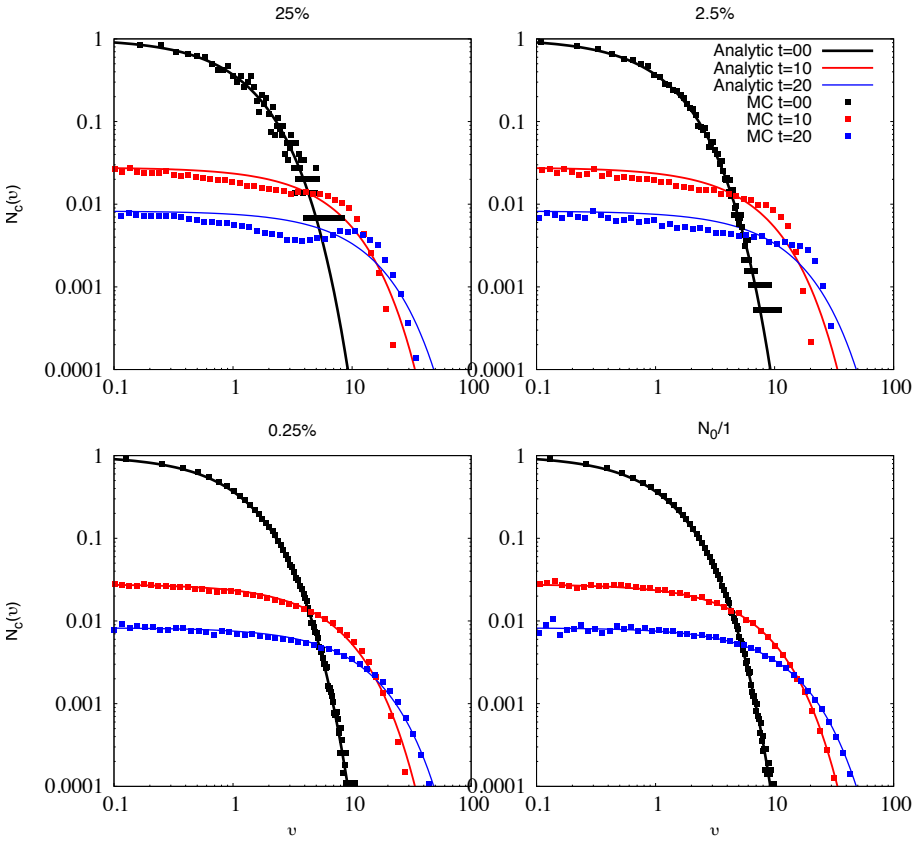


Figure 7.6.: Evolution of the PSD for an initial exponential distribution for $n_0^* = 25\%$, 2.5%, 0.25% and $n_{int} = 1$.

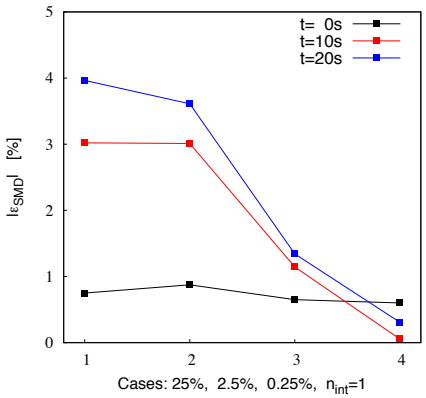


Figure 7.7.: Relative error in the SMD for three residence times t =0, 10, and 20s for different cases of initial parcel internal population.

cases where $n_0^* = 25\%$ and 2.5% it seams that there exists a spline-type trend centered at, approximately, $\upsilon = 5$ and $\upsilon = 10$ after 10 and 20s, respectively. For lower than the aforementioned volumes the densities are underestimated whereas the densities of larger volumes are overestimated. This spline-type structure can be an outcome of the joint effect of the directionality and averaging of the present multi-collision model.

Figure 7.7 summarizes the percentage absolute error in the simulated SMD for the various initial n_{int} and aggregation residence times. In all of the cases the SMD of the initial PSD converges to less than 1% of the analytic equivalent. At aggregation residence times of t =10 and 20s, the coarsest cases where $n_0^* \geq 2.5\%$ exhibit an error which does not exceed $|\epsilon_{SMD}| \approx 4\%$. In the finer cases ($n_0^* = 0.25\%$ and $n_{int} = 1$) the errors are $|\epsilon_{SMD}| \leq 1.3\%$.

Finally, from the analysis of Figs. 7.6 and 7.7, one can conclude that with a choice of $n_0^* \sim \mathcal{O}(10^{-1}\%)$ the aggregation model reproduces with high accuracy the analytic solution for the PSD evolving with a constant kernel. For $n_0^* = 25\%$ the evolution of the mean particle concentration and SMD are captured with an error of less than 2.5% and 4.5%, respectively.

7.1.2.2. Golovin kernel $\beta_{ij} = \beta_c(v_i + v_j)$.

The Golovin (sum) kernel $\beta_{ij} = \beta_c(v_i+v_j)$ is proportional to the interacting particle volumes. Golovin [79] derived an analytic solution for an initial particle population with exponentially-distributed volumes; see Eqn. (7.6). The temporal evolution of the PSD with the aforementioned initial condition reads:

$$\mathcal{N}(v,t) = \frac{(1-\theta)\exp\left[-\frac{v}{v_0}(\theta+1)\right]}{\frac{v}{v_0}\theta^{1/2}}\ \mathrm{I}_1\left(2\frac{v}{v_0}\theta^{1/2}\right), \tag{7.9}$$

where $\theta = 1-\exp(-\beta_c N_0 v_0 t)$ and I_1 is the first order Bessel-I function [220].

An initial concentration N_0, an initial particle mean volume v_0, and a constant β_c equal to 1 are used, as in the case of the constant kernel. The PSD is evolved in time for 0.5 and 2.0 s (as in the work of Rigopoulos and Jones [205]), which are respectively equivalent to a 40% and an 86% level of initial particle depletion. The temporal discretization is fixed to a normalized time-step of $\Delta t^*_{aggr} = 10^{-6}$ (based on $(v_i + v_j) = 1$), which was found sufficient to uncouple the aggregation process following a similar investigation to the constant kernel. As opposed to the constant kernel, a higher number s_n of MC simulations were run such that the initial PSD ($t = 0$) is captured within $|\epsilon_{SMD}| \leq 0.5\%$. This approach was followed to try and minimize the errors produced by a decreased resolution of the initial distribution in order to isolate the aggregation model performance.

Figure 7.8 shows the PSD produced using the Golovin kernel for three residence times ($t = 0,\ 0.5$ and 2 s) and for four cases of initial parcel internal population ($n^*_0 = 25\%$, 2.5%, 0.25% and $n_{int} = 1$). The results agree very well with the analytic solution. The case where $n^*_0 = 25\%$ produces accurately the initial distribution and the evolved PSD at $t = 0.5$ s. At $t = 2$ s it is noticeable that smaller particles are slightly over-estimated compared to those with volumes in the range of $v/v_0 = 1 - 10$, which are under-estimated. For the smaller n^*_0 cases the model captures with high accuracy the analytic PSD at all times t.

When compared to the results from the constant kernel (Fig. 7.6), one may observe that the resolution of the initial particle distribution at $t = 0$ s is very important as it sets the boundary condition for the evolution of the PSD. In addition, in the case of the constant kernel, small particles aggregate with the same kernel-value as larger particles, and due to their

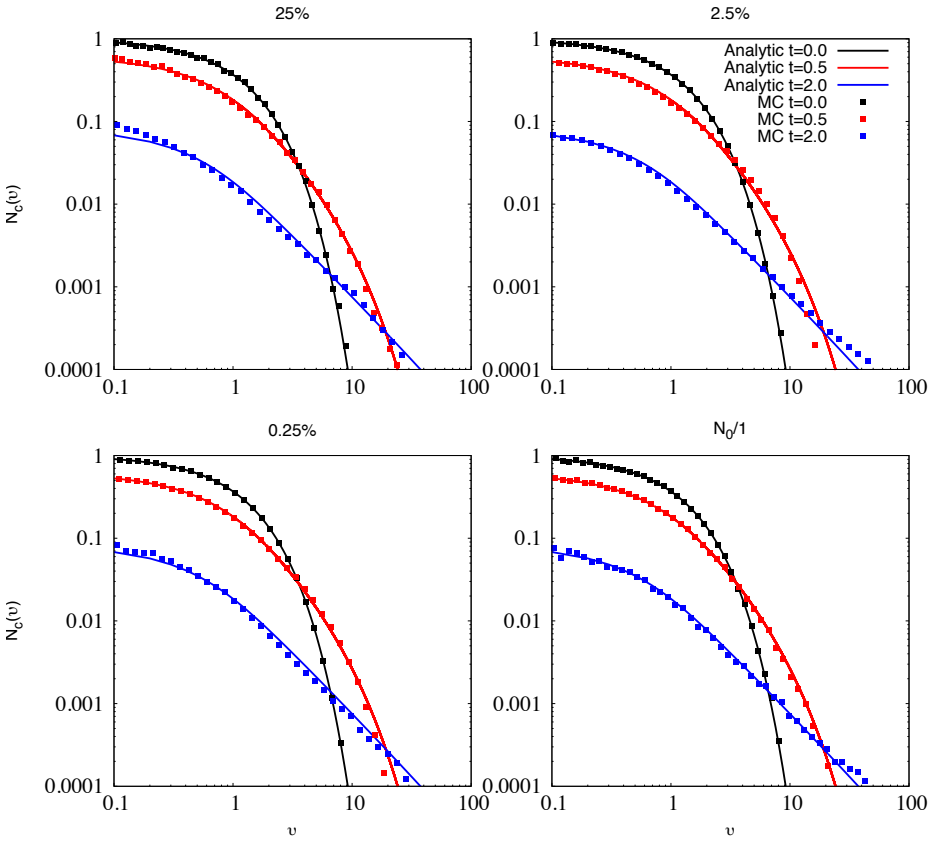


Figure 7.8.: Evolution of the PSD with the Golovin kernel for an initial exponential distribution and $n_0^* V_{cell} = 25\%$, 2.5%, 0.25% and $n_{int} = 1$.

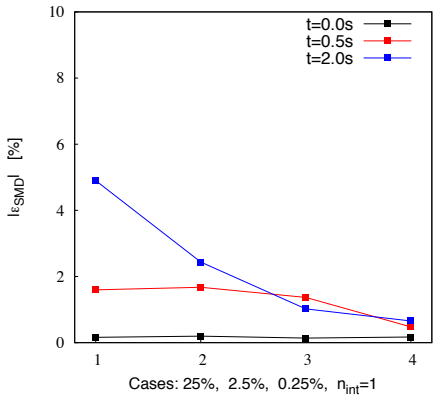


Figure 7.9.: Relative error in the SMD for three residence times t =0, 0.5, 2s for different cases of initial parcel internal population.

higher concentration smaller particles aggregate with a higher probability than larger ones. This leads to a more uniform distribution (depletion) of sizes in the range of $\upsilon/\upsilon_0 < 10$ after the allowed residence times. On the other hand, the Golovin kernel has a more complex effect as its proportionality to υ suggests that larger particles have higher kernel values. However, larger particles have smaller concentrations due to the initial exponentially distributed PSD. The combined effect leads to a less uniform decay of populations. In fact the smallest class, where $\upsilon = 0.1$, has a density of 0.07 after an 86% level of total particle depletion, whereas the density from the constant kernel after an 82% depletion level is 0.03. Therefore, in the Golovin kernel there is an intrinsic directionality in the aggregation process where smaller particles tend to aggregate more with larger particles rather than with particles of similar volumes. Therefore, it can be argued that the directionality of the aggregation model of this work captures better the Golovin kernel. Moreover, this can be the reason for which the spline-type structure in the coarse $n_0^* = 25\%$ and 2.5% is not seen in the PSDs evolved using the Golovin kernel.

Figure 7.9 shows the resulting errors in the SMD calculated using Eqn. (7.7) after s_n simulations for each of the cases considered (n_0^* =25%, 2.5%, 0.25% and $n_{int} = 1$, numbered one to four, respectively). As mentioned the error in the initial PSD is $|\epsilon_{SMD}| \leq 0.3\%$ for all cases. For a residence time of $t = 0.5$ s the SMD is captured within an error of $|\epsilon_{SMD}| < 2\%$. For a

residence time of $t = 2.0$ s the SMD is predicted within $|\epsilon_{SMD}| < 1\%$ for the two fine cases. The coarser cases have approximately the same level of error after $t = 0.5$ s as only a small amount of the initial particle population has been depleted. For a longer residence time ($t = 2.0$ s) the error in the SMD increases for the coarsest cases. However, even for the coarsest case where n_0^* =25%, the model predicts accurately the shape of the PSD as seen in Fig. 7.8 with a relatively small error.

From the previous analysis it can be concluded that the model performs very well when compared to the analytic solutions of the two kernels examined. The level of error is directly related to the level of resolution of the initial population. The model in fact performs better with the assumption of a Golovin (sum) kernel, possibly due to the model's directionality assumption and the intrinsic directionality of the Goloving aggregation process. An initial internal parcel population of $n_0^* \approx 0.25\%$ is sufficient to accurately capture the evolution of the PSD even after high levels of depletion for both a constant and the Golobvin kernel. The accuracy can further increase by appropriately discretizing the PSD, i.e. by setting a limit for the maximum n_{int} of a given size class v as a function of its population density $\mathcal{N}(v)$ as this of Eqn. (4.72). In the following sections the aggregation process and the model performance are investigated in flow-coupled conditions.

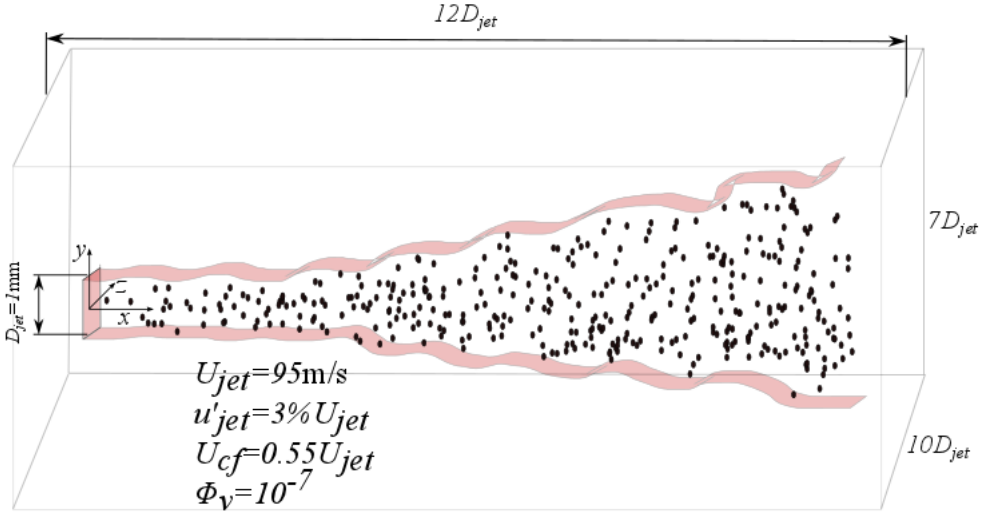


Figure 7.10.: Configuration of nanoparticle-laden planar jet..

7.2. Nanoparticle aggregation in a planar jet

The aggregation model developed is hereby investigated in a nanoparticle-laden planar jet. As a benchmark for comparison purposes, the DNS test case of Miller and Garrick [155] is used. The planar jet of the aforementioned case is two-dimensional and therefore it cannot be considered turbulent. However, the structure of the fluid motion and the particle dispersion characteristics can be correlated to the aggregation process. Miller and Garrick [155] limit their investigation solely to aggregation, which they model using a sectional methodology for the solution of the PBE evolution (see section4.4.3). Therefore, a comparison with the MC aggregation model employed in this work can be easily established.

7.2.1. Configuration and Modelling Parameters

Miller and Garrick [155] performed a DNS of a coagulating aerosol in a two-dimensional, incompressible, and isothermal (T = 300 K) planar jet. Their aim was to investigate the underlying structure of vapor-phase particle growth processes. Figure 7.10 is a sketch of the simulated domain; note that the two-dimensional (x, y) DNS of Miller and Garrick has been extended to a third dimension (x, y, z). The same boundary conditions as in the DNS have been used in the x, y- and periodically extended to the z-dimension.

The diameter of the jet is $D_{jet} = 1$ mm. The velocity distribution is uniform throughout the height of the jet and equal to $U_{jet} = 95$ m/s. The co-flow velocity is $U_{cf} = 0.55U_{jet}$. The resulting Reynolds number based on the jet diameter and velocity is $Re = 4000$, which arguably cannot be considered very turbulent. However, random perturbations of 3% of U_{jet} are added in the cross-stream y-direction to accelerate the length-scale development of large scale vortical structures. The LES domain extends from zero to $12D_{jet}$ and $7D_{jet}$ in the x and y directions, respectively, as in the DNS. The aforementioned inlet conditions are periodically repeated in the z-direction. To reduce the effects of the increased dimensionality of the present LES, the total width of the domain (z-direction) was chosen to be $10D_{jet}$. However, it must be noted that the increased dimensionality may reduce the scales of the vortical structures of the (x, y)-plane as energy is transferred to all three directions. A grid spacing of $\Delta = 0.1$ mm was found sufficient to represent the evolution of the uniform phase ($D_{jet}/\Delta = 10$).

As in the work of Miller and Garrick [155], mono-disperse particles of $d_p = 1$ nm are seeded with a volume fraction of $\phi_v^0 = 10^{-7}$ at the jet inlet. In the LES particles are seeded in a narrow band of width $w_{pin} = D_{jet}/2$ centered at $(x, y, z) = (0, 0, 0)$; depicted by the red region in Fig. 7.10. The particles were restricted to a planar motion (i.e. in the (x, y) plane, given an initial $z \in [-w_{pin}/2 \rightarrow w_{pin}/2]$) by setting their z-directional velocity to zero. For the range of particle diameters and air temperature of the test case the Knudsen number is $Kn >> 1$. Therefore, the free-molecular Brownian aggregation kernel is used; see Eqn. (4.56). Miller and Garrick [155] used a sectional method to approximate the PBE evolution using 10 bins of variable width for particle diameters ranging from 1 to 8 nm. They solved each of the 10 discrete PBE equations; particle inertial effects and consequently particle slip was ignored. Spherical droplets and instantaneous coagulation are assumed. Keeping the latter two assumptions and using the same aggregation kernel, the multi-collision MC method presented in this work is compared to the equivalent results from the DNS.

The condition of equation (4.72) was not used to restrict the number of real particles per parcel (as the initial PSD is mono-disperse) and $V_{rel} = V_{cell}$ was consequently set in Eqn. (4.75) for the calculation of τ_{aggr}. Therefore n_0^* is constant for all parcels entering the domain and equal to 0.2% of the total population of real particles present in the simulation assuming no

aggregation[2]. The LES time-step is $\Delta t \sim \mathcal{O}(10^{-8})$ and a constant $CFL = 0.3$ is used. The time τ'_{aggr} for a cell at the inflow of the simulation is $\tau'_{aggr} \sim \mathcal{O}(10^{-5})$ evaluated using an inlet initial concentration of $N_0 \sim \mathcal{O}(10^{20})$ [#/m^3] and a kernel of $\beta_{ij} \sim \mathcal{O}(10^{-15})$ [m^3/#s]. The limit of Eqn. (7.5) is therefore met; however, a more conservative value of the LES time-step is used as the particle concentration is expected to fluctuate and the kernel will also increase in magnitude as the particles grow in size.

For the purpose of the latter investigation, an aggregation Damkohler number $D^*_{A,aggr}$ is defined as the ratio of a flow time-scale to an aggregation time-scale, similarly to the work of Garrick *et al.* [68], viz:

$$D^*_{A,aggr} = \frac{D_{jet}}{U_{jet}} \frac{\phi^0_\upsilon}{\upsilon_0} \beta_{11}, \tag{7.10}$$

where ϕ^0_υ is the volume fraction of the disperse to continuous phase at the inlet, and υ_0 the initial volume of the particles. The kernel β_{11} is evaluated from the Brownian free-molecular regime equation (4.56), for particles at the inlet with $\upsilon = \upsilon_0$. By varying the density of the solid phase, a range of Damkohler numbers $D^*_{A,aggr} = 0.4 - 18$ can be obtained.

Mean particle diameters are compared with those from the DNS for the equivalent $D^*_{A,aggr}$. The mean statistics of a given Eulerian cell are calculated from the ensemble average over all particles that passed through the equivalent cell during the simulation. The PSD is constructed from the cumulative histogram of all particles passing from the prescribed PSD location. For each axial position the PSD is measured at the centerline and at a distance $y_{0.8}$, where $y_{0.8}$ is the position where the velocity of the flow $U_f(y)$ is $0.8 * (U_f(y) - U_{cf})/(U_c - U_{cf})$ and U_c is the centerline velocity [3]. Each simulation ran for 1800 CPU hours; approximately 1% of the computational time required for the DNS of Miller and Garrick [155].

7.2.2. Results

Figure 7.11 shows the radial distributions of the continuous phase velocity at four axial locations. The results from the LES agree very well with those

[2] In other words the aggregation model was deactivated and the mean number of particles present in the domain at any instant of the simulation was calculated giving $n^*_0 = n_{int}/N_{tot}$.

[3] Similarly to the definition of the mixing layer thickness; see Eqn. (5.7).

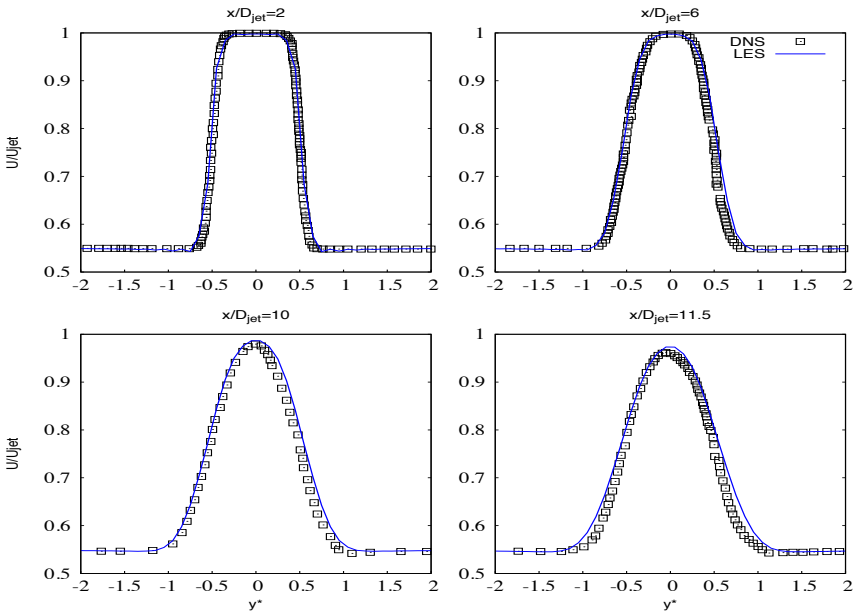


Figure 7.11.: Continuous phase radial velocity-profiles at four axial locations: $x/D_{jet} = 2, 6, 10$ and 11.5.

from the DNS.

Figure 7.12 compares the results for the particle diameters from the LES and DNS at three axial locations, namely $x/D_{jet} = 2, 6$ and 10. No information regarding the density of the aggregating phase particles ρ_p is provided in the work of Miller and Garrick [155]. The Damkohler number was therefore varied to match the mean diameter observed in the DNS at $x/D_{jet} = 2$ resulting to a $D^*_{A,aggr} = 10$. The mean diameter radial distributions at the remaining axial locations agree well with the results from the DNS.

Particles tend to have larger diameters near the shear layer of the Planar jet; see Fig. 7.12. Preferential dispersion can be considered negligible because the particles are very small and react similarly to changes of the flow-field. In addition, the particle concentration level near the shear layers is reduced as the flow is diluted from the particle-free co-flow stream. Therefore, one may assume that the particles near the shear layer have larger mean diameters primarily due to longer flow residence times. The jet decelerates due to the momentum losses to the co-flow slow stream; consequently, the time for which particles can collide increases. Particles expelled at the shear-

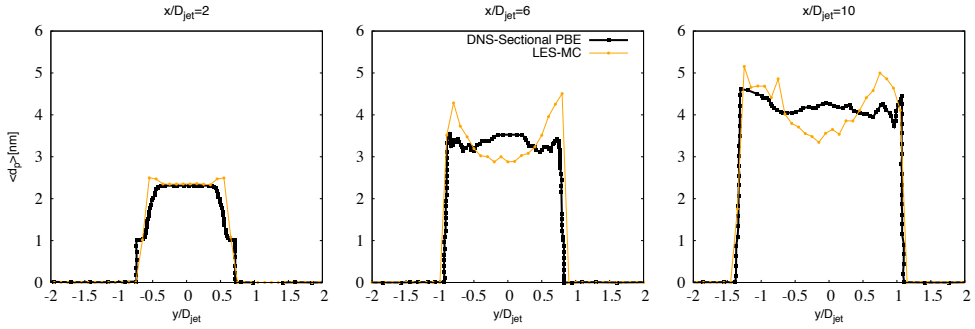


Figure 7.12.: Ensemble average particle diameter compared with the results from the DNS of Miller and Garrick [155] at four axial locations: $x/D_{jet} = 2, 6$ and 10.

layer region therefore undergo more sequential collisions leading to larger sizes. Near the centerline more collisions are present (in absolute numbers) as the particle concentration is higher, however the increased population of particles renders a smaller probability for a given particle to re-collide. Such results also agree with other studies [35, 94, 155, 164, 263, 267].

There is a greater difference between the diameters observed at the centerline and shear layers in the results from the LES compared to those from the DNS. Such a discrepancy can be attributed to the different methodologies used, namely: the Lagrangian MC and Eulerian sectional PBE method. The sectional method includes an intrinsic averaging of diameters in order for the equivalent particles to be accommodated in one of the classes (bins) of the discrete PBE. Moreover, Miller and Garrick [155] used 10 bins with a maximum particle diameter of 8 nm assuming that bigger particles will not form. In addition, their results present temporally averaged diameters, therefore introducing an intrinsic dependance on the presence of particles at the shear-layer. In other words, depending on the sampling rate, a particle might be present or not at the shear layer, in the latter case a bias towards smaller diameters is created once averaging.

As mentioned the initial distribution at $x/D_{jet} = 0$ is mono-disperse and all particles have $d_p = 1$ nm. Figure 7.13 compares the PSD at the jet-core ($y \leq y_{0.8}$) with this at the shear layer ($y > y_{0.8}$) at three axial locations, namely: $x/D_{jet} = 2, 6$ and 10. Note that the PSD has been normalized to the local levels of particle population to allow for a direct comparison between the different positions, hence representing a pdf of particle sizes.

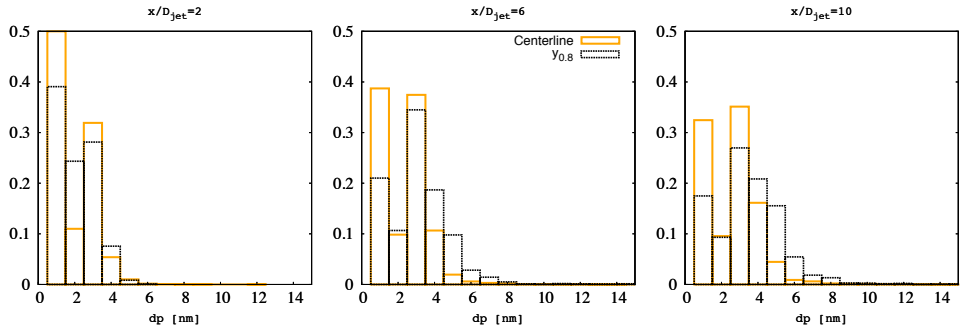


Figure 7.13.: Pdf of particle sizes at the centerline compared to this at the shear layers at three axial locations.

At the centerline of the jet, the distribution develops a bi-modal shape with a second mode at $d_p \approx 3$ nm.

It is important to note that the development of a second mode cannot be seen in the mean particle diameters of Fig. 7.12, stressing the importance of retrieving the complete PSD as opposed to the first moment. From the mean diameters of Fig. 7.12, one may draw the conclusion that all particles tend to have aggregated at least once by the time they reach $x/D_{jet} = 2$. However, from Fig. 7.13 it is noticable that the mean diameter at $x/D_{jet} = 2$ of $d_p \approx 2$ is an outcome of the averaging of the two aforementioned modes. Therefore, particles that aggregated once ($d_p = 2$) are more likely to aggregate a second time before reaching $x/D_{jet} = 2$; a result which is expected by the dependance of β_{ij} with d_p. In fact, the population density of $d_p = 2$ nm particles is smaller than this of $d_p = 3$ nm.

At locations farther downstream the population of 1 nm particles is further reduced and the distribution of particle sizes near the centerline broadens. The second mode of $d_p = 3$ nm observed at $x/D_{jet} = 2$ persists downstream. The particles that did not participate in the aggregation process are the main contributors to subsequent particle growth as the population of the 1 nm class reduces downstream. Notice that near the centerline the population of particles with $d_p \approx 8$ nm is indeed negligible. However, when examining the distribution near the jet shear layer (i.e. for $y > y_{0.8}$), the range of diameters may reach a maximum of $d_p = 14$ nm. Such diameters are not accurately captured in the sectional PBE method as the greatest bin represents the population of particles with $d_p = 8$ nm. Comparing the PSD at the centerline to the one at the shear layer one may conclude that,

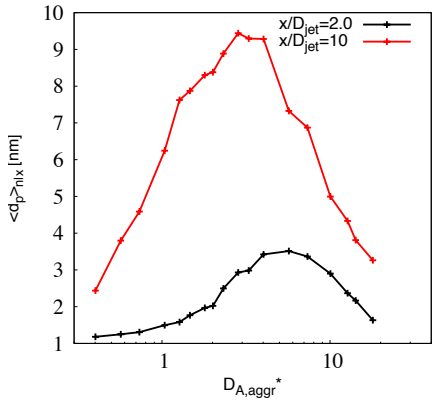


Figure 7.14.: Ensemble average particle diameter at two axial locations for the range of $D^*_{A,aggr}$ investigated.

assuming negligible preferential dispersion, the longer residence time is the main parameter promoting the increased size of particle aggregates.

Figure 7.14 depicts the variation of the mean particle diameter variation with $D^*_{A,aggr}$ at two axial locations: $x/D_{jet} = 2$ and 10. The diameters shown are constructed from the ensemble average of all particles passing from the (y, z)-plane at the prescribed axial locations, i.e. $\langle d_p \rangle_{n|x}$, where the conditionality $n|x$ refers to the number of particles n that passed from a given location x.

For the same flow conditions, particle volume fraction, and initial $d_p = 1$ nm, the variation of the Damkohler number has a prominent and non-linear effect on the aggregation process. The results presented thus far are for a $D^*_{A,aggr} \approx 10$. Further reduction of the Damkohler number initially increases the mean diameters and then reduces them. This is observed at both locations $x/D_{jet} = 2$ and 10. Note that there exists a relative shift of the observed peak diameter versus $D^*_{A,aggr}$. At $x/D_{jet} = 2$ the peak diameter is for a $D^*_{A,aggr} \approx 5$, whereas at the other location the peak is observed at $1/D^*_{A,aggr} \approx 3$.

A reduced Damkohler number suggests a reduced aggregation rate (assuming constant flow conditions, volume fraction, and v_0). However, the number of aggregation events depends linearly on the kernel β_{ij} and with the second power of local concentration levels $\sim (N_c/2)^2$. A reduced aggregation kernel suggests that –in total– less particles will collide at upstream locations (i.e. $x/D_{jet} < 2$ and $x/D_{jet} < 10$ in the first and second mean

diameter measurements, respectively); nonetheless, fewer particles are depleted. The balance between reduced population-depletion upstream and longer residence times downstream, may be the primary reason for the observed non-linear behavior in Fig. 7.14. In other words, there is a limiting behavior in the balance between reduced aggregation rate (low $D^*_{A,aggr}$) followed by a higher particle population (due to less aggregation upstream) and longer residence time downstream (due to the deceleration of the jet), and a high aggregation rate (high $D^*_{A,aggr}$) followed by a lower concentration of particles at the regions of the flow with longer residence times. As expected, a further reduction of the aggregation rate ($D^*_{A,aggr} < 2.5$) results in smaller mean diameters at both axial locations.

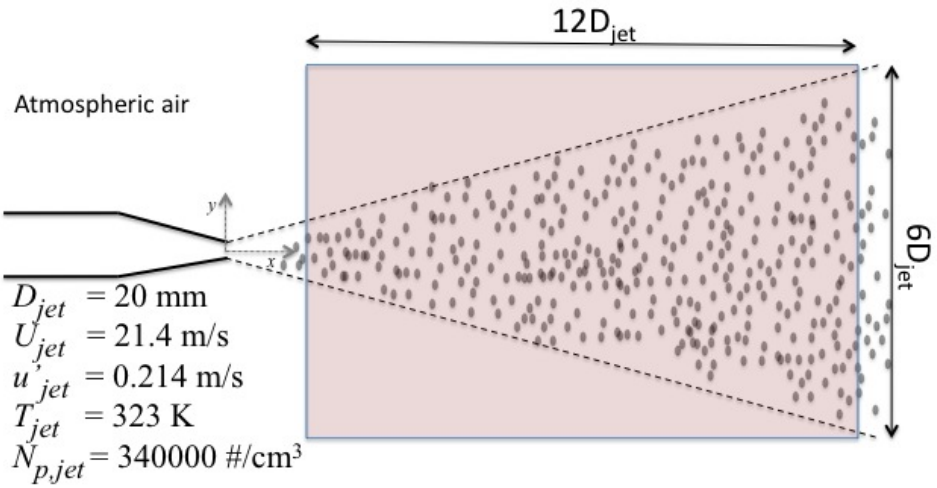


Figure 7.15.: Experimental configuration of Zhu *et al.* [277] and simulated domain.

7.3. SiO_2 aggregation in a turbulent round jet

The aggregation process is hereby investigated in a nanoparticle-laden turbulent round jet. For the purpose of this investigation the recent test case of Zhu *et al.* [277] is studied. In their study, a Silicon Dioxide (SiO_2)-laden jet diffuses into atmospheric air. Their test case addresses solely the aggregation and dispersion of the Silica nanoparticles as other particle processes are not present. This allows for a direct comparison of the experimental and modelled PSD evolution. To the author's knowledge, the test case of Zhu *et al.* [277] has not been investigated computationally by other researchers.

7.3.1. Experimental Configuration and Modelling Parameters

Zhu *et al.* [277] designed an experimental configuration to measure nanoparticle aggregation in a turbulent round jet with particular emphasis on the near field of the jet.

A Nitrogen jet carrying droplets of an aqueous-SiO_2 solution was issued in an evaporator using an air-blast atomizer. In the evaporator the droplets mixed with heated air at 323K. The solvent evaporated and the dried nanoparticles were distributed homogeneously within the heated air. The SiO_2-laden air was subsequently passed through a rectifier unit and

injected via a converging nozzle with a diameter of $D_{jet} = 20$ mm to the lab environment (at atmospheric conditions). Figure 7.15 is a sketch of the final conditioning stages (rectifier, and converging nozzle), the developing jet initial conditions, and the simulation domain.

The jet was turbulent and subsonic with a bulk velocity of $U_{jet} = 21.4$ m/s and a turbulent intensity of $u'_{jet}/U_{jet} = 1\%$. The temperature at the nozzle outlet was $T_{jet} = 323$ K. The Reynolds number based on the jet diameter and jet bulk velocity was $Re = 23516$. Measurements of the velocity and turbulent intensity radial profiles were taken at $x/D_{jet} = 0, 2, 4, 6$ and 8 using tracer particles of 1.4 μm diameter and a Laser Doppler Anemometry (LDA) system.

The PSD and particle concentration were measured using a Scanning Mobility Particle Sizer (SMPS) which consisted of a TSI classifier a long Differential Mobility Analyzer (DMA) and a Condensation Particle Counter (see Chapter 6). The DMA was used to classify the particle sizes and the CPC to count them. The SMPS had a sampling flow rate of $5 \cdot 10^{-6} \mathrm{m}^3/\mathrm{s}$ and a sheath flow-rate of $8.3 \cdot 10^{-7} \mathrm{m}^3/\mathrm{s}$. A scanning residence time of 135 s was allowed for every sample. The nanoparticle concentration at the jet outlet was nearly uniform and equal to $N_{0,jet} = 340000\#/\mathrm{cm}^3$. The diameter-based PSD at the jet exit showed little deviations in the radial direction and had a range of $d_p = 12 - 700$ nm with a SMD of $d_{32} \approx 250$ nm and a mode at approximately 100 nm. Measurements of the particle concentration and PSD were taken at $x/D_{jet} = 0, 2, 4, 6, 8, 10, 14$ and 18 for various radial positions y. The most pronounced discrepancies in the measured PSD were found in the region of $x/D_{jet} = 6 - 10$. Moreover, the measured radial PSDs at $x/D_{jet} = 2$ show a possibly significant preferential dispersion of the particles issued from the jet. Near the shear layer of the developed jet at $x/D_{jet} = 2$, the PSD exhibits a very narrow range with a SMD smaller than this at the nozzle outlet.

A domain that ranged axially from $x/D_{jet} = 2$ to $x/D_{jet} = 12$, radially from $y/D_{jet} = -3$ to $y/D_{jet} = 3$ and $z/D_{jet} = -3$ to $z/D_{jet} = 3$ was used, as shown in Fig. 7.15. A grid-spacing of $\Delta = 1$ mm was used to solve the gaseous phase ($D_{jet}/\Delta = 20$; from previous experience, see chapters 6 and 7.2.1, this resolution was considered adequate). The mean velocity profile at the inlet of the simulation was directly read from the experimental measurements. The inflow turbulence was generated (as outlined in Appendix

A) with a prescribed intensity equal to this of the experimental measurements at $x/D_{jet} = 2$ and an integral length scale of $l_I/\Delta = 2.2$, where Δ is the grid spacing. The Smagorinsky model with $C_s = 0.1$ was used to close the unknown sub grid-scale stresses of the LES momentum equation and accurately captured the evolution of the continuous phase velocity field.

The particles were injected at every time-step in bands. Each band had a different seeding rate and diameter distribution in order to match the equivalent experimental concentrations and PSDs. For each seeding band the CDF for the particle radial location and diameter was generated at the beginning of the simulation and stored for efficient use. For every parcel injected, two random numbers $0 \leq Rn \leq 1$ were sampled from a uniform distribution, each random number was inversely mapped to the equivalent CDF of the radial position and the particle diameter.

The condition (4.72) increased significantly the computational cost for SiO_2 nanoparticles (when $Sc \sim \mathcal{O}[10^2]$ the Batchelor scale is $l_B << \eta_k$). Because the condition (4.72) was too restrictive, Eqn. (4.72) was evaluated for η_k in order to initialize the parcels in the simulation and the volume V_{rel} was consequently taken to be equal to this of a cell Δ^3. A lower- and upper-limit of $n_{int} = 10$ and 100 was set, respectively, which resulted in a parcel to particle resolution of $n_{int}/(N_{domain}V_{domain}) = 10^{-9}$. The mean parcel to particle resolution was estimated from the ratio of the steady-state total parcel-to-real particle population present in the domain when no aggregation was used in the simulation. A very high resolution was chosen to enable the detection of small variations in the evolution of the PSD, and to mitigate the errors that would arise if the initial PSD was under-resolved (see section 7.1).

7.3.1.1. Aggregation modelling assumptions:

The particles are in the nano-scale and $Kn \sim 1$. Therefore, the Brownian aggregation kernel was used. Immediate coalescence and spherical aggregates were assumed. Theses assumptions have to be considered with caution as aggregate morphology, coalescence, and sintering may significantly influence the aggregation process [47]. Spherical particles have a smaller surface area compared to aggregates with fractal shapes and the aggregation rate may be hence underestimated (since the collision probability is proportional to the

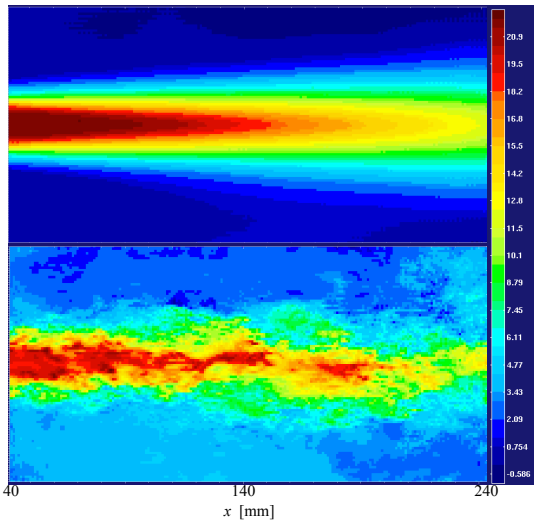


Figure 7.16.: Contour plot of temporal average (top) and instantaneous (bottom) filtered axial-velocity of the continuous phase.

area of the colliding particles). However, Ibaseta and Biscans [90] showed that for fumed silica aggregates with a diameter of of 200 nm, the mean fractal dimension is quite high with $f_D \approx 2.6$. Additionally, the Silica particles have undergone significant aggregation prior to their injection into the domain [277]. Assuming that aggregates consist of many primary particles of constant volume, Jacobson [91] noted that as the population of primary particles in an aggregate increases, its shape becomes more spherical.

Finally, the LES time-step was of the order of $\Delta t_{LES} = 10^{-6}$ with $CFL = 0.3$, which was lower than the aggregation time-step calculated from Eqn. (4.77) and the stability limit set by Eqn. (7.5). A one-way coupling was assumed as the volume fraction at the jet exit was $1.06 \cdot 10^{-9}$. The PSDs at the various measurement points were constructed from the histograms of the parcel diameters. The simulations were ran for approximately 100000 CPU hours.

7.3.2. Results

7.3.2.1. Gas phase

Figure 7.16 presents the contour plots for the temporal average (top) and instantaneous (bottom) LES velocity fields. Note that the simulation domain starts at $x = 40$ mm.

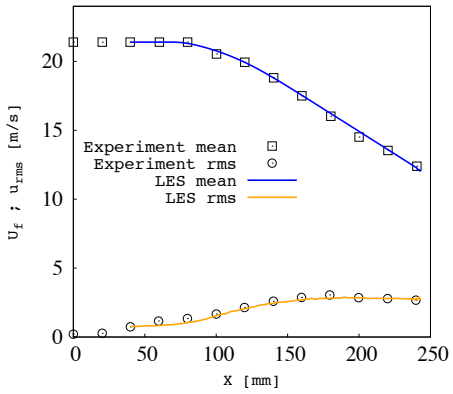


Figure 7.17.: Mean and RMS uniform phase velocity variation in the axial direction.

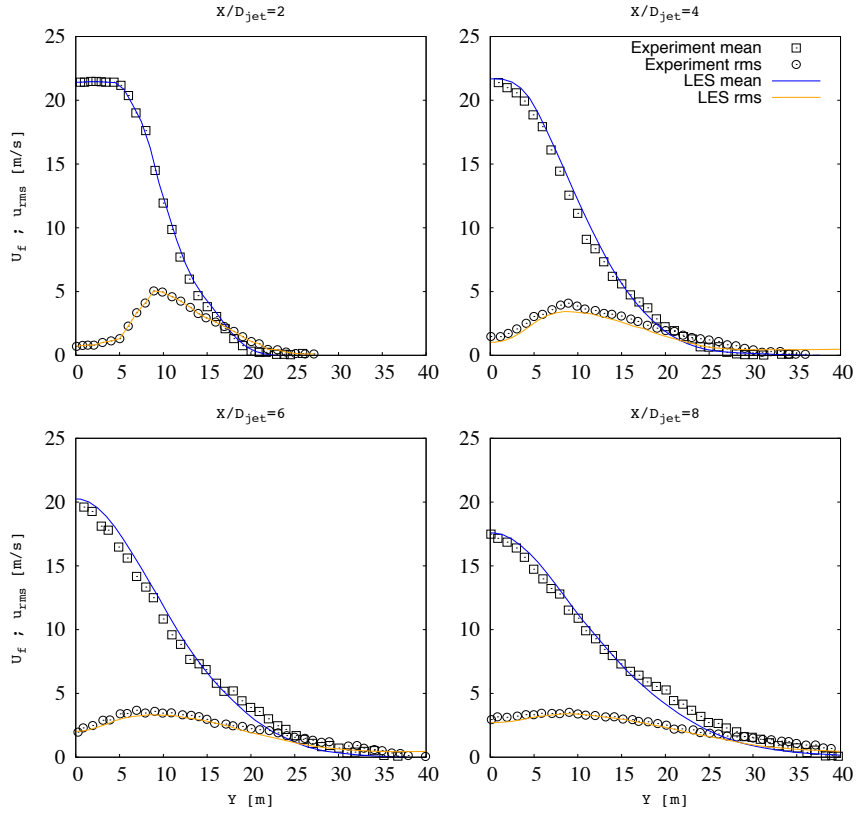


Figure 7.18.: Mean and RMS uniform phase velocity radial profiles at the four measurement points $x/D_{jet} = 2, 4, 6$ and 8.

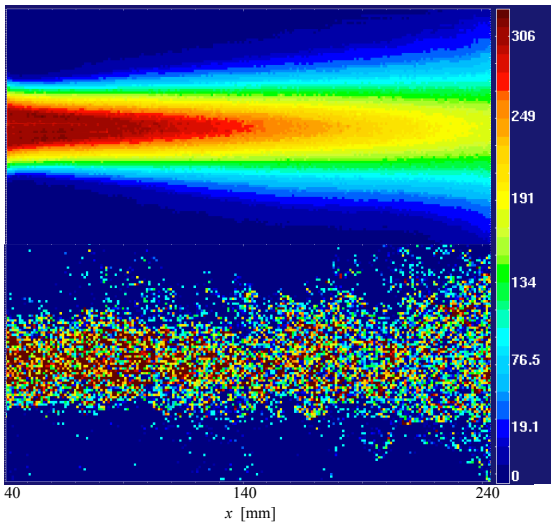


Figure 7.19.: Contour plot of temporal average (top) and instantaneous (bottom) particle concentration fields $N_c[\#/\Delta^3]$.

Figure 7.17 presents the variation of the mean and RMS velocity of the uniform phase in the axial x direction. Both mean and RMS velocities agree very well with the experimental data. The potential core of the jet persists until $x \approx 100$ mm with little to no variation of the centerline velocity U_f.

Figure 7.18 shows the radial profiles of the mean and the RMS uniform phase velocity at the four measurement points of the experiment, namely: $x/D_{jet} = 2, 4, 6$ and 8. For the reasons mentioned in sec. 7.3.1 at $x/D_{jet} = 2$ the experimental values are used for the boundary conditions of the simulation. Further downstream, a good agreement is found with the experimental data.

7.3.2.2. Disperse phase

Figure 7.19 shows the mean (top) and instantaneous (bottom) particle concentration field $N_c[\#/\Delta^3]$. It can be seen that the variation in concentration levels due to the turbulent motions of the continuous phase are significant. Figure 7.20 shows the radial particle concentration levels at four axial locations. The experimental levels of concentration at $x/D_{jet} = 2$ (inlet of simulation domain) were found to significantly underestimate N_c at the measurement positions further downstream if no background particles are present. Using a passive scalar with a value of zero in the jet and of one out-

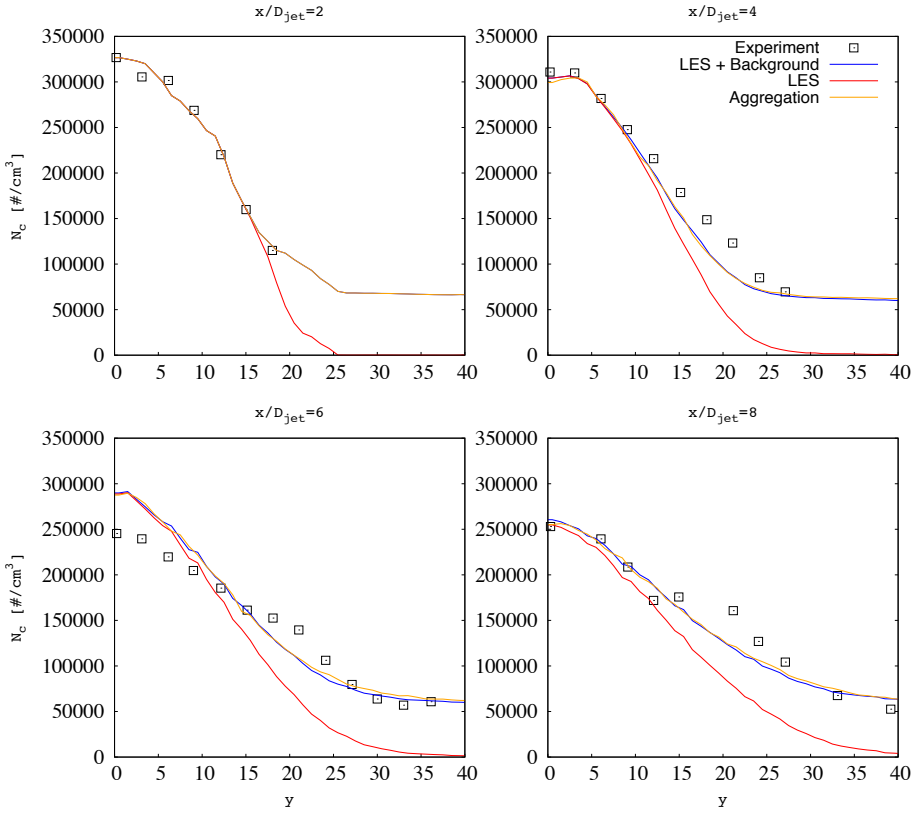


Figure 7.20.: Radial particle concentrations N_c at four axial locations.

side, the simulation was implemented excluding aggregation and including this 'background' particle concentration.

A background particle concentration of $80000\#/\text{cm}^3$ was required to observe the measured concentrations near the 'particle-free' environment. Significantly better agreement to the measured particle concentrations was found with the addition of a background particle concentration. However, in the locations further downstream from the inlet the LES underestimates the concentration levels at $y \approx 20$ mm (see Fig. 7.20). These results suggest that the environment where the jet issued could have been contaminated with airborne soot or recirculated nanoparticles from the experiment.

Figure 7.21 shows the measured and simulated PSD [4] at the inlet of the

[4]The PSDs presented here are normalized. Aggregation does not reduce the area under

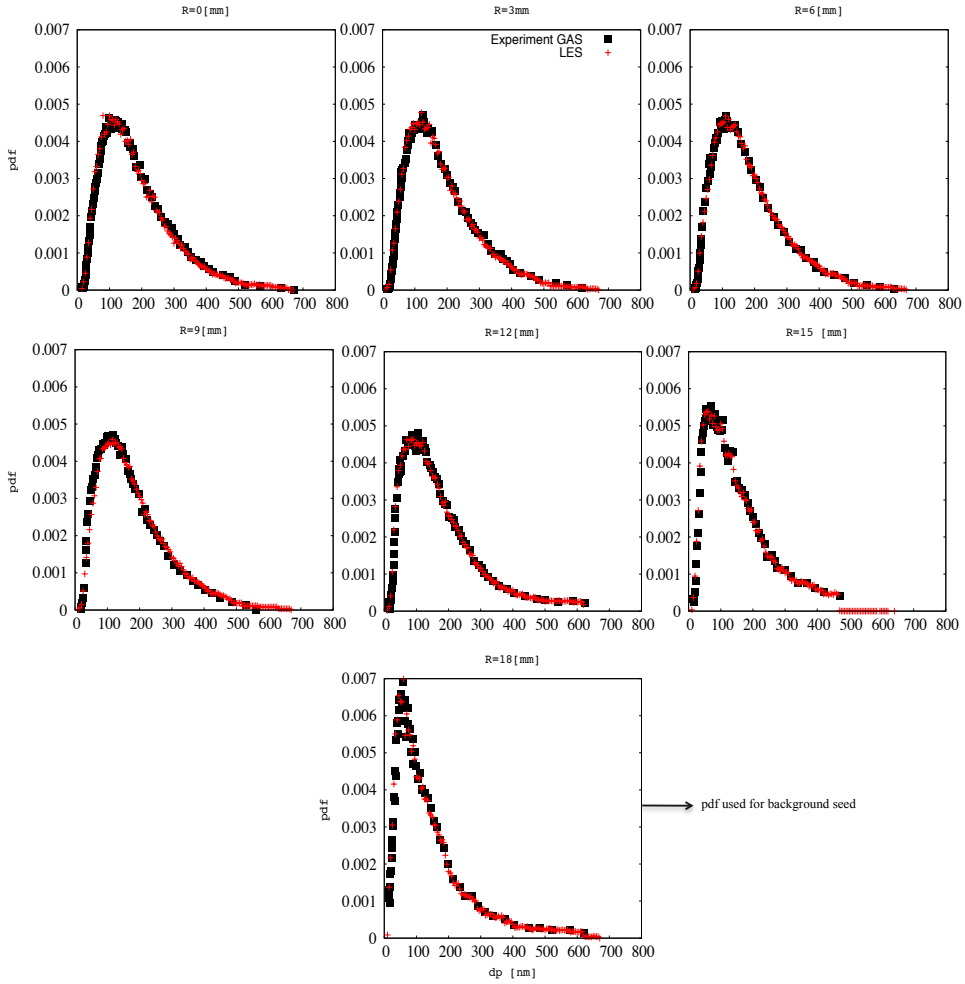


Figure 7.21.: Particle size distributions at the simulation inlet for different radial locations. The PSD at R =18mm is used for the background aggregation process.

simulation domain. The mode of the PSD at the radial location of 18 mm was used to approximate the mean particle diameter of the background particle concentration, namely: $d_p \approx 70$ nm. Note that the PSD at this location is narrower compared to other radial locations at $x/D_{jet} = 2$. Additionally, the mode of the PSD at 18 mm from the centerline is smaller than this of the other PSDs. These results can be explained by a large preferential dispersion, which the simulation was unable to reproduce, or due to a background particle concentration.

The background concentration was included in the aggregation process. Each parcel interacted with the Eulerian background particle concentration field assuming that all background particles have a $d_p \approx 70$ nm, equivalent to the mode of the PSD farthest from the centerline, at $x/D_{jet} = 2$, as shown in Fig. 7.21.

Figure 7.22 compares the measured PSDs to those from the LES at two further axial locations. The LES results show good agreement with the measurements on the jet centreline at $x/D_{jet} = 6$ and 8. However, there is little difference to the simulated PSD when the aggregation model is used compared to the simulations ran without the aggregation model. The greatest difference in the measured PSD is at $x/D_{jet} = 8$ at a radial location of 3 mm (bottom left in Fig. 7.22). The resulting PSD from the simulation at this position does not reproduce the experimental measurements.

Figure 7.23 shows two plots of the Brownian aggregation kernel in the free-molecular regime, see Eqn. (4.56). On the left of Fig. 7.23 is the aggregation kernel as a function of two interacting particle diameters, which are in the range of sizes recorded in the experiment. It can be seen that the kernel reaches its highest values when large particle classes interact with the smallest classes. This interaction reaches a peak of $\beta_{ij} \sim \mathcal{O}(10^{-12}\mathrm{m}^3/\#\mathrm{s})$. However, the experimental PSD is not uniform, hence interacting particle sizes tend to be of similar magnitude. The variation of the Brownian aggregation kernel for two interacting particles of the same diameter ($d_{p,i} = d_{p,j}$) is therefore also shown (see Fig. 7.23 top right). For the range of particles measured, the peak kernel is of the order $\beta_{ij} \sim \mathcal{O}(10^{-14}\mathrm{m}^3/\#\mathrm{s})$.

A minimum aggregation residence time τ_{aggr}, see Eqn. (4.75), can be calculated from the peak kernel and particle concentration data. For the conservative choice where $\beta_{ij} \sim \mathcal{O}(10^{-12}\mathrm{m}^3/\#\mathrm{s})$ and $N_c \sim \mathcal{O}(10^{12}\#/\mathrm{m}^3)$,

the PSD, but redistributes the probabilities. The term PSD is used for consistency.

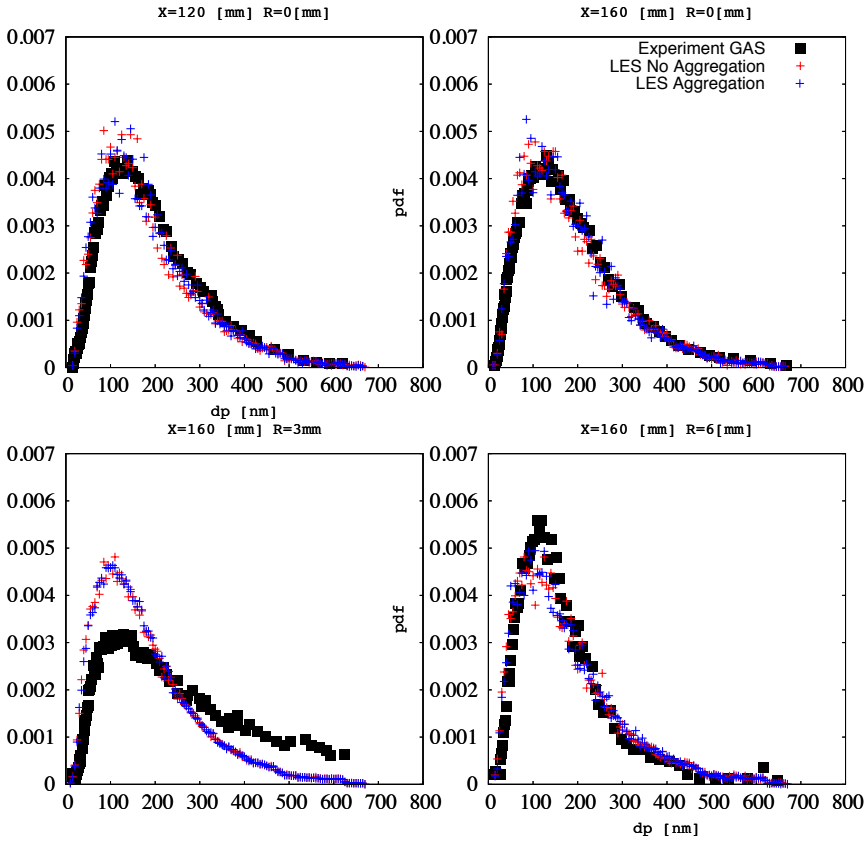


Figure 7.22.: Comparison of measured and simulated PSDs at four locations.

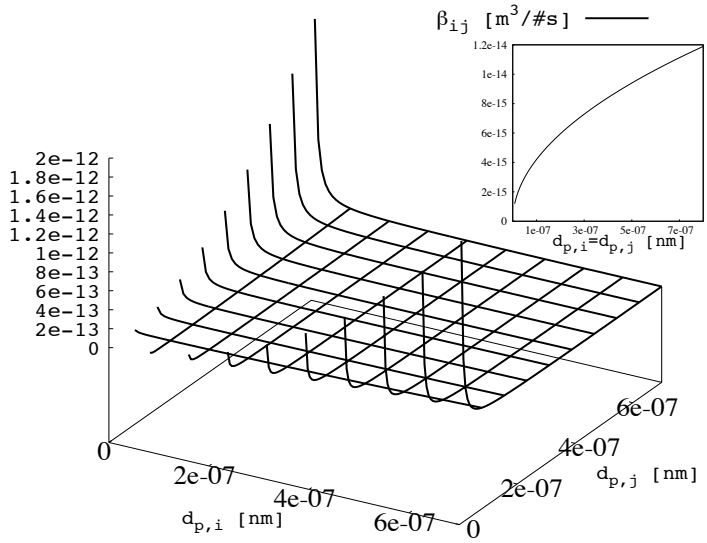


Figure 7.23.: Variation of aggregation kernel for the range of particle-sizes considered (left) and plot of kernel variation for colliding particles with same diameters (top right).

every cell in the domain will have on average an aggregation event every $\tau_{aggr} = \left(\beta_{ij} N_c^2 V_{cell}/4\right)^{-1} \sim \mathcal{O}(10^{-2}\text{s})$. Equivalently, if the maximum kernel for two particles of the same size is used then each cell will have one aggregation event every $\tau_{aggr} \sim \mathcal{O}(1\text{s})$.

The average distance that particles travel during the simulation is 120 mm ($x/D_{jet} = 8$). A flow residence time can be calculated assuming a conservative mean velocity of $U_f \approx 15.5$ m/s, which is equivalent to the axial velocity of the continuous phase at a radial location of 3 mm at $x/D_{jet} = 8$ (see Fig. 7.18). This flow residence time is therefore: $\tau_{flow} \sim \mathcal{O}(10^{-3}\text{s})$. From an order of magnitude perspective the particle concentration levels are not sufficient for the particles to aggregate within the flow residence time, since $\tau_{flow}/\tau_{aggr} \sim \mathcal{O}(10^{-1})$. Note that collision events do take place (with a probability of $\mathcal{P}_{aggr}(1,t) = 10\%$, using Eqn. (4.74) with $t = \tau_{flow}$), however the number of aggregation events is not sufficient to significantly alter the simulated PSD.

Figure 7.24 shows a plot of the cumulative (total) aggregation events that occurred in a residence time of $t = 3.5$ s which is equivalent to $nt = 340000$ timesteps and approximately 3500 flow-through times using that $\tau_{flow} \sim \mathcal{O}(10^{-3}s)$ from the previous example. Collisions between particles occur,

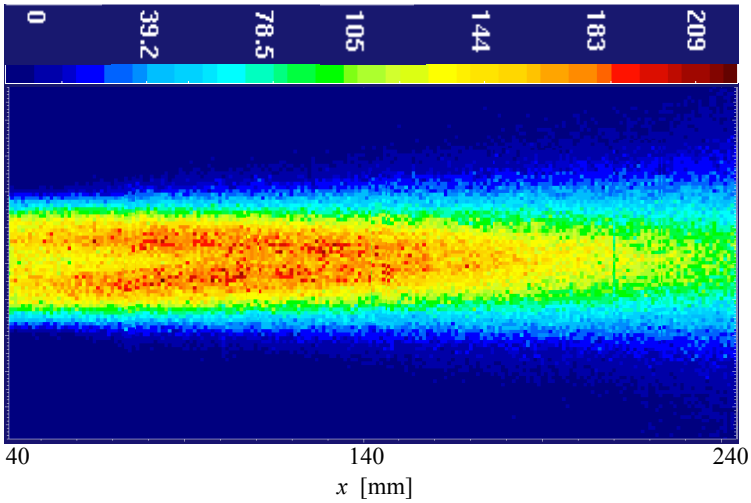


Figure 7.24.: Cumulative (total) aggregation events that occurred in a residence time of $t = 3.5$ s

however, a maximum of approximately 200 aggregation events took place in each cell over a time of $t = 3.5$ s, suggesting a minimum aggregation residence time of $\tau_{aggr} \sim \mathcal{O}(10^{-2}s)$, which is of same order to the one calculated *a priori*. Therefore, although the results from the LES and the predicted levels of aggregation are in good agreement, the simulation cannot capture the experimental PSD at $x/D_{jet} = 8$ and at a radial location of 3 mm (shown in Fig. 7.22). Finally, note that most aggregation events occur near the jet centerline, where the particle concentration is high.

7.4. Conclusions

This chapter investigated the particle aggregation process and model performance with respect to three different test-cases, namely: analytic solutions, a planar jet, and a turbulent round jet.

With respect to the analytic solutions it was shown that the inclusion of internal collisions for every parcel is required to accurately simulate the particle depletion process. The mass errors are at negligible levels for both temporal and parcel internal-particle-number discretization. In addition, a heuristic stability condition was suggested in Eqn. 7.5, for which a constant of $\alpha_{aggr} \sim \mathcal{O}(10^{-2})$ was deemed sufficient in order to de-couple the aggregation process from the temporal discretization and accurately represent the

particle depletion statistics.

The MC model produces accurate results for the evolution of the PSD using both the constant and the Golovin kernels, with errors of $|\epsilon_{SMD}| < 5\%$ in the coarse ($n_0^* \geq 2.5\%$) and $|\epsilon_{SMD}| < 2\%$ in the fine ($n_0^* \leq 0.25\%$) cases of initial internal parcel population. However, the results from the constant aggregation kernel suggested that an initial resolution of $n_0^* \approx 0.25\%$ is required to accurately capture the evolution of the PSD. Higher resolution can be obtained by appropriately discretizing the regions of the initial PSD with lower densities; as for example by using the condition of Eqn. (4.72).

In the Planar jet configuration, the model performance was compared to a sectional model for the evolution of the PBE as implemented in the DNS of Miller and Garrick [155]. Good agreement was found in the continuous phase velocity profiles. With respect to mean particle diameters, the present MC aggregation model agreed well with the results from the DNS at all axial locations. From a comparison between the PSD at the centerline and the one at the shear layer it was concluded that: assuming negligible preferential dispersion, the longer residence time is the main parameter promoting the formation of particles with greater diameters.

The difference between retrieving the complete PSD as opposed to the first moment was noted. The mean particle diameter statistics 'masked' the bi-modal shape observed in the full PSD. In addition, potential problems of using insufficient bins when solving a discrete PBE were shown. A Lagrangian particle tracking allows for an unrestricted range of possible particle sizes; capturing such a range with a discrete Eulerian PBE comes with a significant computational cost. Even though large particles $d_p > 8$ nm were observed near the shear layer, a sectional method would have to solve an additional transport equation for each size-class of $d_p > 8$ nm in every node of the domain.

A non-linear variation of the mean particle diameters at two axial locations with an aggregation-equivalent Damkohler number was observed. It was suggested that the primary reason for this behavior is the balance between reduced population-depletion upstream and longer residence times downstream. When aggregation kernels are smaller fewer particles are depleted upstream. The result is a higher particle population downstream, which when combined with a longer flow residence time (due to the deceleration of the jet) outweighs the reduced magnitude of the kernel β_{ij}.

The experiment of Zhu *et al.* [277] was used to investigate the model performance in a turbulent round jet. In their work, an SiO_2-laden jet was issued in the lab environment. The range of sizes of the particles was in the nano-scales and the free-molecular Brownian aggregation kernel was therefore used. With respect to the continuous phase, both mean and RMS velocities from the LES were found to agree very well with the experimental data. The experimental levels of concentration used as boundary conditions at the inlet of the simulation domain were found to significantly underestimate N_c at the measurement positions further downstream and a background concentration was needed. Significantly better agreement to the measured particle concentrations was found with the addition of this background particle concentration.

The Lagrangian particles were allowed to aggregate with particles from the background Eulerian field. The PSD from the LES was in very good agreement with the equivalent measurements at the inlet of the simulation. The LES results agreed well with the measurements of the PSDs on the jet centerline at $x/D_{jet} = 6$ and 8. However, an insignificant difference was noted in the PSD produced from the LES when the aggregation model was used compared to the case where particles were not allowed to aggregate. The greatest difference between the measured and simulated PSD is at $x/D_{jet} = 8$ at a radial location of 3 mm. From an order of magnitude analysis it was shown that the particle concentration levels are not sufficient for the particles to aggregate within the flow residence time. The reasons for the discrepancy in the measured and simulated PSD at $x/D_{jet} = 8$ are unknown, but they cannot be attributed to aggregation.

8. Summary and Major Conclusions

A disperse particle, immersed in a continuous-phase flow, can be understood as a solid, liquid, or gaseous object, whose length-scales are much smaller than those of the continuous phase. The evolution of particle-laden flows is of central importance in a number of environmental, medical, and industrial applications.

Recent reports have revealed strong links between respiratory diseases and cancers, and the exposure to particulates of 10μm or less in diameter. It is therefore of extreme value to be able to comprehensively control (and/or predict) the size and population of particulates from industrial and domestic emissions. Additionally, advances in industrial processes have enabled the synthesis of highly specific nanoparticles for the mass production of commodities such as drugs, detergents, coffee powders, and composite materials. The ability to predict the evolution of poly-disperse flows has become an indispensable part of the design process. Design parameters can be evaluated and optimized at an early stage of the design and consequently at a lower cost. The simulations of poly-disperse turbulent flows have, therefore, received significant attention due to their predictive capability. However, the description and understanding of such processes is challenging because of a very wide range of length- and time-scales.

In the present study, models were developed, implemented, and validated to describe the particulate phase immersed in a turbulent continuous fluid. The particles considered were inertial and the mixtures investigated were dilute. Moreover, the particle populations were of the order $\mathcal{O}(10^6 - 10^{12})$ and their diameters were much smaller than the Kolmogorov length-scales ($d_p << \eta_k$), therefore rendering a fully resolved (deterministic) solution intractable.

Large Eddy Simulations (LES) of the continuous phase evolution were

combined with the spray probability density function (pdf) for the description of the disperse phase processes. The frameworks of the LES and the spray pdf were outlined in Chapters 2 and 3, respectively. In Chapter 4, three processes investigated were reviewed and the respective models outlined. These processes were: dispersion, nucleation and aggregation. Each model outlined was subsequently implemented and evaluated in a series of test cases. The following major conclusions were drawn:

Dispersion process:

In the context of dispersion, a Lagrangian methodology is advantageous for dilute mixtures because the location of a particle is known and computational power can be allocated more efficiently to solve real particle paths. LES offers the great advantage of directly resolving a wide range of the turbulent length-scales that influence a particle's motion while at a moderate computational cost compared to Direct Numerical Simulations (DNS). However, it was concluded that modelling the sub grid-scale (sgs) velocity of the continuous phase is required for the correct prediction of the dispersion process in LES.

When the sgs was not included, the particle dispersion levels were underestimated in the context of both cases investigated, namely: a particle-laden unbound channel with constant shear and decaying homogeneous turbulence – $\eta_k/d_p \sim \mathcal{O}(10^2)$, and in a particle-laden turbulent mixing layer – $\eta_k/d_p \sim \mathcal{O}(10^1)$. In state of the art Lagrangian Stochastic (LS) dispersion models, a coefficient is used to scale the stochastic contribution to the motion of a particle (be it a fluid or an inertial particle). This coefficient cannot be analytically evaluated, and therefore it is non-universal.

It was shown that the stochastic coefficient is case- and grid-dependent. Additionally, it was shown that when a LS model with a static coefficient is employed the accurate representation of particle dispersion is subject to the mass and consequently relaxation time of a particle. The use of a dynamic model for the evaluation of the dispersion constant can therefore aid in the *a priori* predictive ability of the LES-LS framework. It was shown that the LES-spray pdf dispersion model of Jones and Bini [23, 24] extended by a dynamic evaluation of the dispersion constant can accurately predict the dispersion statistics without the requirement of a free-parameter choice. Moreover, due to the fact that the dispersion constant is coupled to the flow,

it was shown that the extended dynamic model produces smoother results than the equivalent model with a static coefficient.

Throughout this work the assumption of point mass and spherical shape for inertial particles has been made. Therefore, a further extension would be to incorporate the effect of different shapes in the trajectories of a particle (e.g. nano-tubes or soot). Furthermore, it would be interesting to evaluate the model-applicability when the size of the particle is of the order of the mean free path of the molecules in the continuous phase. For example, particles in the nano-scale tend to follow the flow closely, however when they have a comparable size to the mean free path of the fluid molecules they may not view the fluid as a continuum. The incorporation of the Cunningham slip correction could therefore alter the modelled particle trajectories.

Nucleation process:

The second process investigated was nucleation. Nucleation is a process which is directly influenced by the continuous phase as it involves the condensation of a vapor and the formation of droplets which are subsequently transported as distinct entities by the fluid. The highly non-linear nature of the nucleation process makes the rate very sensitive to the fluctuations of the continuous phase state. The level of scales involved often render microscopic/deterministic approaches intractable. Therefore, nucleation is an ideal process for the investigation of the predictive capability of the LES-spray pdf framework.

This study focused on an LES implementation of the nucleation rate provided by the Classical Nucleation Theory (CNT) for a turbulent Dibutyl Phthalate (DBP)-laden Nitrogen jet diffusing in atmospheric air. The nucleation rate was treated in a LES framework and calculated on an instantaneous nodal basis. The use of instantaneous values for the evaluation of the nucleation rate was compared to traditional approaches. It was shown that LES offers a great advantage to traditional approaches because a model is not required for the inclusion of temporal variations of the macroscopic fluid-variables that influence the nucleation rate.

The main incentive in the LES-spray pdf formulation of the nucleation process was therefore to take advantage of the instantaneous rates delivered by the LES. Owing to the intrinsic ability of the stochastic framework to incorporate discrete 'jumps' and the versatility of the spray-pdf state vector

choice, a parameter-free method for the treatment of the CNT nucleation rate as a probabilistic event was developed and evaluated. The model accurately produced the particle concentration levels measured in a turbulent DBP-laden Nitrogen jet. In addition, no significant difference could be seen in the particle concentration statistics when two different models for the incorporation of the filtered-out scales were used. This becomes important when comparing to alternative approaches, where it has been shown that the exclusion of fluctuations (e.g. temporal in RANS and spatial in the EMNM) leads to significant differences in the calculation of particle nucleation rate and concentration.

Further work may include the investigation of the sgs effects when a non-unity Lewis number is used. In such cases a single scalar to evaluate the nucleation rate would not suffice and temporal variations of both temperature and species concentrations would have to be considered. If for example $Le > 1$, nucleation rates would be affected as the condensing vapor is diluted at a slower rate compared to the cooling of the fluid mixture. Computational studies enable the de-coupling of the nucleation and growth process and therefore allow a direct investigation of the 'boundary conditions' (i.e. the diameters of newly formed particles), for condensational growth and aggregation. Turbulence increases the range of the probable diameters of stable clusters and a complex relation between the nucleation residence time and flow time-scale can influence the resulting Particle Size Distribution (PSD) from a nucleation-driven process.

Nucleation is an activated process influenced by numerous parameters and only a minor aspect of it, namely homogeneous nucleation rates, was investigated here. Having proposed a method to treat activated processes in transient environments, the method could be extended for other mechanisms that drive the particle formation process. Nanoparticle synthesis, for example by pyrolysis or inert gas condensation, and formation of soot precursors, in principle could also be treated in a LS framework. The resulting chemical composition of the particles, and the chemistry-driven process by which the particles form, controls their commercial properties.

Aggregation process:

The intersection of particle paths may lead to a collision event and an inelastic collision event to aggregation. Aggregation generally refers to the formation of a new larger particle from two or more smaller ones. Similarly to nucleation, the level of scales involved in aggregation often render microscopic/deterministic approaches intractable. In this work, particles in the nano-scale ($d_p << \eta_k$ and $Kn >> 1$) were investigated, where the aggregation kernel is governed by Brownian motion. However, turbulence can still play a critical role in the aggregation process. Firstly, kernels stemming from kinetic theory are correlated to the local levels of particle concentration and fluid temperature, which fluctuate due to the nature of turbulence. Secondly, flow time-scales govern the residence time for which a given concentration of particles can aggregate locally. LES offers the advantage of retrieving instantaneous values, whereas the LS framework can incorporate the sgs effect on particle concentration statistics into the Lagrangian particle dispersion model.

In the present work aggregation was modelled using a multi-collision differentially weighted Monte Carlo methodology. Lagrangian parcels representing a number of real particles were simulated and the aggregation events were incorporated into the trajectory formulation of the spray-pdf as stochastic jumps. The aggregation model was evaluated and used to investigate three test-cases, namely: analytic solutions of the PSD evolution using a constant and the Golovin kernel, a nanoparticle-laden planar jet, and a SiO_2-laden turbulent round jet.

It was shown that when stochastic parcels are used, their respective internal collisions have to be accounted to accurately simulate the aggregation process. The evolution of the PSD using the developed model accurately reproduced the analytic solutions. A stability condition was estimated for the aggregation time-step in order to temporally de-couple the aggregation events.

In the Planar jet configuration, the model performance was compared to a sectional model for the evolution of the PBE as implemented in the DNS of Miller and Garrick [155]. The model agreed well with the results from the DNS with respect to mean particle diameters. Larger particles were observed at the jet shear layer suggesting that longer flow residence times are responsible for promoting the formation of particles with greater diame-

ters. The difference between retrieving the complete PSD as opposed to the first moment was noted, as in the latter case the mean diameter statistics 'masked' the bi-modal shape of the full PSD. The Lagrangian tracking was found to be advantageous compared to the sectional PBE since the allowed range of particle sizes is unrestricted (and not at the expense of higher computational cost). A non-linear variation of the mean particle diameters with an aggregation-equivalent Damkohler number was observed. This non-linearity suggests a complex balance between the aggregation kernel, the level of particle population depletion, and the flow residence times.

The experiment of Zhu *et al.* [277] was used to investigate the model performance in a turbulent round jet. Although the simulation accurately reproduced the continuous phase statistics and the PSD at various locations in the domain, the aggregation model was found to have a minimal effect on the simulated PSDs. A background concentration was included with which the Lagrangian parcels were allowed to aggregate. The model could not capture the measured PSD at the location where the highest aggregation was observed experimentally. However, from an order of magnitude analysis it was shown that the particle concentration levels were not sufficient for the particles to aggregate within the flow residence time.

The present work highlighted the non-linear relation of aggregation rate, particle concentration, and flow residence time. Future work may include a parametric investigation of the relative effects of the aggregating phase density and volume fraction on the resulting PSD. Turbulence becomes of central importance because correlations are created that can be very difficult to model using an Eulerian PBE.

This study did not extend to the various mechanisms driving the aggregation process and it was limited to spherical aggregates. Therefore, a straight-forward extension would be to include fractal aggregation, which may influence significantly the aggregation rates as the equivalent surface area of the particles, and hence their collision probability, will increase. In addition, modelling of forces that influence aggregation (e.g. van der Waals) poses a significant challenge in a Lagrangian context. Chemically-induced aggregation and the 'evergreen' issue of soot aggregation in turbulent flows are aspects that were not investigated here. It would therefore be very interesting to extend the spray-pdf framework in the context of particle processes driven by chemical kinetics.

Finally, to the author's knowledge there are very limited experiments specifically designed to measure PSDs resulting from Brownian aggregation in turbulent jets. The increasing need for comprehensive predictive models used in the context of complex industrial processes has revealed the need for further experimental work on Brownian aggregation in turbulent jet configurations.

Concluding, the Lagrangian spray-pdf framework for the treatment of the disperse phase combined with a LES of the continuous phase can predict the evolution of poly-disperse turbulent flows. The LS framework can easily accommodate the non-linearities and discrete nature involved in macroscopic treatments of the disperse phase, whereas the LES offers the advantage of retrieving instantaneous values of the flow field at moderate computational cost. The versatility in the choice of the state vector of the spray-pdf allows for an efficient allocation of computational resources towards the solution of the trajectories only at locations where particles are situated. All of the models hereby presented can be both expanded and tailored to case-specific investigations. Finally, it was shown that the LES-spray pdf framework can be used to develop models from phenomenological arguments, without additional free-parameters, that accurately describe complex, turbulent, poly-disperse flows.

The End

Bibliography

[1] J.R. Adam and N.R. Lindblad. The collision, coalescence, and disruption of water droplets. *J. Appl. Phys.*, 39:173, 1968.

[2] R.J. Adrian. Particle-imaging techniques for experimental fluid mechanics. *Annu. Rev. Fluid Mech.*, 23:261–304, 1991.

[3] A.M. Ahmed and S. Elghobashi. Direct numerical simulation of particle dispersion in homogeneous turbulent shear flows. *Phys. Fluids*, 13 (11):3346, 2001.

[4] AIChE. Thermodynamical database. Technical report, American Institute of Chemical Engineers: Design Institute for Physical Property Data, 1997.

[5] D.J. Aldous. Deterministic and stochastic models for coalescence (aggregation and coagulation): a review of the mean-field theory for probabilists. *Bernoulli*, 1:3–48, 1999.

[6] Y. Ammar. *Turbulent agglomeration and break-up of nuclear aerosols.* PhD thesis, Newcastle University, 2008.

[7] S. Anand. *Study of coagulation of dispersing aerosol systems.* PhD thesis, Homi Bhabha National Institute, 2012.

[8] M.P. Anisimov, K. Hameri, and M. Kulmala. Construction and test of laminar flow diffusion chamber: Homogeneous nucleation of DBP and n-Hexanol. *J. Aerosol Sci*, 25:1:23–32, 1994.

[9] D. Anne-Archard, M. d'Olce, M. Tourbin, and C. Frances. Aggregation of silica nanoparticles in concentrated suspensions under turbulent, shear and extensional flows. *Chem. Eng. Sci.*, 95:184–193, 2013.

[10] C. Archambeau. A short introduction to diffusion processes and Ito calculus. Technical report, University College, London: Centre for Computational Statistics and Machine Learning, 2007.

[11] C. Artelt, H.J. Schmid, and W. Peukert. On the relevance of accounting for the evolution of the fractal dimension in aerosol process simulations. *J. Aerosol Sci.*, 34:511–534, 2003.

[12] N. Ashgriz and J.Y. Poo. Coalescence and separation in binary collision of liquid drops. *J. Fluid Mech.*, 221:183, 1990.

[13] F. Azizi and A.M. Al Taweel. Algorithm for the accurate numerical solution of PBE for drop breakup and coalescence under high shear rates. *Chem. Eng. Sci.*, 65:6112–6127, 2010.

[14] J. Badyga and W. Orciuch. Closure problem for precipitation. *Chemical Engineering Research and Design*, 75(2):160–170, 1997.

[15] B.V. Balakin, A.C. Hoffmann, and P. Kosinski. Population balance model for nucleation, growth, aggregation, and breakage of hydrate particles in turbulent flow. *Particles Technology and Fluidization*, 56(8):2052–2062, 2010.

[16] J. Baldyga and W. Orciuch. Closure method for precipitation in inhomogeneous trurbulence. *Proc. 14th Symposium on Industrial Crystallization*, 86:1069, 1999.

[17] R.A. Baurle and S.S. Girimaji. Assumed pdf turbulence-chemistry closure with temperature-composition correlations. *Combust. & Flame*, 134:131–148, 2003.

[18] L.L. Baxter and P.J. Smith. Turbulent dispersion of particles: The stp model. *Energy & Fuels*, 7:852–859, 1993.

[19] R. Becker and W. Doring. Kinetische behandlung der keimbildung in ubersattingten damfen. *Ann. Phys.*, 24:719–52, 1935.

[20] V.M. Bedanov, V.S. Vaganov, G.V. Gadiyak, G. Kodenev, and E. Rubakhin. The experimental determination of number of molecules in the critical embryo. *Khimicheskaya Fisika*, 7:555–563, 1988.

[21] A.S. Berrouk, D. Laurence, J.J. Riley, and D.E. Stock. Stochastic modelling of inertial particle dispersion by subgrid motion for LES of high Reynolds number pipe flows. *J. Turbulence*, 8:50, 2007.

[22] M. Bini. *Large Eddy Simulation of particle and droplet laden flows with stochastic modelling of subfilter scales.* PhD thesis, Imperial College London, 2006.

[23] M. Bini and W. P. Jones. Particle acceleration in turbulent flows: A class of nonlinear stochastic models for intermittency. *Phys. Fluids*, 19:035104–1, 2007.

[24] M. Bini and W. P. Jones. Large eddy simulation of particle laden turbulent flows. *J Fluid Mech*, 614:207–252, 2008.

[25] R. Bleck. Fast, approximate for integrating the stochastic coalescence equation. *J. Geophysical Research*, 75(27):5165–5171, 1970.

[26] G.B.J. De Boer, G.F.M. Hoedemakers, and D. Thoenes. Coagulation in turbulent flow: Part I. *Chem. Eng. Res. Des*, 67:301–307, 1989.

[27] R. Bords, V. John, E. Schmeyer, and D. Thvenin. Measurement and simulation of a droplet population in a turbulent flow field. *Computers & Fluids*, 66:52–62, 2012.

[28] N. Branley and W.P. Jones. LES of turbulent non-premixed flames. *Combust. & Flame*, 127:1914–1934, 2001.

[29] M. Brauer, G. Hoek, P. Van Vliet, K. Meliefste, P.H. Fischer, A. Wijga, L.P. Koopman, H.J. Neijens, J. Gerritsen, M. Kerkhof, J. Heinrich, T. Bellander, and B. Brunekreef. Air pollution from traffic and the development of respiratory infections and asthmatic and allergic symptoms in children. *A. J. Respiratory and Critical Care Medicing*, 8:1092–1098, 2002.

[30] J.R. Brock and P.J. Kuhn. Condensation aerosol formation and growth in a laminar coaxial jet. *J. Aerosol Sci*, 17:11–22, 1986.

[31] I.B. Celik, Z.N. Cehreli, and I. Yavuz. Index of resolution quality for large eddy simulations. *J. of Fluids Engineering*, 127:949–958, 2005.

[32] M.S. Tageldin B.M. Cetegena. Development of mixing and dispersion in an isothermal, droplet-laden, confined turbulent mixing layer. *Combust. Sci. Tech.*, 130:131–169, 1997.

[33] X.Q. Chen and J.C.F. Pereira. Efficient computation of particle dispersion in turbulent flows with a stochastic-probabilistic model. *In. J. Heat Mass Transfer*, 40(8):1727–1741, 1997.

[34] P.C.K. Chu, J.H. Lee, and V.H. Chu. Spreading of turbulent round jet in coflow. *J. Hydraul. Eng.*, 125:193–204, 1999.

[35] M.J. Cocero, S. Ferrero, and F. Miguel. Crystallization of beta-carotene by continuous gas process: Effect of mixer on crystals formation. In *4th International symposium on high pressure process technology and chemical engineering. Venive, Italy*, 2002.

[36] R. Courant, K. Friedrichs, and H. Lewy. On the partial difference equations of mathematical physics. *Mathematische Annalen*, 100:32–74, 1928.

[37] C.T. Crowe, J.D. Schwarzkopf, M. Sommerfeld, and Y. Tsuji. *Multiphase Flows with Droplets and Particles, Second Edition.* CRC Press, 2012.

[38] J.J. Derksen. Direct numerical simulations of aggregation of monosized spherical particles in homogeneous isotropic turbulence. *AICHE J*, 58(8):2589–2600, 2012.

[39] A. Dillman and G.E.A. Meier. A refined droplet approach to the problem of homogeneous nucleation from the vapour phase. *J. Chem. Phys.*, 94:3872–3884, 1991.

[40] C. Dopazo. Relaxation of initial probaility density functions in the turbulent convection of scalar fields. *Phys. Fluids*, 22:20, 1979.

[41] D.R. Dowling and P. Dimotakis. Similarity of the concentration field of gas-phase turbulent jets. *J. Fluid Mech.*, 218:109–141, 1990.

[42] MG Dunn, AJ Baran, and J Miatech. Operation of gas turbine engines in volcanic ash clouds. *ASME Tech. Pap.*, 94-GT-170:., 1994.

[43] P. A. Durbin. Stochastic differential equations and turbulent dispersion. Technical report, NASA Reference Publication 1103, 1983.

[44] M.L. Eggersdorfer, D. Kadau, H.J. Herrmann, and S.E. Pratsinis. Aggregate morphology evolution by sintering: Number and diameter of primary particles. *J. Aerosol Sci*, 46:7–19, 2012.

[45] M.L. Eggersdorfer and S.E. Pratsinis. The structure of agglomerates consisting of polydisperse particles. *Aerosol Sci. Tech.*, 46:347–353, 2012.

[46] M.L. Eggersdorfer and S.E. Pratsinis. Restructuring of aggregates and their primary particle size distribution during sintering. *AICHE J*, 59(4):1118–1126, 2013.

[47] M.L. Eggersdorfer and S.E. Pratsinis. Agglomerates and aggregates of nanoparticles made in the gas phase. *Advanced Powder Tech.*, 25:71–90, 2014.

[48] A. Eibeck and W. Wagner. Stochastic interacting particle systems and nonlinear kinetic equations. *Ann. Appl. Probab.*, 13:845–889, 2003.

[49] L.C. Evans. An introduction to stochastic differential equations version 1.2. Technical report, UC Berkeley, Department of Mathematics, download Feb. 2011.

[50] A.J. Fager, J. Liu, and S.C. Garrick. Hybrid simulations of metal particle nucleation: A priori and a posteriori analyses of the effects of unresolved scalar interactions on nanoparticle nucleation. *Phys. Fluids*, 24:075110, 2012.

[51] P. Fede and O. Simonin. Numerical study of the subgrid fluid turbulence effects on the statistics of heavy colliding particles. *Phys. Fluids*, 18:045103, 2006.

[52] P. Fede, O. Simonin, P. Villedieu, and K. D. Squires. Stochastic modeling of the turbulent subgrid fluid velocity along inertial particle trajectories. In *Center for Turbulence Research: Proceedings of the Summer Program*, page 247, 2006.

[53] H. Feng, M.G. Olsen, R.O. Fox, and J.C. Hill. Conditional statistics for passive-scalar mixing in confined rectangular jet. *Phys. Fluids*, 19:055104, 2007.

[54] H. Feng, M.G. Olsen, R.O. Fox, and J.C. Hill. Conditional statistics of passive-scalar mixing in confined wake flow. *Phys. Fluids*, 20:077105–1, 2008.

[55] B.J. Finlayson-Pitts and J.N. Pitts. Tropospheric air pollution: ozone, airborne toxics, polycyclic aromatic hydrocarbons, and particles. *Science*, 276:1045–1052, 1997.

[56] B. Fitch. Sedimentation of flocculent suspensions: state of the art. *AICHE J*, 25:913–930, 1979.

[57] J. Floyd, A.M. Kempf, A. Kronenburg, and R.H. Ram. A simple model for the filtered density function for a passive scalar in combustion LES. *Combust. Theor. Modeling*, 13(4):559–588, 2009.

[58] R.O. Fox. On the relationship between lagrangian micromixing models and computational fluid dynamics. *Chem. Eng. Process.*, 37:521–535, 1998.

[59] R.O. Fox. *Computational Models for Turbulent Reacting Flows*. Cambridge University Press, 2003.

[60] B.M. Franchetti, F. Cavallo Marincola, S. Navarro-Martinez, and A.M. Kempf. Large eddy simulation of pulverised coal jet flame. *Proc. Combust. Inst.*, 34(2):2419–2426, 2013.

[61] J. Frenkel. A general theory of heterophase fluctuations and pretransition phenomena. *J. Chem. Phys.*, 7:538, 1939.

[62] M. Frenklach. Method of moments with interpolative closure. *Chem. Eng. Sci*, 57:2229–22239, 2002.

[63] S.K. Friedlander. *Smoke, Dust, and Haze: Fundamentals of Aerosol Dynamics*. Oxford University Press, 2000.

[64] N.A. Fuchs. *The Mechanics of Aerosols*. Pergamon Press, 1964.

[65] C. W. Gardiner. *Handbook of Stochastic Methods for Physics, Chemistry and the Natural Sciences*. Springer, 2003.

[66] A. Garmony and E. Mastorakos. Aerosol nucleation and growth in a turbulent jet using the stochastic fields method. *Chem. Eng. Sci*, 63:4078–4089, 2008.

[67] S.C. Garrick. Effects of turbulent fluctuations on nanoparticle coagulation in shear flows. *Aerosol Sci. Tech.*, 45:1272–1285, 2011.

[68] S.C. Garrick, K.E.J. Lehtinen, and M.R. Zachariah. Nanoparticle coagulation via a Navier-Stokes/nodal methodology: Evolution of the particle fields. *J. Aerosol Sci.*, 37:555–576, 2006.

[69] M. Gavaises, A. Theodorakakos, G. Bergeles, and G. Brenn. Evaluation of the effect of droplet collisions on spray mixing. *Proc. Instn Mech. Engrs*, 210:465–475, 1996.

[70] F. Gelbard and J.H. Seinfeld. Numerical solution of the dynamic equation for particulate systems. *J. Comp. Phys.*, 28(3):357–75, 1978.

[71] M. Germano, U.Piomelli, P. Moin, , and W.H. Cabot. A dynamic subgrid-scale eddy viscosity models. *Phys. Fluids*, 23:17601765, 1986.

[72] T. Gerz, U. Schumann, and S.E. Elghobashi. Direct numerical simulation of stratified homogeneous turbulent shear flows. *J. Fluid Mech.*, 200:563, 1989.

[73] S.S. Girimaji. Assumed beta-pdf model for turbulent mixing: Validation and extension to multiple scalar mixing. *Combust. Sci. Tech.*, 78:177, 1991.

[74] S.L. Girshick and C. Chiu. Kinetic nucleation theory: A new expression for the rate of homogeneous nucleation from an ideal supersaturated vapor. *J. Chem. Phys.*, 93:1273, 1990.

[75] S.L. Girshick, C.P. Chiu, and P.H. McMurry. Time-dependent aerosol models and homogeneous nucleation rates. *Aerosol Sci. Tech.*, 13:465–477, 1990.

[76] C. Gobert. *Large Eddy Simulation of Particle-Laden Flow.* PhD thesis, Technische Universitat Munchen, 2010.

[77] C. Gobert and M. Manhart. Subgrid modelling for particle-LES by spectrally optimised interpolation (SOI). *J. Comput. Phys.*, 230:7796–7820, 2011.

[78] A.M. Golovin. On the spectrum of coagulating cloud droplets, II (trans. by C.M. Wade). *Izvestiya Geophysical Series*, 9:880–884, 1963.

[79] A.M. Golovin. The solution of the coagulation equation for cloud droplets in a rising air current. *Bull. Acad. Sci. SSSR Geophys. Ser. (English Transl.)*, pages 482–487, 1963.

[80] L. Granasy. Diffuse interface theory of nucleation. *J. Non-Crystalline Solids*, 162:3:301–303, 1993.

[81] A. Guha. Transport and deposition of particles in turbulent and laminar flow. *Annu. Rev. Fluid Mech*, 40:311–341, 2008.

[82] B. Guo, D.F. Fletcher, and T.A.G. Langrish. Simulation of the agglomeration in a spray using lagrangian particle tracking. *Applied Mathematical Modelling*, 28:273–290, 2003.

[83] B.N. Hale. Application of a scaled homogeneous nucleation rate formalism to experimental data at T much less than Tc. *Phys. Rev. A*, 33:4156, 1986.

[84] K. Hameri, M. Kulmala, E. Krissinel, and G. Kodenyov. Homogeneous nucleation in a laminar flow diffusion chamber: The operation principles and posibilities for quantitative rate measurements. *J. Chem. Phys.*, 105:7683, 1996.

[85] D.C. Haworth. Progress in probability density function methods for turbulent reacting flows. *Prog. Energy Combust. Sci.*, 36:168–259, 2010.

[86] J. Heyder, J. Gebhart, G. Rudolf, C.F. Schiller, and W. Stahlhofen. Deposition of particles in the human respiratory tract in the size range 0.00515 micro-m. *J. Aerosol Sci.*, 17:811–25, 1986.

[87] C.A. Ho and M. Sommerfeld. Modelling of micro-particle agglomeration in turbulent fows. *Chem. Eng. Sci.*, 57:3073–3084, 2002.

[88] H.M. Hulburt and S. Katz. Some problems in particle technology: a statistical mechanical formulation. *Chem. Eng. Sci*, 19:555–574, 1964.

[89] H.J. Hussein, S.P. Capp, and W.K. George. Velocity measurements in a high Reynolds number, momentum-conserving, axisymmetric turbulent jets. *J. Fluid Mech.*, 258:31–75, 1994.

[90] N. Isabeta and B. Biscans. Fractal dimension of fumed silica: Comparison of light scattering and electron microscope methods. *Powder Tech.*, 203(10):206–210, 2010.

[91] M.Z. Jacobson. *Fundamentals of atmospheric modeling.* Cambridge University Press, 1999.

[92] Y.J. Jiang, A. Umemura, and C.K. Law. An experimental investigation on the collision behaviour of hydrocarbon droplets. *J. Fluid Mech.*, 234:171, 1992.

[93] G. Jin, G.W. He, L.P. Wang, and J. Zhang. Subgrid scale fluid velocity timescales seen by inertial particles in large-eddy simulation of particle-laden turbulence. *Int. J. Multiphase Flow*, 36:432–437, 2010.

[94] T. Johannessen, S.E. Pratsinis, and H. Livbjerg. Computational analysis of coagulation and coalescence in the flame synthesis of titania particles. *Powder Tech.*, 118:242–250, 2001.

[95] W. P. Jones. Calculation methods for reacting turbulent flows: A review. *Combust. & Flame*, 48:1–26, 1982.

[96] W. P. Jones. *Turbulence modelling and numerical solution methods for variable density and combusting flows.* In P.A. Libby and F.A. Williams:Turbulent Reacting Flows, ch.6, 1987.

[97] W. P. Jones and C. Lettieri. Large eddy simulation of spray atomization with stochastic modeling of breakup. *Phys. Fluids*, 22:115106–1, 2010.

[98] W.P. Jones, S. Lyra, and A.J. Marquis. Large eddy simulation of a droplet laden turbulent mixing layer. *Int. J. Heat and Fluid Flow*, 31:93–100, 2010.

[99] W.P. Jones, S. Lyra, and S. Navarro-Martinez. Large eddy simulation of a swirl stabilized spray flame. *Proc. Combust. Inst.*, 33:2153–2160, 2011.

[100] A. Kempf, M. Klein, and J. Janicka. Efficient generation of initial and inflow conditions for transient turbulent flows in arbitrary geometries. *Flow Turb. and Combust*, 74:67–84, 2005.

[101] A.M. Kempf. *Large-Eddy Simulation of Non-Premixed Turbulent Flames*. PhD thesis, TU Darmstadt, 2003.

[102] A.M. Kempf, B.J. Geurts, and J.C. Ofelein. Error analysis of large-eddy simulation of the turbulent non-premixed sydney bluff-body flame. *Combust. & Flame*, 158:2408–2419, 2011.

[103] H.T. Kim and W. Chun. The particle size effect on pollutant formation in pulverized coal combustion. *Environ. Eng. Res.*, 3:21–29, 1998.

[104] M. Klein, A. Sadiki, and J. Janicka. A digital filter based generation of inflow data for spatially developing direct numerical or large eddy simulations. *J. Comp. Phys.*, 186:652–665, 2003.

[105] I.L. Klimontovich. *The Statistical Theory of Non-equilibrium Processes in a Plasma*. Pergamon, 1969.

[106] P.E. Kloeden and E. Platen. *Numerical Solution of Stochastic Differential Equations*. Springer, 1999.

[107] M. Knudsen and S. Weber. Luftwiderstand gegen die langsame bewegung kleiner kugeln. *Ann. Phys.*, 36:981–994, 1911.

[108] D.L. Koch and S.B. Pope. Coagulation-induced particle-concentration fluctuations in homogeneous, isotropic turbulence. *Phys. Fluids*, 14(7):2447–2455, 2002.

[109] W. Koch, T.H. Wind, and N. Karfich. Modeling and experimental evaluation of an aerosol generator for very high number currents based on a free turbulent jet. *J. Aerosol Sci*, 24:909–918, 1993.

[110] L.E. Kollar and M. Farzaneh. Modeling the evolution of droplet size distribution in two-phase flows. *Int. J. Multiphase Flow*, 33:1255–1270, 2007.

[111] L.E. Kollar, M. Farzaneh, and A.R. Karev. Modelling droplet collision and coalescence in an icing wind tunnel and the influence of these processes on droplet size distribution. *Int. J. Multiphase Flow*, 31:69–92, 2005.

[112] A.N. Kolmogorov. Dissipation of energy in local isotropic turbulence. *Dolakady Akademii Nauk SSSR*, 32:19–21, 1941.

[113] A.N. Kolmogorov. The local structure of turbulence in incompressible viscous fluid for very larg reynolds numbers. *Dolakady Akademii Nauk SSSR*, 32:299–303, 1941.

[114] A.N. Kolmogorov. A refinement of previous hypotheses concerning the local structure of turbulence in a viscous incompressible fluid at high reynolds number. *J. Fluid Mech.*, 34:1382, 1962.

[115] A. Kronenburg, R.W. Bilger, and J.H. Kent. Modeling soot formation in turbulent methane-air jet diffusion flames. *Combust. & Flame*, 121:24–30, 2000.

[116] J.G. Kuerten. Subgrid modeling in particle-laden channel flow. *Phys. Fluids*, 18:025108, 2006.

[117] J.G. Kuerten and A.W. Vreman. Can turbophoresis be predicted by large-eddy simulation? *Phys. Fluids*, 17:011701, 2005.

[118] R. Kulkarni and W. Polifke. Large eddy simulation of autoignition in a turbulent hydrogen jet flame using a progress variable approach. *J. Combustion*, 2012:11, 2012.

[119] A. Laaksonen, I.J. Ford, and M. Kulmala. Revised parametrisation of the dillman-meier theory of homogeneous nucleation. *Phys. Rev. E*, 49:5517–5524, 1994.

[120] A. Laaksonen, V. Talanquer, and D.W. Oxtoby. Nucleation: Measurements, theory, and atmospheric applications. *Annu. Rev. Phys. Chem.*, 46:489–524, 1995.

[121] B.E. Launder and D.B. Spalding. The numerical computation of turbulent flows. *Computer Methods in Applied Mechanics and Engineering*, 3:269–289, 1974.

[122] B. Lazaro and J. Lasheras. Particle dispersion in a turbulent plane shear layer. *Phys. Fluids*, 1:1035–1044, 1989.

[123] B.J. Lazaro and J.C. Lasheras. Droplet dispersion and transport mechanisms in a turbulent, free shear-layer. *Proc. Combust. Inst*, 22(1):1991–1998, 1988.

[124] B.J. Lazaro and J.C. Lasheras. Particle dispersion in the developing free shear layer. Part 1. Unforced flows. *J. Fluid Mech.*, 235:143–178, 1992.

[125] B.J. Lazaro and J.C. Lasheras. Particle dispersion in the developing free shear layer. Part 2. Forced flows. *J. Fluid Mech.*, 235:179–221, 1992.

[126] B. Van Leer. Towards the ultimate conservative difference scheme III. Upstream-centred finite-difference schemes for ideal compressible flows. *J. Comp. Phys.*, 23:263–275, 1977.

[127] T.K. Lesniewski. *Particle Nucleation and Growth in Turbulent Jets*. PhD thesis, University of California, 1997.

[128] T.K. Lesniewski and S.K. Friedlander. The effect of turbulence on rates of particle formation by homogeneous nucleation. *Aerosol Sci. Tech.*, 23:174–182, 1995.

[129] T.K. Lesniewski and S.K. Friedlander. Particle nucleation and growth in a free turbulent jet. *Proc. R. Soc. London Ser. A*, 454:2477–2504, 1998.

[130] C. Lettieri. *Large Eddy Simulation of Two-phase Reacting Flows*. PhD thesis, Imperial College London, 2010.

[131] Y. Liao and D. Lucas. A literature review of theoretical models for drop and bubble breakup in turbulent dispersions. *Chem. Eng. Sci*, 64:3389–3406, 2009.

[132] Y. Liao and D. Lucas. A literature review on mechanisms and models for the coalescence process of fluid particles. *Chem. Eng. Sci*, 65:2851–2864, 2010.

[133] R.C. Lien and E.A. D'Asaro. The Kolmogorov constant for the lagrangian velocity spectrum and structure functions. *Phys. Fluids*, 14:4456, 2002.

[134] K. Liffman. A direct simulation Monte-Carlo method for cluster coagulation. *J. Comput. Phys.*, 100:116–127, 1992.

[135] J.S. Lighty, J.M. Veranth, and A.F. Sarofim. Combustion aerosols: Factors governing their size and composition and implications to human health. *J. Air and Waste Management Association*, 50:1565–1618, 2000.

[136] D. K. Lilly. A proposed modification of the Germano subgrid-scale closure methods. *Phys. Fluids*, 4:633–635, 1992.

[137] D.K. Lilly. The representation of small-scale turbulence in numerical simulation experiments. *Proc. of the IBM Scientific Computing Symp. on Environmental Sciences*, 1:195–210, 1967.

[138] Y. Lin, K. Lee, and T. Matsoukas. Solution of the population balance equation using constant-number Monte Carlo. *Chem. Eng. Sci.*, 57(12):2241–2252, 2002.

[139] R.J. Litchford and S.M. Jeng. Efficient statistical transport model for turbulent particle dispersion in sprays. *AIAA Journal*, 29:1443, 1991.

[140] E. Loth. Numerical approaches for motion of dispersed particles, droplets and bubbles. *Prog. Energy Combust. Sci.*, 26:161–223, 2000.

[141] J. Lothe and G.M. Pound. Reconsiderations of nucleation theory. *J. Chem. Phys.*, 36:2080–2085, 1962.

[142] T.S. Lundgren. Distribution functions in the statistical theory of turbulence. *Phys. Fluids*, 10(5):969–975, 1967.

[143] H K Versteeg W Malalasekera. *An Introduction to Computational Fluid Dynamics The Finite Volume Method*. Pearson Prentice Hall, 2007.

[144] D.L. Marchisio and R. O. Fox. Solution of population balance equations using the direct quadrature method of moments. *J. Aerosol Sci.*, 36:43–73, 2005.

[145] D.L. Marchisio, R.O. Fox, A.A. Baressi, and G. Baldi. On the comparison between presumed and full pdf methods for turbulent precipitation. *Ind. Eng. Chem. Res.*, 40:5132–5139, 2001.

[146] D.L. Marchisio, R.D. Vigil, and R.O. Fox. Implementation of the quadrature method of moments in CFD codes for aggregationbreakage problems. *Chem. Eng. Sci.*, 58(15):3337–3351, 2003.

[147] S. Markutsya. *Modeling and simulation of nanoparticle aggregation in colloidal systems*. PhD thesis, Iowa State University, 2010.

[148] M. Maxey and J.J. Riley. Equation of motion for a small rigid sphere in a nonuniform flow. *Phys. Fluids*, 26:883–889, 1983.

[149] N. Maximova and O. Dahl. Environmental implications of aggregation phenomena: Current understanding. *Current Opinion in Colloid & Interface Science*, 11:246–266, 2006.

[150] J.E. McDonald. Homogeneous nucleation of vapor condensation. I. Thermodynamic aspects. *American J. Phys.*, 30:870, 1962.

[151] R. McGraw. Description of aerosol dynamics by the quadrature method of moments. *Aerosol Sci. Tech.*, 27:255–265, 1997.

[152] F.R. Menter and Y. Egorov. The scale-adaptive simulation method for unsteady turbulent flow predictions. Part 1: Theory and model description. *Flow Turb. Combust*, 85:112–138, 2010.

[153] V.B. Mikheev, N.S. Laulainen, and S.E. Barlow. The laminar flow tube reactor as a quantitative tool for nucleation studies: Experimental results and theoretical analysis of homogeneous nucleation of Dibutyl-Phthalate. *J. Chem. Phys.*, 113:3704, 2000.

[154] Richard S. Miller and Josette Bellan. Direct numerical simulation and subgrid analysis of a transitional droplet laden mixing layer. *Phys. Fluids*, 12:650, 2000.

[155] S.E. Miller and S.C. Garrick. Nanoparticle coagulation in a planar jet. *Aerosol Sci. Tech.*, 38:79–89, 2004.

[156] J.P. Minier and E. Peirano. The pdf approach to turbulent polydispersed two-phase flows. *Phys. Reports*, 352:1–214, 2001.

[157] P. Moin and K. Mahesh. Direct numerical simulation: A tool in turbulence research. *Annu. Rev. Fluid Mech*, 30:539–78, 1998.

[158] I.I. Montes, G. Rego, C. Camblor, A. Quero, A. Gonzalez, and C. Rodriguez. Respiratory disease in aggregate quarry workers related to risk factors and Pi phenotype. *J. Occup. Environ. Med.*, 46(11):1150–1157, 2004.

[159] S. Mosbach, M.S. Celnik, A. Raj, M. Kraft, H.R. Zhang, and K.O. Kim S. Kubo. Towards a detailed soot model for internal combustion engines. *Combust. & Flame*, 156:1156–1165, 2009.

[160] N.J. Murfield and S.C. Garrick. The effects of unresolved scalar fluctuations during homogeneous nucleation. *Aerosol Sci. Tech.*, 47(7):806–817, 2013.

[161] WHO Fact Sheet N313. Ambient (outdoor) air quality and health. Technical report, World Healt Organization, 2014.

[162] F. Nicoud and F. Ducros. Subgrid-scale stress modelling based on the square of the velocity gradient tensor. *Flow Turb. Combust*, 62:183–200, 1999.

[163] J.J. Nijdam, B. Guo, D.F. Fletcher, and T.A.G. Langrish. Challenges of simulating droplet coalescence within a spray. *Drying Tech.*, 22(6):1463–1488, 2004.

[164] J.J. Nijdam, S.H. Starner, and T.A.G. Langrish. An experimental investigation of droplet evaporation and coalescence in a simple jet flow. *Experiments in Fluids*, 37:504–517, 2004.

[165] G. Oberdorster. Pulmonary effects of inhaled ultrafine particles. *Int. Arch. Occup. Environ. Health*, 74:1–8, 2001.

[166] N. Okong'o and J. Bellan. Consistent large-eddy simulation of a temporal mixing layer with evaporating drops. Part 1: Direct numerical simulation, formulation and a priori analysis. *J. Fluid Mech.*, 499:1–47, 2004.

[167] K. Okuyama, Y. Kousaka, D.R. Warren, R.C. Flagan, and J.H. Seinfeld. Homogeneous nucleation by continuous mixing of high temperature vapor with room temperature gas. *Aerosol Sci. Tech.*, 6:15–27, 1987.

[168] C.T. Onions, editor. *The Oxford Dictionary of English Etymology.* Oxford University Press, 1966.

[169] M. Orme. Experiments on droplet collisions, bounce, coalescence and disruption. *Prog. Energy Combust. Sci.*, 23:65–79, 1997.

[170] D.W. Oxtoby. Homogeneous nucleation: theory and experiment. *J. Phys.: Condens. Matter*, 4:7627, 1992.

[171] R.I.A. Patterson, W. Wagner, and M. Kraft. Stochastic weighted particle methods for population balance equations. *J. Comput. Phys.*, 230(19):7456–7472, 2011.

[172] M. Peglow, U. Cunaus, and E. Tsotsas. An analytical solution of population balance equations for continuous fluidized bed drying. *Chem. Eng. Sci*, 66:1916–1922, 2011.

[173] S.H. Peoples, C.J. Thurn, J.I. Steinmetz, and W.R. Oliver. Assessment of fugitive emissions of proc from petroleum refining operations : final report. Technical report, Sacramento: Radian Corp, 1987.

[174] I. Pesmazoglou, A.M. Kempf, and S. Navarro-Martinez. A dynamic model for the lagrangian stochastic dispersion coefficient. *Phys. Fluids*, 25:125108, 2013.

[175] I. Pesmazoglou, A.M. Kempf, and S. Navarro-Martinez. LES investigation on the effects of turbulence on homogeneous nucleation. In *8th International Conference on Multiphase Flow, Jeju, Korea*, 2013.

[176] I. Pesmazoglou, A.M. Kempf, and S. Navarro-Martinez. Aerosol nucleation in a turbulent jet using large eddy simulations. *Chem. Eng. Sci.*, 116:383–397, 2014.

[177] M.W.A. Pettit, B. Coriton, A. Gomez, and A.M. Kempf. Large eddy simulation and experiments on non-premixed highly turbulent opposed jet flows. *Proc. Combust. Inst*, 33:1391–1399, 2011.

[178] M. Piatkowski and I. Zbicinski. Analysis of the mechanism of countercurrent spray drying. *Transp Porous Med*, 66:89–101, 2007.

[179] C.D. Pierce and P. Moin. A dynamic model for sub-grid scale variance and dissipation rate of a conserved scalar. *Phys. Fluids*, 10:12:3041–3044, 1998.

[180] W. Pietsch. Readily engineer agglomerates with special properties from micro- and nanosized particles. *Chem. Eng. Prog.*, 95(8):67–81, 1999.

[181] U. Piomelli and J. Liu. Large-eddy simulation of rotating channel flow using localized dynamic model. *Phys. Fluids*, 7(4):839–848, 1995.

[182] T. Poinsot and D. Veynante. *Theoretical and numerical combustion.* Edwards, 2005.

[183] D.B. Pope. Pdf methods for turbulent reactive flows. *Prog. Energy Combust. Sci.*, 11:119–192, 1985.

[184] S.B. Pope. Lagrangian pdf methods for turbulent flows. *Annu. Rev. Fluid Mech*, 26:23–63, 1994.

[185] S.B. Pope. *Turbulent Flows.* Cambridge University Press, 2000.

[186] M. Potin-Gautier, P. Grenier, and J. Bonastre. Nouvelle application analytique de la methode de determination des pressions de vapeur par saturation dun gaz inerte. *Anal. Lett.*, 15:1431, 1982.

[187] J. Pozorski and S.V. Apte. Filtered particle tracking in isotropic turbulence and stochastic modeling of subgrid-scale dispersion. *Int. J. Multiphase Flow*, 35:118–128, 2009.

[188] J. Pozorski, M. Knorps, and M. Luniewski. Effects of subfilter velocity modelling on dispersed phase in les of heated channel flow. *J. Phys.: Conf. Ser.*, 333:012014, 2011.

[189] L. Prandtl. Bericht uber die entstehung der turbulenz. *Zeitschrift fur angewandte Mathematik and Mechanik*, 5:136, 1925.

[190] L. Prandtl. Investigation of turbulent flow. *Zeitschrift fur angewandte Mathematik and Mechanik*, 5:136, 1925.

[191] S. E. Pratsinis, W. Zhu, and S. Vemury. The role of gas mixing in flame synthesis of titania powders. *Powder Tech.*, 86:87–93, 1996.

[192] S.E. Pratsinis. Simultaneous nucleation, condensation and coagulation in aerosol reactors. *J. Colloid and Interface Science*, 124(2):416–427, 1988.

[193] H.R. Pruppacher and J.D. Klett. *Microphysics of Clouds and Precipitation, 2nd rev.* Kluwer Academic Publishers, 1997.

[194] J. Qian and C. K. Law. Regimes of coalescence and separation in droplet collision. *J. Fluid Mech.*, 331:59–80, 1997.

[195] KW Ragland, MK Misra, DJ Aerts, and CA Palmer. Ash deposition in a wood-fired gas turbine. *J. Eng. Gas Turbines Power*, 117:509–12, 1995.

[196] H. Reiss. Treatment of droplike clusters by means of the classical phase integral in nucleation theory. *J. Stat. Phys.*, 2:83–104, 1970.

[197] P.C. Reist. *Introduction to aerosol science.* Macmillan Pub Co., 1984.

[198] T. Retsina. Agglomeration: a process to improve fine powder handling. *Food Technology International Europe*, pages 37–39, 1988.

[199] O. Reynolds. An experimental investigation of the circumstances which determine whether the motion of water shall be direct or siuous, and the law of resistance in parallel channels. *Philos. Trans. R. Soc. London*, 174:935–982, 1883.

[200] O. Reynolds. On the dynamic theory of incompressible viscous flows and the determination of the criterion. *Philos. Trans. R. Soc. London*, 186:123–161, 1894.

[201] L.F. Richardson. Atmospheric diffusion shown on a distance-neighbor graph. *Proc. R. Soc. London Ser. A*, 110:709–737, 1926.

[202] L.F. Richardson. *Weather prediction by numerical process.* Cambridge University Press, 1992.

[203] S. Rigopoulos. Pdf method for population balance in turbulent reactive flow. *Chem. Eng. Sci*, 62:6865–6878, 2007.

[204] S. Rigopoulos. Population balance modelling of polydispersed particles in reactive flows. *Prog. Energy Combust. Sci.*, 36:412–443, 2010.

[205] S. Rigopoulos and A.G. Jones. Finite-element scheme for solution of the dynamic population balance equation. *AICHE J*, 49:1127–1139, 2003.

[206] H. Risken. *The Fokker Planck Equation*. Springer, 1984.

[207] P.L. Roe. Characteristic-based schemes for the euler equations. *Annu. Rev. Fluid Mech.*, 18:337, 1986.

[208] S.N. Rogak and R.C. Flagan. Coagulation of aerosol agglomerates in the transition regime. *J. Colloid Interface Sci.*, 151:203–224, 1992.

[209] D.E. Rosner, R. McGraw, and P. Tandon. Multi-variate population balances via moment and Monte Carlo simulation methods. *Ind. Eng. Chem. Res.*, 42:2699–2711, 2003.

[210] J.C. Rotta. Über eine methode zur berechnung turbulenter scheströmungen. *Aerodynamische Versuchsanstalt Rep.*, 69:A14, 1968.

[211] M. Ruger, S. Hohmann, M. Sommerfeld, and G. Kohnen. Euler/Lagrange calculations of turbulent sprays: the effect of droplet collisions and coalescence. *Atomization and Sprays*, 10(1):47–81, 2000.

[212] V. Sabel'nikov and O. Soulard. Rapidly decorrelating velocity-field model as a tool for solving one-point Fokker-Planck equations for probability density functions of turbulent reactive scalars. *Physical Review E - Statistical, Nonlinear, and Soft Matter Physics*, 72(1):1–22, 2005.

[213] P.G. Saffman. The lift on a small sphere in a slow shear flow. *J. Fluid Mech.*, 22:385–400, 1965.

[214] P.G. Saffman and J.S. Turner. On the collision of drops in turbulent clouds. *J. Fluid Mech.*, 1:16–30, 1956.

[215] P. Sagaut. *Large Eddy Simulation for incompressible flows*. Springer, 1998.

[216] Brian Sawford. Turbulent relative dispersion. *Annu. Rev. Fluid Mech.*, 33:289–317, 2001.

[217] J.W.P. Schmelzer, editor. *Nucleation theory and applications*. Wiley-VCH, 2005.

[218] J.L. Schmitt, G.W. Adams, and R.A. Zalabsky. Homogeneous nucleation of ethanol. *J. Chem. Phys.*, 77(4):2089–2097, 1982.

[219] H.C. Schwarzer, F. Schwertfirm, M. Manhart, H.J. Schmid, and W. Peukert. Predictive simulation of nanoparticle precipitation based on the population balance equation. *Chem. Eng. Sci.*, 61:167–181, 2006.

[220] W.T. Scott. Analytic studies of cloud droplet coalescence. *J. of Atmospheric Sciences*, 25:54–65, 1968.

[221] B. Shotorban and F. Mashayek. Modeling subgrid-scale effects on particles by approximate deconvolution. *Phys. Fluids*, 17:081701, 2005.

[222] B. Shotorban and F. Mashayek. A stochastic model for particle motion in large-eddy simulation. *J. Turbulence*, 7:N18, 2006.

[223] J. Siera-Pallares, D. L. Marchisio, M.T. Parra-Santos, J. Garcia-Serna, F. Castro, and M.J. Cocero. A computational fluid dynamics study of supercritical antisolvent precipitation: Mixing effects on particle size. *AICHE J*, 58(2):385–398, 2012.

[224] J. Smagorinsky. General circulation experiments with the primitive equations, I. The basic experiments. *Monthly Weather Review*, 152:9199, 1963.

[225] M. Smith and T. Matsoukas. Constant-number Monte Carlo simulation of population balances. *Chem. Eng. Sci.*, 53(9):1777–1786, 1998.

[226] M.V. Smoluchowski. Versuch einer mathematischen theorie der koagulationskinetik kolloider lsungen. *Z. Phys. Chem.*, 92:129168, 1917.

[227] R.M.C. So and B.C. Hwang. On similarity solutions for turbulent and heated round jets. *J. App. Math. Phys.*, 37:624, 1986.

[228] M. Sommerfeld. Validation of a stochastic lagrangian modelling approach for inter-particle collisions in homogeneous isotropic turbulence. *Int. J. Multiphase Flow*, 27:1829–1858, 2001.

[229] O. Stein. *Large Eddy Simulation of Combustion in Swirling and Opposed Jet Flames*. PhD thesis, Imperial College of London, 2009.

[230] O.T. Stein, G. Olenik, A. Kronenburg, F. Cavallo Marincola, B.M. Franchetti, A.M. Kempf, M. Ghiani, M. Vascellari, and C. Hasse. Towards comprehensive coal combustion modelling for LES. *Flow Turb. Combust*, 1:1–26, 2012.

[231] S. Stolz, N. A. Adams, and L. Kleiser. An approximate deconvolution model for large-eddy simulation with application to incompressible wall- bounded flows. *Phys. Fluids*, 13:997, 2001.

[232] J.W. Su, Z.L. Gu, and X.Y. Xu. Advances in numerical methods for the solution of population balance equations for disperse phase systems. *Sci China Ser B-Chem*, 52 n. 8:1063–1079, 2009.

[233] S. Subramaniam. Statistical representation of a spray as a point process. *Phys. Fluids*, 12:2413–2431, 2000.

[234] S. Sundaram and L.R. Collins. Collision statistics in an isotropic particle-laden turbulent suspesion. Part 1. Direct numerical simulations. *J. Fluid Mech.*, 335:75–109, 1997.

[235] Y. Sung, V. Raman, and R.O. Fox. Les based multiscale modelling of tio2 nanoparticle synthesis in a turbulent flame reactor using detailed nucleation chemistry. *Chem. Eng. Sci*, 66(19):4370–4381, 2011.

[236] P.K. Sweby. High resolution schemes using flux-limiters for hyperbolic conservation laws. *Society for Industrial and Applied Mathematics Journal of Numerical Analysis*, 21:995–1011, 1984.

[237] D.J. Thomson. Criteria for the selection of stochastic models of particle trajectories in turbulent flows. *J. Fluid Mech.*, 180:529–556, 1987.

[238] F. Toschi and E. Bodenschatz. Lagrangian properties of particles in turbulence. *Annu. Rev. Fluid Mech.*, 41:375–404, 2009.

[239] W. S. J. Uijttewaal and R. V. A. Oliemans. Particle dispersion and deposition in direct numerical and large eddy simulations of vertical pipe flows. *Phys. Fluids*, 8:2590, 1996.

[240] L. Valino. Field Monte Carlo formulation for calculating the probability density function of a single scalar in a turbulent flow. *Turb. & Combust.*, 60(2):157–172, 1998.

[241] R.E.M. Verdurmen, P. Menn, J. Ritzert, S. Blei, G.C.S. Nhumaio, T. Sonne Srensen, M. Gunsing, J. Straatsma, M. Verschueren, M. Sibeijn, G. Schulte, U. Fritsching, K. Bauckhage, C. Tropea, M. Sommerfeld, A.P. Watkins, A.J. Yule, and H. Schnfeldt. Simulation of agglomeration in spray drying installations: The EDECAD project. *Drying Tech.*, 22:6:1403–1461, 2004.

[242] G. Y. Di Veroli. *Stochastic modeling of particle formation in turbulent flows via the transported PBE-PDF method.* PhD thesis, University of Manchester, 2009.

[243] G. Y. Di Veroli and S. Rigopoulos. Modeling of aerosol formation in a turbulent jet with the transported population balance equation-probability density function approach. *Phys. Fluids*, 23:043305–1, 2011.

[244] G. Di Verolli and S. Rigopoulos. Modeling of turbulent precipitation: A transported population balance-pdf method. *AICHhE J.*, 56:878, 2010.

[245] J. Villermaux and J.C. Devillon. Representation de la coalescence et de la re-dispersion des domaines de segregation dans un modele d'interaction phenomenologique. In *Proceedings of the Second International Symposium on Chemical Reaction Engineering, pages 1-13, Elsevier, New York*, 1972.

[246] K. Vogiatzaki and S. Navarro-Martinez. Direct modelling of the filtered source term by series expansion. In *13th International Conference on Numerical Combustion, Crete, Greece*, 2011.

[247] P.E. Wagner. *Aerosol Microphysics II.* Springer, 1982.

[248] W. Wagner. Stochastic, analytic and numerical aspects of coagulation processes. *Mathematics and Computers in Simulation*, 62:265–275, 2003.

[249] C. Wall, B.J. Boersma, and P. Moin. An evaluation of the assumed beta probability density function subgrid-scale model for large eddy simulation of nonpremixed, turbulent combustion with heat release. *Phys. Fluids*, 12(10):25222529, 2000.

[250] H. Wang, K. Luo, and J. Fan. Direct numerical simulation and cmc (conditional moment closure) sub-model validation of spray combustion. *Energy*, 46:606–617, 2012.

[251] Q. Wang and K.D. Squires. Large eddy simulation of particle-laden turbulent channel flow. *Phys. Fluids*, 8:1207, 1996.

[252] W. Wang, S. Fan, D. Liang, and X. Yang. Experimental study on flow characters of CH3CCl2F hydrate slurry. *Int. J. Refrig.*, 31:371–378, 2008.

[253] J. Wedekind, R. Strey, and D. Reguera. New method to analyze simulations of activated processes. *J. Chem. Phys.*, 126:134103, 2007.

[254] RA Wenglarz and RG Fox. Physical aspects of deposition from coal-water fuels under gas turbine conditions. *J. Eng. Gas Turbines Power*, 112:9–14, 1990.

[255] M. Wilck, K. Hameri, F. Stratmann, and M. Kulmala. Determination of homogeneous nucleation rates from laminar-flow diffusion chamber data. *J. Aerosol Sci*, 29:8:899–911, 1998.

[256] F.A. Williams. Spray combustion and atomisation. *Phys. Fluids*, 1 n.6:541–545, 1958.

[257] J. Williamson. Low storage Runge-Kutta schemes. *J. Comp. Phys.*, 35:48–56, 1980.

[258] J. D. Wilson and B.L. Sawford. Review of Lagrangian stochastic modles for trajectories in turbulent atmosphere. *Boundary-Layer Meteorology*, 78:191–210, 1996.

[259] J. Wu and S. Menon. Aerosol dynamics in the near field of engine exhaust plumes. *J. Applied Metereology*, 40:795–809, 2001.

[260] S. Wysocky. *Joint Euler-Lagrange Method for Moving Surfaces in Large-Eddy Simulation.* PhD thesis, Imeprial College London, 2012.

[261] Y. Xiong and S.E. Pratsinis. Formation of agglomerate particles by coagulation and sintering: Part I. A two-dimensional solution of the population balance equation. *J. Aerosol Sci*, 24(3):283–300, 1993.

[262] Y. Yamamoto, M. Potthoff, T. Tanaka, T. Kajishima, and Y. Tsuji. Large-eddy simulation of turbulent gas-particle flow in a vertical channel: effect of considering inter-particle collisions. *J. Fluid Mech.*, 442:303–334, 2001.

[263] J. Yan, K. Luo, J. Fan, Y. Tsuji, and K. Cen. Direct numerical simulation of particle dispersion in a turbulent jet considering inter-particle collisions. *Int. J. Multiphase Flow*, 34:723–733, 2008.

[264] F. Yeh and U. Lei. On the motion of small particles in a homogeneous isotropic turbulent flow. *Phys. Fluids*, 3:2571–2586, 1991.

[265] G.H. Yeoha and J.Y. Tub. Two-fluid and population balance models for subcooled boiling flow. *Appllied Mathematical Modelling*, 30(11):1370–1391, 2006.

[266] M. Yu and J. Lin. Nanoparticle-laden flows via moment method: A review. *Int. J. Multiphase Flow*, 36:144–151, 2010.

[267] M. Yu, J. Lin, L. Chen, and T. Chan. Large eddy simulation of a planar jet flow with nanoparticle coagulation. *Acta Mechanica Sinica*, 22:293–300, 2006.

[268] M. Yu, J. Lin, and H. Xiong. Quadrature method of moments for nanoparticle coagulation and diffusion in the planar impinging jet flow. *Chin. J. Chem. Eng.*, 15(6):828–836, 2007.

[269] M. C. Yuen and L. W. Chen. On drag of evaporating liquid droplets. *Combust. Sci. Tech.*, 21:537–542, 1976.

[270] J. Zeldovich. Theory of the formation of a new phase. *J. Expl. Theoret. Phys. (USSR)*, 12:525, 1942.

[271] H. Zhao, F.E. Kruis, and C. Zheng. Reducing statistical noise and extending the size spectrum by applying weighted simulation particles in Monte Carlo simulations of coagulation. *Aerosol Sci. Tech.*, 43:781–793, 2009.

[272] H. Zhao, F.E. Kruis, and C. Zheng. A differentially weighted Monte Carlo method for two-component coagulation. *J. Comp. Phys.*, 229:6931–6945, 2010.

[273] H. Zhao and C. Zheng. A population balance-Monte Carlo method for particle coagulation in spatially inhomogeneous systems. *Computers & Fluids*, 71:196–207, 2013.

[274] H. Zhao C. Zheng. Two-component brownian coagulation: Monte Carlo simulation and process characterization. *Particuology*, 9:414–423, 2011.

[275] G. Zhou. *Numerical simulations of physical discontinuities in single and multi-fluid flows for arbitrary Mach numbers.* PhD thesis, Chalmers University of Technology, 1995.

[276] K. Zhou and T.L. Chan. Simulation of homogeneous particle nucleation in a free turbulent jet. *Aerosol Sci. Tech.*, 45:8:973–987, 2011.

[277] J. Zhu, H. Qi, and J. Wang. Nanoparticle dispersion and coagulation in a turbulent round jet. *Int. J. Multiphase Flow*, 54:22–30, 2013.

[278] Y. Zou, M.E. Kavousanakis, I.G. Kevrekidis, and R.O. Fox. Coarse-grained computation for particle coagulation and sintering processes by linking quadrature method of moments with monte-carlo. *J. Comp. Phys.*, 229:5299–5314, 2010.

[279] A. Zucca, D.L. Marchisio, A.A. Baressi, and R.O. Fox. Implementation of the population balance equation in cfd codes for modelling soot formation in turbulent flames. *Chem. Eng. Sci.*, 61:87–95, 2006.

[280] A. Zucca, D.L. Marchisio, M. Vanni, and A.A. Barresi. Validation of bivariate DQMOM for nanoparticle processes simulations. *AIChE J.*, 2007:918–993, 53.

Appendices

A. PsiPhi Operation

The following sections briefly explain the basic concepts and methodologies employed by the Eulerian PsiPhi code. For the sake of generality the analysis is made for an un-filtered scalar quantity ϕ. The transport equation for ϕ reads:

$$\underbrace{\frac{\partial \phi}{\partial t}}_{\text{accumulation term}} + \underbrace{\frac{\partial (\phi U_i)}{\partial x_i}}_{\text{convective term}} = \underbrace{\frac{\partial J_i}{\partial x_i}}_{\text{diffusive term}} + \underbrace{\dot{S}_\phi}_{\text{source term}} \tag{A.1}$$

Transport equations of the type of (A.1) require discretization to be solved numerically. The equations are split (discretized) into elements of finite spatial and temporal width for which the equations can actually be solved. The number (width) of discrete elements used to solve each transport equation governs the resolution of the simulation.

A.0.1. Discretization in Space

PsiPhi uses a Finite Volume Method (FVM) for the spatial discretization. The FVM uses finite size control volumes where the equations are integrated. The interested reader may refer to Versteeg and Malalasekera [143] for an extensive review of the FVM in the context of CFD.

Integrating Eqn. (A.1) over a finite control volume V_{cell} yields:

$$\int_{V_{cell}} \frac{\partial \phi}{\partial t} dV + \int_{V_{cell}} \frac{\partial}{\partial x_i} (\phi U_i) dV = \int_{V_{cell}} \frac{\partial}{\partial x_i} \left[J_i(\phi) \right] dV + \int_{V_{cell}} \dot{S}_\phi dV. \tag{A.2}$$

For reasons that will become apparent, it is convenient to replace the convective and diffusive volume integrals of Eqn. (A.3) with surface integrals

using the divergence theorem[1], viz:

$$\frac{\partial}{\partial t}\int_{V_{cell}} \phi dV + \int_{\Delta A} \phi U_i e_i dA = \int_{\Delta A} J_i(\phi) e_i dA + \int_{V_{cell}} \dot{S}_\phi dV \qquad \text{(A.3)}$$

where e_i is the outward-pointing, unit-normal, vector on the boundaries of the control volume.

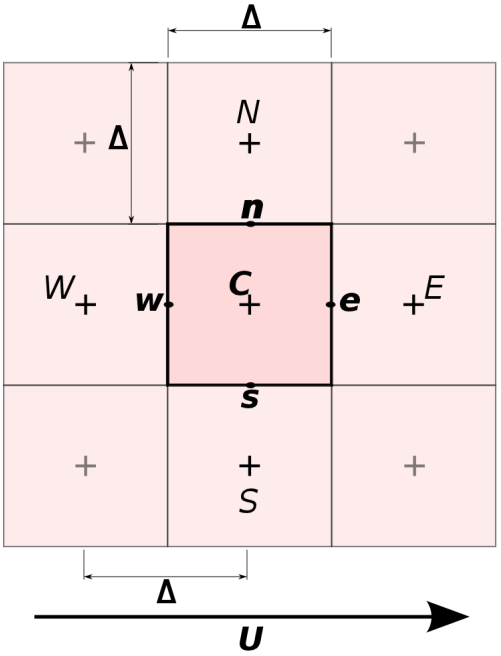


Figure A.1.: Finite Volume Method domain decomposition and indexing.

The four terms of equation (A.1) are solved in a series of control volumes (computational cells). Figure A.1, depicts a two-dimensional domain that has been discretized with a number of finite size control volumes. The PsiPhi code utilizes a structured, Cartesian, and pseudo staggered grid. Each computational cell has dimensions $\Delta \times \Delta \times \Delta$, and consequently a volume of $V_{cell} = \Delta^3$, where Δ is the grid spacing. The faces f_c of each cell are marked $f_c = n, e, s, w, front, back$ and represent the equivalent cardinal directions. The faces $front$ and $back$ are used to extend the solution to three dimensions and mark the cells 'front' and 'back' of the $2D$ Figure A.1.

Using as a frame of reference the cell-centre marked C the surrounding

[1] $\int_{V_{cell}} \frac{\partial \psi}{\partial x_i} dV = \int_{\Delta A} \psi e_i dA$

cell-centres are marked following the indexing used for cell faces (now in upper-case), namely $N, E, S, W, FRONT, BACK$. Having established the notation, the solution for each of the terms of Eqn. (A.1) proceeds as follows:

The remaining volume integrals (term I and IV) are approximated using equation (A.4) and can be readily evaluated for every computational cell:

$$\int_{V_{cell}} \phi dV = \phi_C V_{cell} \quad ; \quad \int_{V_{cell}} \dot{S}_\phi dV = \dot{S}_{\phi,C} V_{cell}. \tag{A.4}$$

The convective term (area integral) is rewritten as a sum over all fluxes $F_{C_{f_c}}$ passing through the faces normal to the control volume multiplied by the equivalent surface array ΔA_{f_c}. For equally sized grid spacing in all directions, the surface area is constant for all cell faces and $\Delta A_{f_c} = \Delta A$ yielding:

$$\int_{\Delta A} (\phi U_i) e_i dA = \sum_{f_c=n,e,s..} \phi_{f_c} U_{i,f_c} e_{i,f_c} \Delta A = \sum_{f_c=n,e,s..} F_{C_{f_c}} \Delta A. \tag{A.5}$$

Note that the index f_c represents values at the cell boundaries and differ to those at cell centers where upper-case letter indexes are used.

The diffusion term is discretized in a similar fashion to the convective term, where $F_{D_{f_c}}$ is now the diffusive flux passing through the faces normal to the control volume. The resulting sum is now over the diffusive fluxes through each surface boundary of the computational cell, namely:

$$\int_{\Delta A} J_i(\phi) e_i dA = \sum_{f_c=n,e,s..} J_{i,f_c}(\phi_{f_c}) e_{i,f_c} \Delta A = \sum_{f_c=n,e,s..} F_{D_{f_c,}} \Delta A, \tag{A.6}$$

where the diffusion coefficient with subscript f_c depicts the flux at the equivalent face. The dot product with the unit normal vector e_{i,f_c} gives the magnitude of the diffusive flux normal and outwards of the face f_c.

Inserting Eqn. (A.4)-(A.6) into Eqn. (A.3) yields the discrete transport equation (A.7) of ϕ solved for every cell of the domain.

$$\frac{\partial}{\partial t}(\phi_C V_{cell}) + \sum_{f_c} F_{C_{f_c,}} \Delta A = \sum_{f_c} F_{D_{f_c,}} \Delta A + \dot{S}_{\phi_C} V_{cell}. \tag{A.7}$$

At this point one may notice that for the solution of (A.7) values at cell boundaries and cell centers are required. PsiPhi uses a staggered grid, i.e.

the velocities are computed and stored at cell boundaries whereas all other variables are stored at cell-centres. Therefore, the values of the remaining transported quantities need to be interpolation at cell boundaries.

Convective fluxes at cell boundaries:
The simplest interpolation method to retrieve the values of the transported quantity ϕ at the cell boundaries $\phi_{f_c=n,e,s,..}$ is the Upwind Differencing Scheme (UDS). The UDS utilizes the scalar value at the upstream cell-centre to evaluate the equivalent ϕ_{f_c}. In the diagram of Figure A.1, the flow is from West to East. In this case, the value at the interface (for example at the East and West boundaries $f_c = e, w$) is approximated using the upstream cell-centre value (C and W), viz:

$$\phi_{f_c=e} \approx \phi_C \quad \text{or} \quad \phi_{f_c=w} \approx \phi_W. \tag{A.8}$$

UDS may have a significant truncation error because it is first-order accurate. UDS may therefore lead to over-diffusion and an unphysical smoothening of the scalar fields.

The Central Differencing Scheme (CDS) is a more accurate (second-order accuracy) alternative to UDS. To retrieve the value at the cell interface the average value of the two adjacent cells is used, for example:

$$\phi_{f_c=e} \approx \tfrac{\phi_E+\phi_C}{2} \quad \text{and} \quad \phi_{f_c=n} \approx \tfrac{\phi_N+\phi_C}{2}. \tag{A.9}$$

The CDS has a smaller truncation error compared to the UDS, however this truncation error may lead to instabilities. These instabilities can lead to values outside the physical range of the scalar.

An intermediate between the stable yet over-diffusive UDS and the unstable but accurate CDS is the Total Variation Diminishing (TVD) scheme. A TVD scheme inhibits convection from increasing the total variation of the transported scalar by indirectly bounding its value between the neighboring cell extrema (i.e. neighboring minimum and maximum values). A value at a given cell surface is given by:

$$\phi_{f_c=e} \approx \phi_C + \frac{B(r)(\phi_C - \phi_W)}{2}, \tag{A.10}$$

where the flux limiter $B(r)$, is a function of the gradient r, which is defined

as:

$$r = \frac{\phi_E - \phi_C}{\phi_C - \phi_W}. \tag{A.11}$$

There is a number of functional relations for the TVD flux limiter in the literature, such as the Van Leer [126], SUPERBEE [207], and Sweby [236], among others (see [143]). In this work the non-linear CHARM limiter function is used as defined by Zhou [275]:

$$B(r) = \begin{cases} r(3r+1) & : \quad r > 0 \\ 0 & : \quad r \leq 0 \end{cases} . \tag{A.12}$$

Diffusive fluxes at cell boundaries:

As for the discretization of the convection term, the diffusion term also requires knowledge of the diffusive flux at cell boundaries as shown in equation (A.6). To evaluate J_{i,f_c} a gradient diffusion approximation is used that assumes that the diffusion rate is proportional to the gradient of the variable ϕ evaluated at the cell interface:

$$J_{i,f_c}(\phi_{f_c}) = D_\phi \frac{\partial \phi}{\partial x_i}\bigg|_{f_c}, \tag{A.13}$$

where D_ϕ is the constant of proportionality for the transported quantity.

The diffusion flux (for example across the eastern boundary of the cell) is therefore given by:

$$F_{D_{f_c=e}} = D_\phi \frac{\partial \phi}{\partial x_i}\bigg|_{f_c=e} e_{i,f_c=e} \approx D_\phi \frac{\phi_E - \phi_C}{\Delta} \Delta A_{f_c=e}. \tag{A.14}$$

A.0.2. Discretisatization in Time

A LES provides solutions to transient fields, consequently the transport equations must be integrated in time. Equation (A.1) can be rearranged such that the RHS involves solely spatial discretization whereas the LHS only temporal, viz:

$$\frac{\partial \phi}{\partial t} = -\frac{\partial (\phi U_i)}{\partial x_i} + \frac{\partial J_i(\phi)}{\partial x_i} + \dot{S}_\phi = RHS(\phi) \tag{A.15}$$

The temporal evolution can be discretized by a series of time intervals nt of duration Δt. The discrete formulation of (A.15) depends on the scheme

used.

The most straight forward scheme is the Euler-Explicit. The value of ϕ at a time-step $nt+1$ is calculated using its value at nt and $RHS(\phi)$ evaluated at nt, namely:

$$\phi^{nt+1} \approx \phi^{nt} + \Delta t \times RHS(\phi^{nt}) \tag{A.16}$$

All values in the right hand side of (A.16) can be readily evaluated from the known ϕ^{nt} of the previous time-step. The drawback of the Euler-Explicit scheme is that it is only first-order accurate.

As a remedy to the low accuracy of the Euler-Explicit scheme, PsiPhi uses a third order low-storage Runge-Kutta scheme [257]. The time integration is split into three sub-steps whose size depends on the previous sub-step, and each sub-step is weighted differently:

$$\begin{aligned}
\phi^{nt+\frac{1}{3}} &\approx \phi^{nt} + \tfrac{\Delta t}{3} \times a_1 RHS(\phi^{nt}) \\
\phi^{nt+\frac{3}{4}} &\approx \phi^{nt+\frac{1}{3}} + \tfrac{5\Delta t}{12} \times \left[a_2 RHS(\phi^{nt+\frac{1}{3}}) + b_2 RHS(\phi^{nt})\right] \\
\phi^{nt+1} &\approx \phi^{nt+\frac{3}{4}} + \tfrac{\Delta t}{4} \times \left[a_3 RHS(\phi^{nt+\frac{3}{4}}) + b_3 RHS(\phi^{nt+\frac{1}{3}}) + \tfrac{b_2}{a_2} RHS(\phi^{nt})\right]
\end{aligned} \tag{A.17}$$

where the weights are:

$$a_1 = \frac{1}{3}, \;\; a_2 = \frac{15}{16}, \;\; a_3 = \frac{8}{15}, \;\; b_2 = -\frac{75}{144}, \;\; b_3 = -\frac{51}{81}. \tag{A.18}$$

The interested reader may refer to [101, 229] for an extensive analysis of the employed Runge-Kutta scheme.

Finally, a low time-step width Δt increases resolution similarly to a low grid spacing Δ. A limiting maximum time-step is required to enforce stability. The most obvious distabilizing effect would occur if the temporal integration had a longer time-step compared to the cell flow-through time, i.e. if $\Delta/U < \Delta t$. In their work, Courant, Friedrichs, and Lewy [36] provide a limiting equation for the time-step width also termed the 'CFL condition', viz:

$$\Delta t \leq CFL \left(\frac{\Delta}{\max(|\mathbf{U}|)} \right) \tag{A.19}$$

The CFL condition states that the global time-step width of the integration should not exceed the minimum flow through time of the cell in the domain with the maximum velocity magnitude $|U|$. The constant 'CFL' is usually in the range of $0 < CFL < 1$. In this work and unless stated otherwise

$CFL = 0.3$.

A.0.3. Boundary Conditions

The boundary conditions for the simulation govern both the progress and the initialization of these variables. Depending on the test case investigated, the boundary conditions must facilitate both computational feasibility and accurate representation of the flow's physics. This section overviews the various boundary and initial conditions of the PsiPhi code.

Inlet Conditions:
A *Dirichlet* condition is used to prescribe the flow properties at the inlet of the domain.

$$\phi(x_i, t) = \phi_{in}(x_i, t) \tag{A.20}$$

Equation (A.20) prescribes the values of the transported and derived quantities at the inlet of the simulation. However, in turbulent flows the inflow fields experience fluctuations in their magnitude. These fluctuations must comply with the statistical characteristics of the particular case considered. If uncorelated random noise is superimposed to the values prescribed by Eqn. A.20, then these fluctuations will rapidly dissipate in the domain. Therefore, the spatial and temporal correlations of the fluctuations at the inlet have to comply with the statistical properties of the turbulent flow under investigation.

PsiPhi creates a pseudo-turbulent field with the experimental values of rms velocities and integral length-scales. Depending on the domain size and length scale in question, a number of *white-noise* planar slices (of the size of the inlet plane) are generated for every time-step. These slices are subsequently filtered to generate the experimental correlations of the velocity field, and scaled to a prescribed rms velocity. The fluctuating components are then superimposed to the prescribed values $\phi_{in}(x_i, t)$ at the inflow for every time-step. A complete description of the operation of the inflow-turbulence generator exceeds the scope of this work; the interested reader may refer to Klein et al. [104] and Kempf et al. [100].

The inlet conditions may include periodicity. Periodic boundaries are used to spatially extend the domain in a certain direction by using the outflow conditions as the boundary conditions for the inflow. In a periodic

domain the inlet condition of (A.20) changes and the prescribed $\phi_{in}(x_i, t) = \phi_{out}(x_i, t-\Delta t)$, where $\phi_{out}(x_i, t-\Delta t)$ is the field at the outlet of the periodic side in the previous time-step.

Outlet Conditions:
A *von-Neumann* condition is used for the transported scalars and a *positive-outflow* conditions is used for the momentum at the open boundaries of the domain.

$$\frac{\partial \phi_{out}}{\partial x_j} n_j = 0 \quad ; \quad U_{i,out} = max(U_i, 0) \tag{A.21}$$

The *von-Neumann* condition used here sets a zero gradient for the scalar normal to the outlet boundary. The velocity field is clipped to enforce a positive outflow thus avoiding fictitious mass re-entering the domain. The potential problems of this approach is that the positive outflow condition may supress recirculation regions near the domain outflow. A large enough simulation domain has to be selected to avoid the influence of the outflow boundaries on upstream locations of the domain that are of interest.

Finally, The code employes an *Immersed Boundary* method to treat walls within the domain. In the context of this work, only inflow/outflow boundary conditions are used as the cases considered do not include internal walls. The interested reader may refer to the work of [260] for an overview of the immersed boundary treatment.

B. Collision Array Calculation

The aggregation kernel is symmetric and hence it needs to be calculated once per pair i, j. The parcels within a given cell are therefore sorted in ascending diameters. The sorting is implemented using an intrinsic function which returns the element index location of the maximum diameter that appears *first* in the cell-particle array. Therefore even when two parcels are of equal mean diameters the sorting method will randomly place them in two adjacent –yet different– cells. Using the aforementioned model assumption of one directional aggregation the collisions array developed for each cell is upper diagonal (given the ascending order allocation) with a lower diagonal equal to zero. Consider for example a cell containing a total of $n_{tot,cell} = 5$ parcels, the collisions from $i \rightarrow j$ are:

$$n_{coll,ij} = \begin{bmatrix} n_{coll,11} & n_{coll,12} & n_{coll,13} & n_{coll,14} & n_{coll,15} \\ 0 & n_{coll,22} & n_{coll,23} & n_{coll,24} & n_{coll,25} \\ 0 & 0 & n_{coll,33} & n_{coll,34} & n_{coll,35} \\ 0 & 0 & 0 & n_{coll,44} & n_{coll,45} \\ 0 & 0 & 0 & 0 & n_{coll,55} \end{bmatrix}. \tag{B.1}$$

The calculation of the aggregation kernel and the relative number of collisions can be implemented in a nested loop whereby the outer loop iterates from say $i = 1 : n_{tot,cell}$ whereas the inner loop from $j = (1+i) : (n_{tot,cell}-1)$, where i and j are the parcel indices. This way the condition of (4.76) is implicitly taken into consideration and also the problem of not counting or double counting the collisions of two parcels with same mean diameters is avoided. The calculated array is then clipped according to Eqn. (4.73) if the total number of collisions exceeds the number of particles of the donor parcel $n_{int,i}$.